Investigating the brain in mouse models of Duchenne muscular dystrophy

Emine Bagdatlioglu

A thesis submitted for the degree of Doctor of Philosophy

Newcastle University
Faculty of Medical Sciences
Institute of Genetic Medicine
September 2017

Abstract

Duchenne muscular dystrophy (DMD) is an X-linked recessive muscle wasting disease caused by mutations in the *DMD* gene, which encodes the large cytoskeletal protein dystrophin. Alongside severe muscle pathology, one-third of DMD patients exhibit cognitive problems ranging from reduced verbal intelligence to severe autism. There is conclusive evidence that the muscle pathology exhibited by DMD patients is progressive, yet it remains unknown whether the cognitive impairments in DMD are also progressive. Previous studies have highlighted a cognitive impairment in the *mdx* mouse model of DMD, but no studies have investigated if this cognitive impairment worsens with age. We assessed the consequences of dystrophin deficiency on brain morphology and cognitive function in two dystrophin-deficient mouse models (*mdx* and *Cmah-/-mdx* mice). The overall project aim was to identify outcome measures to monitor central nervous system (CNS) pathology non-invasively in DMD mice.

Magnetic resonance imaging (MRI) identified a total brain volume increase in DMD mice, alongside morphological changes in brain ventricles. Behavioural testing revealed a deficit in hippocampal spatial learning and memory, particularly long-term memory, in *mdx* mice, which appears to progressively worsen with age. Immunoblotting identified a progressive reduction of aquaporin-4 (AQP4) expression, the major water channel of the CNS, in DMD mice. Moreover, contrast enhancing MRI and Evans blue extravasation demonstrated a progressive impairment in blood-brain barrier (BBB) integrity in *mdx* mice. Proteomic profiling of the *mdx* cerebellum identified changes in expression of mitochondrial subunit complexes, suggestive of changes in mitochondrial function. Additionally, elevated levels of inflammatory markers were identified and confirmed in the *mdx* cerebellum.

Our studies suggest that dystrophin deficiency causes a progressive cognitive impairment in *mdx* mice. We also present evidence showing that changes in osmotic equilibrium may be involved in the pathogenesis of DMD, with reductions in AQP4 expression and BBB disruptions. We speculate that some of the changes in the *mdx* cerebellar proteome, in comparison to wild type mice,

serve as compensatory mechanisms whilst others may contribute directly to cognitive dysfunction in DMD. These results support a role for dystrophin in normal brain morphology and cognitive function.

Dedication

This thesis is dedicated to patients with Duchenne muscular dystrophy and their families.

Acknowledgements

I would like to thank my supervisors Professor Volker Straub and Professor Andrew Blamire for their help, support, and guidance throughout this project and for also providing me with the opportunity to undertake this research. I am grateful for the opportunities and support that I have received from the John Walton Muscular Dystrophy Research Centre.

I would also like to thank Dr Andreas Roos and Dr Steven Laval for their advice with practical aspects of this project. Thanks to my PhD assessors, Professor Helen Arthur and Professor David Elliott, for their insightful knowledge. The animal care staff: Brigid Griffin, Steve Smith, Lynne Todd, and other members of the FGU have been instrumental in helping me with mouse work, without which this research would not have been possible. I would like to thank Dr Chris Blau and Ella Dennis for their help with the X-ray of mice.

Thank you to Dr Alison Blain and Elizabeth Greally for your time, support, and friendship over the past 4 years, you really helped me to settle into the team, made me feel welcome, and our discussions regarding the project have been incredibly beneficial.

Many thanks to Dr Paola Porcari and Dr Dara O'Hogain for setting up the MRI scan protocols. Thank you to Dr Ross Laws, Tracey Davey and Professor Jochaim Weis for their work on electron microscopy. I would also like to thank Vietxuan Phan for her work on cerebellar proteomic profiling.

A special thanks to my family: my parents, brothers, and sister for their continuous support and for always encouraging me to strive further, I am proud to share this with you.

Thank you to my friends at the IGM and outside, Yasmin Issop and Lauren Phillips, I have really enjoyed working together over the past 4 years and your constant encouragement, kindness, and help has been invaluable.

Lastly, I want to thank Tom Sage, for your never-ending patience, unwavering belief in my ability to complete this thesis, and immeasurable support.

This work was funded by the Medical Research Council UK.

Table of Contents

List of Figures

List of Tables

List of abbreviations

123 I-MZ SPECT	I-123 iomazenil single photon emission computed tomography
^{1}H MRS	High resolution localized magnetic resonance spectroscopy
3V	Third ventricle
4V	Fourth ventricle
Ab	Antibody
ABD	Actin binding domain
ACE	Angiotensin converting enzyme
ACN	Acetonitrile
AD	Alzheimer's disease
ADHD	Attention deficit hyperactivity disorder
ADP	Adenosine diphosphate
AGC	Automatic gain control
APAF-1	Apoptotic protease activating factor 1
AQP1	Aquaporin-1
AQP4	Aquaporin-4
ASD	Autism spectrum disorder
ATP	Adenosine triphosphate
BBB	Blood-brain barrier
BCA	Bicinchoninic Acid protein assay kit
BCSFB	Blood cerebrospinal fluid barrier
BDNF	Brain derived neurotrophic factor
BLA	Basolateral nucleus of the amygdala
BLAST	Basic local alignment search tool
BMD	Beckers muscular dystrophy
bmp	Beats per minute
bp	Base pairs
BSA	Bovine Serum Albumin
CA	Cornu Ammonis
Ca^{2+}	Calcium
$CaCl_2$	Calcium chloride

CAT	Clinical Assessment for Attention
CBF	Cerebral blood flow
CD38	Cluster of differentiation 38
CD47	Cluster of differentiation 47
CER	Cerebellum
CI NDUFB8	Complex 1 NADH dehydrogenase
CID	Collision induced dissociation
CII SDHB	Complex 2 Succinate dehydrogenase complex iron sulphur
CIII UQCRC2	Complex 3 Cytochrome b-c1 complex
CIV MTCO1	Complex 4 Cytochrome c oxidase
CK	Creatinine kinase
CMAH	Cytidine monophospho-Nacetylneuraminic acid hydroxylase
CNS	Central nervous system
CP	Choroid plexus
CSF	Cerebrospinal spinal fluid
CSP	Cavum septum pellucidum
CV-ATP5A	Complex 5 ATP synthase
Cys	Cysteine rich domain
D3V	Dorsal third ventricle
Da	Dalton
DAPI	4',6-diamidino-2-phenylindole
DG	Dentate gyrus
DGC	Dystrophin glycoprotein complex
dH_2O	Distilled water
DMD	Duchenne muscular dystrophy
dNTPs	Deoxynucleotide
DS	Downs syndrome
DTI	Diffusion tensor imaging
DTT	Dithiothreitol
EBD	Evans blue dye
EC	Entorhinal cortex
ECM	Extracellular matrix
EDTA	Ethylenediaminetetraacetic acid

EES	Extravascular extracellular space
EF-hand	Intracellular calcium binding motif
ER	Endoplasmic reticulum
ETC	Electron transport chain
EtOH	Ethanol
F1/F2	Filial 1/2 hybrid
FA	Fractional anisotropy
FDR	False discovery rate
FE	Field Echo
FGU	Functional genomics unit
Fmr1 KO	Fragile X syndrome knock out mouse
FOV	Field of view
FSAP	filter-aided sample preparation
FSEMS	Fast sequence echo magnetization sequence
FSIQ	Full scale intelligence quotation
FSIQ	Full scale IQ
FXS	Fragile X syndrome
GABA	gamma-aminobutyric acid
$GABA_A$-R	GABA A receptor
GAPDH	Glyceraldehyde 3-phosphate dehydrogenase
GAT3	GABA transporter 3
Gd	Gadolinium
GEF	Guanine nucleotide exchange factor
GEMSLL	Gradient echo multi slice look locker sequence
GFAP	Glial fibrillary acidic protein
GL	Granular layer
GLM	General linear model
GM	Grey matter
GO	Gene ontology
GuHCl	Guanidine hydrochloride
HCl	Hydrogen chloride
HIP	Hippocampus
HP	Hippocampus

HPLC	High performance liquid chromatography
IAA	Iodoacetamide
IF	Immunofluorescent staining
iNPH	idiopathic pressure hydrocephalus
IP	Intraperitoneal
IQ	Intelligence Quotient
IV	Intravenous
K	Potassium
Kb	Kilobase
kDa	Kilodalton
KI	Kyphotic index
Kir4.1	Potassium channel
KOH	Potassium hydroxide
LC-MS	Liquid chromatography–mass spectrometry
LTP	Long-term potentiation
LV	Lateral ventricle
M	Mean
m/z	Mass/charge
mA	Milliamps
MAG	Myelin-associated glycoprotein
mdx	C57BL/10ScSn-Dmdmdx mouse model
MEMS	Multi echo multi slice sequence
MES	2-(N-morpholino)ethanesulfonic acid
MF	Mossy fibres
ML	Molecular layer
MOPS	3-(N-morpholino)propanesulfonic acid
MRI	Magnetic resonance imaging
mRNA	Messenger Ribonucleic acid
MRS	Magnetic resonance spectroscopy
ms	Milliseconds
MSn	Number of MS/MS experiments
NAA	N-acetylaspartic acid
NaCl	Sodium chloride
NADH	Nicotinamide adenine dinucleotide
$NaHCO_3$	Sodium bicarbonate

NCAM	Neural cell adhesion molecule
Neu5Ac	N-actyl neuraminic acid
Neu5Gc	N-Glycolylneuraminic acid
NL2	Neuroligin-2
NMO	Neuromyelitis optica
nNOS	Neuronal nitric oxide synthase
NO	Nitric oxide
NOR	Novel object recognition
NOS	Nitric oxide synthase
NS	Non-significant
NVU	Neurovascular unit
OCT	Optimal cutting temperature compound
OXPHOS5	Oxidative phosphorylation antibody cocktail
PAG	Periaqueductal grey
PBS	Phosphate buffer saline
PC	Purkinje cell
PCR	Polymerase chain reaction
PDGFC	Platelet-derived growth factor C
PDZ	PSD-95/Discs large/Zona occludens 1
PET	Positron emission tomography
PFA	Paraformaldehyde
PFC	Prefrontal cortex
PG	Parahippocampal gyrus
PIQ	Performance intelligence quotation
PL	Purkinje neuron layer
PML	Paramedian lobule
PNS	Peripheral nervous system
PolySia	Poly sialic acid
ppm	Parts per million
RIPA buffer	Radioimmunoprecipitation assay buffer
ROI	Region of interest
RT	Retention time
RT	Room temperature
SBFSEM	Serial block face scanning electron microscopy

SC	Subicular complex
SD	Standard deviation
SDS-PAGE	Sodium dodecyl sulphate polyacrylamide gel electrophoresis
SE	Spin echo sequence
SEM	Standard error of the mean
SEMS	Sequence echo magnetization sequence
Sias	Sialic acids
SNAP25	Synaptosomal associated protein 25
SOP	Standardized operating procedure
SPM	Statistical parametric mapping
S-SCAM	Synaptic scaffolding molecules
T	Tesla
***T_1*-w**	T_1 weighted scan
***T_2*-w**	T_2 weighted scan
TAE	Tris base, acetic acid, EDTA
TBS	Tris-buffered saline
TBST	Tris-buffered saline and tween 20
TBV	Total Brain Volume
TE	Echo time
TEM	Transmission electron microscopy
TFA	Trifluoroacetic acid
TGFβ	Transforming growth factor beta
TH	Target hole
TI	Inversion time
TLE	Temporal lobe epilepsy
TQ	Target quadrant
TR	Repetition time
TSP-1	Thrombospondin-1
TSP-2	Thrombospondin-2
UTR	Untranslated region
v/v	Volume/volume
V3V	Third Ventricle
VBM	Voxel based morphometry
VDAC	Voltage dependent anion channel

VIQ	Verbal intelligence quotation
WAIS-III	Wechsler Adult Intelligence Scale III
WB	Western blot
WISC	Wechsler Intelligence Scale for Children
WM	White matter
WW	Domain that contains 2 conserved tryptophans and binds praline-rich proteins

Chapter 1. Introduction

1.1 Duchenne muscular dystrophy

Duchenne muscular dystrophy (DMD) is an X-linked recessive disease, occurring at an incidence of 1 in 3,600-10,000 live male births (Emery, 1991; Mah *et al.*, 2014). Although rare it remains the commonest of all muscular dystrophies. The less severe allelic form, Becker muscular dystrophy (BMD) occurs less frequently (1 in 10,000) and the clinical course is milder (Emery, 1991) (Bushby *et al.*, 1991). DMD is characterised by a severe pathology of the skeletal musculature causing progressive loss of muscle, with premature death frequently occurring in the third decade of life as a result of cardiac and respiratory complications (Wallace and McNally, 2009). This fatal disease arises from mutations in the *DMD* gene; the largest gene in the human genome, with 79 exons spanning 2.4 Mb (Davies *et al.*, 1988), and coding for a 427 kDa intracellular protein named dystrophin (Monaco *et al.*, 1986; Hoffman *et al.*, 1987a; Hoffman *et al.*, 1992; Roberts *et al.*, 1993). The extremely large size of the *DMD* gene contributes to a complex mutational spectrum, with more than 7000 mutations identified and a high spontaneous mutation rate is associated with this gene (Bladen *et al.*, 2015). Approximately one-third of DMD cases are as a result of spontaneous mutations whereas the other two-thirds occur through maternal inheritance (Aartsma-Rus *et al.*, 2006). Dystrophin forms part of a membrane spanning protein complex, the dystrophin-glycoprotein complex (DGC; Figure 1.1), which plays a pivotal role in anchoring the intracellular cytoskeleton to the extracellular matrix, stabilising the sarcolemma during muscle contraction (Hoffman *et al.*, 1987b; Campbell and Kahl, 1989; Ahn and Kunkel, 1993; Brown, 1997). Absence of dystrophin disrupts the DGC causing increased muscle membrane fragility. A cascade of events including influx of calcium into the sarcoplasm, activation of proteases and pro-inflammatory cytokines, and mitochondrial dysfunction, cumulate in progressive muscle degeneration (Blake *et al.*, 2002; Allen *et al.*, 2010; Gumerson and Michele, 2011). The severe phenotype associated with DMD is most often associated with out-of-frame mutations (Monaco *et al.*, 1988; Koenig *et al.*, 1989), causing complete loss of functional dystrophin protein. Whereas in-frame mutations allow for the synthesis of an internally truncated but partially functional

dystrophin protein product and are found in BMD patients, although exceptions to the reading frame hypothesis occur in <10% of all DMD mutations (Aartsma-Rus *et al.*, 2006). Although dystrophin is most abundantly expressed in muscle tissues, it is also expressed in the central nervous system (CNS) with the brain harbouring high amounts of dystrophin and its various isoforms. Considerable research has been devoted to understanding the role of dystrophin in muscle cells, its role in the brain has received less attention.

1.1.1 Clinical phenotype

DMD was first detailed in 1852 by an English physician: Edward Meryon (Meryon, 1852), the clinical manifestations of eight boys from three families were described, which highlighted progressive muscle wasting and weakening confined to muscles, leaving the nervous system unaffected (Meryon, 1852). This disorder was later named after Guillaume Benjamin Amand Duchenne who was indeed the first to study patient biopsies (Duchenne, 1868).

Progressive muscle wasting and weakness is the major hallmark of DMD, where patient muscle fibres are vulnerable to contraction induced damage, yet despite efforts of muscle to regenerate, muscle mass is gradually lost. DMD usually presents within the first few years of life, between the ages of two and five years old, and is characterised by calf muscle hypertrophy and a delay in motor milestones e.g. slow to begin walking, difficulties running and climbing stairs (Bushby *et al.*, 1999). The Gowers manoeuvre becomes evident when patients have difficulties rising from the ground and begin using their arms to climb up their body (Gowers, 1879). By the second decade of life patients are usually wheelchair dependent due to loss of strength in their lower limb muscles. Loss of function of all extremities occurs in the later stages of the disease due to progressive weakness of the shoulder girdle and arm muscles (Blake *et al.*, 2002).

Cardiac involvement is also a major characteristic of DMD with 90% of patients exhibiting cardiac dysfunction including 25% of patients under the age of 6 years old (Finsterer and Stollberger, 2003). Common cardiac complications in DMD include myocardial ischemia (leading to necrosis), conduction defects, and/or arrhythmias (Eagle *et al.*, 2002). One of the leading causes of death is

cardiomyopathy, where the heart chambers are dilated and ventricles have poor contractility causing a decreased ejection fraction (Finsterer and Stollberger, 2003). In the heart, degeneration of cardiomyocytes leads to fibrosis. Initially, this phenomenon affects particularly the posterobasal segment of the left ventricle (Goodwin and Muntoni, 2005). Loss of cardiomyocytes in DMD leads to an increase wall stress and the myocardium has an increased vulnerability to pressure overload *in vivo* compared to normal (Kamogawa *et al.*, 2001). Progressively, systolic left ventricle function decreases and myocardial oxygen consumption increases, eventually leading to left ventricular dilation and left ventricular dysfunction (Fayssoil *et al.*, 2010; Spurney, 2011).

In addition, patients often suffer from spinal deformities such as thoracolumbar kyphosis and scoliosis, resultant of asymmetric weakening of the muscles supporting the spine (Yamashita *et al.*, 2001; Eagle *et al.*, 2007). Furthermore, respiratory involvement is evident in later stages of the disease with assisted ventilation sought initially at night but progressing to a more permanent state (Lo Mauro *et al.*, 2010). A low bone mineral density, lower lean tissue and higher fat mass compared to healthy age matched controls results from DMD patients' immobility and one study found that by the age of 13 years old 47% of patients were obese and 34% were underweight primarily as a consequence of swallowing difficulties (Martigne *et al.*, 2011).

1.1.2 Current care strategies for DMD

There is currently no cure for DMD and treatment strategies aim to alleviate symptoms in addition to reducing muscle necrosis (Guglieri and Bushby, 2010). Strategies focus on optimising growth and development, promoting a well-balance diet, participating in physical and recreational activity, and delaying the onset of secondary complications through ongoing medical and psychosocial support (Zamani *et al.*, 2016; Wong *et al.*, 2017).

Supportive interventions include timely administration of corticosteroids. Corticosteroids are a group of steroid hormones produced naturally by the body and are involved in a wide variety of physiological processes such as the immune response, stress response, and regulation of inflammation (Greaves, 1976). Corticosteroids are an important treatment option in DMD as they have

anti-inflammatory, immunosuppressive, anti-proliferative, and vasoconstrictive effects, to slow the progression of inflammatory damage. Historically, corticosteroids have offered benefit to DMD patients through the stabilisation of muscle strength and function, delaying progression of scoliosis, prolonging independent ambulation and delaying onset of cardiomyopathy (Mendell *et al.*, 1989; Griggs *et al.*, 1991; Moxley *et al.*, 2005; Kinali *et al.*, 2007; Markham *et al.*, 2008). Other treatment options include respiratory care, where supportive strategies such as non-invasive positive pressure ventilation, assisted airway clearance, and mechanical cough assistance, can help some DMD patients live beyond their third decade of life (Lo Mauro *et al.*, 2010). Preventative cardiac care is also available through the early use of angiotensin-converting enzyme (ACE) inhibitors or beta-blockers to delay the progression of cardiomyopathy (Bushby *et al.*, 2010). Additionally, there are currently multiple therapeutic trials looking to restore, repair, and/or prevent further damage to muscle and it is hoped that in the future life expectancy and quality of life will improve further for DMD patients (Mendell *et al.*, 2013; Mah, 2016; Robinson-Hamm and Gersbach, 2016).

1.2 The dystrophin-glycoprotein complex (DGC)

1.2.1 DGC in muscle

In skeletal muscle, the DGC is comprised of three sub-complexes and their constituent proteins: the dystroglycan complex, the transmembrane sarcoglycan-sarcospan complex, and the cytoplasmic complex of dystrophin, dystrobrevins, and syntrophins (Ervasti and Campbell, 1991; Yoshida *et al.*, 1994). The dystroglycan complex consists of both α and β subunits (Allikian and McNally, 2007). The extracellular protein laminin-α_2 binds directly to α-dystroglycan, which in turn binds to β-dystroglycan, thus providing the initial link in the DGC to the extracellular milieu (Ervasti and Campbell, 1991). The cytoplasmic proteins of the DGC include α-dystrobrevin, α- and β-syntrophin, and dystrophin. α-dystrobrevin directly interacts with cytoplasmic dystrophin and β_1-and β_2- syntrophin (Lapidos *et al.*, 2004). α-syntrophin interact directly with dystrophin at its C-terminal as well as with α-dystrobrevin (Blake *et al.*, 2002). A more recently identified cytoplasmic DGC member, dysbindin, resides in muscle, where it associates with α-dystrobrevin (Benson *et al.*, 2001). In

skeletal muscle, neuronal nitric oxide synthase (nNO) interactions with the DGC are primarily through α-syntrophin (Adams *et al.*, 2001). In the absence of dystrophin, nNOS detaches from the sarcolemma, attenuating nitric oxide (NO) production. This leads to functional ischemia, in skeletal muscle, due to impaired vascular relaxation and in the heart decreased NO production is known to contribute to the development of a myopathy (Kanai *et al.*, 2001). Through syntrophin, the DGC is thought to anchor a variety of signalling molecules including: nNOS, kinases, and transporters in the muscle membrane, which are hypothesised to contribute to the secondary disease features such as inflammation and alteration of muscle regeneration (Kameya *et al.*, 1999; Inoue *et al.*, 2002). In addition, syntrophin interacts with aquaporin-4 (AQP4), a water channel, via a PDZ-binding domain (see Figure 1.1).

Dystrophin is the best characterised component of the complex (Koenig *et al.*, 1988; Ervasti and Campbell, 1993) and is organised into four (general) functional domains. First is the N-terminal actin-binding domain (ABD), containing two calponin homology motifs. The second is the triple-helical rod domain which is characterised by 24 spectrin- like repeats in three sub-regions separated by 4 proline rich hinges and contains a second ABD (able to bind actin primarily by electrostatic interaction (Amann *et al.*, 1998)) and the binding site for nNOS. The third is a cysteine-rich region responsible for binding to β-dystroglycan (composed of a WW domain, two EF hands EF1 & EF2, and a zinc-finger domain). Finally, the C-terminal end binds to α- and β-syntrophin and dystrobrevin (Koenig *et al.*, 1988). A change in dystrophin expression levels has a disproportionately large effect on the integrity of the DGC in muscle relative to other DGC components (Ervasti *et al.*, 1990).

Utrophin (a product of the *UTRN* gene) is an autosomal homologue of dystrophin. Similar to dystrophin, utrophin contains an N-terminal actin-binding domain and a C-terminal dystroglycan-binding domain (Tinsley *et al.*, 1992). Utrophin is expressed ubiquitously in many fetal and adult tissues, including liver, spleen, skeletal muscle and testes (Love *et al.*, 1991). Utrophin localises in the neuromuscular junction of adult skeletal muscles, where it is focused at the sarcolemma in regenerating muscle fibers (Tinsley *et al.*, 1992). Utrophin therapy has improved dystrophic symptoms in mice (Squire *et al.*, 2002).

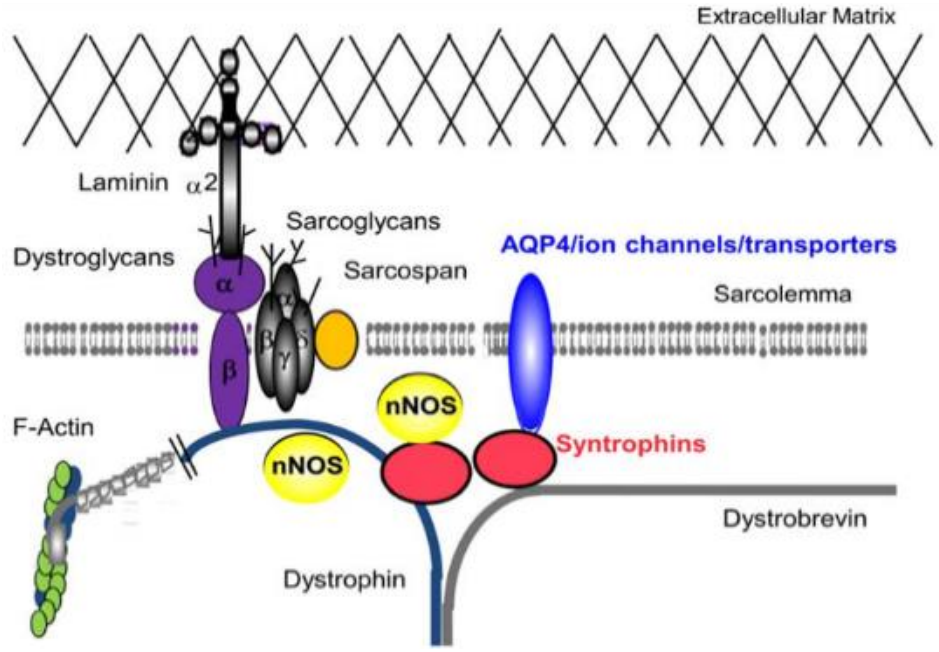

Figure 1.1: A schematic representation of the components of the muscle dystrophin-glycoprotein complex (DGC). This complex protein network is known as the dystrophin-glycoprotein complex (DGC) and has multiple interactions with other proteins. The DGC is critical in connecting the cytoskeleton of muscle fibres to the surrounding extracellular matrix by spanning the cell membrane. Dystrophin interacts with sarcomeric F-actin at its N-terminus (NH_2) and transmembrane protein β-dystroglycan at a cysteine-rich domain (Cys) close to its C-terminus (COOH), where dystrophin is associated with nNOS. β-dystroglycan interacts with the sarcoglycan complex as well as α-dystroglycan on the extracellular side of the sarcolemma. Aquaporin-4 (AQP4) is a major water channel enriched at the sarcolemma of skeletal muscle and is theorised to have a role in accommodating the rapid changes in cell volume and hydrostatic forces that may occur during muscle contraction to prevent sarcolemma damage (Crosbie *et al.*, 2002). Figure from:(Khurana and Davies, 2003; Nichols *et al.*, 2015).

1.2.2 The DGC in brain

Within the CNS dystrophin is expressed in a specific population of neurons responsible for higher order functions, including learning and memory. Dystrophin is localised to cerebellar Purkinje cells (PCs), hippocampal neurons, and pyramidal neurons of the cerebral cortex of the human brain (Lidov *et al.*, 1990). Dystrophin expression is greatest in the cerebellum where it is localised as discrete puncta along the somatic and dendritic membranes of PCs in both mice (Lidov *et al.*, 1990; Lidov *et al.*, 1993) and humans (Uchino *et al.*, 1994). Dystrophin has is also been identified to extensively colocalise within a subset of γ-aminobutyric acid type A ($GABA_A$) receptor clusters found in the cerebellum, hippocampus and cerebral cortex (Knuesel *et al.*, 1999).

In addition to dystrophin expression in the brain, other DGC components have also been found to be expressed within the CNS. Both α- and β-dystroglycan are found in pyramidal neurons of the cortex (Zaccaria *et al.*, 2001). Cerebellar Purkinje cell (PC) dendrites and soma reportedly express α-dystroglycan in a punctate distribution similar to that seen for dystrophin (Zaccaria *et al.*, 2001). More recently, sarcoglycans have been detected within the CNS; ε-sarcoglycan has been localised to PC soma and dendrites identified by immunofluorescence imaging (Chan *et al.*, 2005). Syntrophins, one of the cytoplasmic proteins of the DGC, has been observed in the granule cells of the cerebellum in both isoforms α_1 and β_2 (Gorecki *et al.*, 1997). In contrast to the DGC of muscle fibres, the transmembrane protein sarcospan has not been identified in the CNS and is not believed to be a member of the neuronal DGC (Pilgram et al., 2010). Furthermore, the brain DGC contains proteins that are not expressed in the muscle DGC, including β-dystrobrevin and γ-syntrophin (Piluso *et al.*, 2000).

Unlike muscle tissue, there are multiple DGC-like complexes present in the brain (Blake *et al.*, 1999). Discrepancies regarding the precise localisation of dystrophin and various DGC components in the CNS are perhaps due to variation in the quality of immune-detection methods (i.e. staining and protein analysis). For example, dystrophin localisation in the cerebellum has yielded inconsistent results; some studies report abundant cytoplasmic staining of full-length dystrophin in mouse cerebellum (Lidov *et al.*, 1990), whereas others report negligible cytoplasmic labelling (Huard and Tremblay, 1992).

1.3 The DMD gene and dystrophin

The *DMD* gene has 7 promoters resulting in various sized dystrophin protein products (Figure 1.2). The promoters located in the proximal region of the gene give rise to three full-length dystrophin isoforms: Dp427b (brain), Dp427m (muscle) and Dp427p (Purkinje), which have the same number of exons, but differ in terms of their respective promoter and unique first exon (Holder *et al.*, 1996). The brain promoter drives expression predominantly in the hippocampal cortical neurons, the Purkinje promoter in PCs, and the muscle promoter in both skeletal muscle and cardiomyocytes (Muntoni *et al.*, 2003). As a consequence

of splicing events and alternative transcripts, four shorter dystrophin isoforms are created (via promotors located in introns) producing protein products Dp260 in retina, Dp140 in brain, retina and kidney, Dp116 in Schwann cells, and Dp71 with ubiquitous expression in most non-muscle tissues (Byers *et al.*, 1993; D'Souza *et al.*, 1995). Full length dystrophin (Dp427), absent from patients with DMD, is found in neurons which are specifically involved in cognitive functions, including memory formation and learning: cerebellar PCs, and the pyramidal neurons of the cerebral cortex and hippocampus (Mehler, 2000). The shortest dystrophin isoform, Dp40, is produced by alternative splicing of the Dp71 transcript and little is known about its function, but it is theorised to have a role in presynaptic function via interactions with synaptic vesicles (forming a novel complex) in the mouse brain and is therefore implicated in cognitive functioning (Tozawa *et al.*, 2012).

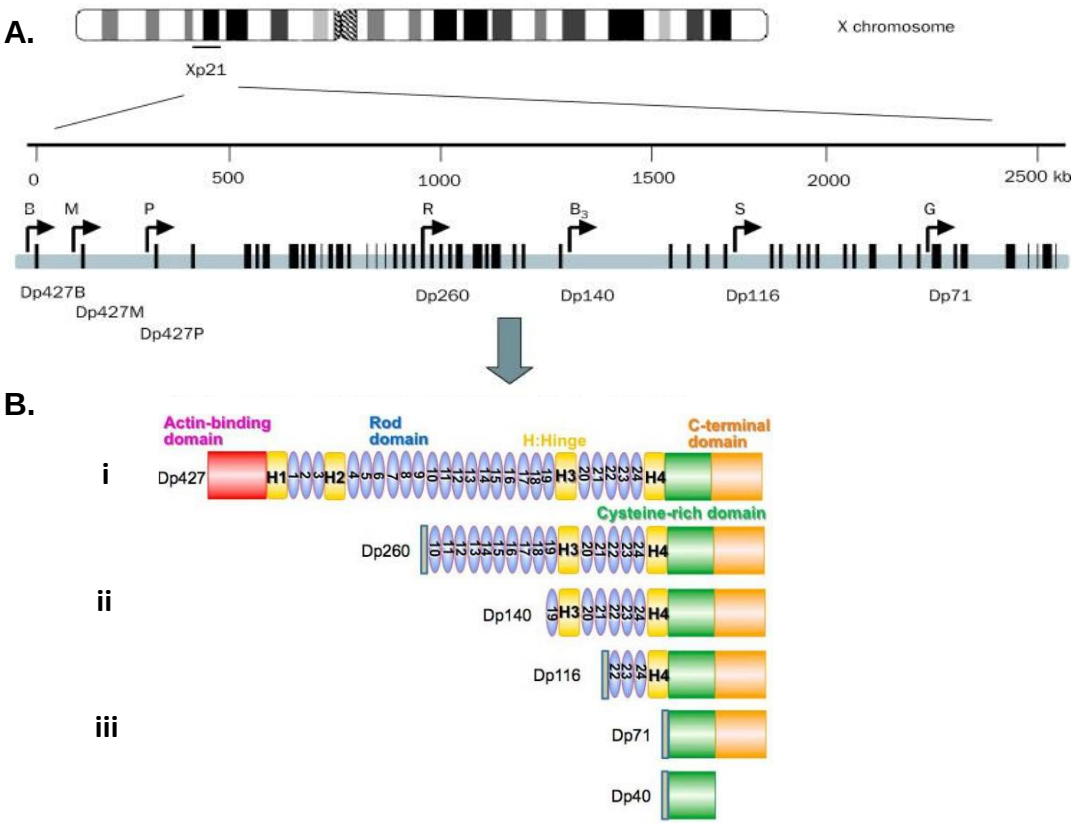

Figure 1.2: Genomic organisation of the *DMD* gene and dystrophin protein isoforms. A. Shows the location of the DMD locus at Xp21. The black arrows indicate the various promoters: the brain promoter (B), the muscle promoter (M), and Purkinje promoter (P) which give rise to full-length dystrophin (Dp427b, Dp427m, and Dp427p respectively). Another brain promoter (B_3) also gives rise to the shorter Dp140 isoform implicated in cerebral dysfunction (Moizard *et al.*, 1998), which alongside with the Dp71 isoform, controlled under a general (G) promoter, is associated with cognitive impairment in DMD patients (Moizard *et al.*, 1998). Dp260 is predominantly expressed in the retina. **B.** i. Structure of the full-length 427 kDa isoform of dystrophin, which consists of an N-terminal actin binding domain, a rod domain of 24 spectrin-like repeats, a cysteine rich region, a carboxy-terminal domain (COOH) and also possesses 4 hinge regions. ii. Summarises the Dp140 shorter isoform structure which has only 6 spectrin-like repeats and 3 hinge regions in the rod domain. iii. The short isoform Dp71, expressed in most tissues, lacks any of the central rod domain repeats and possesses only 1 hinge region. The shortest isoform of dystrophin, Dp40, is thought to lack all or most spectrin- like repeats in addition to the COOH terminal region. Figure adapted from: (Blake *et al.*, 1995; Muntoni *et al.*, 2003; Nichols *et al.*, 2015).

1.4 Cognitive functioning in DMD

Intellectual impairment has long been recognised as a disease symptom in DMD. Indeed, even in the earliest reports of the disease, De l'electrisation localisée, patients were identified with an obvious cognitive deficit (Duchenne,

1868). Developmental delay has also been detailed by clinicians to be amongst the first signs at disease presentation. However, prior to 1960 the cause of cognitive disability in DMD patients was attributed to functional disabilities and social environment (Morrow and Cohen, 1954) and until recently relatively few studies had addressed this disease parameter.

It is generally acknowledged that the average IQ of DMD patients is 85, one standard deviation below the norm (Cotton *et al.*, 2001; Cotton *et al.*, 2005) and the frequency of mental retardation is also higher in DMD; 20.9% versus 3% in the general population (Cohen *et al.*, 1968) (based upon IQ scores). Approximately one-third of patients with DMD have some degree of cognitive deficit frequently manifesting itself in memory impairment, but ranging from reduced verbal intelligence (Cotton *et al.*, 2001; Hendriksen and Vles, 2006) to severe autism (Wu *et al.*, 2005). Literature documenting cognitive impairments in DMD remains inconclusive regarding the severity of verbal intelligence affected (Cotton *et al.*, 2001). Compliance data for 32 studies from 1960-1999 were examined to determine the relationship between verbal intelligence quotation (VIQ) and performance intelligence quotation (PIQ) (Cotton *et al.*, 2005). The results from the analysis of 1224 children and young adults with DMD (aged between 2-27 years old) with variable cognitive impairment revealed that VIQ and PIQ were one standard deviation below the population mean, with at least one-third of DMD patients in the study producing scores indicative of mental retardation (Cotton *et al.*, 2005). Overall this study demonstrated and confirmed a decreased general cognitive functioning in DMD and illustrated a decreased verbal relative to non-verbal cognitive ability, but not to a high extent (Cotton *et al.*, 2005). The potential association between VIQ, full-scale intelligence quotation (FSIQ) and PIQ in DMD was examined and revealed that age and disease severity were indeed related with more advanced IQ impairments exhibited in older DMD patients. However, there was no difference in age groups with respect to PIQ, FSIQ or VIQ (Cotton *et al.*, 2001).

Memory deficits in DMD patients compared to age matched controls have also been reported (Anderson *et al.*, 1988). During a task boys were asked to recall the position of a series of pictures from the Peabody Picture vocabulary test (Dunn 1959). DMD patients had severe difficulties in the serial positioning

memory task in comparison to relative controls (Anderson *et al.*, 1988). More specifically, DMD patients had significant impairments in remembering the first four pictures presented in a series of eight. These studies are indicative of impairments in both verbal and visual memory of DMD patients (Anderson *et al.*, 1988).

There is conclusive evidence that the muscle pathology exhibited by DMD is progressive, yet it remains unknown whether the cognitive impairments in DMD are also progressive in nature. One study found no significant difference between FSIQ scores within a group of 29 DMD patients upon serial administration of the Wechsler Intelligence Scale for Children (WISC) two to six years after initial testing (Prosser *et al.*, 1969). However, VIQ appeared to increase with age whereas PIQ remained static. Conversely, a significant negative correlation between age and VIQ among DMD patients has been reported, suggestive of an intellectual decline in verbal domains with increasing age (Black, 1973). However, no correlation analysis between PIQ and VIQ was performed in these DMD patients. Other studies have yielded equally inconsistent results, DMD patients aged younger than 9 years old showed no difference on FSIQ, VIQ, or PIQ in comparison to DMD patients aged 10 years and over (Dorman *et al.*, 1988). In contrast other reports have noted that defects in verbal abilities were more prominent in younger versus older DMD patients (Miller *et al.*, 1985).

Although numerous studies define the cognitive deficit observed in DMD patients to be non-progressive in nature (Billard *et al.*, 1992), this proposition remains conjectural due to the lack of concrete long-term studies investigating this disease parameter. Additionally, these previous studies do no correlate intellectual abilities with morphological brain changes in DMD patients.

More recently investigators are highlighting a potentially progressive nature of cognitive aspects in older DMD patients. Recent studies have established that dystrophin colocalises with $GABA_A$ receptor ($GABA_A$-R) clusters at the postsynaptic membrane (Kueh *et al.*, 2011). The GABAergic system plays a key role in a variety of distinct neuronal processes, including regulation of neuronal excitability, synchronicity of local networks, and neuronal plasticity (Macdonald

and Olsen, 1994; Varju *et al.*, 2001). Additionally, the impact of the $GABA_A$-R on cognitive function has been emphasised in neurological disorders, including schizophrenia, trauma, and autism (Rudolph and Mohler, 2014). Moreover, there is recent evidence to suggest a significant decline in $GABA_A$-R within the prefrontal cortices of DMD patients (Suzuki *et al.*, 2017). Remarkably, the observed decline was more pronounced in older adult DMD patients, indicating that the observed decline in $GABA_A$-R was likely part of the disease process. Furthermore, investigators detected cognitive dysfunction in the Wisconsin Card Sorting Test (WCST), although IQ and global memory were virtually unaffected (Suzuki *et al.*, 2017). Likewise, age-related differences in WCST scores in the DMD group suggested that cognitive dysfunction would be progressive, as younger DMD patients out performed older DMD patients (18-37 years old) (Suzuki *et al.*, 2017).

1.4.1 Variable protein expression in DMD

There is a variable degree of cognitive deficits within the DMD population, possibly due to different mutations in the *DMD* gene. The probable link between the loss of dystrophin and brain abnormalities remains elusive with no concrete genotype-phenotype profile existing. Mutations in all parts of the *DMD* gene can be associated with cognitive impairment (Bushby *et al.*, 1995). However, mutations in the distal region of the *DMD* gene are more highly associated with cognitive abnormalities, as mutations encompass Dp140 and Dp71, compared to proximal gene mutations (Bushby, 1992; Lenk *et al.*, 1993; Daoud *et al.*, 2009; Taylor *et al.*, 2010). An apparent association of mental retardation and specific deletions has also been observed, with approximately 70% of patients with a deletion in exon 52 of the *DMD* gene exhibiting cognitive impairments (Rapaport *et al.*, 1991). Most recently, an association between the degree of cognitive impairment and the presence of mutation in the Dp71 isoform has been reported (Daoud *et al.*, 2009). Dp71 is the major product of the *DMD* gene in the brain but the precise function of this shortened DMD isoform remains unknown. High levels of Dp71 have been noted in neonatal and in adult brains, particularly in the hippocampus and in some layers of cerebral cortex (Sarig *et al.*, 1999). Subcellular distribution analysis has identified a gradual increase in brain expression from embryo to adult and Dp71 is mainly found in synaptic membranes, microsomes, and to a lesser extent synaptic vesicles and

mitochondria (Haenggi *et al.*, 2004). There is now substantial evidence that despite their rarity, all patients with mutations involving the Dp71 isoform have severe intellectual disability (Lenk *et al.*, 1993). Recent reports have identified multiple Dp71 transcripts, generated by several alternative splicing events, in the mouse brain and retina suggesting that these Dp71 isoforms are differentially regulated in tissues (Aragon *et al.*, 2017) and may have different functional roles.

With increasing amounts of research focusing upon the cognitive dysfunction observed in DMD, more evidence is emerging of a link between increased severity of cognitive impairment and loss of Dp140 and Dp71 isoforms. Other researchers have looked at the role of mutations affecting Dp140 in DMD, and concluded that mild mental retardation is significantly more frequent with mutations affecting Dp140 (Daoud *et al.*, 2009; Doorenweerd *et al.*, 2014). Additionally, there is increasing evidence detailing a significant effect of grouped isoform involvement on FSIQ which is clearly identifiable when the data are categorised into 5 groups: Dp427, Dp260+Dp140utr (mutations located in the extended 5′UTR of the Dp140 isoform, which leave the Dp140 promoter intact), Dp140pc (indicate mutations that affect the promoter and/or coding region of the Dp140 isoform), Dp116, and Dp71 (Figure 1.3). The data presented in the study identified that assignment of mutations to isoform groups provided a better explanation for the greater percentages of the variance in FSIQ compared to the consideration of the effects of mutations purely by location (Taylor *et al.*, 2010).

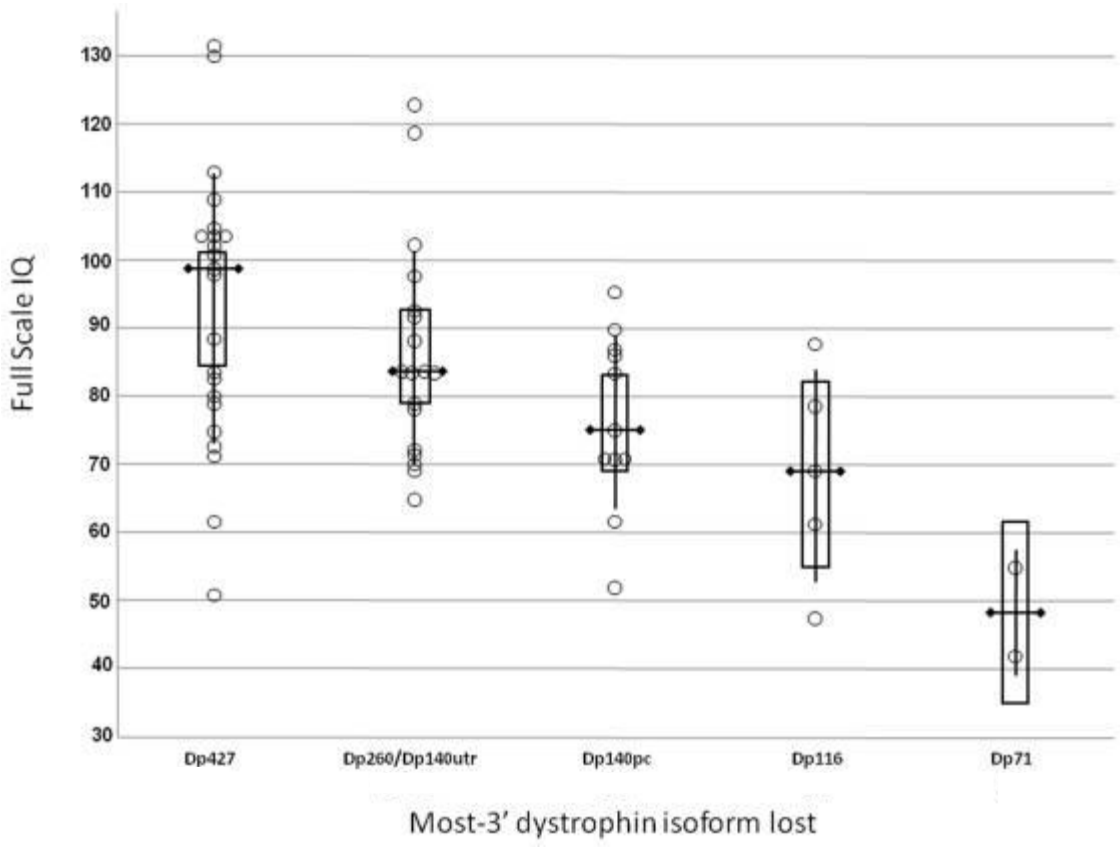

Figure 1.3: Effect of cumulative loss of dystrophin isoforms on full scale intelligence quotient (FSIQ) (adapted from (Taylor *et al.*, 2010)). A boxplot representation of patient full-scale intelligence quotient (FSIQ) data classified by the most 3′ dystrophin isoform affected by a mutation (each open circle represents a patient). There is a significant effect of grouped isoform involvement on FSIQ identified when the data were categorised into 5 groups: Dp427, Dp260+Dp140utr, Dp140pc, Dp116 and Dp71.

1.5 Potential role of dystrophin in the CNS

The understanding of dystrophin isoform expression and function within the brain remains to be fully elucidated. There are many types of cells within the nervous system which can be broadly split into two categories: neurons and glia (Figure 1.4). Within these categories there are many types of cells that differ in their structure, chemistry, and function. Neurons are the most important cells for the unique functions of the brain, it is neurons which can sense changes, communicate these changes to other neurons and command the bodies' response to these sensations. On the other hand, glia are thought to contribute to brain function mainly by insulating, supporting, and nourishing neighboring neurons (Mark F. Bear, 2007).

Neurons can be classified based on their number of neurites (axons and dendrites that extend from the soma), dendrites (branching projection of the neurons; in the cerebral cortex pyramidal cells are an abundant dendritic cell type), connections (neurons which only communicate with other neurons are known as interneurons), axon length (Golgi type I, II and III neurons based on their extend of projection from one part of the brain to the other), and neurotransmitter (amino acids, peptides, monoamines) (Mark F. Bear, 2007).

The most numerous glia in the brain are astrocytes, cells filling spaces between neurons. Astrocytes have multiple functions in the brain such as regulating the chemical content of the extracellular space and modulation of the blood-brain barrier (BBB) (Abbott *et al.*, 2010). Myelinating glia includes oligodendroglia and Schwann cells. Oligodendrocytes wrap around the neuronal axons for faster electrical signal transduction (Mark F. Bear, 2007) (Figure 1.4).

Other non-neuronal cells include ependymal cells and microglia. Ependymal cells provide the lining of fluid filled ventricles within the brain and also contribute to directing cell migration during brain development (Jiménez *et al.*, 2014). Microglia's function as phagocytes to remove debris left by dead or degenerating neurons or glia and present the main form of active immune defense (Kreutzberg, 1996).

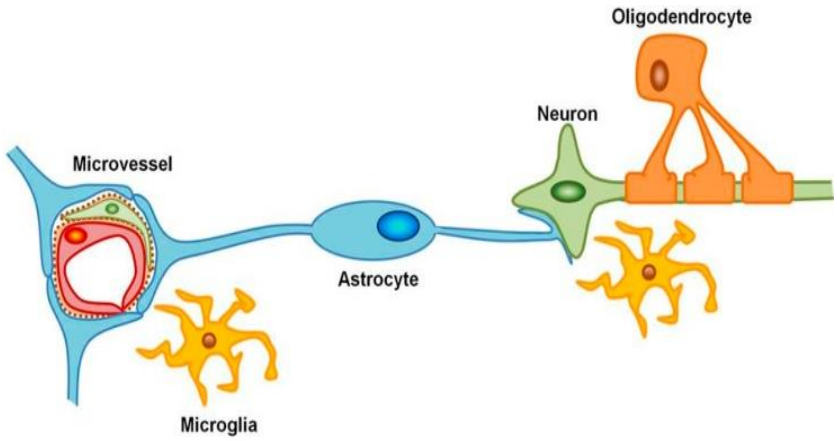

Figure 1.4: A schematic representation of the main cell types in the brain. Adapted from: (Abeysinghe *et al.*, 2016). Astrocytes are the most numerous brain glia and participate in many brain functions including ion homeostasis. Microglia, resident macrophage cells, acts as the first and main form of active immune defence in the central nervous system (CNS). The CNS houses oligodendrocytes for myelin synthesis, as neurons in the CNS are covered by a myelin sheath, providing electrical insulation.

Many investigators have postulated roles for the DGC in the CNS, but unambiguous evidence has yet to emerge. Current literature suggests that neuronal DGC composition is complex, with numerous isoforms expressed in different tissues and neuron specific localisation (Lidov *et al.*, 1993; Hendriksen *et al.*, 2015a). It has been suggested that the DGC may be acting as an adaptor between the actin cytoskeleton and membrane bound receptors acting to anchor molecules which are critical for neuronal functioning (Yoshihara *et al.*, 2003). The DGC may also participate in the formation and maintenance of macromolecular signalling complexes (Tokarz *et al.*, 1998). Furthermore, it is hypothesised that dystrophin may play a role in stabilising the postsynaptic apparatus during brain maturation in order to maintain a certain network status critical for synaptic plasticity (Brunig *et al.*, 2002). Dp427, for example, has been found to colocalise with $GABA_A$ receptors (Figure 1.5). It is hypothesised that following $GABA_A$ receptor insertion into the neural membrane, dystrophin is essential for their anchoring and clustering, which in turn is necessary for correct signal transduction. As a consequence, lateral diffusion of these receptors may be inhibited, hence contributing to their stabilisation (Craig and Kang, 2007; Hendriksen *et al.*, 2015a) (Figure 1.5). Other dystrophin isoforms appear to be expressed in a cell-specific manner: Dp140 appears to be associated with microvascular glia cells (Blake and Kroger, 2000), Dp116 is most abundantly found in Schwann cells of peripheral nerves, and Dp71 is the most highly expressed dystrophin in the brain (under control of the general promotor (G-dystrophin)) and is expressed in both neurons and glia (Austin *et al.*, 2000).

Overall the theory is that DGC components have a higher preference to localise at the post-synaptic membrane of neurons in brain regions that are critical for memory and learning abilities (the hippocampus, cerebral cortex, and cerebellum) which suggests that there is an extensive colocalisation with proteins involved in excitatory/inhibitory synapses (Lidov *et al.*, 1990; Brunig *et al.*, 2002; Levi *et al.*, 2002). Thus, it appears that the neural DGC plays a role in maintenance of receptors and ion channels.

Hypotheses regarding the variable expression of the cognitive deficits exhibited in DMD have highlighted the role of the cerebellum as paramount (Snow *et al.*,

2013). Numerous members of the DGC are distinctively localised in cerebellar PCs and their strong presence suggests that DGC members are essential for normal cerebellar functioning. The distinctly dense localisation of numerous members of the DGC in cerebellar PCs, and the comprehensive presence of dystrophin particularly in these neurons, is suggestive that DGC members, including dystrophin, play pivotal physiological roles in these neurons, and therefore contribute to proper cerebellar functioning (Grady *et al.*, 2006; Snow *et al.*, 2014).

A. Neuron **B. Astrocyte**

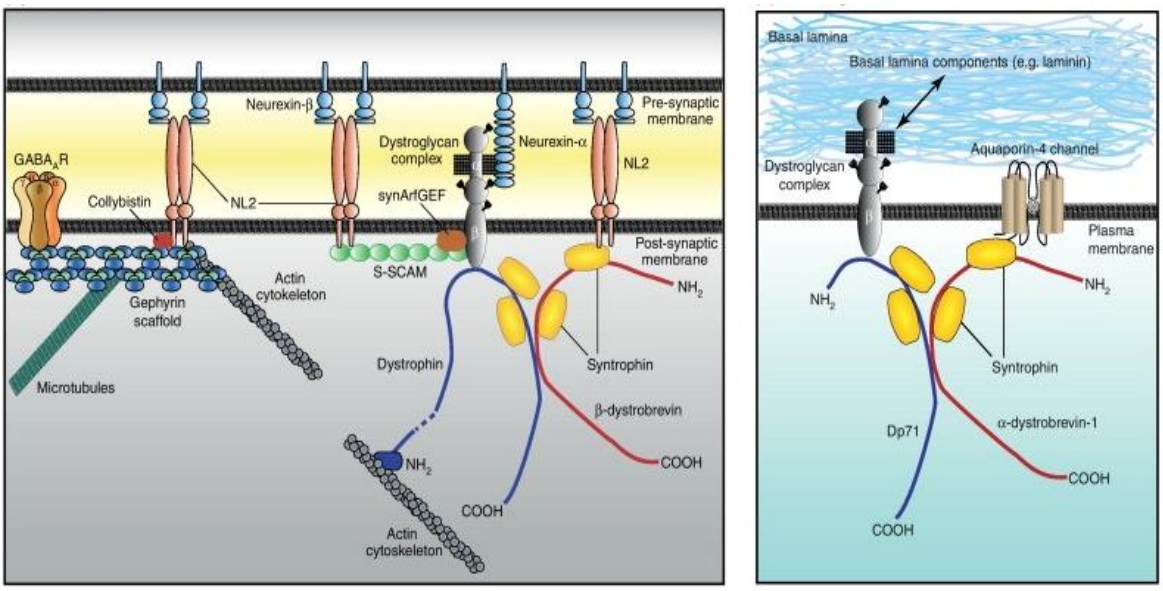

Figure 1.5: **Models of how the DGC and components may function within brain tissue** Adapted from (Waite *et al.*, 2012). **A.** Schematic representation of how the DGC may function within neurons. Neurexin-neuroligin trans-synaptic adhesion complexes drive the post-synaptic recruitment of scaffolding molecules where $GABA_A$-receptors ($GABA_A$-Rs) are anchored (Luscher et al., 2011a). Gephyrin, a scaffold protein, is critical for $GABA_A$-R clustering. NL_2 (neuroligin-2)-mediated activation of GEF (guanine nucleotide exchange factor) collybistin recruits Gephyrin to the postsynaptic membrane (Luscher et al., 2011b). In the cerebellum and hippocampus it is theorised that DGC-like complexes participate in Gephyrin –independent clustering of $GABA_A$-Rs (Brunig et al., 2002). It is hypothesised that the DGC is recruited to the postsynaptic membrane through a different neurexin-dystroglycan interaction and an indirect interaction with NL_2 via the synaptic scaffold protein S-SCAM (synaptic scaffolding molecules) (Sumita et al., 2007). SynArfGEF (ADP ribosylation factor), a GEF that shows preferential localisation to the inhibitory postsynaptic specialisations, associated with S-SCAM/NL_2/DGC complexes and could induce local actin cytoskeletal remodelling at inhibitory post-synaptic sites through activation of Arf6 and therefore regulate lateral diffusion and stabilisation of $GABA_A$-Rs (Fukaya et al., 2011). **B.** Hypothetical schematic representation of an astrocyte where the DGC-like complexes comprising Dp71, dystroglycan and the syntrophins are found at the specialised end-feet processes of perivascular astrocytes, where they cluster and co-purify with AQP4 channels. This interaction is theroised to involve PDZ (PSD-95/Discs large/Zona occludens 1) domain of α-syntrophin and a PDZ binding motif in the C-terminal tail of AQP4 (Amiry-Moghaddam *et al.*, 2003; Nicchia *et al.*, 2004b).

1.6 The Cerebellum and dystrophin

The cerebellum has a predominant role in controlling motor coordination (Glickstein and Doron, 2008) and more recent studies confirm the importance of

the cerebellum in non-motor functions including cognitive processing (Akshoomoff and Courchesne, 1992). The cerebellum contains almost half of the neurons within the brain (Andersen *et al.*, 1992) with multiple input and output projections, to both motor areas and non-motor areas of the cerebral cortex. The major anatomical subdivisions of the cerebellum include the flocculonodular lobe, which receives information on balance and equilibrium (Dow, 1961), and the lateral and vermal hemispheres (Figure 1.6). It has been widely documented that damage to the vermal hemisphere results in impaired motor behaviour, affecting equilibrium (Joyal *et al.*, 1996). Damage to the lateral hemisphere, which has received less attention, indicates this as being the cerebellar region involved in cognition. In addition, studies have documented activation of inferior-lateral hemispheres, particularly the activation of the M1 region in humans, whilst performing cognitive tasks e.g. mental imagery (Ryding *et al.*, 1993). Cognition is less easily definable in rodents but can be addressed through processes underlying abilities deemed to be 'cognitive' (e.g. spatial learning). To illustrate, lesions to the lateral cerebellar hemispheres hamper spatial learning abilities but have no effect on motor capabilities (Lalonde and Strazielle, 2003), however lesions to the vermal cerebellum cause impaired visual guidance to target platforms (Joyal *et al.*, 1996). Granted, cognitive abilities differ between the species, and any extrapolation of cognitive function from rodents to man must be treated with caution, but what is evident is that there is clear localisation of motor and mental functioning within sub-regions of the cerebellum.

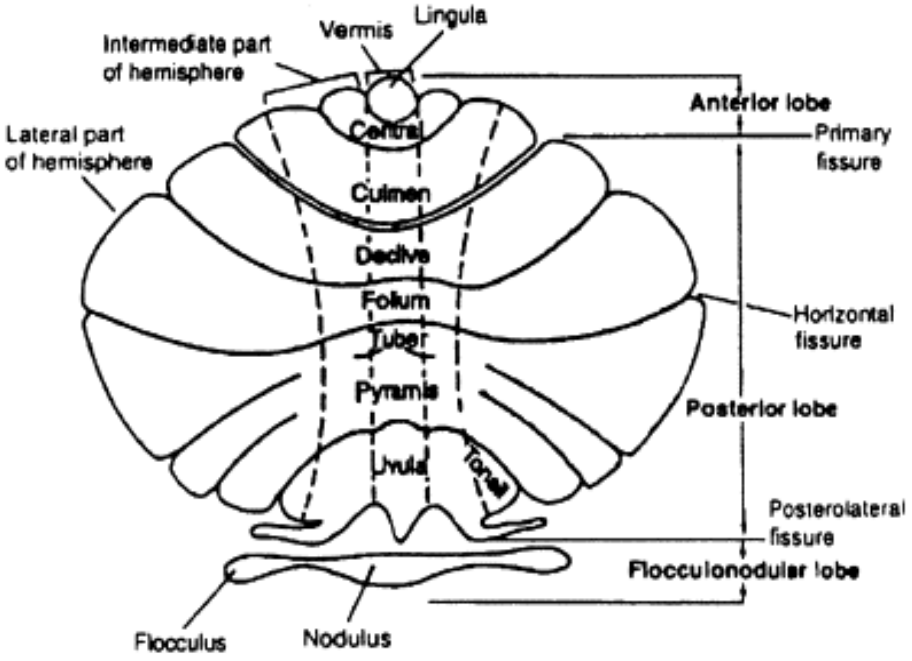

Figure 1.6: A schematic representation of the anatomical and functional division of the cerebellum. (Figure adapted from (Lai, 2010; Haines and Dietrichs, 2012)). The main body of the cerebellum is divided by the primary fissure into anterior and posterior lobes. The posterolateral fissure separates the flocculonodular lobe. Shallower fissures divide the anterior and posterior lobes into nine lobules (Lai, 2010). The vermal cerebellum lies along the midline of the cerebellum, receiving information via spinocerebellar tracts regarding multimodal sensory input which in turn controls proximal and trunk muscle movement (Dow, 1961). The projections of the vermal cerebellum enter the brainstem and cortical areas via the fastigial deep cerebellar nuclei, which control the proximal movement of the body. The vermal hemisphere is separated from the lateral hemisphere by the intermediate zone, which receives distinct somatosensory input via spinocerebellar tracts concerning distal muscle movement (Dow, 1961). This zone projects to the interposed deep cerebellar nuclei. The 'Spinocerebellum' thus consists of vermal and intermediate zones. In contrast the lateral hemisphere, lying bilaterally of the vermal zone, receives information solely from the cerebral cortex (Dow, 1961). Phylogenetically this is deemed the newest portion of the cerebellum and is thus termed the 'Cerebrocerebellum' and is associated with cognitive functioning.

Cerebellar circuitry is complex with three cellular layers comprised of five neuronal subtypes. The granular cell layer (GCL) houses a vast number of granule cells, Golgi interneurons, and mossy fibres. The Purkinje layer (PL), is a monolayer of PC bodies (Mark F. Bear, 2007) (Figure 1.7). The final, outermost layer is the molecular layer (ML), comprised of the dendrites of PCs, basket and satellite cells, and granule cell axons. P-dystrophin, the third full length DMD gene product, is expressed in the PCs, which are the neurons that receive the highest synaptic input in the brain (Mark F. Bear, 2007). Synapses between the

PCs and parallel fibres are involved in synaptic plasticity and are subject to modification of their strength, dependent upon their successive summation, hence the importance of this neuronal subtype in cognitive function.

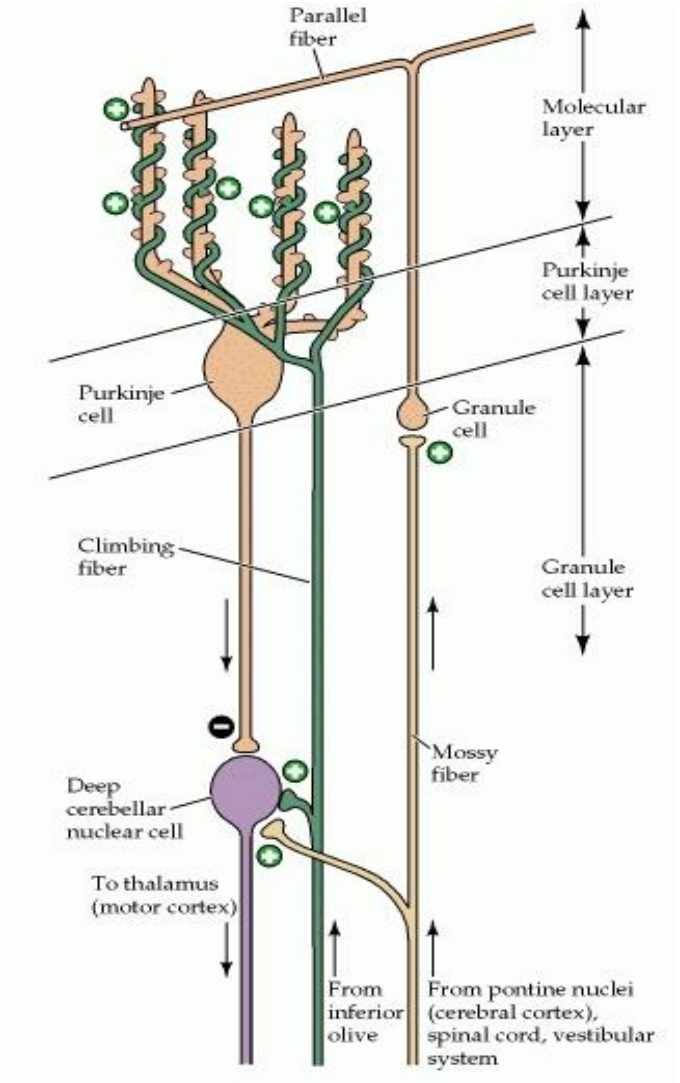

Figure 1.7: A schematic representation of cerebellar internal circuitry. '+'= excitatory synapse, '-'= inhibitory synapse. This rich interconnected sub-circuit and cortical neuronal arrangement is preserved across the subdivisions of the cerebellum (i.e. flocculonodular lobe, vermal and lateral regions). The only difference between the regions is the source of the mossy fibre (MF) input as well as the deep cerebellar nuclei (DCN) through which the processed signal ultimately leaves the cerebellum (Ito, 2006) Figure adapted from: (Purves D, 2001).

In addition to the expression of dystrophin in cerebellar PCs, other DGC components have also been identified (Smalheiser and Kim, 1995; Zaccaria *et al.*, 2001; Alessi *et al.*, 2006; Grady *et al.*, 2006). Within the cerebellum, α-dystroglycan is reported in membranes of PC dendrites and somata in a

punctate distribution similar to that reported for dystrophin (Smalheiser and Kim, 1995). Moreover, electron microscopy studies show preferential localisation of α-dystroglycan to postsynaptic specialisations in PCs (Zaccaria *et al.*, 2001). β-dystroglycan was recently identified in PCs and follows a similar punctate distribution as dystrophin in these cells. In PCs, both α-dystrobrevin and β-dystrobrevin have been identified (Grady *et al.*, 2006). Dystrobrevins appear in PCs and show a close colocalisation with dystrophin, gephyrin, and $GABA_A$-R clusters. This distribution indicates the presence of dystrobrevins at postsynaptic receptor sites (Grady *et al.*, 2006). Another component of the DGC; syntrophin, has been reported in brain tissue, including observation of both α_1- and β_2- isoforms of syntrophin within granule cells of the cerebellum (Gorecki *et al.*, 1997). Alternate γ_1- and γ_2-syntrophin isoforms are present in PCs (Alessi *et al.*, 2006). The γ-isoforms do not appear to form a strong association with dystrophin as is the case with α- and β-syntrophin isoforms. Syntrophins, however, have been shown to form a complex with Na^+ channel proteins in studies of membrane extracts from brain tissue (Gee *et al.*, 1998), but this relationship has not been examined in cerebellar tissue specifically. Syntrophin also interacts with inward rectifying K^+ channels from cerebellar tissue, as illustrated using protein purification techniques (Leonoudakis *et al.*, 2004). It is clearly evident that the DGC and its components have numerous and complex functions within the cerebellum. It is therefore widely accepted that loss of dystrophin from the DGC has a pivotal and complex impact on PC functioning by disrupting the DGC.

There are various claims that cognitive impairment seen in DMD is the result of a cerebellar disorder. Based on a cumulating research, it is proposed that the deficits in immediate verbal memory, or “limited verbal span”, seen in those with DMD, are cerebellar-mediated and arise from aberrations within the cerebrocerebellar loops emanating from the lateral cerebellum (Cyrulnik and Hinton, 2008). Authors hypothesise that an absence of dystrophin within the cerebellum impairs the maintenance and development of phonological memory stores and information rehearsal through cerebrocerebellar loops, likely due to impaired synaptic transmission (Cyrulnik and Hinton, 2008). A positron emission topography (PET) study showed that glucose metabolism is reduced in DMD, in areas that typically contain dystrophin, including the cerebellum (Lee *et al.*,

2002). Additionally, post-mortem studies have documented a decreased number of cerebellar PCs, consistent with the theory that the cognitive impairment observed in DMD is due to cerebellar dysfunction (Jagadha and Becker, 1988).

1.7 The hippocampus and dystrophin

The hippocampus has been identified as a key component in the consolidation of information particularly that pertaining to attention and memory (Mark F. Bear, 2007). The hippocampus is linked to a variety of memory systems including:

- Declarative memory; the long-term storage of facts.
- Procedural memory; the memory of skills, habit or behaviour.
- Working memory; the temporary storage and manipulation of information which is a necessity for the performance of complex cognitive tasks (i.e. reasoning and learning).

Hebb (1948) defined the hippocampus as an extension of the cerebral cortex and a complex structure consisting of multiple components. The hippocampal formation is comprised of four *Cornu Ammonis* areas, CA4 through to CA1, which are densely packed with pyramidal cells, the dentate gyrus (DG), the parahippocampal gyrus (PG), which includes the subicular complex (SC), and the entorhinal cortex (EC) (Figure 1.8). The small sub-regions of the hippocampus belie the fact that each region is in itself an intricate network of neurons which are postulated to each have unique functions within memory (Masser *et al.*, 2014). The pyramidal cells in the CA1 region of *mdx* mice have been shown to have an increased susceptibility to hypoxia induced damage, resulting in a synaptic transmission loss (Mehler *et al.*, 1992). This data suggests that DMD patients may exhibit increased susceptibility of neuronal populations to cumulative hypoxic insults contributing to the development of cognitive impairments.

The hippocampus is also one of the major sites of neurogenesis; the process where new neurons are generated from neural stem cells and progenitor cells, within the brain. The phenomenon of adult neurogenesis has been found to occur within the DG of the hippocampus (Gould and Gross, 2002).
Given our current understanding of the cellular basis of memory, adult neurogenesis may be a mechanism by which synaptic plasticity and associated memory are enhanced in the hippocampus. Neuronal progenitor cells from the sub-granular zone of the DG migrate into the granule cell layer, where they differentiate into neuronal or glial cells (Becker, 2005). Newly generated neuronal cells can then extend their axons into the CA3 region of the hippocampus shortly following their mitosis; axons from these cells can then form adjacent synapses (van Praag *et al.*, 1999). Younger granular cells appear to be more 'plastic' i.e. they have an enhanced long-term potentiation (LTP) inducible by a lower threshold induction (Schmidt-Hieber *et al.*, 2004), which is not inhibited by GABA (Wang *et al.*, 2000). It is therefore reasonable to presume that new cells form synaptic connections more rapidly.

However, increased proliferation of neurons in the DG may also disrupt information processing within the hippocampus. Thus, abnormally high or low levels of neurogenesis and the resulting abnormal patterns of synaptic connectivity or neural activity may contribute to cognitive impairments reported in DMD. Although the full functional relevance of adult neurogenesis remains unclear, it is theorised that hippocampal adult neurogenesis is important for learning. The proposed mechanisms behind the relationship between improved learning abilities and increased neurogenesis include: computational theories that new neurons increase memory capacity (Becker, 2005) and that new neurons help the DG to avoid the problem of catastrophic interference when adapting to new environments (Wiskott *et al.*, 2006).

Adult neurogenesis is subject to various regulatory factors including growth hormones and corticosteroids (Gould and Gross, 2002). Systemic administration of NOS inhibitors into adult mice increases cell proliferation in neurogenic regions of the brain, but decreases neuronal differentiation, indicating that nitric oxide (NO) can play an important role in regulating neurogenesis (Cheng *et al.*, 2003). Loss of nNOS expression and activity in

muscle is a pathologically important consequence of dystrophin deficiency and dystrophin mutation may in turn disrupt adult neurogenesis by promoting cell proliferation in the DG, suppressing neuronal differentiation. Thus loss of muscle nNOS may underlie defects in the CNS in DMD (Deng *et al.*, 2009).

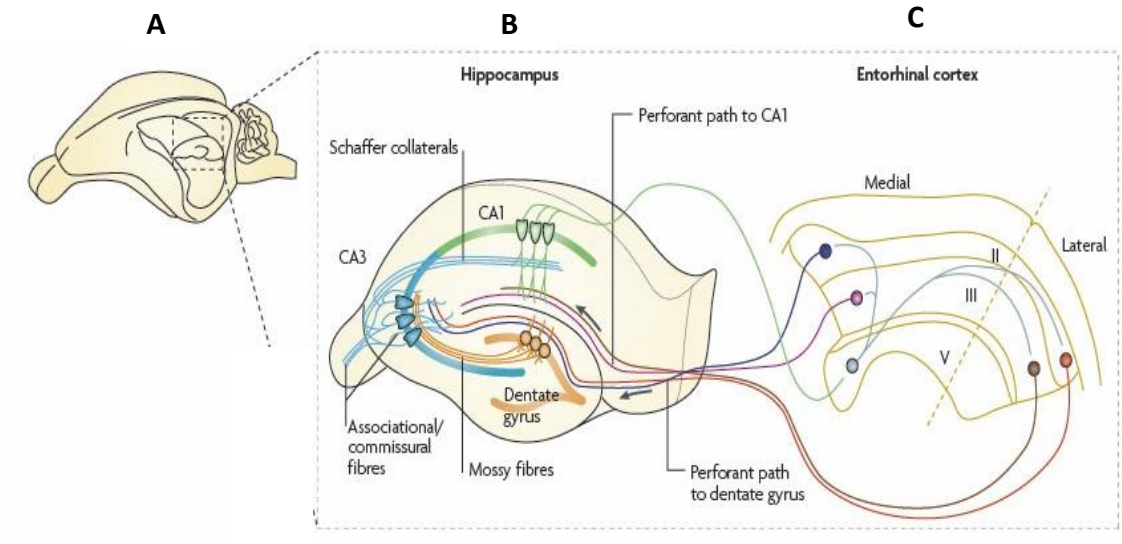

Figure 1.8: A schematic representation of the organisation of the anatomical and functional division of the mouse hippocampus. A. Diagram of a mouse brain showing the position of the hippocampus and a sagittal hippocampal slice. **B.** Circuitry and anatomical sub-regions within a hippocampal slice. **C.** Circuitry of the Entorhinal cortex (EC) linking with the subdivisions of the hippocampus. The EC provides the majority of external input to the hippocampus via axons of the perforant path. Projections from the CA1 region form a distinct pathway to the medial layer V of the EC known as the temporoammonic path. Figure adapted from: (Neves *et al.*, 2008)

1.8 Fluid movement within the brain

1.8.1 The blood-brain barrier (BBB)

BBB separates the parenchyma of the CNS from the blood. Formation of the BBB consists of endothelial cells, which line brain capillaries and are sealed by tight junctions unique to the brain microvasculature (Abbott and Friedman, 2012). The endothelium of the BBB provides both structural and functional support through interactions with several cellular and non-cellular components including: astrocytes, microglial cells, pericytes, and basement membranes (Obermeier *et al.*, 2013). This is known as an interactive cellular complex: neurovascular unit (Obermeier *et al.*, 2013) (Figure 1.9). The main role of the

BBB it to restrict the diffusion of substances, that are potentially neurotoxic, whilst still allowing the passage of essential molecules i.e. glucose. It is well documented that disruption of the BBB can contribute to numerous brain pathologies including Alzheimer's disease (Abbott and Friedman, 2012).

Aquaporins are a family of proteins that function as water channels in the brain. There are two main aquaporins in the CNS: AQP1 and AQP4. AQP1 is localised at the apical membrane of the choroid plexus (CP) whereas AQP4 is located in the astrocyte foot processes that surround capillaries in the CNS and the basolateral membrane of the ventricular ependymal cells (Nicchia *et al.*, 2004b). AQP1 has previously been implicated in choroidal CSF secretion, driven mainly by carbonic anhydrase and Na^+/K^+ ATPase (Owler *et al.*, 2010). AQP4 has been found in astrocytic endfeet, external and internal glial limiting membranes and the basolateral membrane of ependymal cells. The DGC is essential for the localisation of AQP4 to the endfeet of astrocytes, where its primary role is regulating the distribution of water through the brain. AQP4 also colocalises with the inwardly facing potassium channel- Kir4.1, which is crucial for the spatial buffering of potassium and thus neuronal excitability (Iacovetta *et al.*, 2012).

Mice deficient for AQP4 have increased seizure threshold in comparison to wild type (Binder *et al.*, 2006). Interestingly there is a higher incidence of seizures and epilepsy reported in the DMD population (Hendriksen *et al.*, 2015b), indicating a possible role for dystrophin and AQP4 in regulating neuronal excitability. However, there are discrepancies regarding the importance of AQP4 in maintaining the integrity of the BBB (Nicchia *et al.*, 2004a). Astrocytes at the BBB interface of the *mdx* brain show an age-related reduction in AQP4 expression, and AQP4 reduction was associated with swollen astrocyte processes (Frigeri *et al.*, 2004). AQP4 deficiency was associated with BBB breakdown, with consequent vasogenic oedema, and the presence of swollen perivascular astrocytes, indicating a close relationship between BBB integrity and control of the water flux by astroglial cells (Nicchia *et al.*, 2004b). Similarly, skeletal muscle fibres from *mdx* mice exhibited an age-dependent reduction in AQP4 expression with levels of the protein being 90% lower in 12 months old mutant mice as compared with age-matched control mice (Frigeri *et al.*, 2004).

These studies strongly implicate an essential role of AQP4 both in muscle and brain in maintaining the osmotic potential of tissues rich in dystrophin.

1.8.2 The blood-cerebral spinal fluid barrier (BCSFB)

The blood-cerebrospinal fluid barrier (BCSFB) functions together with the BBB and the meninges, to control the internal environment of the brain. However, the BCSFB displays fundamentally different properties to the BBB.

The production and circulation of CSF is carried out by four cavities (ventricles) located within the brain. The brain choroid plexus (CP) consists of epithelial tissue masses highly vascularised with fenestrated blood vessels of which there are four within the brain located in each ventricle (left and right lateral ventricles, third ventricle and fourth ventricle) and in turn produce two thirds of the CSF in the brain (Garton and Piatt, 2004; Liddelow, 2015). The remaining third of CSF is thought to be produced by the surface of the ventricles and the lining of the subarachnoid space (Liddelow, 2015). This fluid circulates in the ventricular system, subarachnoid spaces and spinal canal, where the plexuses are essential for controlling the homeostasis of CSF composition through regulation of movement of essential ions and molecules into, and metabolites out of the fluid (Liddelow, 2015). The BCSFB barrier is compromised predominately of the CP with other contributions from the arachnoid and arachnoid villi on the outer surface of the brain. Within the CP the basolateral membrane utrophin A and colocalised dystrophin impart structural stability, transmembrane signalling, and ion/water homeostasis (Johanson *et al.*, 2011).

The blood-brain barrier (BBB) and the blood cerebral spinal fluid barrier (BCSFB) provide protective restriction barriers, formed by bands of tight junctions between adjacent cells, which impede the movement of molecules into the CNS. When either is compromised, the brain is subjected to defects in fluid handling, impacting upon the brain’s osmotic equilibrium which in turn could have effects on normal cognitive functioning i.e. causing hydrocephalus.

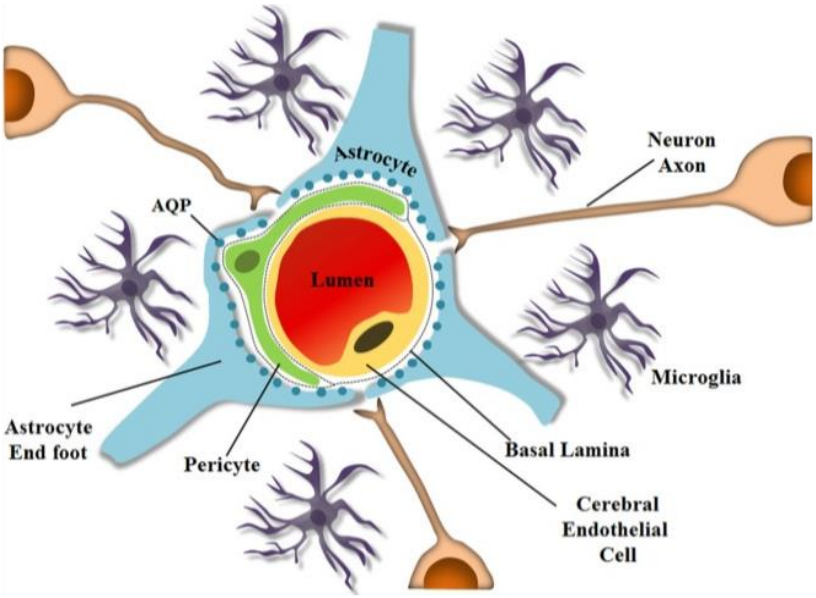

Figure 1.9: Schematic representation of the neurovascular unit (NVU) in the brain. The NVU is important in maintaining optimal brain function. Pericytes and astrocytes are important in barrier induction and maintenance. Within the brain dystrophin and other members of the DGC are diversely expressed, where they have essential roles in various protein complexes that anchor receptors to specialised membrane sites. Notably AQP4, which is the main water channel of the CNS, contributing to brain water homeostasis, is observed in the subpial membrane domains of astrocytes, where it is most abundant. AQP4 is theorised to interact with dystrophin and other members of the DGC, including β-dystroglycan (Waite *et al.*, 2012). Figure adapted from: (Dubois *et al.*, 2014).

1.9 Alteration of brain structure in DMD patients

Although macroscopic brain alterations like ventricular enlargement and cortical atrophy have been indicated in some DMD patients, imaging studies and brain autopsies have yielded ambiguous findings. One study concluded that no gross or histological brain abnormalities were found in DMD patients (Dubowitz and Crome, 1969b) after assessing 21 DMD boys on autopsy and found only one case of abnormal brain weight and two cases where there were ‘striking histological abnormalities’. Similarly, an MRI study in DMD boys found no focal or generalised brain changes, but the sample was very small (n=4) (Bresolin *et al.*, 1994). In another study of 15 DMD boys and 15 age-matched controls, no significant difference between these two groups in relative ventricular size was

found, but the boys participating in the study were still young (<13 years old) (Rae *et al.*, 1998). Cortical atrophy has also been identified in DMD but was found to be higher in patients older than 10 years (Yoshioka *et al.*, 1980), the patients in this study did however show slight ventricular dilation.

In contrast, a number of other studies have reported a broad range of brain abnormalities in DMD. The abnormalities identified include neuronal loss, heterotopia, gliosis, neurofibrillary tangles, Purkinje cell loss, dendritic abnormalities (length, branching and intersections), disordered architecture, astrocytosis, and perinuclear vacuolation (Rosman and Kakulas, 1966; Rosman, 1970; Jagadha and Becker, 1988; Itoh *et al.*, 1999; Anderson *et al.*, 2002). One study reported that macroglossia was associated with a lower IQ in DMD but the sample size was only small (Bresolin *et al.*, 1994).

Most recently it has been reported that both grey and white matter is affected in boys with DMD at a whole brain level (Doorenweerd *et al.*, 2014). Thirty DMD patients were examined and it was shown that they had a smaller total brain volume, smaller grey matter volume, lower white matter fractional anisotropy, and higher white matter mean and radial diffusivity than healthy controls (Doorenweerd *et al.*, 2014). The study also investigated the effect of expression of the dystrophin isoform Dp140, which has previously been implicated in cognitive ability (Felisari *et al.*, 2000). DMD patients also performed worse on neuropsychological examination also, with the subgroup that was null for Dp140 showing the highest grey matter volume differences and performing worse on information processing (Doorenweerd *et al.*, 2014). These findings thus suggest that there is an important role for the Dp140 dystrophin isoform in cerebral development.

1.10 The use of corticosteroids in DMD

In animals, hippocampal injury has been shown to be caused by over exposure to corticosteroids causing both reversible and irreversible changes in hippocampal structure and cognition (McEwen, 1997). In humans, chronic use of steroids can have both physiological and psychological side effects, including increased appetite, osteoporosis (altered bone remodelling), rapid mood swings, anxiety and depression (Brown and Chandler, 2001). In addition,

steroid treatment can affect brain morphology, studies of steroid treatment in asthmatic patients or patients suffering from rheumatic diseases demonstrated a reduced hippocampal and amygdala volume (Brown *et al.*, 2008). Since the majority of patients with DMD are currently receiving corticosteroids, the results pertaining to changes identified in the brain (Doorenweerd *et al.*, 2014; Doorenweerd *et al.*, 2017a), may be confounded as steroid treatment could have an effect on brain morphology. This highlights the importance of preclinical research; the effect of dystrophin deficiency can be studied in treatment and treatment naïve conditions without surpassing ethical boundaries.

1.11 Mouse models for DMD

Animal models are a fundamental component of preclinical research. It is essential that animal models are well characterised and accurately mirror the disease severity and progression in patients, in addition to providing a reliable prediction of treatment effect (Varga *et al.*, 2010). In order for an animal model to be deemed 'good', it must meet a number of criteria: a similar genetic basis as the human patient; key hallmarks of the disease; readily available; easy to maintain; a well characterised disease progression; a robust phenotype and a reproducible disease course. Mice are commonly used as animal models because they are cost-effective to house, easy to genetically manipulate, and relatively close to humans (Varga *et al.*, 2010).

1.11.1 The mdx mouse model of DMD

Currently the best characterised and gold standard mouse model of DMD is the *mdx* mouse. This naturally occurring dystrophin deficient mouse model has a premature stop codon in exon 23 of the *Dmd* gene, a null allele for dystrophin protein expression (Bulfield *et al.*, 1984), and was discovered in 1984 in a *C57BL/10* wild type colony. This genetically appropriate murine homologue of DMD, lacking full length dystrophin expression, but retaining the shorter isoforms including Dp71 and Dp140 implicated in cognitive functioning (Moizard *et al.*, 1998), also exhibits deficits in cognitive ability expressed in terms of memory retardation paradigms (Muntoni *et al.*, 1991), and passive avoidance tests such as impaired retention in the T-maze (Vaillend *et al.*, 1995). The *mdx* mice were shown to forget newly learned information much faster than control mice (Vaillend *et al.*, 1995). Discrepancies regarding the validity of the *mdx*

mouse as a model for DMD result from the reduced disease severity these mice portray. Loss of ambulation, cardiac and respiratory related muscle weakness and reduced lifespan are all hallmarks of DMD, but these pathological effects are less pronounced in the *mdx* mouse (Stedman *et al.*, 1991; Connolly *et al.*, 2001). With the exception of the diaphragm, no other tissues exhibit fibrosis extensive enough to cause muscle loss which is comparable enough to that of DMD patients (Chamberlain, 2010). A number of approaches have been employed to increase the disease severity of the *mdx* mouse but the discrepancies regarding the phenotype still remain (Willmann *et al.*, 2009). The lack of knowledge regarding the function of dystrophin within the brain calls into question whether the *mdx* mouse models the human brain phenotype, especially considering the mild muscular phenotype of the *mdx* mouse.

1.11.2 The Cmah-/-mdx mouse model of DMD

To circumvent the issue regarding the mild disease phenotype expressed by the *mdx* mouse a double mutant mouse, the *Cmah-/-mdx*, carrying a homozygous human-like mutation in the mouse *Cmah* gene, has been generated (Chandrasekharan *et al.*, 2010). This model has thus far demonstrated a more severe pathology, exhibiting a muscle phenotype that more closely resembles that of DMD patients (Chandrasekharan *et al.*, 2010).

Cytidine monophospho-N-acetyl neuraminic acid hydroxylase (*CMAH*) gene is known to have been deleted in humans approximately 3 million years ago, prior to brain expansion during evolution (Chou *et al.*, 2002). However, it is present in nearly all other mammals (Hedlund *et al.*, 2007). It encodes for CMAH, an enzyme found in the cytosol that catalyses the generation of N-glycolylneuraminic acid (Neu5Gc) from N-acetylneuraminic acid (Neu5Ac) (Figure 1.10).

All vertebrae cells express a dense glycan layer often terminated with sialic acids, which have multiple functions due to their location and diverse modifications. Sialic acids are a large group of more than 50 naturally occurring acidic, nine-carbon backbone monosaccharides. Neu5Gc and Neu5Ac are the most commonly found sialic acid in mammals and have been found to play a role in cell-to-cell adhesion, in inflammatory processes, as well as in immune

response (Diaz *et al.*, 2009). Contrasting with other organs that express various ratios of Neu5Ac and Neu5Gc dependent upon the variable expression of *CMAH*, Neu5Gc expression in the brain is very low in all vertebrates, suggesting that neural expression is detrimental to animals (Naito-Matsui *et al.*, 2017). In addition there is the theory that low levels of residual brain Neu5Gc in other mammals somehow limited brain expansion and that the human *CMAH* mutation released our ancestors from such a constraint (Chou *et al.*, 2002).

Due to the deletion, humans lack Neu5Gc and no alternate de novo pathway has been found (Bergfeld and Varki, 2014). However, several studies have shown Neu5Gc to be sparsely expressed in human tumours and neural precursor embryonic stem cells (Malykh *et al.*, 2001). Furthermore, a low level of Neu5Gc has been found in normal human tissues as a consequence of incorporation from diet, particularly those rich in red meat and milk, that accumulates throughout life (Diaz *et al.*, 2009). Several studies have established that mice homozygously deleted for *Cmah* have an increased susceptibility to certain pathogens, disturbed hearing and inner ear morphology, defective wound healing, and increased glucose intolerance (Kavaler *et al.*, 2011).

Recently, the incorporation of this deletion into the *mdx* mouse aimed to create a mouse model that has a more similar phenotype to that of the DMD patient in addition to a more homologous genetic background. Currently, there is only one study which describes the effect of the *Cmah* deletion in mouse skeletal muscle, demonstrating increased disease severity and significantly reduced lifespan (Chandrasekharan *et al.*, 2010). It is theorised that this particular change in sialylation capacity is a major contributor to the mild phenotype exhibited by the *mdx* mouse, given that the *CMAH* gene is absent in DMD patients, who show a more severe phenotype. This is possibly due to two unrelated mechanisms, firstly reduced strength and expression of the DGC and secondly increased activation of the complement system (Chandrasekharan *et al.*, 2010). The first involves both weakened expression and function of the DGC, including reduced ECM binding to α-dystroglycan and reduced expression of utrophin, with a similar homology to dystrophin, that when overexpressed can ameliorate disease, as well as reduced expression of other DGC members (Deconinck *et*

al., 1997). Additionally, loss of DGC expression or strength would contribute to the weakening of the sarcolemmal membrane and the integrity in muscle fibres (Bardor *et al.*, 2005). Secondly, the metabolic accumulation of dietary Neu5Gc, generation of Neu5Gc-specific antibodies and the deposition of activated (C5b-9) complement on muscle fibres (Nguyen *et al.*, 2005). Because *Cmah*-deficient *mdx* myofibers, like DMD myofibers, appear to preferentially take up Neu5Gc from diet, they may better mimic the role of dietary Neu5Gc in priming immune responses to regenerating muscle, a process that would seed the destruction of the very cells needed to overcome dystrophic muscle damage (Chandrasekharan *et al.*, 2010). This could potentially speed up skeletal muscle wasting in DMD, the mechanism that eventually causes muscle failure and mortality in patients.

For the current study both the *mdx* mouse model and the *Cmah-/-mdx* double-mutant mouse model will be employed in all experiments in order to ascertain whether any phenotypic differences, regarding cognitive functioning, exist between these mice.

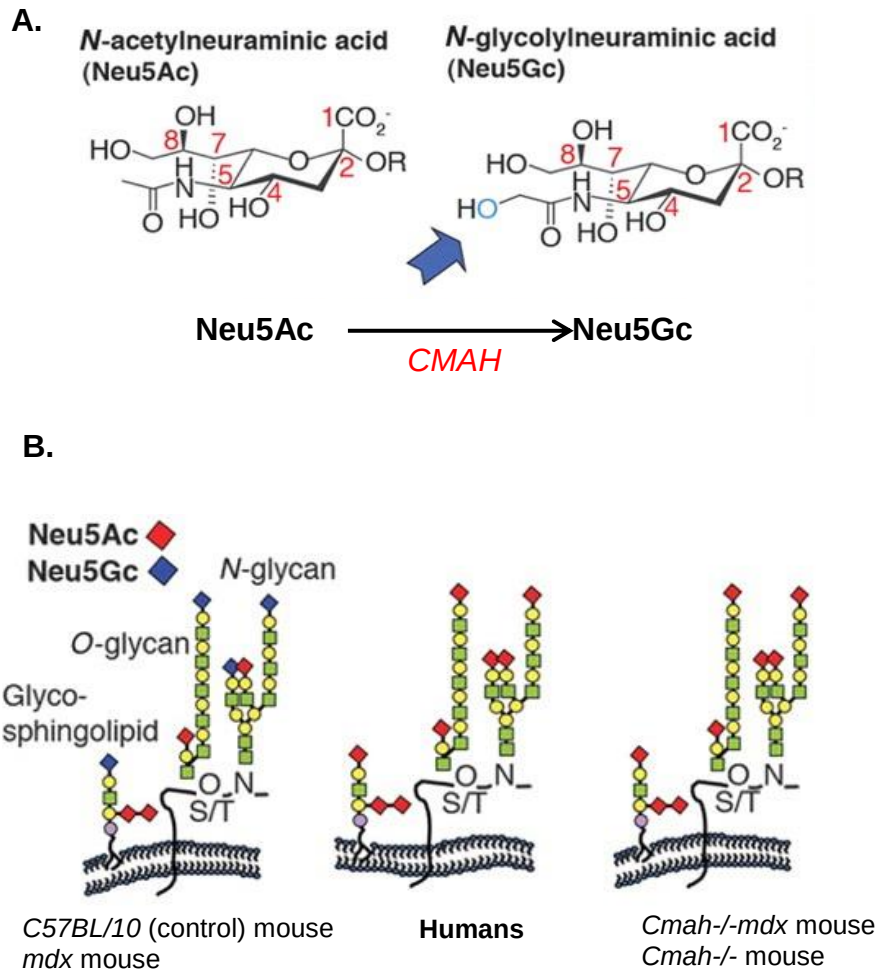

Figure 1.10: Differing expression levels of Neu5Ac and Neu5Gc in human and mice cells. **A.** N-glycolylneuraminic acid (Neu5Gc) differs from N-acetylneuraminic acid (Neu5Ac) by an additional oxygen at the 5 position of this sialic acid. **B.** Since mice express a functional *Cmah* gene they are capable of incorporating sialic acids (Sias) at the outer ends of glycolipids and glycoproteins that is usually either Neu5Gc or Neu5Ac. Humans and Cmah null mice, by contrast, contain an inactivating deletion in *Cmah*, and therefore do not express Neu5Gc on the surface of glycoconjugates but instead have increased Neu5Ac. Figure adapted from: (Chandrasekharan *et al.*, 2010).

1.12 Statement of aims

1.12.1 Overall study aims:

As therapy development for DMD has rapidly expanded in recent years, there is urgent need to develop reliable outcome measures to monitor disease progression and treatment effects. There is wide availability of standardised operating procedures (SOPs) to unify experimental protocols for characterisation of the *mdx* mouse muscle and cardiac phenotypes, which can subsequently be employed to monitor treatment effect, but no such SOPs exist for identifying and monitoring cognitive dysfunction in the *mdx* mouse. Non-invasive methods are essential for detecting and monitoring CNS pathology in dystrophin deficient mice. The overall aim of this study was to employ non-invasive methods: MRI and behavioural studies, to assess the CNS in DMD mice. The *mdx* mouse is routinely used for drug development studies and there is now an increased interest in understanding the origin of cognitive dysfunction in DMD. The lack of outcome measures to study the loss of dystrophin on brain function in the *mdx* mouse hinders the prospect of developing SOPs to ensure comparable, robust, and consistent findings between labs.

Given that the current knowledge regarding brain dystrophin expression and function is sparse, it is envisaged that a combination of techniques will afford a better insight into the function of neuronal dystrophin. The major focus of this project will be the development and application of quantitative MRI, including contrast enhanced methods, to assess structural and pathological brain changes in mouse models of DMD. Non–invasive methods, such as *in vivo* imaging and behavioural studies are important for longitudinal measurements but additionally, we aim to complement these studies by utilising histological investigations and immunoanalysis of brain tissue to determine potential biochemical alterations.

The *mdx* mouse will be compared against another mouse model of DMD, the *Cmah-/-mdx* mouse model, to establish whether the *mdx* mouse is the most appropriate preclinical mouse model for studying the brain phenotype seen in DMD boys.

1.12.2 Hypotheses to be tested

1. Loss of the *CMAH* gene correlates with brain expansion in mice.
2. A blood-brain barrier (BBB) impairment causes changes to brain osmotic equilibrium and becomes more apparent with increasing age in *mdx* mice.
3. Cognitive impairment is progressive in *mdx* mice and cognition can be monitored using a battery of behavioural tests.
4. Non-invasive imaging will reveal neuroimaging biomarkers that have the potential to be used for preclinical studies in the DMD mouse models.

1.12.3 Specific chapter aims

Chapter 3

The aim of this chapter is to longitudinally monitor, in the same mouse, changes in DMD mouse brains between 4 and 18 months old. Specifically, this chapter will employ MR imaging techniques to gain an insight into how the brain develops over time in DMD mouse models (*mdx* and *Cmah-/-mdx* mice) compared to age matched control mice.

Chapter 4

This chapter aims to monitor if the cognitive dysfunction, due to the loss of full-length dystrophin, progresses with increasing age in *mdx* mice. Additionally this study will characterise for the first time the *Cmah-/-mdx* mouse behavioural phenotype and determine how, if at all, the *mdx* and *Cmah-/-mdx* mice differ from each other cognitively.

Chapter 5

This chapter aims to determine if the BBB is disrupted due to the loss of full length dystrophin by utilising a combination of techniques including: immunohistochemical studies, immunoanalysis of brain tissue and quantitative MRI.

Chapter 6

This chapter aims to determine the biochemical changes occurring in the *mdx* cerebellum due to the loss of full-length dystrophin, which is abundant in Purkinje cells.

Chapter 2. Materials and Methods

2.1 Buffers and solutions

Phosphate buffered solution (PBS)

2 x PBS tablets

1000 ml dH_2O

4% (w/v) paraformaldehyde (PFA) in PBS

2 x PBS tablets

500 ml dH_2O

3 pellet NaOH

40 g PFA

pH 7.4 (adjusted with NaOH)

Volume adjusted to 1000 ml dH_2O

Tris-buffered saline (TBS) 10x

60.5 g Trizma base

87.6 g NaCl

pH 7.5 (adjusted with HCL)

0.5% (v/v) Tween 20 in TBS

100 ml TBS 10x

899.5ml dH_2O

500 µl Tween 20

DNA digestion buffer

50 mM Tris HCl

100 mM EDTA

100 mM NaCl

1% (w/v) sodium dodecyl sulphate (SDS)

pH 8

Tris-EDTA (TE) buffer

10 mM Tris

1 mM EDTA

7.4 pH

Tris acetic acid EDTA (TAE) buffer

400 mM Tris

10 mM EDTA

11.4% (v/v) acetic acid

7.6 pH (with Trizma base and acetic acid)

Protein lysis buffer (PLB)

10 ml RIPA buffer

1 tablet cOmplete ULTRA protease inhibitor

MES SDS protein running buffer

50 ml MES SDS protein running buffer (20x)

950 ml dH_2O

Western Blot transfer buffer (10x)

30.3 g Trizma base

144 g glycine

Volume adjusted to 1000 ml dH_2O

Western Blot transfer buffer (1x)

100 ml 10x transfer buffer

200 ml methanol

700 ml dH_2O

5% milk powder blocking solution

5 g instant dried skimmed milk powder

100 ml TBST

Alcian blue stock solution (filtered with Whatman paper (3 mm CHR))

0.6 g (0.3%) Alcian blue 8GX

200 ml of 70% ethanol

Alizarin red stock solution (filtered with Whatman paper (3 mm CHR))

0.2 g (0.1%) Alizarin red S

200 ml of 95% ethanol

Skeletal staining solution

850 ml 70% ethanol

50 ml Alcian blue stock solution

50 ml Alizarin red stock solution

50 ml Acetic acid

1% KOH; 20% Glycerol

10 g KOH

800 ml dH_2O

200 ml glycerol (added whilst stirring)

Cresyl Violet staining solution (filtered with Whatman paper (3 mm CHR))

2.50 g Cresyl Violet acetate crystal powder

500 ml dH_2O

1.50 ml acetic acid

Incubated at 60°C

Sudan black B (filtered with Whatman paper (3 mm CHR))

0.3% w/v Sudan black B

70 ml ethanol

30 ml dH20

Thiocarbohydrazide (TCH) solution (filtered with 0.22 µm Millipore syringe)

0.1g thiocarbohydrazide

10 ml dH_2O

Incubated at 60°C

Coomassie Blue staining solution (1 litre)

400 ml ethanol

500 ml dH_2O

100 ml acetic acid

Coomassie de-staining buffer 1 (1 litre)

477.5 ml dH_2O

100 ml acetic acid

400 ml ethanol

22.5 ml glycerol

Coomassie de-staining buffer 2 (1 litre)

877.5 ml dH_2O

500 ml acetic acid

100 ml ethanol

22.5 ml glycerol

2.2 Standard molecular biology techniques

2.2.1 DNA extractions

At weaning (~3 weeks old) mice were marked for individual identification by removing a small part of one or both ears in an individual-specific pattern. Ear clips were placed into Eppendorf tubes and 0.5 ml DNA Digestion Buffer was added to each tube. 12.5 µl of Proteinase K (20 mg/ml; Roche) was added to each tube (a final concentration of 0.5 mg/ml). Samples were incubated for 2 hours at 55 °C on a heat block and were gently shaken to aid complete disruption of tissue. Samples were removed from the heat block and 700 µl of Phenol/Chloroform/Isoamyl Alcohol (25:24:1, v/v) (Invitrogen) was added. Tubes were then shaken vigorously until a uniform emulsion was obtained. Samples were centrifuged at 14, 000 rpm for 5 minutes and the top (aqueous) phase transferred to a new Eppendorf tube and 1 ml of 100% EtOH (VWR) added. Samples were inverted 15 times and stored at -80°C for 1 hour. Samples were then centrifuged at 14,000 rpm for 20 minutes at 4 °C. Supernatants were discarded and 1 ml of precooled 75% EtOH added to each tube. Samples were then centrifuged at 8, 000 rpm for 5 minutes at 4 °C. Supernatants were discarded and pellets left to air dry for ~30 minutes. Pellets were then re-suspended in 50 µl 1x TE buffer and incubated at 65°C to allow the DNA to re-dissolve.

2.2.2 Measuring DNA concentrations

Sample concentration was determined using a NanoDrop spectrophotometer (Thermo Scientific, NanoDrop 2000) and samples stored at -20°C until use.

2.2.3 Genotyping

Genotyping was performed by polymerase chain reaction (PCR) using genomic DNA isolated from ear punches. PCR amplification was conducted using a thermal cycler (SensoQuest, Labcycler 48).

2.2.4 Genotyping mdx mice

The *mdx* mouse is the result of a point mutation in exon 23 which means that it is difficult to distinguish between the wild type and mutant alleles. A long non-specific tail was added to the wild type allele-specific primer which resulted in a

larger band for the wild type allele. Secondly, the wild type and mutant allele-specific primers were mixed together in the reaction (Shin *et al.*, 2011) . Competition between these two primers reduces erroneous binding and extension.

Each 20 µL reaction contained 10 µl dH_2O, 4 µL of 5 × GoTaq Flexi buffer (Promega, Fitchburg, WI), 1 µl of 10 mM dNTPs (Promega), 2 µl of 2 mM $MgCl_2$, 1 µl GoTaq DNA polymerase (Promega), ~150 ng ear DNA, and three primers (Table 2.1) including 1 µl of common forward (0.66 µM), 1 µl wild type allele-specific primer (0.66 µM) and 1 µl mutant allele-specific primer (0.66 µM). PCRs were run using the following program:

1. Initial denaturing: 98°C for 2 minutes
2. Denaturing: 88°C for 30 seconds
3. Annealing: 58°C for 30 seconds
4. Extension: 72°C for 30 seconds
5. Last extension: 72°C for 30 seconds
   (30 cycles for steps 2-4)
6. Hold at 4°C

Primer name	Primer sequences (5'-3')	Band size
Common forward	GCG CGA AAC TCA TCA AAT ATG CGT TAG TGT	
Wild type reverse	GAT ACG CTG CTT TAA TGC CTT TAG TCA CTC AGA TAG TTG AAG CCA TTT **G**	134 bp
Mutant reverse	CGG CCT GTC ACT CAG ATA GTT GAA GCC ATT TT**A**	117 bp

Table 2.1: Primers used for *mdx* mouse genotyping. The underlined nucleotides are not present in the dystrophin gene. The bolded letters represent allele-specific nucleotides at the position of the mutation (Shin *et al.*, 2011). Copies of genotyping results can be found in the appendix.

2.2.5 Genotyping Cmah mice

Standard PCR was employed for amplification of the *Cmah* gene, each 25 µl reaction contained 14.5 µl of dH_2O, 1 µl of 10 mM dNTPs (Promega), 2.5 µl MolTaq buffer (Molzym), 2 µl MolTaq enchancer (Molzym), 1 µl MolTaq

(Molzym) as the DNA polymerase, 1 µl of common forward (10 µM), 1 µl of mutant reverse (10 µM) and 1 µl wild type reverse (10 µM) primers (Table 2.2) and ~150 ng DNA. PCRs were run using the following program:

1. Initial denaturing: 94°C for 5 minutes
2. Denaturing: 94°C for 30 seconds
3. Annealing: 60°C for 30 seconds
4. Extension: 72°C for 30 seconds
5. Last extension: 72°C for 5 minutes
   (30 cycles for steps 2-4)
6. Hold at 4°C

Primer name	Primer sequences (5'-3')	Band size
Common forward	TCC CAG ACC AGG AGG AGT TA	
Wild type reverse	CTT CCA GTT GTG CTT TGT GC	~297 bp
Mutant reverse	GTC AGG AAA CAG CAC CAA CA	~ 400 bp

Table 2.2: Primers used for *Cmah* mouse genotyping. Copies of genotyping results can be found in the appendix.

2.2.6 Agarose gel electrophoresis

Agarose gels (2-3%) (NBS Biologicals) were prepared with 1x Tris-Acetate-EDTA and Safe View (concentration 0.5 µg/ml) (NBS Biologicals). 15 µl of samples and 4 µl of 6x loading dye were loaded onto gels. Gels were subjected to electrophoresis at 90-120 volts in 1x TAE buffer for 60-90 minutes. DNA was then visualised under UV light, using GelDoc-it 310 Imaging system. The size of the DNA fragments was determined relative to 1 Kb or 100 bp ladders (25 ng/ml) (Promega).

2.2.7 DNA purification by gel extraction

For the isolation and purification of a single DNA band, the desired product was visualised and excised under a UV transilluminator. The band was extracted and purified from the agarose gel using QIAquick Gel Extraction Kit (Qiagen) according to manufacturer's instructions.

2.2.8 DNA sequencing and alignments

Sequencing was carried out by sequencing service MWG Biotech in Ebersberg, Germany. 15 µl of purified plasmid DNA at a concentration of 100 ng/µl was sent with 15 µl of the appropriate primer at 5 pmol/µl. Sequence alignments were carried out using the online Basic Local Alignment Search Tool (BLAST).

2.3 Animal work

2.3.1 Animal care and husbandry

Mice used for this study were housed under controlled temperature (~25°C) and light conditions (12:12 hour light: dark cycle), with food and water *ad libitum*. The investigations conformed to the Guidance for the Care and were performed under the terms of the Animals (Scientific Procedures) Act 1986, authorised by the Home Office UK under PPL70/8538 held by Professor Volker Straub. All experiments were performed at animal care facilities at Newcastle University, UK and were granted ethical approval by the Animal Welfare and Ethical Review Board, Newcastle University.

2.3.2 Transgenic mice used in this study

C57BL/10ScSnOlaHsd (control) mice were purchased from Harlan Laboratories (Indianapolis, USA) *mdx* (C57BL/10ScSn-mdx/J) mice and B10.Cg-Cmahtm1Avrk Dmdmdx/PtmJ (*Cmah-/-mdx*) mice were purchased from The Jackson Laboratory (Maine, USA). All mice were bred and maintained in the Functional Genomics Unit (FGU) at Newcastle University. Control *C57BL/10* and *mdx* mouse colonies were maintained by Elizabeth Greally (PIL I3B796363) and *Cmah-/-mdx* and *Cmah-/-* mouse colonies were maintained by Emine Bagdatlioglu (PIL I34A747CC). Homozygous *mdx* mice are viable and were bred either as pairs of one male and one female or trios of one male and two females. *Cmah-/-mdx* homozygous mice are also viable but due to issues with breeding (small litters produced and lack of successful breeding) mice were either bred as homozygous or heterozygous pairs. Offspring were housed together in groups of 2-6 mice per cage.

2.3.2.1 Generation of Cmah-/- mouse

In order to have the adequate control models for the *Cmah-/-mdx* mouse a *Cmah-/-* mouse was generated/bred (Figure 2.1) at the Functional Genomics Unit (FGU), Newcastle University.

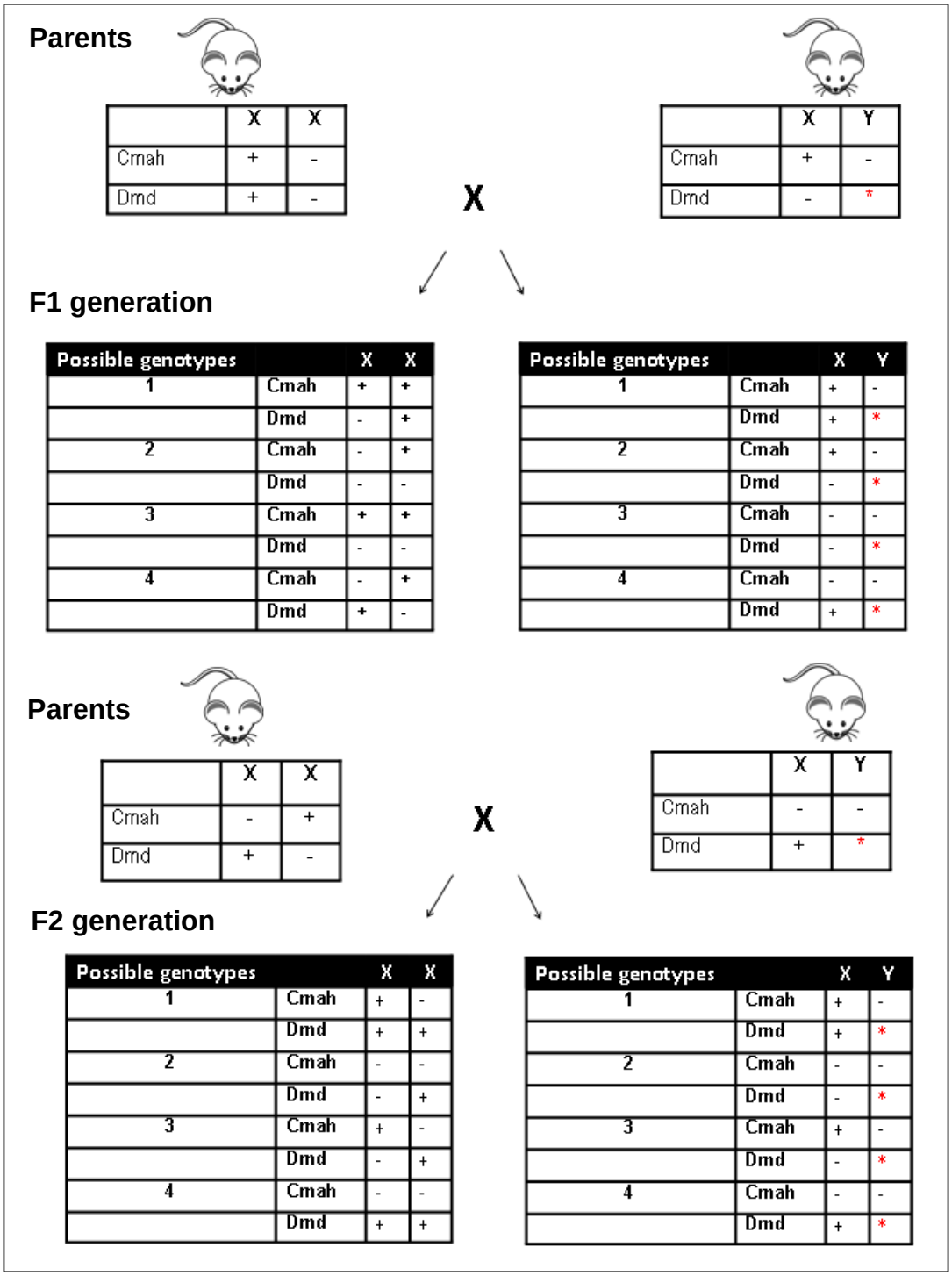

Figure 2.1: Generation of *Cmah-/-* mouse model. The model was generated by back crossing a *Cmah* $^{+/-}$*/Dmd* $^{+/-}$ female with a *Cmah*$^{+/-}$*/Dmd* $^{-/*}$ male in order to obtain a *Cmah*$^{-/-}$*/Dmd*$^{+/+}$ female and *Cmah*$^{-/-}$*/Dmd*$^{+/*}$ male mice. Homozygous mice were bred to maintain the *Cmah-/-* mouse colony. Red star = gene not present on Y chromosome.

2.4 Behavioural testing

Mice were transferred from the FGU to the Keith Unit, Newcastle University, at least 2 weeks prior to the beginning of behavioural testing. Mice were kept in home cages (4 mice per cage) at a constant temperature with food and water *ad libitum*. Mice from at least two different litters (for each genotype, at each time point investigated) were tested to avoid litter specific effects. All tests were reordered using Panasonic SDR-S26 SD video cameras and blank DVDS (TDK T19444 16x DVD+R). Video recordings were viewed using Windows media player.

2.4.1 Barnes maze testing

2.4.1.1 Procedure

The Barnes maze is a task that measures spatial learning and memory aspects of cognition (Sunyer *et al.*, 2007). The surface of the maze was coloured grey, acting as a contrasting colour for clear observation of the mouse movements. Surrounding the edges of the maze were 20 holes, 7.5 cm apart and each 5 cm in diameter (Figure 2.2). Four of these holes contained a place for a small, detachable, dark box containing an opaque chamber for the mouse to enter (Sunyer *et al.*, 2007). This box was referred to as the target box and the hole containing this, the target hole. The openness of the maze surface should drive the mice into this chamber, no other aversive stimulus (e.g. bright light) was provided. Surrounding the maze were 4 boards (15 cm away from the edge of the maze and 30 cm above the maze), equally spaced from the maze and far enough away to prevent the mice from jumping onto them. Each board contained a different shape (triangle, circle, square and a cross) as a reference for the mice to find the target box, but also to prevent the mice observing the whole test room. The investigator also became a reference for each trial, wearing a white lab coat and remaining in the same position throughout the trials. Testing on the Barnes maze was split into phases, as described below.

2.4.1.2 Adaptation phase

Mice were given at least 15 minutes for habituation within the test room prior to the start of experiments. Mice were transported from their home cage to the Barnes maze in a black plastic tray where they were placed in a dark cylindrical

chamber at the centre of the maze (Sunyer *et al.*, 2007). After 10 seconds had passed in the chamber the mouse was released. The investigator then carefully guided the mouse to the target box. The mouse was not forced into the box to avoid stress, but if the mouse would not enter the box then the mouse was placed facing the box and the base of the tail pulled gently to usher the mouse into the box (Berta *et al.*, 2007). If this did not work, then the mouse was placed in the box directly (Berta *et al.*, 2007). Once inside, mice were allowed to habituate in the target box for 2 minutes (Berta *et al.*, 2007).

2.4.1.3 Spatial Acquisition

Before testing, the surface of the maze was cleaned using 70% w/v EtOH to remove olfactory stimuli. Mice were placed in the cylindrical chamber in the centre of the maze and after 10 seconds, released and allowed to explore the maze for 3 minutes (Berta *et al.*, 2007). In this time the primary errors (nose pokes not in the target hole before it is found), total errors (nose pokes before mouse enters the target hole), primary latency (time to find the target hole) and total latency (time to enter the hole) were recorded. If the mice did not enter the target box in the 3 minutes they were guided carefully into the box (Berta *et al.*, 2007). If mice did not enter the target box in the 3 minute allocated time period they were given a 1 minute penalty in order to discriminate between the mice that took exactly 3 minutes to enter the target box. Once inside, the mice were left for 1 minute before returning to their home cages. There were 4 trials per day per mouse for 4 days and in between each trial the mice were given a 15 minute interval, where they were returned to their home cage. In this time the remaining mice were tested.

2.4.1.4 Short-term Memory

On day 5 the target box was removed. The target hole for each mouse was the same as on previous days and the same procedure carried out for testing as previously described. This time the mice were allowed to explore the maze for 90 seconds and in that time a number of measures were recorded: primary latency, primary errors, total errors and the preference for holes around the maze (total head pokes in individual holes around the maze). After the allocated 90 seconds, mice were removed from the maze and testing was finished (Berta *et al.*, 2007). From the head pokes in various holes around the maze a success

score was created. This was the number of head pokes in a hole, multiplied by a given value for that hole (Figure 2.2). Values were based on orientation around the target hole; with the target hole itself having a value of 10. The score for the individual holes was then totalled to create an overall success score. The amount of time the mouse spent in the target quadrant was also recorded.

2.4.1.5 Long-term Memory

On day 12, the same procedure as on day 5 is performed without any training between days 5 and 12 (Berta *et al.*, 2007).

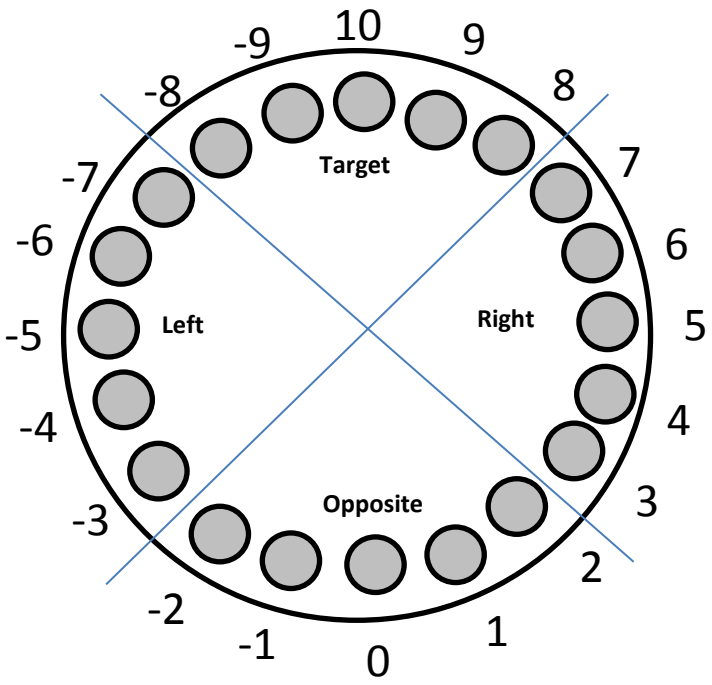

Figure 2.2: Schematic representation of the Barnes maze test. Blue line separates out each quadrant. Values around the outside represent the distance from the target hole. Success scores were generated for short-term and long-term memory where the number of head pokes in a hole is multiplied by a given value for that hole. The higher the success score the more successful the mouse has been in locating the target hole.

2.4.2 Novel Object Recognition

Mice were given a 10 minute habituation to an arena of dimensions 48×31×20 cm, once a day for 4 days. On the fifth day, mice were exposed to Novel Object Recognition in two phases. In the first phase (sample), mice explored two identical objects (A1 and A2) for 3 minutes (Ennaceur and Delacour, 1988). Objects were either polystyrene spheres or stars, depending on randomization. Objects were chosen based on difference in shape, to ensure novelty in the

trials and also similarity in size to the mice. Mice were then given a 15 minute inter-trial retention delay (memory consolidation of objects and location). In this period, the objects and arena were cleaned with 70% w/v EtOH to remove olfactory stimuli and the mice were returned to their home cage. Mice were then exposed to the second (choice) phase, in which the identical objects were replaced by one novel object (B1) and one familiar object (A3) (Ennaceur and Delacour, 1988) and again mice explored these for 3 minutes. Location and the novel object itself were varied, to avoid condition place preference. During both phases an exploratory action of the objects was defined as the mouse touching the object with its nose or directing its nose ≤2 cm from the object. Sitting on the object was not considered exploratory movement.

Average time spent with the objects was recorded in both phases of testing. From this, D2 ratios' were calculated for statistical analysis of the choice (test) phase. These create a value between +1 and -1, where +1 is total preference for the novel object, -1 is total preference for the familiar object and 0 is no preference for either object. D2 ratios were calculated by determining the proportion of total time spent exploring either of the objects (B1-A3/B1+A3) (Ennaceur and Delacour, 1988; Ennaceur *et al.*, 2005).

2.5 Histological studies

2.5.1 Sample Preparation

Mice were killed by cervical dislocation and the brain excised from the cranial cavity. The Singer Protocol for the dissection of rodent brain was followed (Spijker, 2011). Tibialis anterior muscle served as control tissue for staining. The tissue was then weighed (PGW M Precision balances, AE Adam), mounted on a cork disc (20 mm Diameter x 3 mm thick) supported with a coverslip (VWR), and protected with OCT (Pyramid Innovation) before being snap frozen in isopentane on dry ice. Tissue was then stored at -80°C until use.

Dissected brains were placed in PBS, to prevent dehydration. The cerebellum was then separated from the cerebral cortex by making an incision dorsally through the pons. When the majority of white matter had been removed the brain was rotated ventrally and the cerebellum was separated from the

colliculus inferior. Finally the remaining part of the pons was removed. The isolated cerebellum was snap frozen in isopentane on dry ice, placed in an Eppendorf tube and stored at -80°C.

2.5.2 Cryosectioning

10 µm -20 µm coronal sections of brain tissue and 8 µm sections of muscle tissue were cut using a cryostat. (Microm HM 560, Zeiss). For brain tissue the regions of interest (ROIs) were delineated by visualisation of their position in accordance to known landmarks or other noticeable characteristics and in congruence with The Mouse Brain Atlas in Stereotaxic co-ordinates (third edition) (Paxinos, 2008). Sections were mounted onto Superfrost Plus slides (VWR); air dried for 30 minutes, wrapped in cling film and then stored at -80°C until use.

2.5.3 Staining Procedure with Cresyl Violet

Slides were removed from the -80°C freezer and allowed to defrost at room temperature. After 30 minutes slides were removed from their cling film wrapping and given a further 10 minutes to fully defrost at room temperature. The slides were immersed in Cresyl Violet solution for 10 minutes and dehydrated through a series of alcohol steps (95% EtOH (VWR) for 10 minutes then 100% EtOH for 10 mins). Slides were then cleared with 2 x 3 minute immersions in Histoclear (National Diagnostics, USA). DPX mounting medium (BDH) and a coverslip were applied and the slides left to air dry overnight. Images of Cresyl Violet staining were captured using a Zeiss Axioplan Brightfield imaging microscope and AxioVision 4.8 software.

2.5.4 Evans Blue Extravasation

2.5.4.1 Evans Blue Dye Solution Preparation

10 mg Evans blue dye (EBD) (Sigma) was diluted into 1 ml of PBS (life technologies). The solution was then passed through a 0.22 µl filter and stored at -20 °C until use.

2.5.4.2 Analysis of BBB Integrity Using Evans Blue Dye

Mice were given an intraperitoneal injection, into the right side of the peritoneal cavity, with a bolus of 0.1 mL/10 g EBD. After injection, animals were returned to their cage and allowed food and water *ad libitum***.** After 24 hours, the mice were killed by cervical dislocation and the brain excised and rapidly mounted and frozen in OCT medium (Pyramid). Serial 10 µm slices from the cerebral cortex were mounted onto Superfrost Plus slides (VWR). Slides were dipped in ice cold acetone (−20 °C) for 10 minutes and then washed in PBS 3 x 5 minutes. The sections were then mounted with Vectashield mounting medium (Vector Laboratories, Inc.) and a glass coverslip.

2.5.4.3 Image acquisition and quantification of EBD extravasation

EBD was visualised on a Zeiss Axio ImagerZ1 (Carl Zeiss Germany Ltd.) fitted with a Zeiss Axiocam camera (Carl Zeiss Germany Ltd.) using the 20x and 40x objectives, Zeiss ApoTome and AxioVision version 4.8 software. By fluorescence microscopy analysis, EBD staining showed a bright red emission. In order to make comparisons between different genotypes and ages images were collected at standardised exposure settings. All digital images were stored as raw images (TIFF files) without any processing of the image.

2.5.5 Immunofluorescence labelling

Sides were thawed at room temperature and sections were circled with an ImmEdge Hydrophobic Barrier PAP Pen (Vector Laboratories). Sections were fixed in 4% PFA (Paraformaldehyde, Sigma) in 1 x PBS (Phosphate Buffered Saline, Gibco) for 15 minutes and permeabilised by passing slides through a series of methanol dilutions (70% methanol for 10 minutes, 95% methanol for 10 minutes, 100% methanol for 10 minutes, 95% methanol for 10 minutes and 70% methanol for 10 minutes). Sections were subsequently blocked in 8% bovine serum albumin (BSA) (Sigma) in 1x PBS for 1 hour at room temperature. Sections were incubated with 50 µl of primary antibody diluted in blocking medium at 4°C overnight. The next day sections were incubated with a secondary antibody diluted in blocking medium for 1 hour at room temperature. Sections were washed several times with 1x PBS between incubation periods. Sections were then covered with 0.3% w/v Sudan Black B (Sigma) for 3 minutes. Sections were washed several times with 1x PBS-T, before they were

mounted in Vectashield mounting medium with DAPI (Vector Laboratories, Inc.) and a glass coverslip. Slides were stored at 4°C, protected from light, until imaging.

2.5.5.1 Immunofluorescence Image acquisition

Fluorescent immunostaining was visualised on a Zeiss Axio Imager (Carl Zeiss Germany Ltd.) fitted with a Zeiss Axiocam camera (Carl Zeiss Germany Ltd.) using the 20x and 40x objectives, Zeiss ApoTome and AxioVision version 4.8 software. An average exposure time was taken for 594 nm and 488 nm channels using the *C57BL/10* control cerebellar sections at the corresponding time points, and was then applied to mutant mouse images.

2.5.6 Electron Microscopy

6 month old and 12 month old control *C57BL/10* and *mdx* mice (n=2 mice per genotype at each time point) were sacrificed via cervical dislocation. The cerebellum was separated from the midbrain and 1 mm^3 region from the lateral cerebellar hemisphere was removed using a scalpel and fixed in 0.1M cacodylate buffer (pH 7.5) containing 4% PFA and 2.5% glutaraldehyde (Electron Microscopy Sciences).

NCMIR method for 3D EM was followed (https://www.ncmir.ucsd.edu/sbem-protocol/).Briefly, tissues were washed in cold cacodylate buffer (containing 2mM calcium chloride) before incubation in osmium solution containing 3% potassium ferrocyanide in 0.3M cacodylate buffer with 4mM calcium chloride in 4% aqueous osmium tetroxide (EMS), on ice for one hour. Tissues were then washed 5 x 3 minutes in dH_2O at room temperature. Tissues were then placed in thiocarbohydrazide (TCH) solution for 20 minutes and washed again in dH_2O (5 x 3 minutes). Tissues were incubated at room temperature in solution containing 2% osmium tetroxide. After washing with dH_2O (5 x 3 minutes) tissues were stored in 1% uranyl acetate overnight at 4°C. The following day tissues were incubated in 0.6% lead aspartate solution, washed in dH_2O and then dehydrated in gradient EtOH before being transferred to acetone. Tissues were then embedded in epoxy resin. Standard TEM was then performed on sectioned tissues to identify areas for serial block-face scanning electron microscopy (SBFSEM) (Purkinje cell and mitochondrial rich areas). A series of

serial 70 nm thick were captured on a Gatan 3view housed in a Zeiss Sigma FEG SEM and imaged stacks collected on Digital Micrograph v.3.31.734.0. Images were captured in this way in order to perform SBFSEM at a later stage.

2.6 Skeletal investigations

2.6.1 Radiography and Establishment of Kyphotic Index

18 month old mice were identified by ear markings and then briefly anaesthetised with 5% isofluorane in an anaesthetic chamber. Radiographs (X-rays) were performed on 18 month old mice with a Faxitron radiography system (Faxitron X-Ray, Lincolnshire, IL) at 23 kV for 5 seconds. X-rays were taken in two positions: mouse laid prone and mouse laid on its right-hand side, in order to image both scoliosis and kyphosis respectively.

DICOM raw images were then imported into ImageJ (https://imagej.nih.gov/ij/), and measurements made using the measuring tool. A previously established protocol, to demonstrate the spine curvature of mice (the kyphotic index), by drawing two lines between the caudal margin of the seventh cervical vertebra and the caudal margin of the sixth lumbar vertebra was used (Laws and Hoey, 2004)

2.6.2 Skeletal preparation

Adult male mice were sacrificed via CO_2 inhalation. An incision was made into the abdominal cavity using a scalpel and the internal organs and any fat were carefully removed. The skin was removed, as was the skin covering the tail, ensuring the skeletal elements were not destroyed. The mouse carcass was then placed into glass container and incubated on a shaker at room temperature as follows:

- 4 days in 95% Ethanol (VWR)
- 3 days in Acetone (VWR)
- 1 day wash with dH_2O
- 10 days in skeletal staining solution

- 4 months in 1% KOH (Sigma); 20% Glycerol (Sigma). This solution was changed every two weeks and soft tissue was removed gently using forceps.
- Skeletons were then transferred successively into 50% Glycerol, 70% Glycerol and 100% Glycerol before final storage in 100% Glycerol.

Skulls were then imaged using a Zeiss stereomicroscope and AxioVision software and imported into ImageJ (https://imagej.nih.gov/ij/).

2.7 Proteomic Analysis

2.7.1 Protein sample preparation

2.7.1.1 Tissue lysis and carbamidomethylation

Comparative proteome profiles were generated for control *C57BL/10* and *mdx* mouse cerebella (n=4/genotype) at 6 months old using a total global protein extraction method. Each cerebellum was ground and lysed in 1 mL of 50 mM Tris-HCl (pH 7.8) buffer containing 150 mM NaCl, 1% SDS. The suspension was then centrifuged at 13,500 x g for 30 min at 4°C and the cell lysate containing the extracted proteins was collected.

As membrane proteins are notoriously underrepresented in global protein extraction procedures and in order to also identify changes in membrane proteins control *C57BL/10* and *mdx* mouse cerebella (n=4/genotype) at 6 months were separately used for enrichment of membrane-associated proteins. Each sample was lysed in 1 mL of 0.1 M $NaHCO_3$ (pH 10.7) buffer containing cOmplete Mini protease inhibitor cocktail (Sigma) on ice for 30 min. Samples were then centrifuged at 68.000 x g for 30 min at 4°C to pellet the membrane fractions. The membrane fractions were re-suspended in 0.3 mL of 50 mM Tris-HCl (pH 7.8) buffer containing 150 mM NaCl, 1% SDS, and cOmplete Mini protease inhibitor cocktail.

Protein concentration for both the global and membrane fractions was determined by BCA assay according to the manufacturer's protocol. Cysteines of the proteins were then reduced by addition of 10 mM DTT at 56°C for 30 min,

followed by alkylation of free thiol groups with 30 mM IAA at room temperature in the dark for 30 min.

2.7.1.2 Sample preparation and trypsin digestion

Sample preparation and proteolysis were performed using filter-aided sample preparation (FASP). Briefly, 100 µg of protein was diluted 10-fold with freshly prepared 8 M urea/100 mM Tris-HCl (pH 8.5) buffer and placed on a centrifugal device Nanosep 30 KDa Omega (Life Science). The device was centrifuged at 13,800 g at room temperature for 20 minutes (this was used for all centrifugation steps). In order to eliminate residual SDS, three washing steps were carried out with 100 µL of 8 M urea/100 mM Tris-HCl (pH 8.5). For buffer exchange the device was washed three times with 100 µL of 50 mM NH_4HCO_3 (pH 7.8). Next, 100 µL of proteolysis buffer comprising of trypsin (Promega) (1:25 w/w, protease to substrate), 0.2 M GuHCl and 2 mM $CaCl_2$ in 50 mM NH_4HCO_3 (pH 7.8), was added to the device and incubated at 37°C for 14 hours and 22 hours for global and membrane fractions respectively. Afterwards, the generated tryptic peptides were recovered by centrifugation with 50 µL of 50 mM NH_4HCO_3 followed by 50 µL of dH_2O. Finally, peptides were acidified by addition of 10 % TFA (v/v) and digests were quality controlled in a reversed-phase HPLC.

2.7.2 Liquid chromatography - mass spectrometry

2.7.2.1 LC-MS/MS analysis

Replicates were measured using a Dionex UltiMate 3000 RSLCnano System, coupled to an Orbitrap Elite Mass Spectrometer (both from Thermo Scientific). In brief, peptides were pre-concentrated on a 100 µm x 2 cm C18 trapping column for 10 minutes using 0.1 % TFA (v/v) at a flow rate of 20 µL/min followed by separation on a 75 µm x 50 cm C18 main column (both from Acclaim Pepmap, Thermo Scientific) with a 115 min LC gradient ranging from 3-45 % of 84 % ACN, 0.1 % FA (v/v) at a flow rate of 250 nL/min. Mass spectrometry (MS) survey scans were acquired in the Orbitrap from m/z 300 to 1500 at a resolution of 60,000 using the polysiloxane ion at m/z 371.101236 as lock mass. The ten most intense signals were subjected to collision induced dissociation (CID) in the ion trap, taking into account a dynamic exclusion of 30 s. CID spectra were acquired with a normalized collision energy of 35 % and an

activation time of 10 ms. AGC target values were set to 10^6 for Orbitrap MS and 10^4 for ion trap MSn scans, and maximum injection times were set to 100 ms for both full MS and MSn scans.

2.7.2.2 Label free data analysis

Data analysis of the acquired label free quantitative MS data was performed using the Progenesis Qi software from Nonlinear Dynamics (Newcastle upon Tyne, U.K.) in which alignment of MS raw data was conducted by automatically selecting one of the LC-MS files as reference. After peak picking, only features within retention time and m/z windows from 0-115 min and 300-1500 m/z, with charge states +2, +3, and +4 were considered for peptide statistics and analysis of variance (ANOVA). MS/MS spectra were exported in an mgf file as peak lists.

The mgf peak lists were searched against a concatenated target/decoy version of the mouse Uniprot database, (downloaded on 22/07/2015, containing 16,473 target sequences) using Mascot 2.4.0 (Matrix Science), X! TANDEM Vengeance (2015.12.15.2) and MS-GF+ Beta (v10282) (12/19/2014) with the help of searchGUI 2.8.0. Trypsin with a maximum of two missed cleavages was selected as enzyme. Carbamidomethylation of cysteine was set as fixed and oxidation of methionine was selected as variable modification. MS and MS/MS tolerances were set to 10 ppm and 0.5 Da, respectively.

PeptideShaker software 1.9.2 (http://code.google.com/p/peptide-shaker/) was used for interpretation of peptide and protein identifications from searchGUI and Mascot. Combined search results were filtered at a false discovery rate (FDR) of 1% on the protein level and exported using the advanced PeptideShaker features that allow direct re-import of the quality-controlled data into Progenesis Qi. Peptide sequences containing oxidized methionines were excluded for further analysis. Only proteins that were quantified with unique peptides were exported. For each protein the average of the normalised abundances (obtained from Progenesis Qi) from the replicate analyses was calculated to determine the ratios between the *mdx* mice and control (*C57BL/10*) mice. Only proteins which were (i) commonly quantified in all the replicates with (ii) one or more unique peptides, (iii) an ANOVA p-value of <0.05 (Progenesis Qi) and (iv) an average $\log_2$ ratio of which protein that was either higher than the up-regulated

cut-off or lower than the down-regulated cut-off was considered as regulated. The cut-off values were determined based on the 2x standard deviation and the normal distribution from all identified protein's log_2 ratio in which the bell curve is symmetric around the mean. Therefore, an average log_2 ratio of a protein which < -2.08 or > 2.38 (corresponding to ~5.22-fold regulation; log_2 ratios of 1.10) for comparative membrane-associated profile and an average log_2 ratio < -0.93 or > 0.99 (corresponding to ~1.99-fold regulation; log_2 ratios of 0.98) for comparative global profile were considered as regulated.

2.8 Protein extraction and Western Blotting

2.8.1 Sample preparation

Brain tissue was homogenised and lysed in protein lysis buffer and left on ice for 30 minutes. The lysates were transferred to Eppendorf tubes and centrifuged at 700 g, 4°C for 10 minutes. The supernatants containing the extracted proteins were collected and then centrifuged at 10 000 g at 4°C for 30 minutes. The pellet was discarded and the supernatant from each tube was transferred to an Eppendorf tube and stored at -20°C until use.

2.8.2 Protein quantification

Protein concentration was measured using the Qubit Fluorometer (Invitrogen by Life Sciences) according to the manufacturer's recommendations.

2.8.3 SDS-PAGE and Western Blotting

25 µg of brain lysates were mixed with 7.5 µl of 4xNuPage LDS sample buffer (Life technologies) and 3 µl 10xNuPage reducing agent (Life technologies) in a final volume of 20 µl in an Eppendorf tube and were then denatured in a heat block at 95°C for 5 minutes. 7 µl Chameleon Duo Ladder (Licor) and the total volume of samples (~30 µl) were resolved on 4-12% Novex NuPAGE Gels (Life Technologies) in a tank (Life Technologies, Novex Mini-Cell) filled with MES (Thermofisher Scientific) running buffer. Gels were run for 45 minutes at 200 volts using an X cell SureLock Mini-Cell Electrophoresis system (Life Technologies). Proteins were then transferred to PVDF membrane (Licor) for 90 minutes at 350 mA in ice-cold 1x transfer buffer in a transfer tank (Mini Trans-Blot Electrophoresis Transfer Cell, BIO-RAD). Following transfer, the membrane

was soaked in methanol for 1 minute then rinsed in dH_2O. Transfer was confirmed by staining the membrane with Ponceau S (Sigma) for 5 minutes. Following de-staining with dH_2O the membrane was blocked for 1 hour in 5% milk in TBS-T on a shaker at room temperature. The membrane was incubated with primary antibodies (Table 2.3) diluted in 5% milk in TBS-T overnight at 4°C. The next day, primary antibodies were drained off and the membrane was rinsed three times in in 1x TBS-T for 5 minutes each. The membrane was incubated with secondary antibodies (Table 2.3) diluted in 5% milk in TBS-T at room temperature on a shaker for 1 hour in the dark. Membranes were washed with TBS-T 3 x 5 minutes each, followed by a wash in TBS. Protein bands were detected with an Odyssey Family Imaging System (Licor Biosicences).

Membranes were stored in TBS at 4°C and protected from light. Stripping of membranes was carried out using a restore fluorescent stripping buffer (Thermofisher Scientific) as per manufacturer's instructions. Membranes were stripped and re-probed a maximum of 2 times (for Oxphos 5 and VDAC/Porin antibodies only).

2.8.4 Staining protein gels with Coomassie Blue

Following electrophoresis the gel was washed with dH_2O in a small tray. 10 ml of Coomassie Blue staining solution was applied to the gel and the gel left to incubate for 1 hour at room temperature on a shaker. The Coomassie Blue stain was then removed and 10 ml of de-staining buffer one was applied and the gel was left for 1 hour at room temperature on a shaker. De-staining buffer one was then removed and 10 ml of de-staining buffer two was applied for 1 hour at room temperature on a shaker. Following the removal of de-staining buffer two the gel was soaked in dH_2O, covered with paper towels (to remove background staining) and left overnight at room temperature. The following day the protein bands were detected with an Odyssey Family Imaging System (Licor Biosicences).

Antibody	Description	Application in this study	Supplier	Product number
Alexa Fluor® 488	Donkey anti-mouse	IHC (1:500)	Life Technologies	ab150105
Alexa Fluor® 488	Goat anti-rabbit	IHC (1:500)	Life Technologies	ab150073
Alexa Fluor® 594	Donkey anti-rabbit	IHC (1:500)	Life Technologies	ab150076
Anti-AQP1	Rabbit polyclonal	WB (1:1000)	Abcam	ab15080
Anti-AQP4	Rabbit polyclonal	WB (1:500)	Abcam	ab4182
Anti-GABA transporter GAT3	Rabbit polyclonal	WB (1:500)	Alomone Labs	AGT-003
Anti-GABA(A)α_2	Rabbit polyclonal	WB (1:200)	Alomone Labs	AGA-002
Anti-GAPDH	Mouse monoclonal	WB (1:1000)	Abcam	ab6276
Anti-Gelsolin	Rabbit polyclonal	WB (1:1000)	Abcam	ab74420
Anti-GFAP	Mouse monoclonal	IHC (1:1000)	Abcam	ab10062
Anti-Oxphos 5	Mouse monoclonal	WB (1:1000)	Abcam	ab110413
Anti-Porin	Mouse monoclonal	WB (1:1000)	Abcam	ab15895
Anti-TSP-1	Rabbit polyclonal	WB (1:500) IHC (1:500)	Abcam	ab85762
Anti-Fribrinogen α chain	Rabbit polyclonal	WB (1:1000) IHC (1:1000)	Abcam	ab217931
IRDye® 680CW	Goat anti-Rabbit IgG	WB (1:15000)	Licor	926-32211
IRDye® 800CW	Donkey anti-Mouse IgG	WB (1:15000)	Licor	926-32213

Table 2.3: Antibodies used in this study. (WB: Western Blot, IHC: Immunohistochemistry).

2.9 Magnetic Resonance Imaging

All MR imaging protocols were designed by either Dr Paola Porcari or Dr Dara O'Hogain.

2.9.1 Data Acquisition

Images were obtained following induction of anaesthesia with 4% Isofluorane (Abbott, USA) and 0.5 l/min oxygen in an anaesthetic chamber. For MRI brain

examination, mice were laid prone on a home-made mouse holder keeping the head fixed by a bite bar in order to ensure that the head was positioned at the isocenter of the magnet.

Body temperature was maintained using a warm air device (SA Instruments) set at 37°C and anaesthesia was maintained using 1.5% Isofluorane and 0.5 l/min oxygen via a nose cone controlled with regard to respiratory effort (~50 bpm), monitored through an MRI-compatible small animal monitoring and gating system. A small amount of lubricating eye gel (Carbomer 0.2%, BluMont) was applied to prevent the corneas for drying during scanning.

MRI images were acquired using a 7.0 Tesla horizontal bore Varian scanner (Varian Medical System, Palo Alto, CA, USA) equipped with a 12-cm inner diameter actively shielded 37 gradient set (Magnex Scientific, Oxford, UK). A 39 mm (inner diameter) volume coil (Rapid Biomedical GmbH, Germany) was used as a radiofrequency (RF) transceiver for MR imaging of mouse brain.

2.9.2 FSEM T_2 and SEM T_1 Imaging Parameters

The MRI protocol included scout images to determine the correct positioning of the mouse brain, T_2-weighted (T_2-w) fast spin-echo (FSE) images and T_1-weighted (T_1-w) spin-echo (SE) images. For each mouse, axial, sagittal and coronal T_2-w images were acquired using the following parameters: repetition time/effective echo time (TR/TE eff) = (7000/40) ms, number of averages=4, field of view (FOV) = 25 x 25 mm^2, matrix (MTX) = 256 x 256, in plane resolution = 98 µm x 98 µm, slice thickness = 0.7 mm. In order to ensure that the whole brain was imaged, the numbers of slices for coronal, sagittal and axial acquisitions were 23, 19 and 15, respectively. Coronal T_1-w SE images were acquired for each mouse using the following parameters (TR/TE) = (900/16.07) ms, number of averages = 4, field of view (FOV) = 25 x 25 mm^2, matrix (MTX) = 256 x 256, in plane resolution = 98 µm x 98 µm and slice thickness=0.7 mm.

2.9.3 Brain Volumetric Analysis

Brain volumes were estimated for each mouse according to the following formula:

$$\textbf{Total Volume} = \Sigma^{n}_{j=1}\, d \cdot A_j \qquad [1]$$

Where $\mathbf{A_j}$ is the cross sectional area on the **jth** slice through the mouse brain, **n** indicates the total number of the considered slices and d the slice thickness (0.7mm).

The cross sectional areas of the mouse brain were determined by drawing the ROIs on the MRI images of mouse brain by using ImageJ software (https://imagej.nih.gov/ij/). Specifically, ROIs were outlined according to the Mouse Brain Atlas (Paxinos and Franklin 2001) on coronal T_2-w images of mouse brain. Areas of morphological brain regions; cerebellum (including colliculus), ventricle system (LV=lateral ventricle, 3V= third ventricle, D3V= dorsal third ventricle, 4V= fourth ventricle) and hippocampus were also estimated, according to formula [1], by drawing the cross sectional areas on coronal T_2-w images.

2.9.4 MEMS T_2 Imaging Parameters

T_2 relaxation times of different brain regions (hippocampus, caudate putamen, cerebral cortex, corpus callosum, cerebellum) of *C7BL/10*, *mdx*, *Cmah-/-mdx,* and *Cmah-/-* mice aged 6 and 18 months old (n=4/genotype/time point) were determined using a multi-echo-multi-slice (MEMS) sequence (TR/TE = 3500/8 ms, NE = 12, slice thickness = 1 mm, in plane resolution = 196 x 196 μm^2). T_2-maps of mouse brain were computed for each slice on a voxel by voxel basis as a function of TE (12 echo times were employed, starting from 8 to 96 ms with an echo spacing of 8 ms).

For each mouse, the total scan time for brain volume measurements was 1.5 hours and approximately 2 hours when T_2 measurements were included. Following each experiment mice were recovered and returned to their cages with food and water *ad libitum*.

2.9.5 T_1 mapping with Gadolinium enhancement

Mice were first anaesthetised using 4% Isofluorane and 0.5 l/min oxygen in an anaesthetic chamber. Mice were then transferred to a heated blanket and

anaesthetic was maintained using 1.5% Isofluorane and 0.5 l/min oxygen via a nose cone. A heat lamp was briefly placed next to the mouse's tail in order to dilate the tail vein. Once a vein was visible by eye a custom-made cannula was inserted and flushed with a small volume of saline to ensure the cannula was correctly placed. Tissue glue was then applied to avoid disruption of the cannula throughout the procedure.

The mouse was then transferred to the MRI scanner and onto a home-made mouse holder keeping the head fixed by a bite bar in order to ensure that the head was positioned at the isocenter of the magnet. An IV infusion line was attached to the end of the cannula, once the mouse was in the correct position, a syringe containing 0.2 mmol/kg Gd (Gadovist) was attached to the end. The concentration of gadolinium given to the mouse was calculated based on mouse weight and diluted in saline to a volume of 150 µl.

Following power calibration a series of scout images was obtained to determine the correct positioning of the mouse brain. Pre-contrast baseline imaging was performed using a modified T_{1-} mapping Look-Locker multi-slice sequence (Kim *et al.*, 2011). The look-locker protocol is a gradient-echo multi-slice sequence (GEMSLL) optimized for efficient T_{1-} mapping. This method is advantageous because it acquires the series of inversion time (TI) time points rapidly following a single inversion. GEMSLL images were acquired using the following parameters: repetition time/echo time (TR/TE) = 13.2/6.63 ms, number of averages= 2, matrix (MTX) = 96 × 96, field of view (FOV) = 20 × 20 mm^2, flip angle = 5°, 6 TI (0.005, 0.12, 0.24, 1.5, 2.5, 3.5), TR (inv) = 34.46 s, number of slices=9 and slice thickness= 1.2 mm. Following the T_{1-} mapping scan a series of eight coronal T_1-*w* SEM images was acquired with the following parameters (TR/TE) = (900/16.07) ms, number of averages = 2, field of view (FOV) = 25 x 25 mm^2, matrix (MTX) = 256 x 256, in plane resolution = 98 µm x 98 µm and slice thickness=1 mm. GAD was injected 20 seconds before the end of the second T_1-*w* SEM scan (Figure 2.3). A post-contrast agent T_{1-} mapping scan was performed, after the acquisition of eight T_{1-}w SEMS images, approximately 42 minutes following GAD injection (Figure 2.3).

The total time spent by each mouse in the magnet was 2 hours. Following each experiment mice were recovered and returned to their home cages with food and water *ad libitum*.

Tissue infiltration of the tracer was assessed using T_{1}- mapping where a relative increase in T_1 contrast indicates increased Gadovist uptake. Gadovist (Gd-DO3A-butrol) is a gadolinium based contrast enhancing agent referred to from here on out as Gd.

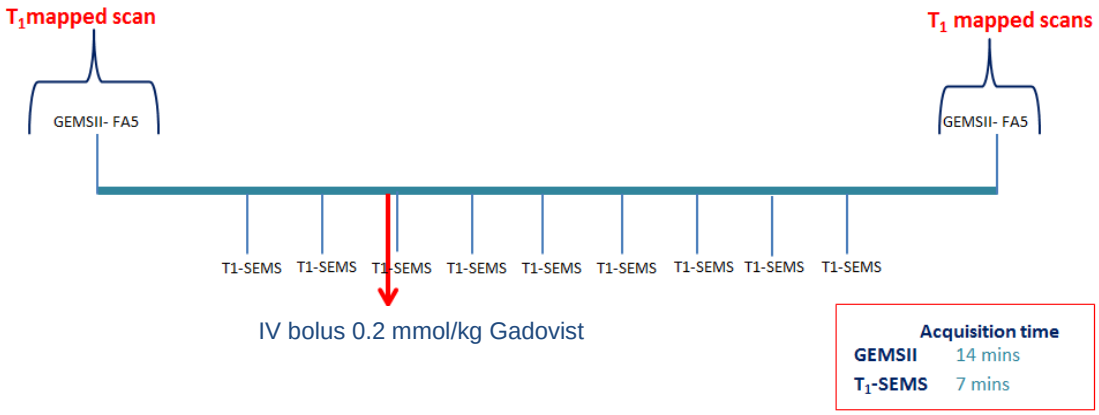

Figure 2.3: Timeline for T_1 mapping experiment with gadolinium enhancement.

Acquired images were processed using VNMRJ Math function to calculate apparent T_1 maps, as well as M(0) (apparent equilibrium magnetisation), S(0) (true equilibrium magnetisation) and RMS residual (error) maps.

Scans were converted to Matfiles and a correction for the effects of the Look-Locker RF-pulse train on magnetization was implemented (using a Matlab script written by Dr Dara O'Hogain) from Formula [3] below.

$$M(t)=M^{*}_{0}- (M_0+M^{*}_{0}) \exp (-t/T^{*}_{1})$$

Or

$M(t)= A-B \exp(-t/T^*_1)$

Where A, B, and T_1 may be obtained by a three-parameter fit.

$A=M^*_0=M_0T^*_1/T_1$

And

$B=M_0 +M^*_0 =M_0 (1 +T^*_1/T_1)$

Therefore

$T_1=T_1^*((B/A)1)$

or

$$T_1 = T_{1apparent}\left\{\left(\frac{M_0+M_0^*}{M_0^*}\right)-1\right\} \quad \textbf{[3]}$$ (Deichmann *et al.*, 1999)

Images were then analyzed using the freely available analysis software ImageJ. Quantification of the concentration of Gadolinium in brain tissue *in vivo* is possible using both the T_1 mapped values and Formula 4:

$R_{1post} = R_{1pre} + r_1[Gd]$, where $r = 1/T_1$ **[4]**

Where R_{1post} and R_{1pre} are the relaxation rates of the tissue post and pre Gd injection, [Gd] is the concentration of contrast agent and r_1 is the relaxivity of the contrast agent at 7T.

In order to measure the relative relaxation rate of Gd, Gadovist 1.0 mmol/ mL, was diluted with saline in an Eppendorf and measured as 6.49 mM^{-1} s^{-1} using an inversion recovery spectroscopy pulse sequence. The r_1 relaxation rates before and after contrast enhancement were measured from the T_1 maps of brain tissue, which in turn could be used to calculate the concentration of contrast agent in each region of interest as shown in Figure 2.4.

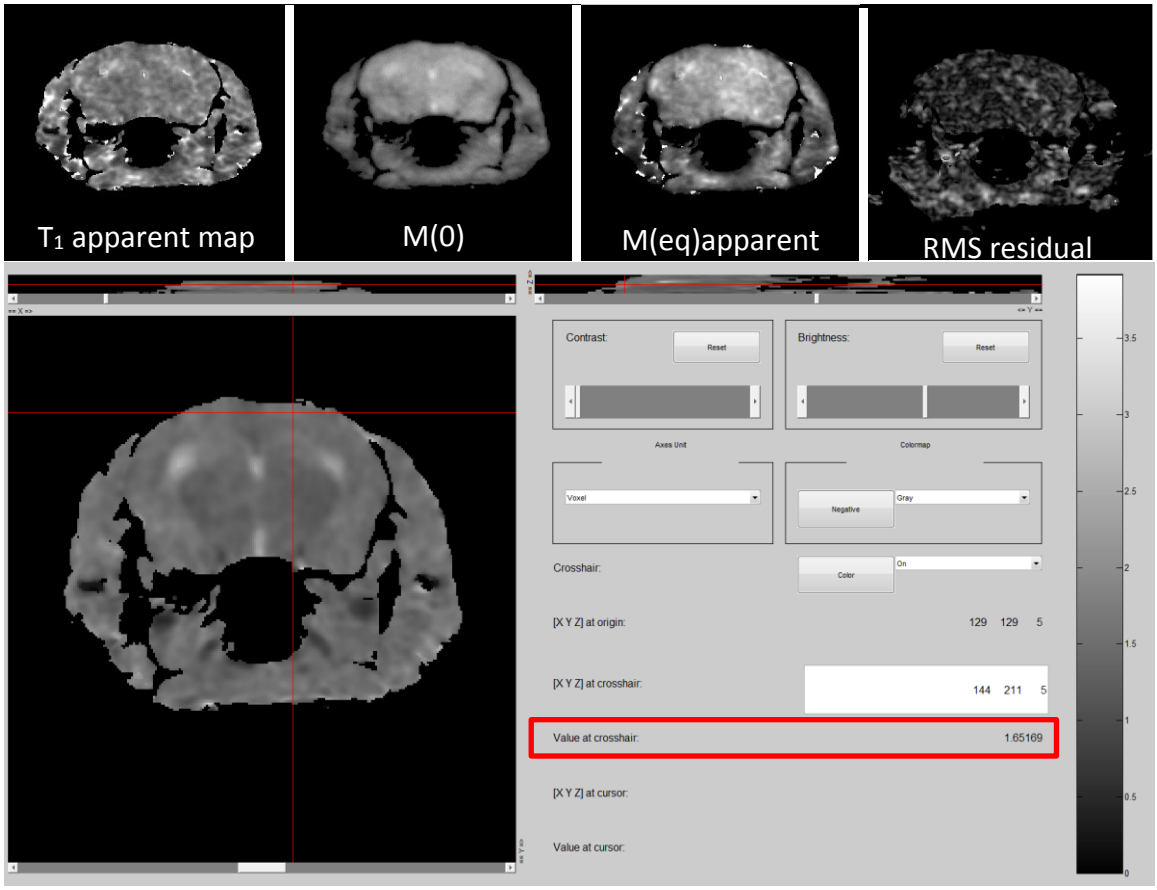

Figure 2.4: Representative images created using VNMRJ Math function.VNMRJ was used to calculate apparent T_1 maps, as well as M(0) (apparent equilibrium magnetisation), S(0) (true equilibrium magnetisation) and RMS residual (error) maps. Taken together these maps are used to create a corrected T_1 map used for calculating correct concentration and T_1 value shows accurate comparison with that of the literature ((DiFrancesco *et al.*, 2008), Mouse cortex at 7 T = 1.612).

2.9.5.2 BBB permeability index calculation

ROI's were assigned to a number of brain regions (cerebellum, hippocampus, ipsilateral cortex and contralateral cortex) and an average T_1 value was obtained from each ROI in T_1 maps acquired pre-and post-Gd administration. The BBB permeability index defined as the difference of R_1 (=1/T_1) values between post-and pre-Gd administration was calculated for each ROI at all time points.

2.9.6 Brain Water Content Measurements

Brain water content was determined using a dry and wet method. *C57BL/10, mdx, Cmah-/-mdx*, and *Cmah-/-* mice aged 6 months (n=4/genotype) were sacrificed by cervical dislocation and brains were rapidly excised from the cranial cavity. After brains were removed the hemispheres were separated along the interhemispheric plane and the cerebellum was removed. Both hemispheres and the cerebellum were then weighed (PGW M Precision balances, AE Adam) separately to assess their wet weights and then dried for 24 hours at 100°C to determine their dry weights. The water content was expressed as the following formula 5: Brain water content measurements were taken to compare against T_2 *in vivo* measurements.

[(wet weight)-(dry weight)]/ (wet weight)] x 100%	**Formula [5]**

2.10 Statistical analysis

Statistical analyses were performed with IBM SPSS Statistics 22.0 software. Repeated measures ANOVA were used for measurements taken from the same mouse over time (longitudinal MRI study), with students paired t-test used as post-hoc testing where a significant main effect was identified. A one-way ANOVA was used to measure kyphotic index and T_1-mapping data with Bonferroni post-hoc testing. A two-way ANOVA was used to measure wet:dry brain measurements, T_2 relaxation rates (6 and 18 months old), D2 ratio from the NOR task (4, 6, and 12 months old), and Barnes maze probe trials (4, 6, and 12 months) with Bonferroni post-hoc testing. Mixed measures repeated ANOVA was used to measure the Barnes maze test parameters (primary latency, total latency, primary errors, total errors) over time (4, 6, and 12 months).

Proteomic data were analysed using ANOVA (Progenesis Stats) and unpaired students t-test, $p<0.05$ was considered statistically significant and $p<0.01$ was considered very statistically significant.

Chapter 3. Using magnetic resonance imaging to detect and monitor changes in the mouse brain

3.1 Introduction

Magnetic resonance imaging (MRI) is a non-invasive imaging technique which provides spatially sensitive information on tissue structure. Sequences are specifically designed to quantify the proton density and the relaxation times (T_1 and T_2) of the mobile protons (Dunn and Zaim-Wadghiri, 1999). T_1-weighted (T_1-*w*) images (short TR and TE) with recovery of magnetisation occurring along the Z-axis, where the contrast between grey and white matter allows for accurate identification of anatomical structures. Whereas T_2- weighted (T_2-*w*) images, with contrast produced by fast spin echo (FSE) sequences (long TR and TE) and recovery occurring in the X-Y plane, allows for the identification of pathological features due to fat appearing dark and water appearing bright. T_1-w and T_2-w scans provide qualitative information regarding brain changes.

3.1.1 Studies in DMD patients

Post-mortem studies in the brains of DMD patients have failed to find consistent abnormalities, although only a few studies have been performed (Dubowitz and Crome, 1969a; Jagadha and Becker, 1988). Brain MRI studies in DMD patients have been very limited until recently, with studies restricted to case reports and there is only one study reported which used a quantitative voxel based morphometry analysis and resting state functional MRI with a region of interest in the motor cortex (Lv *et al.*, 2011). Recent studies in DMD patients increasingly use MRI to investigate the effect of dystrophin-deficiency on brain morphology (Doorenweerd *et al.*, 2014; Doorenweerd *et al.*, 2017a; Doorenweerd *et al.*, 2017b; Suzuki *et al.*, 2017).

A study looking at 30 DMD patients (aged 8-18 years old) detected a change in grey matter and total brain volume, both of which were found to be smaller in comparison to 22 age-matched controls (Doorenweerd *et al.*, 2014). Interestingly, the study found that DMD patients who were predicted to have a loss of the Dp140 isoform (hypothesised to have particular importance in CNS function (Lidov *et al.*, 1995)) were more severely affected in terms of total brain

and grey matter volumes in addition to a lower neuropsychological performance (Doorenweerd *et al.*, 2014). This study found that the reduced grey matter volume in DMD was global, whereas previously reported data isolated changes to the left primary somatosensory cortex, although no analysis of absolute grey matter volumes was performed in this case (Lv *et al.*, 2011). On the other hand, white matter examination showed no difference in volume between DMD patients and healthy controls, but detailed a significant difference on a microstructural level as shown by diffusion tensor imaging (DTI). DMD patients demonstrated structural changes suggestive of reduced fibre density, increased membrane permeability, or decreased structural organisation (Doorenweerd *et al.*, 2014). Whole brain quantitative MRI allowed the detection of reduced grey matter volume and white matter alterations in DMD boys that had not previously been reported. The reduction in grey matter volume was seen in both patients where Dp140 was present and Dp140 was absent, suggesting that this change in grey matter volume was related to the loss of full-length dystrophin (Dp427). The limitations of this study included the ages of the DMD boys investigated, as maximum global grey matter volume was reached between 6-9 years of age (Courchesne *et al.*, 2000), and the use of steroid treatment, which may have effects on brain morphology.

Radiological studies in DMD patients detailed glucose hypometabolism utilising positron emission tomography (PET) and altered metabolic concentrations by magnetic resonance spectroscopy (MRS) (Rae *et al.*, 1998; Lee *et al.*, 2002). The authors suggested this might indicate cytoarchitectural alterations, but it might also be a result of lower cerebral blood flow (CBF). A recent study looking at 28 DMD patients (aged 8-16 years old) and healthy aged matched controls demonstrated that CBF was reduced by 17%. Moreover, this study demonstrated that the changes in CBF were independent to the change in grey matter volume (Doorenweerd *et al.*, 2017a).

Interestingly the CBF was lowest in DMD patients null for Dp140 expression. Dp427 has previously been identified in neuronal post-synaptic membranes (Lidov *et al.*, 1990) whereas Dp140 was hypothesised to interact with astrocytic end feet (Nico *et al.*, 2005), which are associated with pericytes and microvessels, where pericytes closely regulate oxygen and glucose demands

upon sensory stimulation (Hall *et al.*, 2014). The limitations of this study included the presence of cardiac dysfunction in DMD patients. Indeed, cardiomyopathy is a common clinical symptom affecting 95% of patients by the age of twenty (Judge *et al.*, 2011) and previous studies have outlined a reduced CBF correlating to cognitive impairment in patients awaiting a heart transplant (Gruhn *et al.*, 2001).

3.1.2 Studies in the mdx mouse

Studies in the *mdx* mice have used *in vivo* MRI, high resolution localised magnetic resonance spectroscopy (^{1}H MRS), and *ex vivo* DTI to investigate alterations in brain structure and metabolites from mature brains (9 months old) (Xu *et al.*, 2015). They detailed an obvious difference in ventricle size and volume in *mdx* mice, in the absence of any changes in total brain volume. They suggested that the enlargement of ventricles was most likely due to grey matter atrophy or compression from excess CSF. The study also detailed changes in DTI measurements between *mdx* and aged matched controls. These findings were suggestive of a more continuous movement of water molecules with less restrictions and boundaries in the *mdx* mouse prefrontal cortex (PFC), although no statistical difference in DTI was found between grey and white matter regions of the cerebellum (Xu *et al.*, 2015). Utilising MRS, the study found alterations in metabolite concentrations in *mdx* mouse brains particularly in the hippocampus (HP) and the PFC regions, where dystrophin is normally abundantly expressed. Significant elevations of taurine (in PFC), glutathione (in HP), phosphocholine (in HP), and a significant reduction in GABA (in HP), were observed in *mdx* mice (Xu *et al.*, 2015). An imbalance of such metabolites has important consequences for functions such as osmoregulation, oxidative stress, membrane phospholipid synthesis, and GABAergic neurotransmission in the brain. Historical studies in the *mdx* mouse brain also detailed abnormal brain metabolism utilising ^{31}P- MRS, which can potentially influence CBF and glucose metabolism (Tracey *et al.*, 1996). Moreover, similarly to DMD patients the *mdx* mouse has showed an 18% reduction in CBF compared to wild type mice and a reduction in AQP4 in the brain, associated with swollen perivascular astrocyte processes and coupled with impaired development of the BBB (Goodnough et al., 2014).

As therapy development has rapidly expanded in recent years there is an urgent need to develop reliable outcome measures to monitor disease progression and treatment effect. The limited number of sensitive outcome measures to measure and monitor the DMD brain phenotype, together with the need to avoid invasive techniques in patients makes MRI a particularly attractive option. This is also reflected in the increasing interest in quantitative MR from pharmaceutical industry and regulatory bodies, where trial protocols are encouraged to include these techniques.

3.1.3 Aims

To date, almost all studies investigating cognitive dysfunction in DMD patients and in the *mdx* mice have detailed outcomes from one age group. There is conclusive evidence that the muscle pathology seen in DMD is progressive but it remains unclear if the cognitive impairment exhibited by approximately one-third of DMD patients is also progressive. Unlike muscle tissue, where invasive diagnostic measures such as a muscle biopsy are feasible (but are not desirable), non-invasive imaging is the only acceptable method for monitoring changes in the brain. Recent reports alluded that cognitive disability increases in DMD patients with increasing age (Suzuki *et al.*, 2017), therefore the overall aim of this chapter is to assess if qualitative and quantitative MRI protocols can detect changes in DMD mouse brains over time. Specifically, the aims of this chapter are:

- To establish structural MR imaging protocols for the application in mutant mouse brains to determine and monitor potential morphological changes.
- To monitor a cohort of control *C57BL/10* and DMD mice over a period of 18 months to evaluate the long-term effect of dystrophin-deficiency on the brain.
- To determine if there are structural brain differences or changes in regions of the mouse brain with age (utilising voxelwise tools in the Statistical Parametric Mapping (SPM) software).

3.2 Total brain volume (TBV) measurements

In order to determine total brain volume (TBV), images in T_1-w coronal, T_2-w-coronal, -sagittal, and –axial planes were acquired on a 7T MRI scanner (Figure 3.1). The same eight mice per genotype were repeatedly scanned between 4 and 18 months old in order to longitudinally monitor changes in TBV in the same animal over time. Images were analysed using the polygon tool in ImageJ (https://imagej.nih.gov/ij/) to manually outline around each brain slice from T_1-w coronal (25 slices), T_2-w coronal (25 slices), T_2-w sagittal (19 slices), and T_2-w axial (15 slices) images. The TBV was then calculated according to formula [1] (Figure 3.2).

Following a repeated measures ANOVA, there was a significant interaction between age and genotype on TBV ($F_{3, 26}$=19.39, p<0.01). At 4 months old *Cmah-/-mdx* mice exhibited a substantial enlargement in TBV (Table 3.3) compared to age matched control *C57BL/10*, *mdx,* and *Cmah-/-* mice. Interestingly, at 4 months old *Cmah-/-* mice also had an enlarged total brain volume (Table 3.4) compared to control *C57BL/10* and *mdx* mice, however, it was not as large as *Cmah-/-mdx* mice indicating that it is the loss of both Neu5Gc and dystrophin which contributes to a significant increases in TBV. At 4 months old control *C57BL/10* (Table 3.1) and *mdx* (Table 3.2) mice had comparable TBV.

Between 4 months and 18 months old control *C57BL/10* mouse brains increased by a total of 5.29±1.03 %, with the largest increase in TBV observed between 4 months and 6 months old (3.05±1.03 %). The *mdx* mouse brain also increased in volume between 4 months and 18 months old with an even larger TBV increase of 7.52±1.38 %. In contrast to the surge in increase of TBV observed in control *C57BL/10* mice, the *mdx* mice brains steadily increased in size between 4 months and 18 months old (Figure 3.3 and Figure 3.4). Remarkably, between 4 months and 6 months old the *Cmah-/-* and *Cmah-/-mdx* mouse brain volumes remained unchanged in volume. The *Cmah-/-mdx* mice did however have a 4.43±0.91 % increase in TBV between 4 months and 18 months old. In contrast, *Cmah-/-* mice (2/8 mice) MR images showed clearly focal atrophy of the brain restricted to the outer layer of the cortex which can be

traced to the primary somatosensory cortex, lateral parietal association cortex, and medial parietal association cortex (mouse brain atlas(Paxinos, 2008)) (Figure 3.5). Counter to the increase in TBV observed in the other genotypes, the *Cmah-/-* mice had a reduction in TBV of 3.25±1.76 % between 4 and 18 months old (Figure 3.4). Interestingly, the largest change in TBV was observed between 6 and 12 months old regardless of genotype.

Taken together, the results indicate that the control *C57BL/10* mouse brain increases in size by a small but significant amount between 4 months and 18 months old ($p<0.05$). However, the *mdx* mouse brain volume increased considerably more ($p<0.01$).

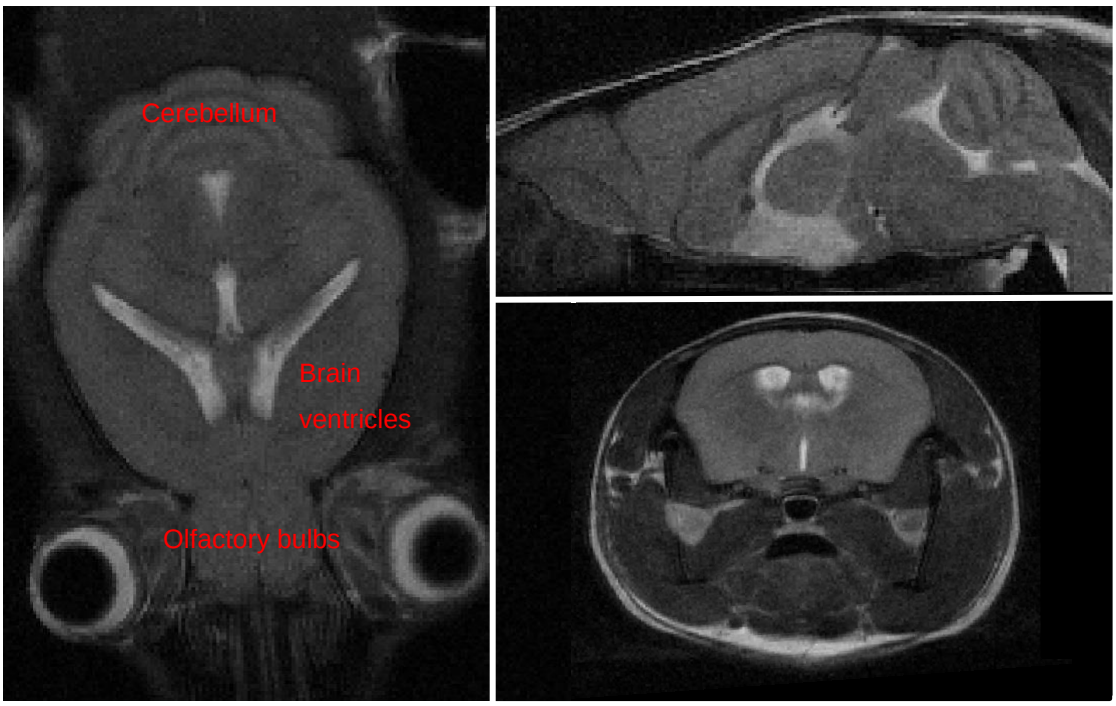

Figure 3.1: Representative T_2-w magnetic resonance images (MRI) of axial (left panel), sagittal (upper right panel) and coronal (lower right panel) control *C57BL/10* mouse brain at 4 months old.

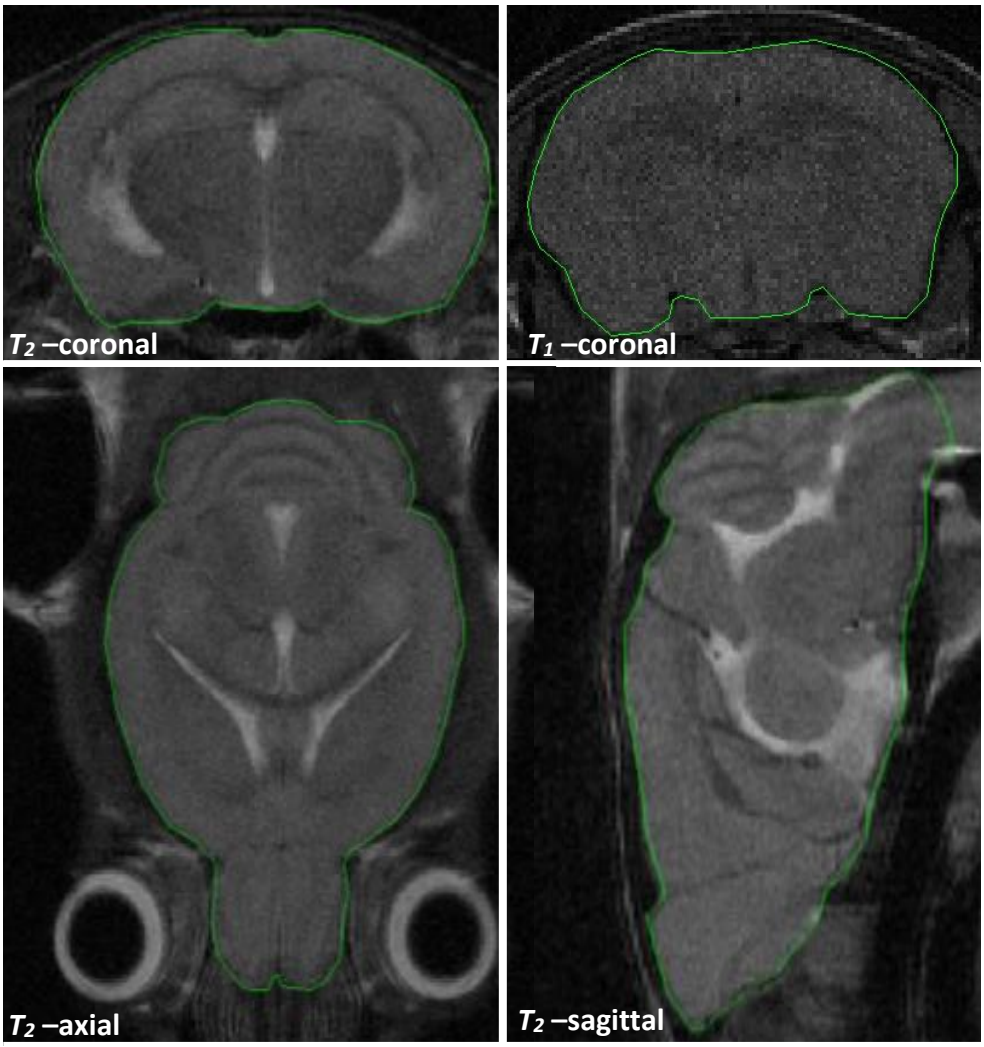

Total Volume = $\Sigma^{n}_{j=1}$ d. Aj Formula [1]

Where **Aj** is the cross sectional area on the **jth** slice through the mouse brain, **n** indicates the total number of the considered slices and **d** is the slice thickness (0.7mm).

Figure 3.2: Representative MR images demonstrating the method used for the estimation of total brain volume (TBV) in all mice using the polygon tool in ImageJ. The outline of each brain from representative T_1-w coronal, T_2-w -coronal, -axial, and -sagittal images are delineated in green. Formula [1] was used for calculating total brain volume. Images are shown for control *C57BL/10* mice only at 4 months old.

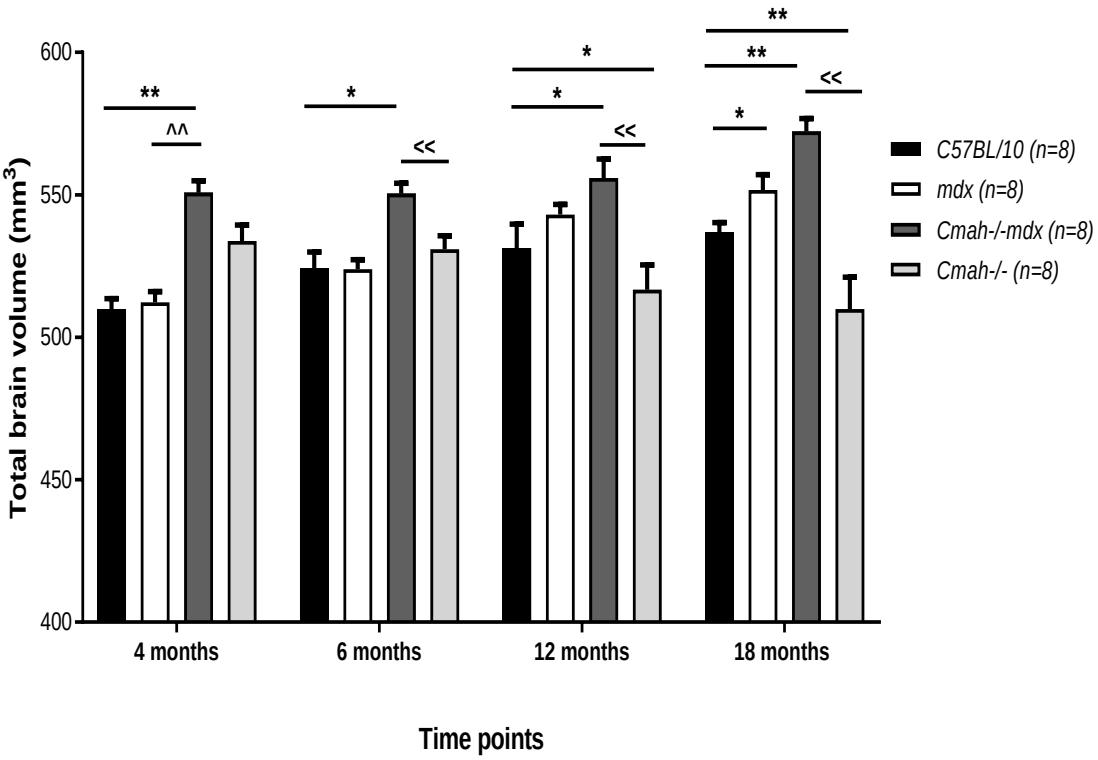

Figure 3.3: Bar graph displaying longitudinal comparison of total brain volume (TBV). MRI derived TBV for the same mice at 4 months old (n=8/genotype), at 6 months old (n=8/genotype), at 12 months old (n=8/genotype), and 18 months old (n=8/genotype). Interestingly, control *C57BL/10* mouse brain increased in volume between 4 and 18 months old. *Cmah-/-mdx* mice had the largest TBV at all time points investigated. Control *C57BL/10*, *mdx*, and *Cmah-/-mdx* mouse TBV increased between 4 and 18 months old, whereas *Cmah-/-* mouse TBV gradually decreased between 4 and 18 months old. Data presented as mean ±SEM, *p<0.05, **p<0.01, ^ denotes difference to *mdx* mice, < denotes difference to *Cmah-/-mdx* mice.

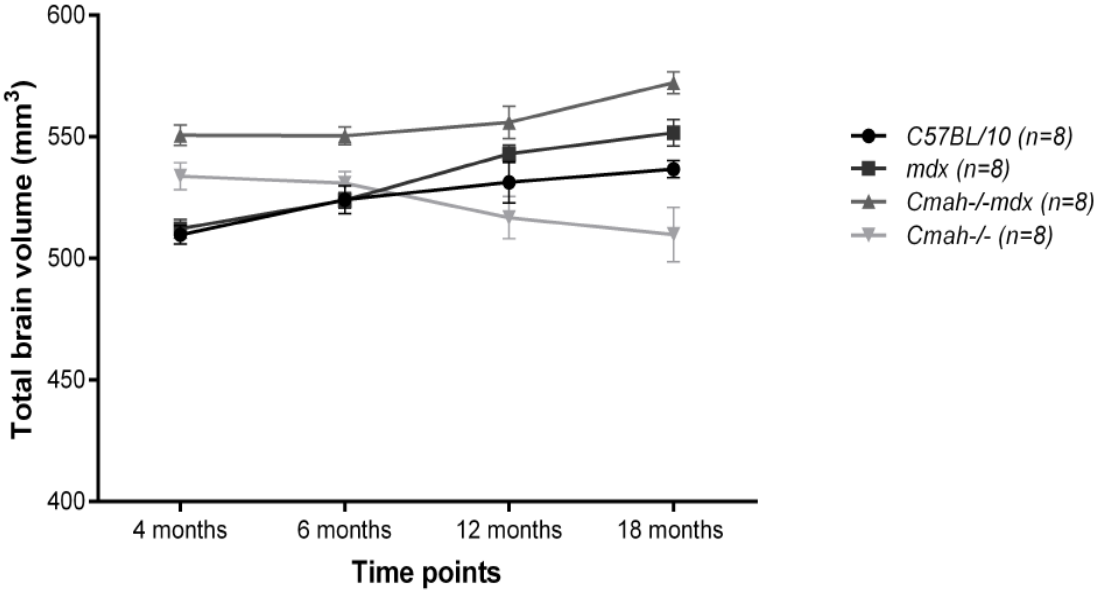

Figure 3.4: Line graph displaying longitudinal comparison of total brain volume (TBV). Estimated TBV in the same mice at 4 months old (n=8/genotype), at 6 months old (n=8/genotype), at 12 months old (n=8/genotype), and 18 months old (n=8/genotype). Although TBV varied between each mouse, an overall increase in TBV was evident in control *C57BL/10*, *mdx* and *Cmah-/-mdx* mouse brains but *Cmah-/-* mice showed brain atrophy from 6 months onwards. Control *C57BL/10* mouse brain increased significantly with increasing age. DMD mice (*mdx* and *Cmah-/-mdx* mice) had the largest TBV at 18 months old. Data presented as mean ±SEM.

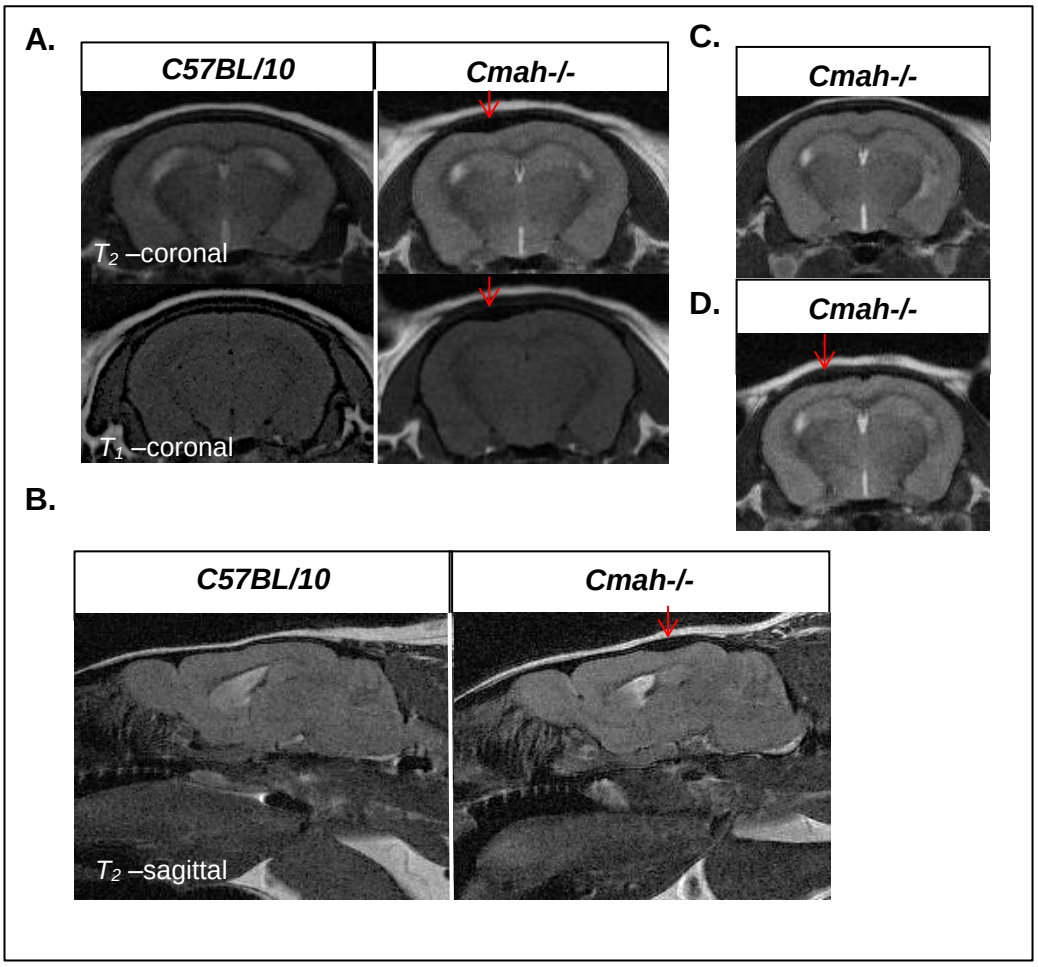

Figure 3.5: Focal atrophy in the *Cmah-/-* mouse brain. A. Coronal MR images where the red arrow indicates an area of focal brain atrophy seen only in *Cmah-/-* mice at 18 months old, which is evident on both T_1- and T_2-weighted images. **B.** Sagittal MR images where the red arrow indicates the same region of atrophy observed on coronal MR images. The representative sagittal images are from control *C57BL/10* and *Cmah-/-* mice at approximately the same slice. The effect of atrophy, which is clearly visible on MR images, was observed in 2/8 *Cmah-/-* mice at 18 months old. Atrophy such as this was not observed in any other mouse strain. **C.** T_2-*w* coronal image from the same *Cmah-/-* mouse at 12 months old displaying no sign of atrophy. **D.** T_2-w coronal image from a second *Cmah-/-* mouse at 18 months old showing similar but less severe signs of atrophy.

***C57BL/10* mice total brain volumes at 4 months old**				
Mouse	Coronal T_2-*w* Total Volume (mm^3)	Axial T_2-*w* Total Volume (mm^3)	Sagittal T_2-*w* Total Volume (mm^3)	Mean volume across all orthogonal planes (mm^3)
***C57Bl/10*_1**	516	514	508	513
***C57Bl/10*_2**	527	536	536	533
***C57Bl/10*_3**	517	513	516	515
***C57Bl/10*_4**	534	536	534	535
***C57Bl/10*_5**	496	493	515	501
***C57Bl/10*_6**	516	499	517	511
***C57Bl/10*_7**	498	493	513	501
***C57Bl/10*_8**	488	484	498	490
			Average brain volume for *C57Bl/10*=	512
Mean Volume for each MRI acquisition (mm^3)	512	508	517	

Table 3.1: Volumetric comparison between all *C57BL/10* mice using T_2-*w* images acquired across all orthogonal planes. Comparable values were obtained across all orthogonal planes.

***mdx* mice total brain volumes at 4 months old**				
Mouse	Coronal T_2-*w* Total Volume (mm^3)	Axial T_2-*w* Total Volume (mm^3)	Sagittal T_2-*w* Total Volume (mm^3)	Mean volume across all orthogonal planes (mm^3)
***mdx* _1**	519	510	511	513
***mdx* _2**	521	522	523	522
***mdx* _3**	516	515	516	516
***mdx* _4**	526	529	523	526
***mdx* _5**	514	520	527	520
***mdx* _6**	528	522	530	527
***mdx* _7**	505	515	517	512
***mdx* _8**	499	495	526	507
			Average brain volume for *mdx* =	**519**
Mean Volume for each MRI acquisition (mm^3)	516	516	522	

Table 3.2: Volumetric comparison between all *mdx* mice using T_2-*w* images acquired across all orthogonal planes. Comparable values were obtained across all orthogonal planes.

Cmah-/-mdx mice total brain volumes at 4 months old				
Mouse	Coronal T_2-*w* Total Volume (mm^3)	Axial T_2-*w* Total Volume (mm^3)	Sagittal T_2-*w* Total Volume (mm^3)	Mean volume across all orthogonal planes (mm^3)
***Cmah-/-mdx* _1**	556	557	554	556
***Cmah-/-mdx* _2**	562	552	540	551
***Cmah-/-mdx* _3**	556	552	556	555
***Cmah-/-mdx* _4**	565	561	563	563
***Cmah-/-mdx* _5**	549	552	551	551
***Cmah-/-mdx* _6**	542	549	545	545
***Cmah-/-mdx* _7**	542	543	537	541
***Cmah-/-mdx* _8**	531	538	534	534
Average brain volume for *Cmah-/-mdx* =				**550**
Mean Volume for each MRI acquisition (mm^3)	550	551	548	

Table 3.3: Volumetric comparison between all *Cmah-/-mdx* mice using T_2-*w* images acquired across all orthogonal planes. Comparable values were obtained across all orthogonal planes.

	Cmah-/- mice whole brain volumes at 4 months old				
	Mouse	Coronal T_2-*w* Total Volume (mm^3)	Axial T_2-*w* Total Volume (mm^3)	Sagittal T_2-*w* Total Volume (mm^3)	Mean volume across all orthogonal planes (mm^3)
	***Cmah-/-* _1**	546	548	549	548
	***Cmah-/-*_2**	557	549	551	552
	***Cmah-/-*_3**	532	544	549	542
	***Cmah-/-*_4**	520	523	510	518
	***Cmah-/-*_5**	519	537	534.	530
	***Cmah-/-*_6**	534	533	541	536
	***Cmah-/-*_7**	538	541	550	543
	***Cmah-/-*_8**	536	537	545	539
Average brain volume for *Cmah-/-* =					**538**
Mean Volume for each MRI acquisition (mm^3)		535	539	541	

Table 3.4: Volumetric comparison between all *Cmah-/-* mice using T_2-*w* images acquired across all orthogonal planes. Comparable values were obtained across all orthogonal planes.

3.3 Morphological findings

3.3.1 Brain ventricle system

The brain ventricle system was visible in all planes of the MR images acquired. ROI's were identified on T_2-weighted coronal images for volumetric measurements within the brain ventricular system (Figure 3.6). The mouse brain atlas served as a reference for the accurate depiction of brain structures with the anatomical points on the skull, Bregma and Lambda (Paxinos, 2008). Following a repeated measures ANOVA there was a significant interaction between age and genotype on ventricle volume ($F_{3, 28}$=5.79, p<0.05). The first striking difference identified using MRI was the significant reduction in the ventricular volume and size of the *Cmah-/-* mice (Figure 3.7). This effect was apparent in all eight *Cmah-/-* mice and although the ventricle system did increase in volume as the mice aged (between 4 and 18 months), they still remained much smaller in volume compared to age matched control *C57BL/10* mice (Figure 3.8, Figure 3.10 and Figure 3.11). In addition to the lateral ventricular (LV) volume reduction, the third ventricle (including ventral (V3V) and dorsal third ventricle (D3V)) was also significantly smaller in volume in *Cmah-/-* mice (Figure 3.10). A notable loss of CSF from the ventricular spaces was also seen in 3/8 *Cmah-/-* mouse brains (Figure 3.8).

The DMD mouse lateral ventricles (LV) were enlarged compared to age matched control *C57BL/10* mice (Figure 3.8 and Figure 3.9). The dilation of LVs was particularly prominent in the coronal and axial MR images acquired. Although this effect was significant in *Cmah-/-mdx* between 4 and 18 months old, it eluded significance in *mdx* mice until 12 months old (Figure 3.10). There was no difference in the volume of the 4V between any genotype at any time point investigated (Figure 3.10). The total relative ventricular volume was also increased in DMD mice brains and was significantly increased in *mdx* mice compared to control mice from 12 months onwards. Although there was a difference observed between ventricles at 4 months, 12 months, and 18 months old, at 6 months old there was no difference found in the ventricle system of control *C57BL/10*, *mdx,* and *Cmah-/-mdx* mouse brains. Interestingly, the 6 month old time point was where the largest observation of total brain volume increase was detected (Figure 3.3), suggesting that the brain volume increases

faster than the brain ventricular system, given that these measurements were relative.

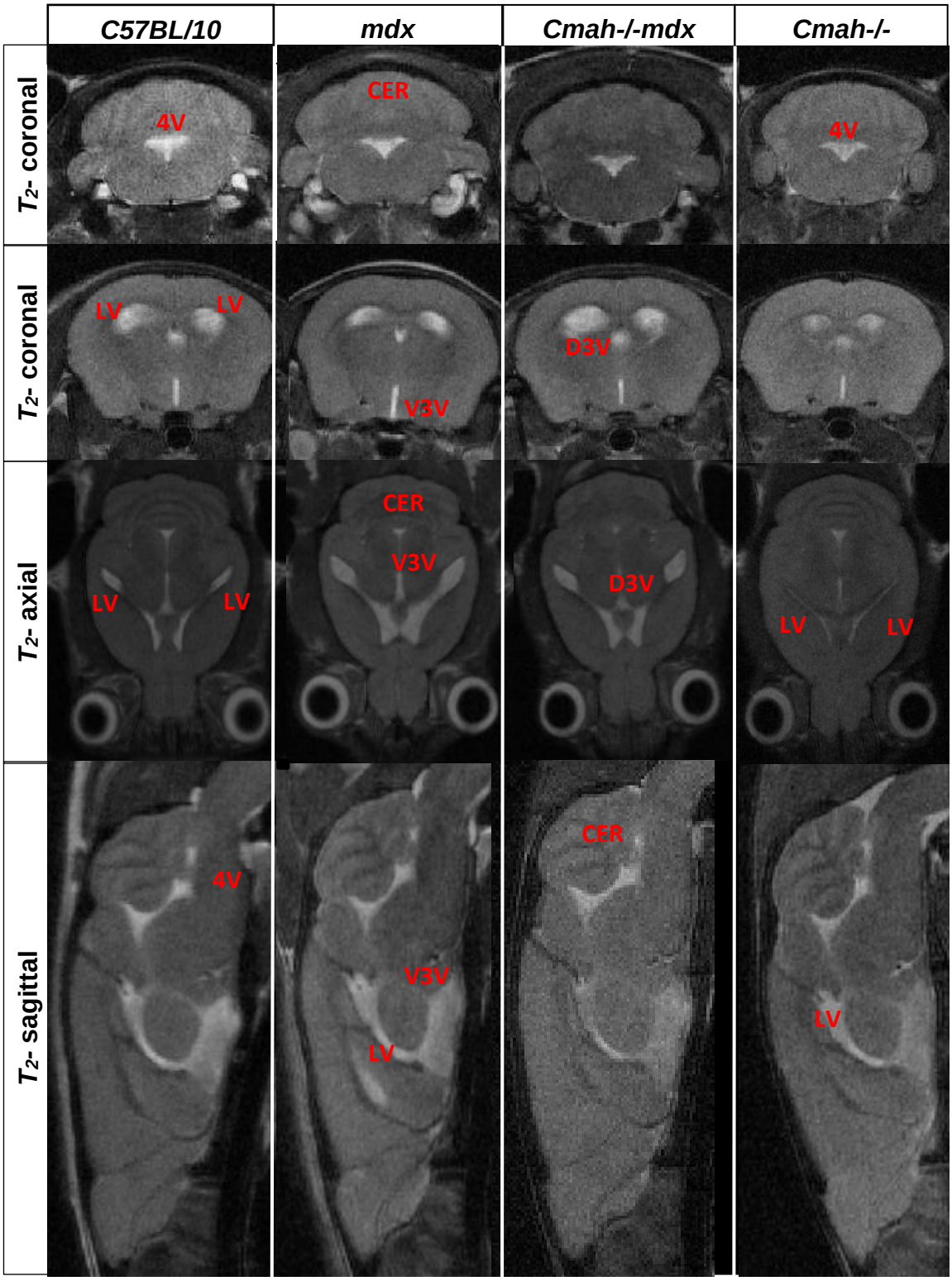

Figure 3.6: Representative *T_2-w* axial, sagittal, and coronal MR images. Images show the lateral ventricle (LV), ventral third ventricle (V3V), dorsal third ventricle (D3V), fourth ventricle (4V), and cerebellum (CER) for control *C57BL/10*, *mdx*, *Cmah-/-md,* and *Cmah-/-* mice at 4 months old. Ventricles appear lager in DMD mouse brains.

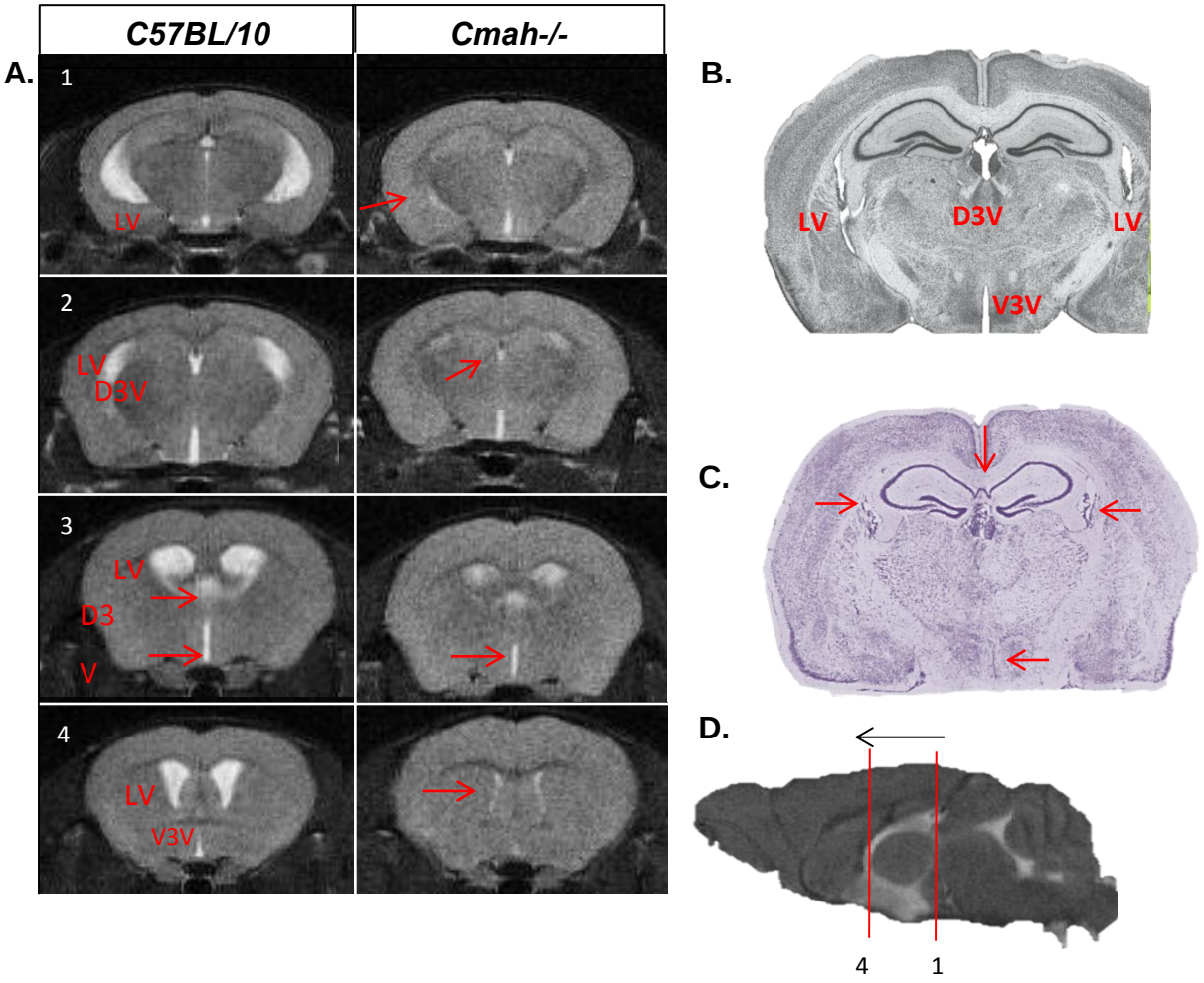

Figure 3.7: Changes in *Cmah-/-* mouse brain ventricular system. A. Representative T_2-w coronal MR images from control *C57BL/10* and *Cmah-/-* mice displaying lateral ventricles (LV), ventral third ventricle (V3V), and dorsal third ventricles (D3V) at 4 months old. Red arrows highlight particular ventricles in *Cmah-/-* mice which are abnormal compared to control mice. Substantial reduction in the LV, V3V, and D3V was evident across all MR images acquired, delineating these ventricles in the *Cmah-/-* mouse brain. **B.** The Allen mouse brain histology atlas showing the correct formation of the LV, V3V, and D3V. **C.** Cresyl violet stained cryosection (20 µm) of a *Cmah-/-* mouse brain corresponding to the mouse brain atlas image, detailing the reduction in size of the LV, 3V, and D3V. **D.** Sagittal MR image where red lines indicate the regions where the coronal images were acquired, black arrow indicates the direction of slices 1-4.

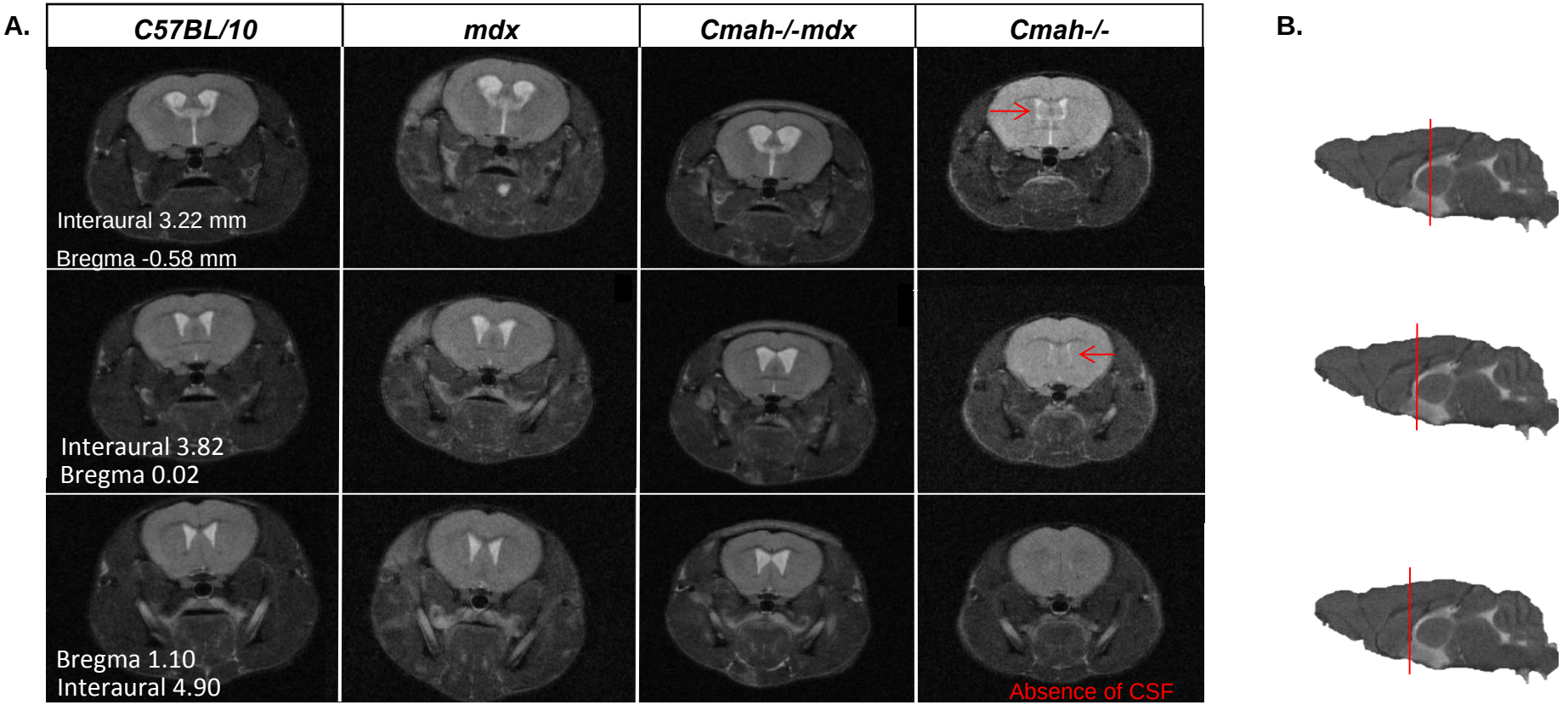

Figure 3.8: MR images of the mouse brain ventricular system. A. Representative T_2-*w* coronal images of control *C57BL/10*, *mdx*, *Cmah-/-mdx,* and *Cmah-/-* lateral ventricles highlighting the substantial reduction in lateral ventricle size in the *Cmah-/-* mice brains (red arrows) and the notable absence of CSF (n=8 mice/genotype). Images were taken from 4 month old mice, however, the effect was also evident at all other time points (6, 12, and 18 months old). Interaural and Bregma points, from the mouse brain atlas, are provided for accurate depiction of brain structures with the anatomical points. **B.** Sagittal images where the red line indicates approximately where the coronal slice was acquired through the mouse brain.

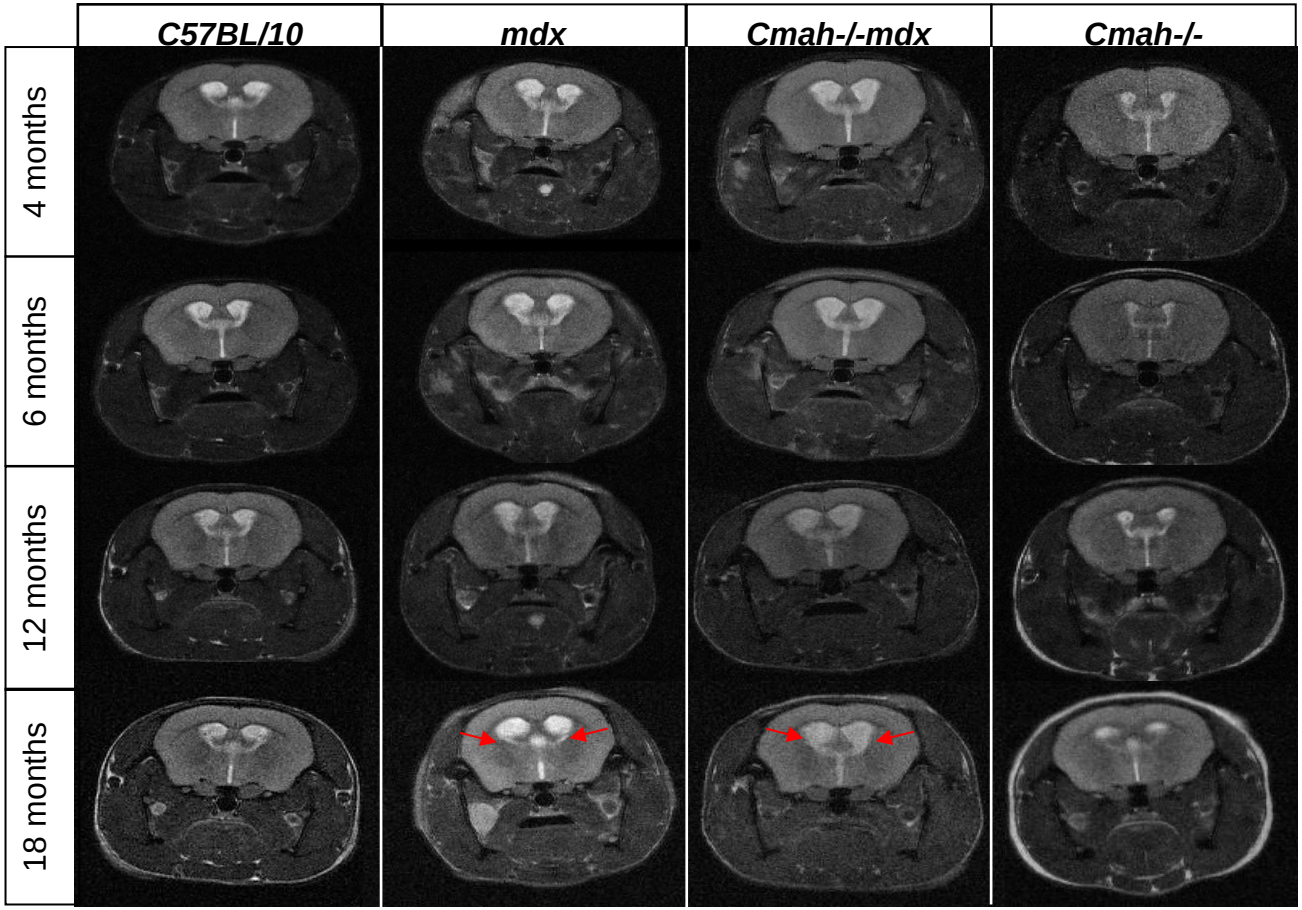

Figure 3.9: *T_2-w*-coronal MR images of control *C57BL/10, mdx, Cmah-/-mdx* and *Cmah-/-* lateral ventricles taken from the same mouse between 4 months and 18 months old. There is an enlargement of the lateral ventricular volume in DMD mouse models (*mdx* and *Cmah-/-mdx* mice) between 4 and 18 months old (red arrows). *Cmah-/-* mouse lateral ventricles (LV) also increased slightly with age. Little to no changes were observed in control *C57BL/10* mouse brain ventricles over time.

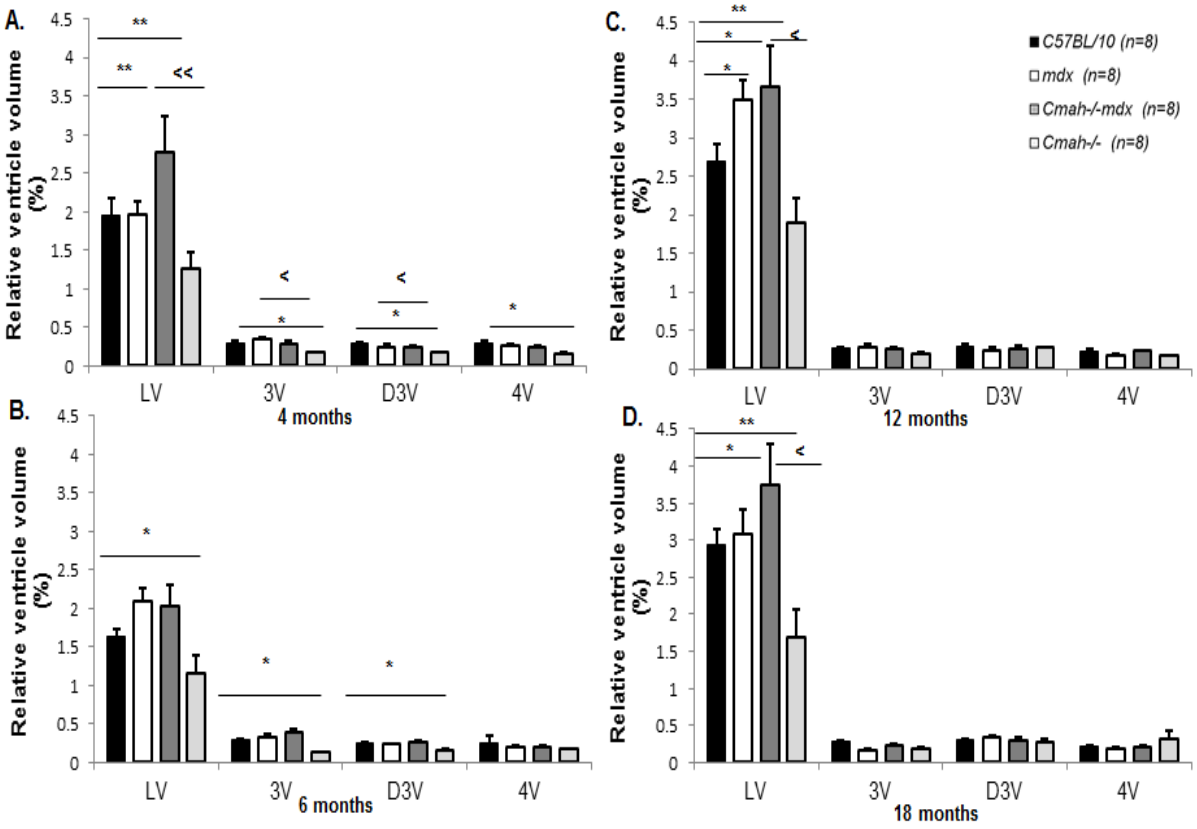

Figure 3.10: Bar graphs displaying relative ventricular volume in the same mice between 4 and 18 months old. LV= lateral ventricle, 3V= third ventricle, D3V= dorsal third ventricle, and 4V= fourth ventricle. **A.** Relative ventricle volume at 4 months old, showing that *Cmah-/-mdx* mice have significantly larger LVs compared to *mdx* and aged matched control mice. *Cmah-/-* mice also displayed a large reduction in the 3V volume compared to age matched control *C57BL/10* mice. **B.** Relative ventricle volume at 6 months old. Interestingly no significant difference in ventricle volume was observed between control *C57BL/10*, *mdx,* and *Cmah-/-mdx* mice, only *Cmah-/-* mice showed a reduction in LVs, 3V and D3V volume. **C.** Relative ventricle volume at 12 months old, showing that both *mdx* and *Cmah-/-mdx* have significantly larger LVs compared to aged matched control *C57BL/10* mice. **D.** Relative ventricle volume at 18 months old, showing a significant reduction in *Cmah-/-* mice LVs compared to all other genotypes. *Cmah-/-mdx* mice had the largest increase in LV volume between 4 and 18 months old. Data presented as mean± SEM, *p<0.05, **p<0.01, < denotes difference to *Cmah-/-mdx* mice.

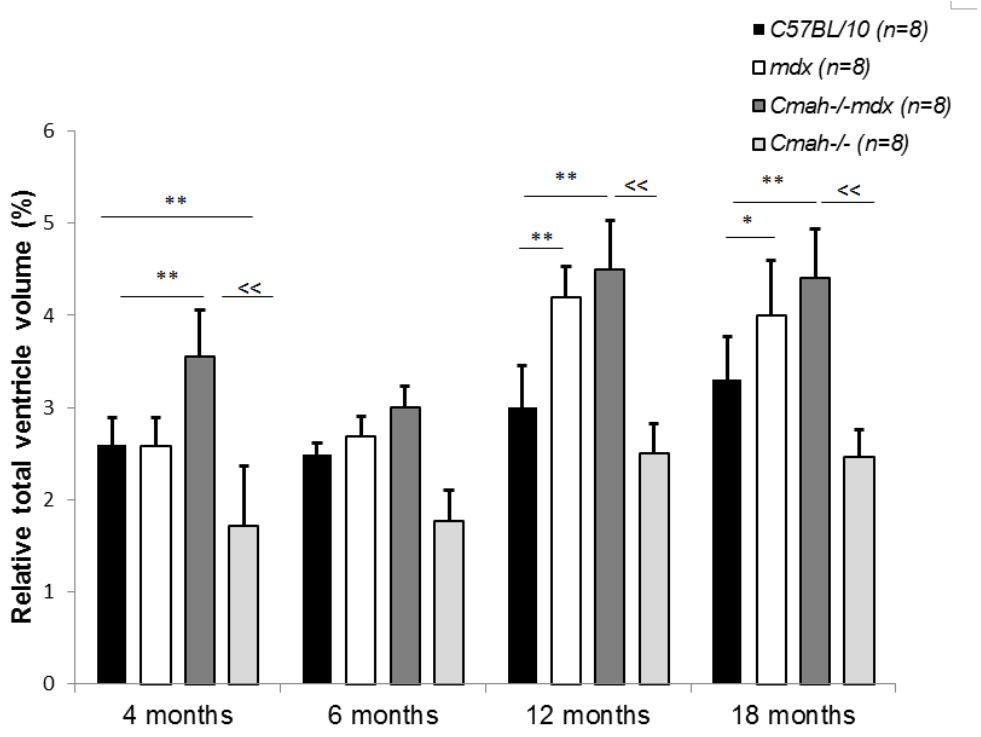

Figure 3.11: Bar graph displaying the relative total ventricular volume of the same mice between 4 and 18 months old. Relative total ventricle volume is calculated based on the total volume of the ventricle system expressed as a percent of total brain volume. At 4 months old the *Cmah-/-mdx* mice had a significantly larger total ventricular volume, whereas the *Cmah-/-* mice had the smallest total ventricular volume. From 12 months onwards both DMD mice models had a significantly larger total ventricle volume compared to age matched controls. Total ventricular volume increased with increasing age in all genotypes. Data presented as mean ± SEM, *p<0.05, **p<0.01 vs control *C57BL/10* mice, < denotes difference to *Cmah-/-mdx* mice.

The ventricles in *Cmah-/-mdx* mice appeared morphologically different compared to the ventricles of age matched control *C57BL/10* and *Cmah-/-* mice (Figure 3.12). The D3V merged into the LV at a more posterior position than that observed in the control *C57BL/10* mice indicating that there were changes in the development of the ventricular system in *Cmah-/-mdx* mice. This effect was apparent in 2/8 *Cmah-/-mdx* mice scanned in the longitudinal study and was also evident at all time points investigated. The formation of this 'fifth brain ventricle' was similar to the human disorder known as Cavum Septum Pellucidum (CSP), which is a normal variant CSF space between the leaflets of the septum pellucidum. CSP is present in all foetuses but by the age of 6 months the septal leaves fuse in an anterior-posterior manner, forming the normal ventricle system. Less than 15% of adults have CSP but it has been associated with neurological disorder, including schizophrenia and post-traumatic stress disorder, due to under development of the limbic system (Khanra *et al.*, 2016). This suggests that *Cmah-/-mdx* mice could have additional cognitive abnormalities, due to the presence of CSP and its association will malformation of limbic structures, including the hippocampus.

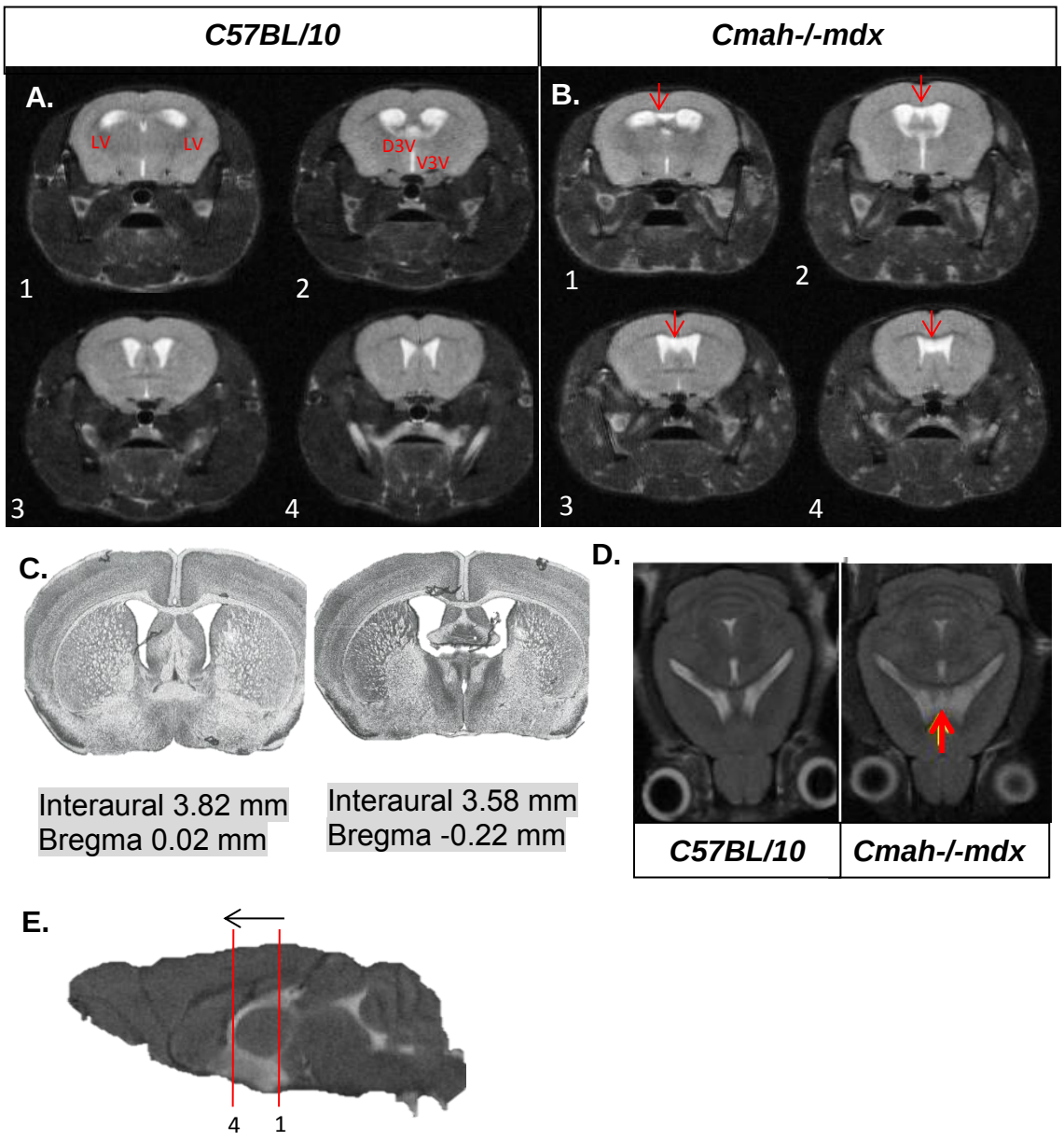

Figure 3.12: Abnormalities in the brain ventricular system of *Cmah-/-mdx* mice. A. Representative T_2-w coronal MR images from control *C57BL/10* mice at 4 months old which delineates the normal formation of the lateral ventricles (LV), dorsal third ventricle (D3V), and ventral third ventricle (V3V). **B.** Representative T2-w coronal MR images from *Cmah-/-mdx* at 4 months old showing changes in the structure of the LV and D3V (red arrow). **C.** The Mouse Brain Histology atlas (Paxinos, 2008) showing the correct formation of the LV and D3V. **D.** Representative T_2-w axial MR images from control *C57BL/10* and *Cmah-/-mdx* mice at 12 months old demonstrating the persistent nature of this ventricular abnormality (red arrow indicates CSP). **E.** Sagittal images where the red line indicates approximately where the coronal slice was acquired through the mouse brain.

3.3.2 Cerebellar volume measurements

The cerebellum is a grey and white matter structure at the posterior end of the brain which has a distinctive web-like appearance seen in all three orthogonal views (Figure 3.6). The distinctive appearance is the result of the white matter cerebellar lobule strips appearing hypointense in a T_2-weighted image. The cerebellum can be found from Bregma -4.96 mm to Bregma -8.24 mm in the histology atlas (Paxinos, 2008). In the axial view, the cerebellum is located superior to the 4V, the pons and the medulla. Figure 3.13 shows the paraflocculus and flocculus lobules, which with the crus 1 ansiform lobule and the simple lobule, make up the lateral cerebellar regions and have thus been included in all cerebellar volume measurements.

The volume of the cerebellum was measured from serial coronal T_2-weighted MR images of control *C57BL/10* and mutant mice, covering the same anatomical region in the brain and collected between 4 and 18 months old (Figure 3.13 and Figure 3.14). Following a repeated measures ANOVA, no difference in the cerebellar volume was observed in any genotype between 4 and 18 months old (Figure 3.15) ($F_{3, 26} = 1.11$, $p=0.38$). There was also no interaction between age and cerebellar volume.

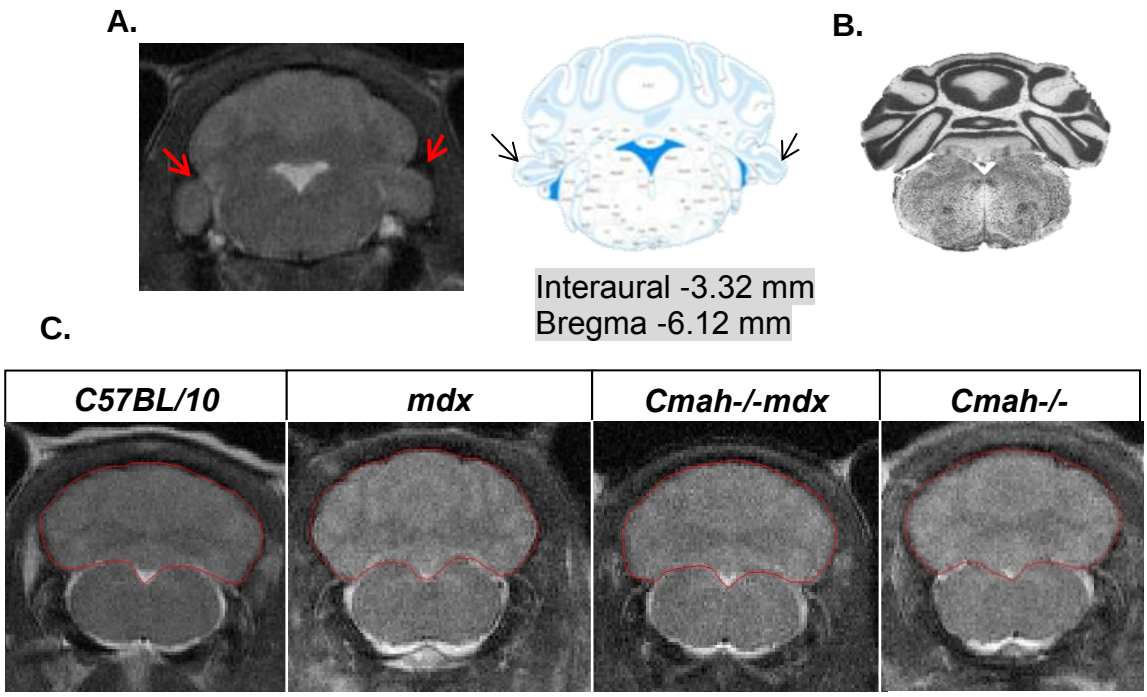

Figure 3.13: Cerebellar volume measurements. **A.** *T_2-w* coronal MR image showing the paraflocculus and floculus lobules of the lateral cerebellum (red arrows) and the corresponding image from the mouse brain atlas (black arrows) **B.** The mouse brain atlas image corresponding to the coronal section of the mouse brain displayed in C. **C.** Representative coronal *T_2-w* MR images of control *C57Bl/10*, *mdx*, *Cmah-/-mdx,* and *Cmah-/-* mouse cerebellum delineated in red following ROI analysis on ImageJ.

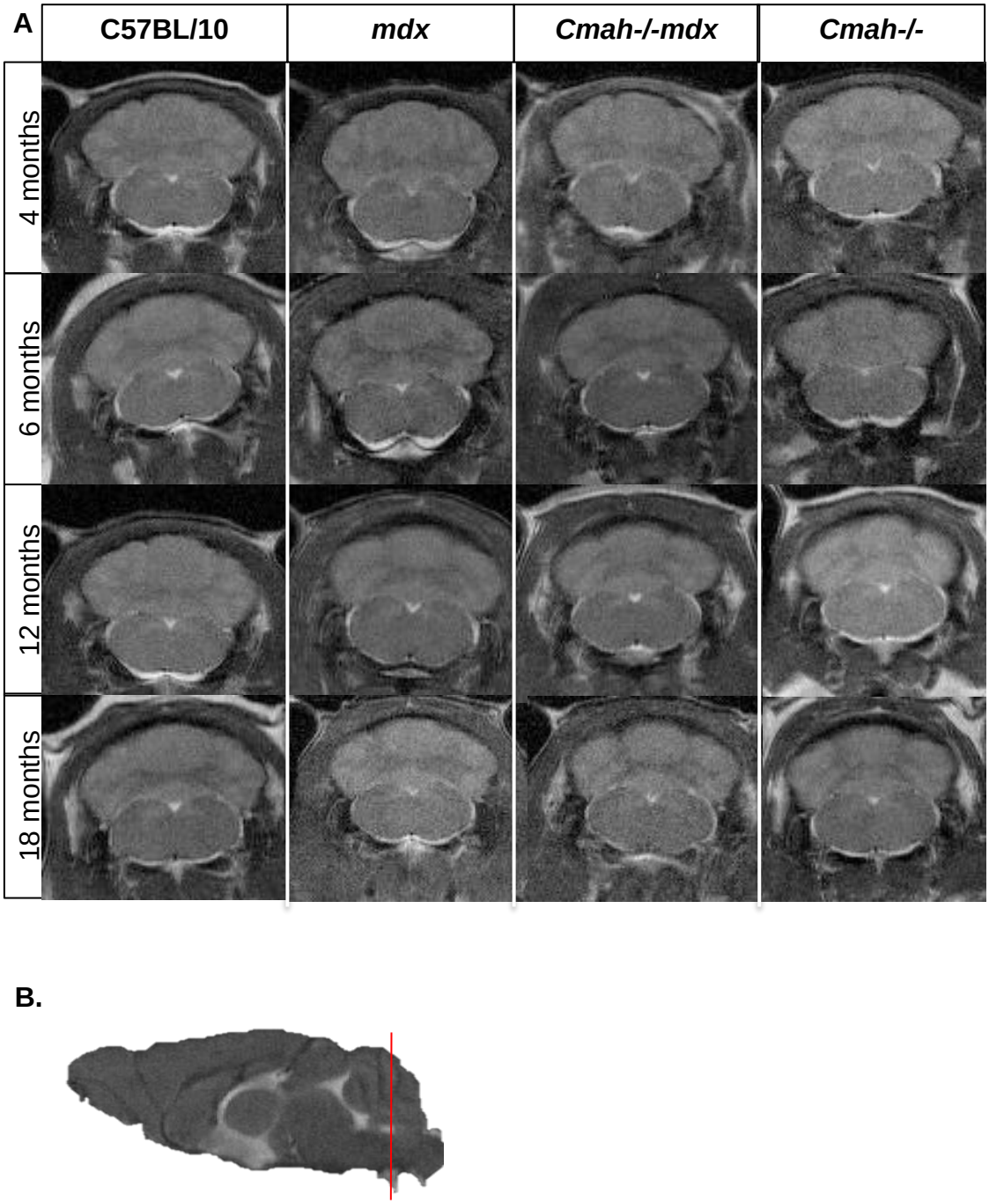

Figure 3.14: No morphological changes were identified in the cerebellum. **A.** *T_2-w* coronal MR images of control *C57BL/10, mdx, Cmah-/-mdx,* and *Cmah-/-* cerebellum taken from the same mouse between 4 months and 18 months old. There were no morphological or volume changes between any genotype in the cerebellum. **B.** Sagittal image where the red line indicates the approximate slice corresponding to the coronal images.

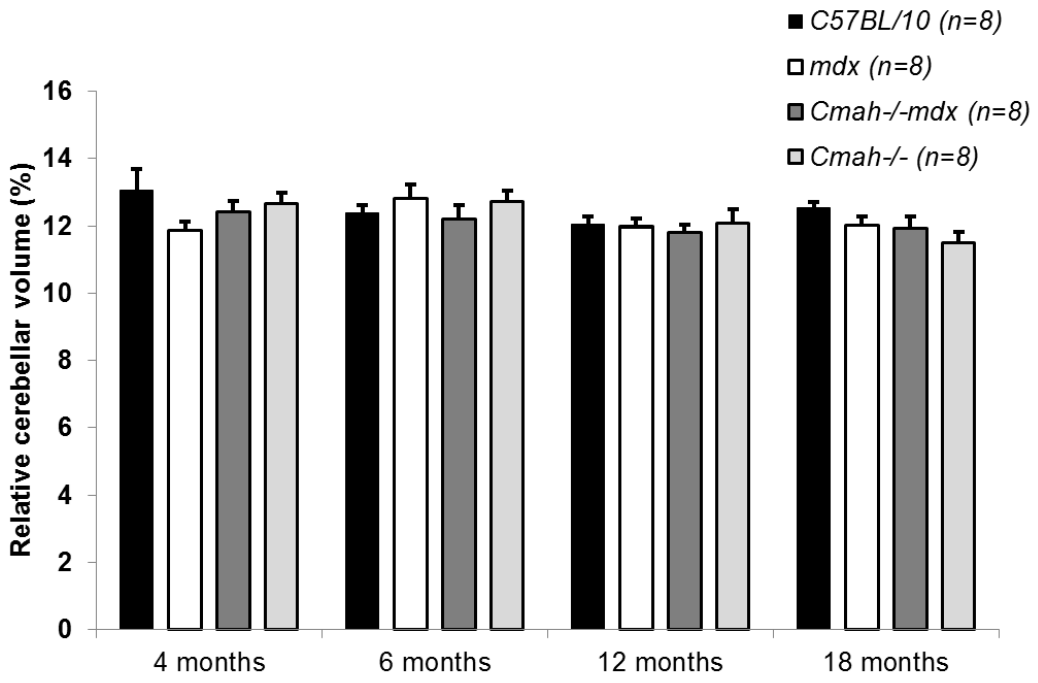

Figure 3.15: Bar graph displaying the relative cerebellar volume in the same mice between 4 and 18 months old. Relative cerebellar volume is calculated based on the volume of the cerebellum expressed as a percentage of total brain volume (TBV). Overall, there was no difference between relative cerebellar volume in any genotype between 4 and 18 months old. Data presented as mean ± SEM.

3.3.3 Hippocampal volume measurements

The volume of the hippocampus was measured using representative T_2-weighted MR images from *C57BL/10*, *mdx, Cmah-/-mdx,* and *Cmah-/-* mice, covering the same anatomical region in the brain and collected between 4 and 18 months old (Figure 3.16). The whole hippocampus (CA1, CA3, DG and general hippocampal areas) was utilised for hippocampal volume estimations which were delineated according to the Mouse Brain atlas (Paxinos, 2008). Serial T_2-weighted MR images were considered in order to accurately measure the entire volume of the hippocampus (Figure 3.7). Following a repeated measures ANOVA, there was a significant interaction between age and genotype on ventricle volume ($F_{3, 26}$=3.45, p<0.05).

The hippocampal volume varied between genotypes and between age groups. The hippocampal volume was comparable between control *C57BL10* and *mdx* mice at all time points (Figure 3.17) although the hippocampus was slightly larger in *mdx* mice at 4 months old. The hippocampus was largest in *Cmah-/-*

mdx mice at 12 months old. The hippocampal volume was reduced in the *Cmah-/-* mice between 4 and 12 months old compared to both *Cmah-/-mdx* mice and control *C57BL/10* mice. However by 18 months old all mice had comparable relative hippocampal volumes (Figure 3.17).

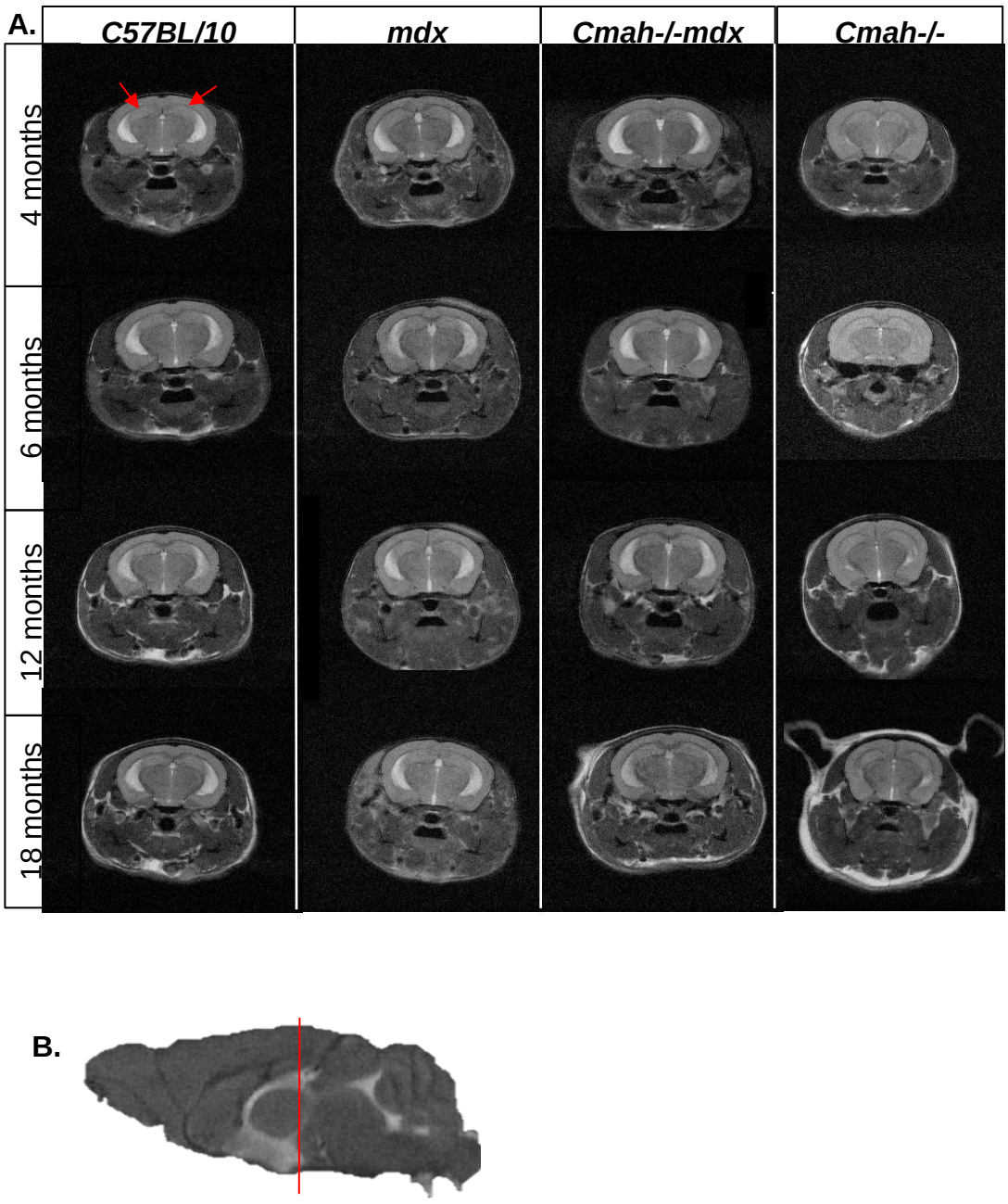

Figure 3.16: No morphological changes detected in the hippocampus. (Red arrow delineates hippocampus on first panel of images). **A.** T_2-w coronal MR images of control *C57BL/10*, *mdx*, *Cmah-/-mdx*, and *Cmah-/-* hippocampus taken from the same mouse between 4 months and 18 months old. There were no morphological changes, but volume fluctuated in DMD mouse models between 4 and 18 months old. **B.** Sagittal image where the red line indicates the approximate slice corresponding to the coronal images.

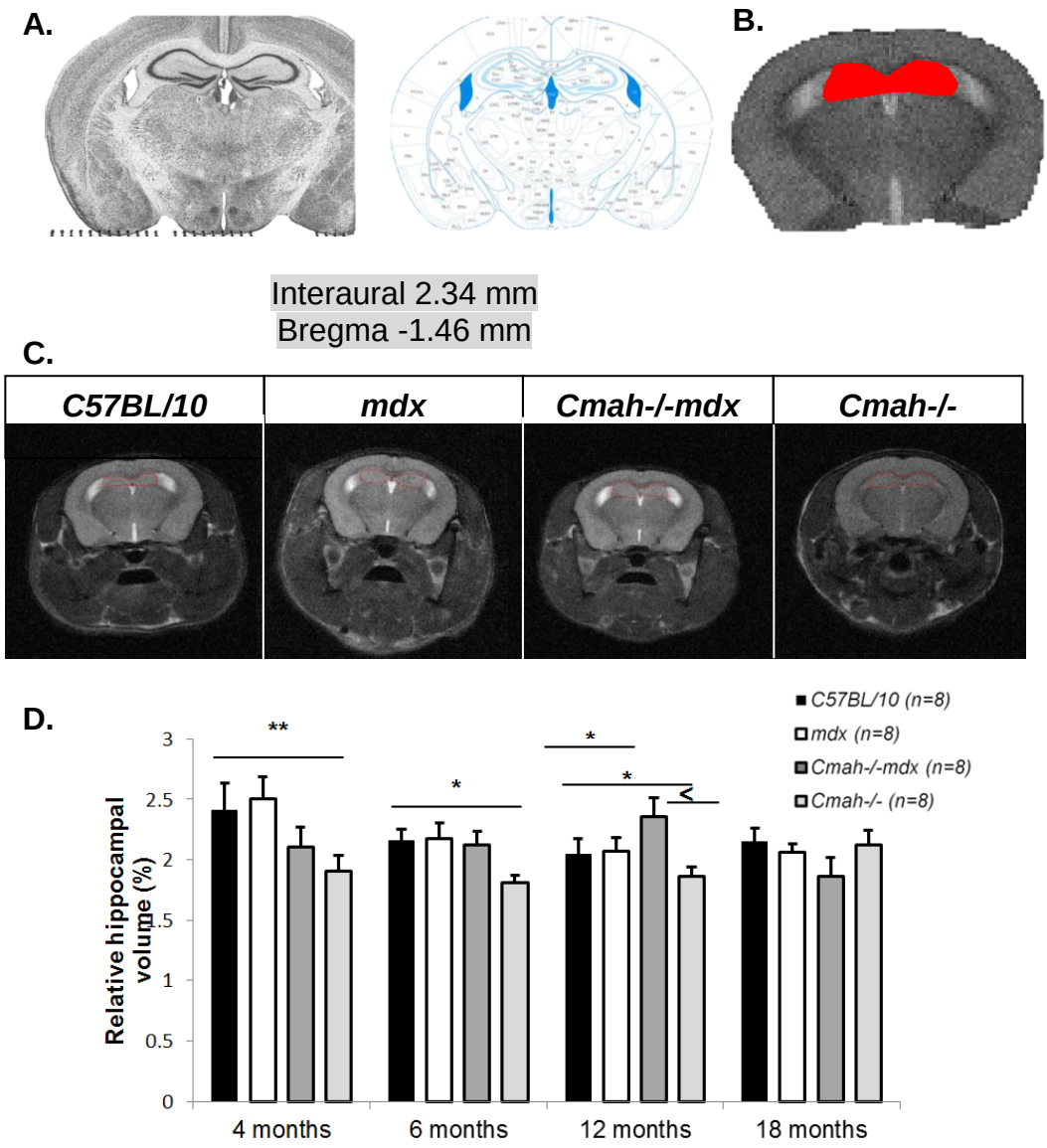

Figure 3.17: Hippocampal volume measurements. A. Images taken from the Mouse Brain atlas (Paxinos, 2008) delineating the hippocampus with corresponding interaural and bregma points for accurate depiction of structures. **B.** Representative coronal MR image where filled ROI corresponds to the hippocampus. **C.** Representative coronal T_2-*w* MR images of control *C57BL/10*, *mdx*, *Cmah-/-md,* and *Cmah-/-* mouse hippocampus delineated in red following ROI analysis on ImageJ. **D.** Bar graph displaying the relative hippocampal volume between 4 and 18 months old taken from the same mice. The relative hippocampal volume was calculated based on the volume of the hippocampus expressed as a percent of total brain volume. There was no significant difference between relative hippocampal volume in any genotype by 18 months old, although the hippocampal volume appeared to vary across the time points investigated. Data presented as mean ± SEM, *p<0.05, **p<0.01 vs control *C57BL/10* mice, < vs *Cmah-/-mdx* mice.

3.3.4 Heterozygous Imaging

In order to determine if the changes in TBV and ventricular volume were due to the loss of the *Cmah* gene, a heterozygous mouse was scanned at 4 months old. Heterozygous and homozygous mice, for a particular gene, can show differences in phenotypes, therefore we sought to determine if the homozygous deletion of the *Cmah* gene was responsible for the changes we observed in ventricular volume.

There was a slight reduction in the *Cmah*+/- lateral ventricular volume, but overall the relative total ventricular volume was comparable to that of control *C57BL/10* mice rather than the *Cmah*-/- mice ($p>0.05$) (Figure 3.18). The TBV of the *Cmah*+/- mouse was slightly increased compared to that of the control *C57BL/10* mice TBV, but it was slightly smaller in volume compared to the *Cmah*-/- mice, suggesting that it is the homozygous loss of the *Cmah* gene responsible for the increase in TBV and reduction in ventricular volume ($p>0.05$) (Figure 3.18).

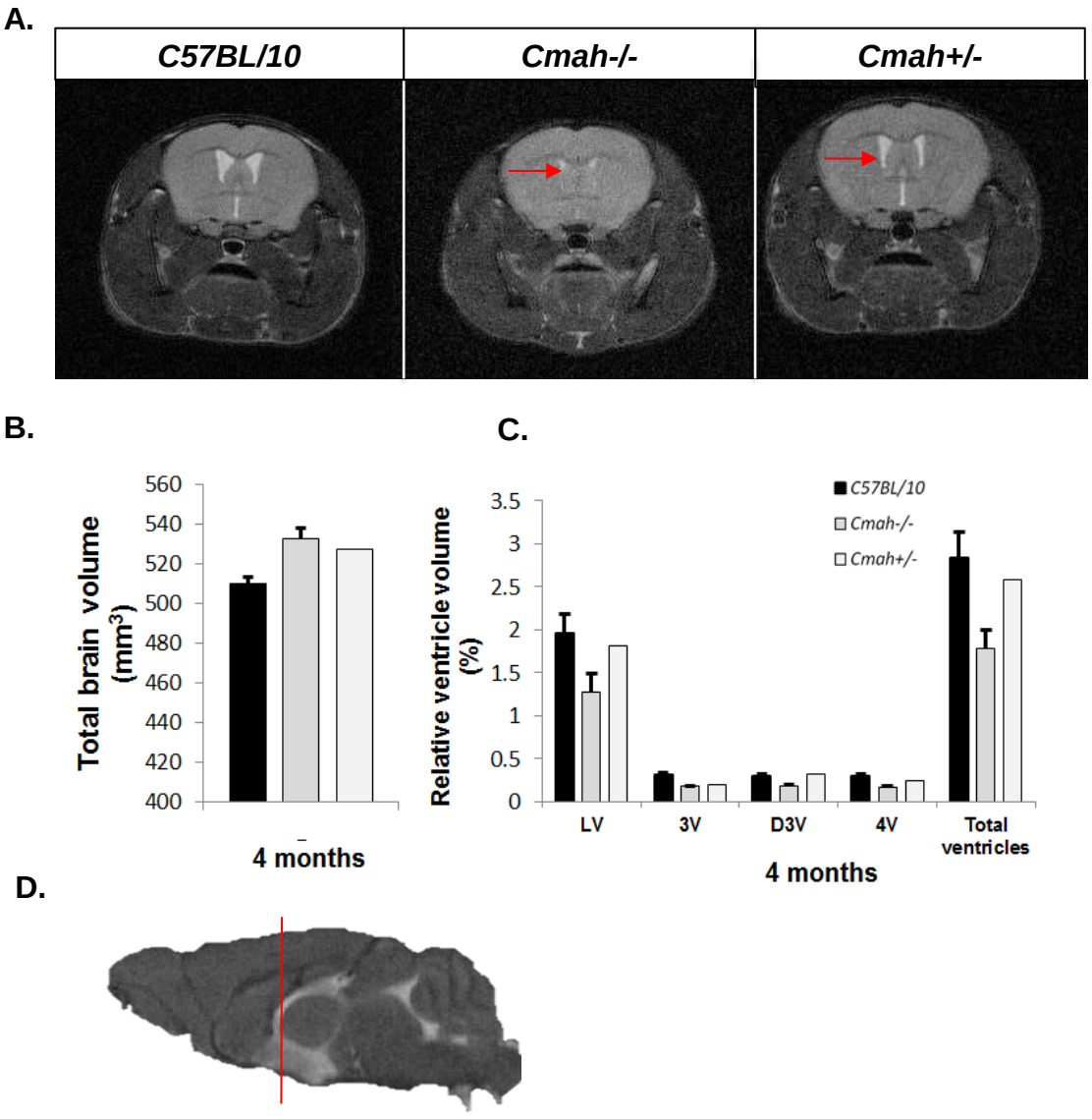

Figure 3.18: Volume measurements from a *Cmah+/-* mouse brain. **A.** Representative coronal T_2-*w* MR images of control *C57BL/10*, *Cmah-/-,* and *Cmah+/-* mice at 4 months old. A slight reduction in ventricle volume was observed in the *Cmah+/-* mice compared to control *C57BL/10* mice, but it was not as severe as in *Cmah-/-* mice (red arrows). **B.** Bar graph displaying total brain volume (TBV) comparison between *Cmah+/-* mouse, *Cmah-/-* mice, and control *C57BL/10* mice. **C.** Bar graph displaying relative ventricle volume at 4 months old. Interestingly *Cmah+/-* mouse displayed a comparative ventricular volume to control *C57BL/10* mice. LV =lateral ventricles, 3V =third ventricle, D3V= dorsal third ventricle and 4V= fourth ventricle. **D.** Sagittal image where the red line indicates the approximate slice corresponding to the coronal images. (n=8 for control *C57BL/10* and *Cmah-/-* mice, and n=1 for *Cmah+/-* mice).

3.4 Impact of muscle hypertrophy on skeletal development

3.4.1 Alteration of head shape

DMD is characterised by muscle hypertrophy and muscle weakness, which in turn can have subsequent effects on skeletal growth and development, such as facial and dental morphology changes (Egli *et al.*, 2017). It has previously been demonstrated that the average temporal muscle thickness was significantly increased in DMD patients when compared to aged matched controls (Straathof *et al.*, 2014). In addition a rounder shape of the head compared to more ovoid shaped in healthy controls was also observed. It has been implied that such skeletal changes in the oral-facial region may result in a decreased bite force (Straathof *et al.*, 2014). Interestingly, the skull and overall head shape of DMD mouse models differ from that of control *C57BL/10* mice and *Cmah-/- mice*, as indicated by temporal muscle hypertrophy observed qualitatively (Figure 3.19). There appeared to be changes in the head circumference with the DMD mice showing a larger, slightly rounder head shape. Temporalis muscles were wider in DMD mice between 6 and 12 months old (Figure 3.20), following a repeated measures ANOVA there was a significant interaction between age and genotype on temporal muscle thickness ($F_{3, 28}$=13.66, p<0.01)

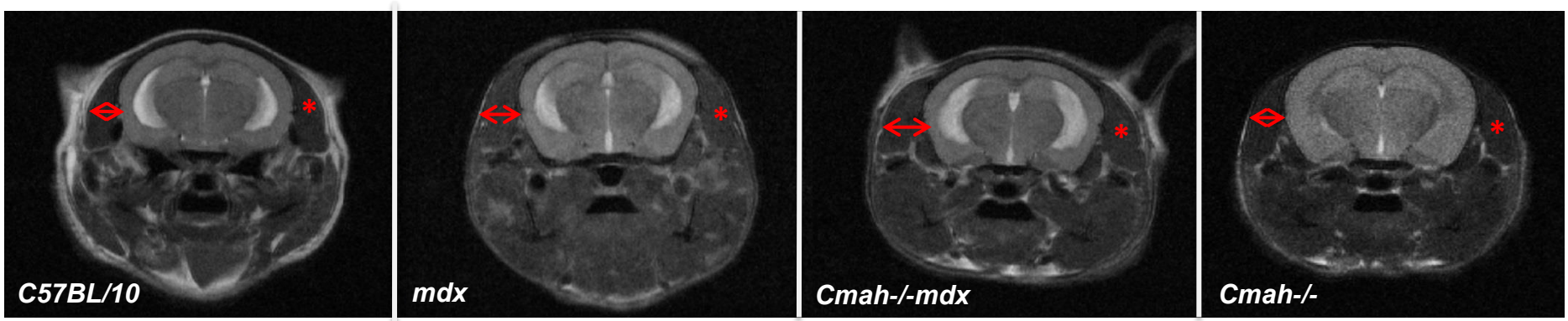

Figure 3.19: Representative T_2-weighted coronal images showing changes in head shape of DMD mouse models. Hypertrophy of the temporal muscle (red arrow) caused DMD mice to have a much rounder head shape compared to control mice.

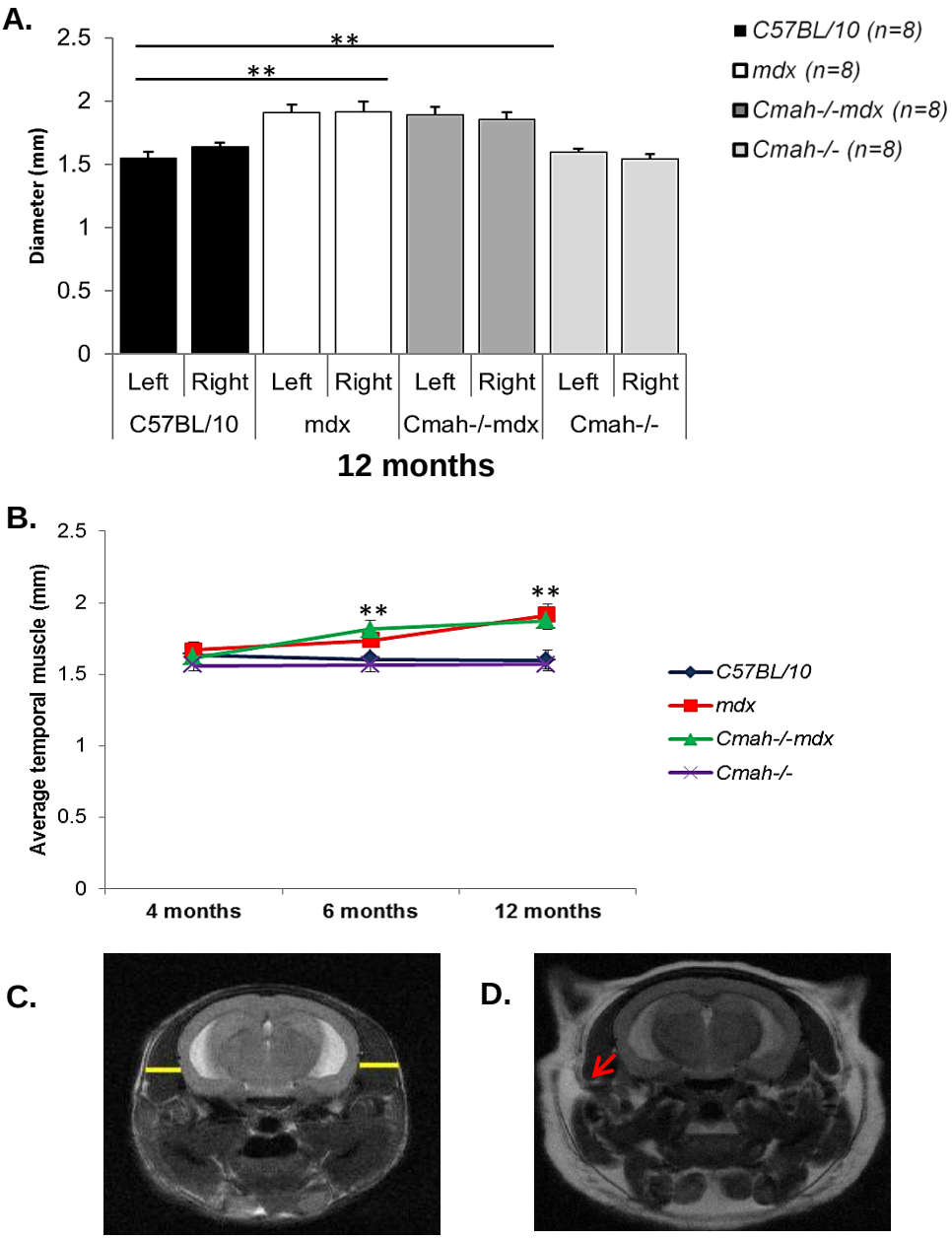

Figure 3.20: Quantification of temporal muscle thickness longitudinally in the same DMD mice. A. Average thickness of left and right temporal muscles in control *C57BL/10*, *mdx*, *Cmah-/-mdx,* and *Cmah-/-* mice at 12 months old. There is bilateral temporal muscle hypertrophy in DMD mice at similar levels in both models. **B.** Correlation between temporal muscle thickness (averaged values for left and right) and age in control *C57Bl/10*, *mdx*, *Cmah-/-mdx,* and *Cmah-/-* mice (n=8 mice per genotype at each time point). **C.** Representative T_2-w coronal MR image where yellow line represents the measurements taken for temporal muscle thickness. The widest part of the temporalis muscle from the approximately the same slice was measured in each mouse at corresponding time points. **D.** Representative T_2-w coronal image demonstrated increased amount of fat in head muscles of mice at 18 months old which hindered correct measurements of temporal muscle thickness and this time point was excluded from the analysis. Data presented as mean ± SEM, **p<0.01 vs control *C57BL/10* mice.

Changes in cranial head shape, as previously reported by MRI analysis, and as seen in DMD boys was further investigated using X-ray analysis. Mechanical forces exerted by skeletal muscles can influence bone structure and, therefore, secondary effects of muscle weakness or hypertrophy could lead to differences in bone development, particularly the development of the skull. It has been suggested that reduced bite force is related to skeletal changes in the oral-facial region (Egli *et al.*, 2017). Dental malocclusion in DMD has been reported as the result of imbalance of muscle strength along with changes in jaw bone development (Straathof *et al.*, 2014). Additionally, a larger skull may allow for further expansion of the brain, given that the mouse TBV increases with increasing age. There is a dynamic interaction between the developing brain and skull growth in humans, with 25 to 27% increase in whole brain and intracranial volume between early childhood and adolescence (Reiss *et al.*, 1996; Courchesne *et al.*, 2000).

In DMD mice, particularly the *Cmah-/-mdx* mice, there was widening of the squamosal bones (Figure 3.21). This widening may allow for further expansion of the brain and could account for the larger brain volume observed in these models (Figure 3.3). In addition to the changes in skull shape, further skeletal abnormalities were found associated with spinal development. By the age of 18 months old DMD mice had developed severe thoracolumbar kyphosis and scoliosis (Figure 3.22 and Figure 3.23).

It has also previously been reported that the *Cmah-/-mdx* mice have a significantly reduced lifespan compared to both control *C57BL/10* and *mdx* mice, suggesting that they were a better mouse model for DMD (Chandrasekharan *et al.*, 2010) but in this study all eight *Cmah-/-mdx* mice survived to the 18 months old time point and it was the *mdx* mice which struggled to survive due to the increased susceptibility of spontaneous rhabdomyosarcoma causing severe spinal deformities (Figure 3.23) (Chamberlain *et al.*, 2007).

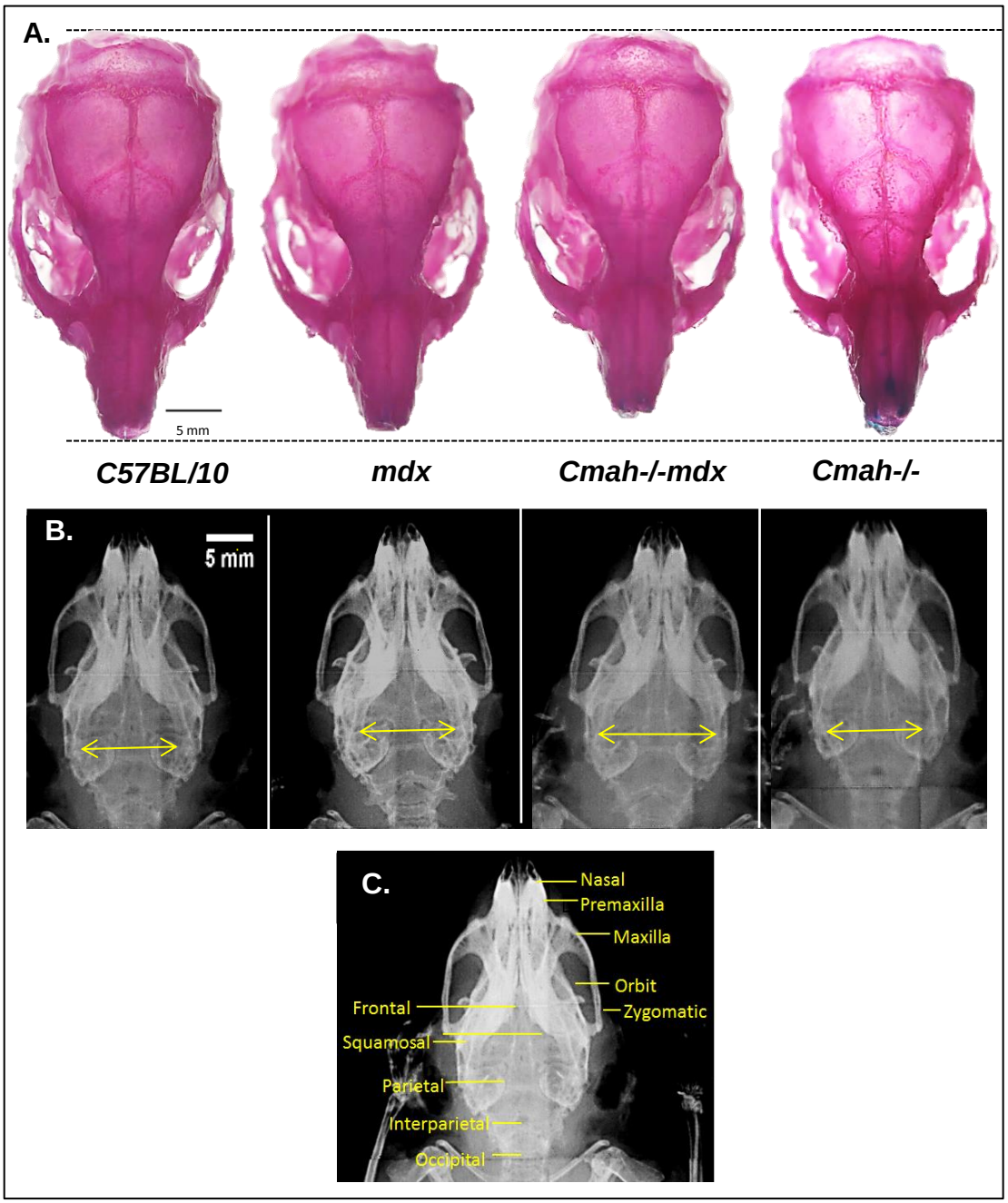

Figure 3.21: Skull measurements. A. Representative skeletal prepared skulls from mice aged 4 months old (n=2 mice per genotype) showing changes in the skulls of DMD mice (*mdx* and *Cmah-/-mdx*) particularly widening of the squamosal bones. Scale bar= 5 mm. **B.** Representative radiographs of the mouse skull aged 18 months old (n=4 mice per genotype). Yellow arrow represents widening of the squamosal bones. **C.** Labelled radiograph of mouse skull. Scale bar = 5 mm.

A.

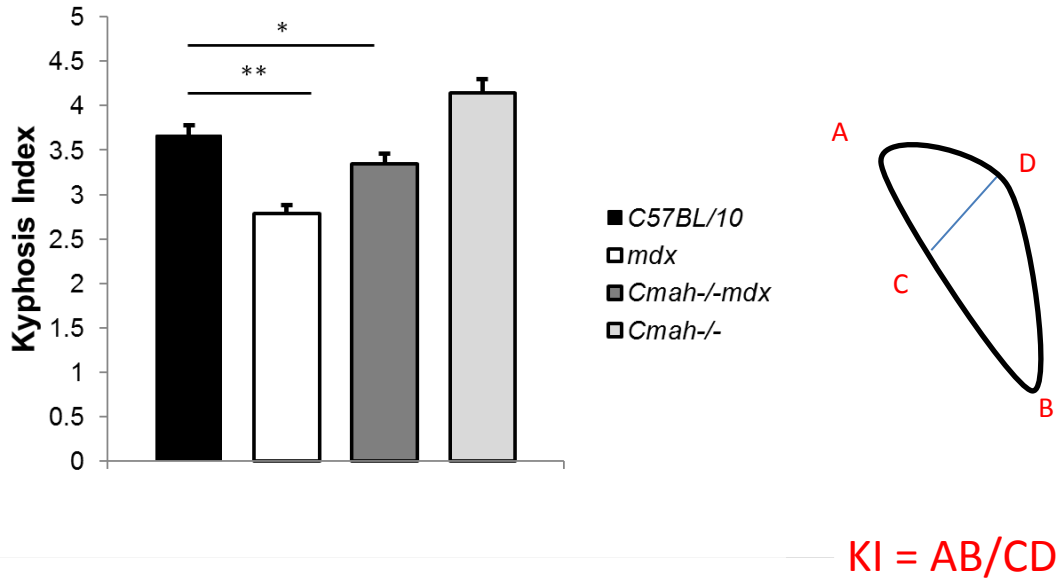

B.

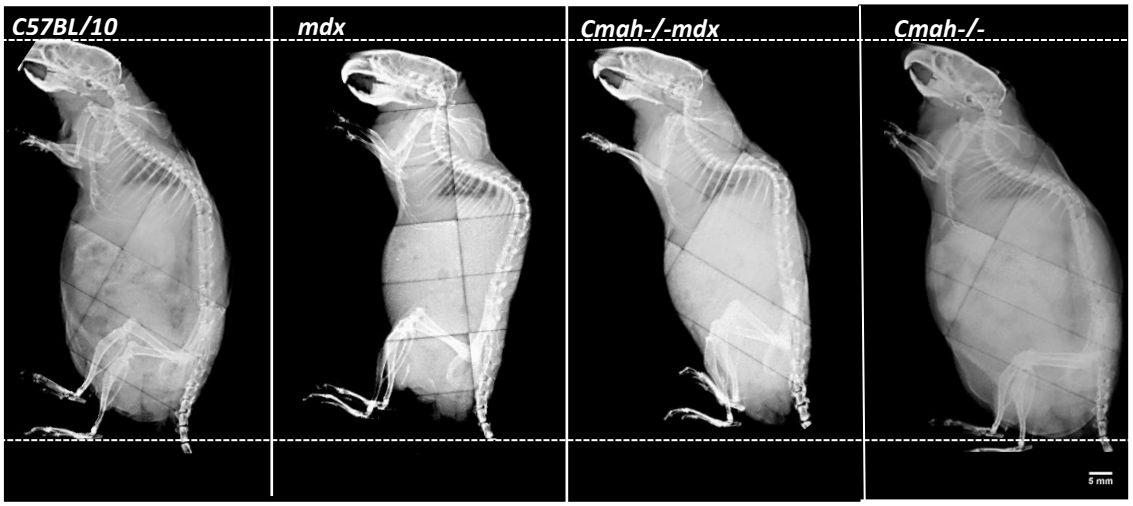

Figure 3.22: Kyphosis index (KI) in mice calculated from radiographs of anesthetised mice positioned in right lateral recumbency. Line AB is the length of a line drawn from the posterior edge of C7 to the posterior edge of L6, usually where it contacts the wing of the ilium (which is more consistently identifiable than the sacral border). Line CD is the distance from line AB to the dorsal border of the vertebral body farthest from that line. Increase in line CD indicates an increase in kyphosis. KI = AB/CD. **A.** Bar graph displaying the KI in mice aged 18 months old. DMD mice had significant kyphosis compared to control *C57BL/10* mice. Data presented as mean ± SEM, *p<0.05 compared to control *C57BL/10* mice **B.** Example radiographs from mice aged 18 months old (n=4 mice per genotype). Scale bar= 5 mm.

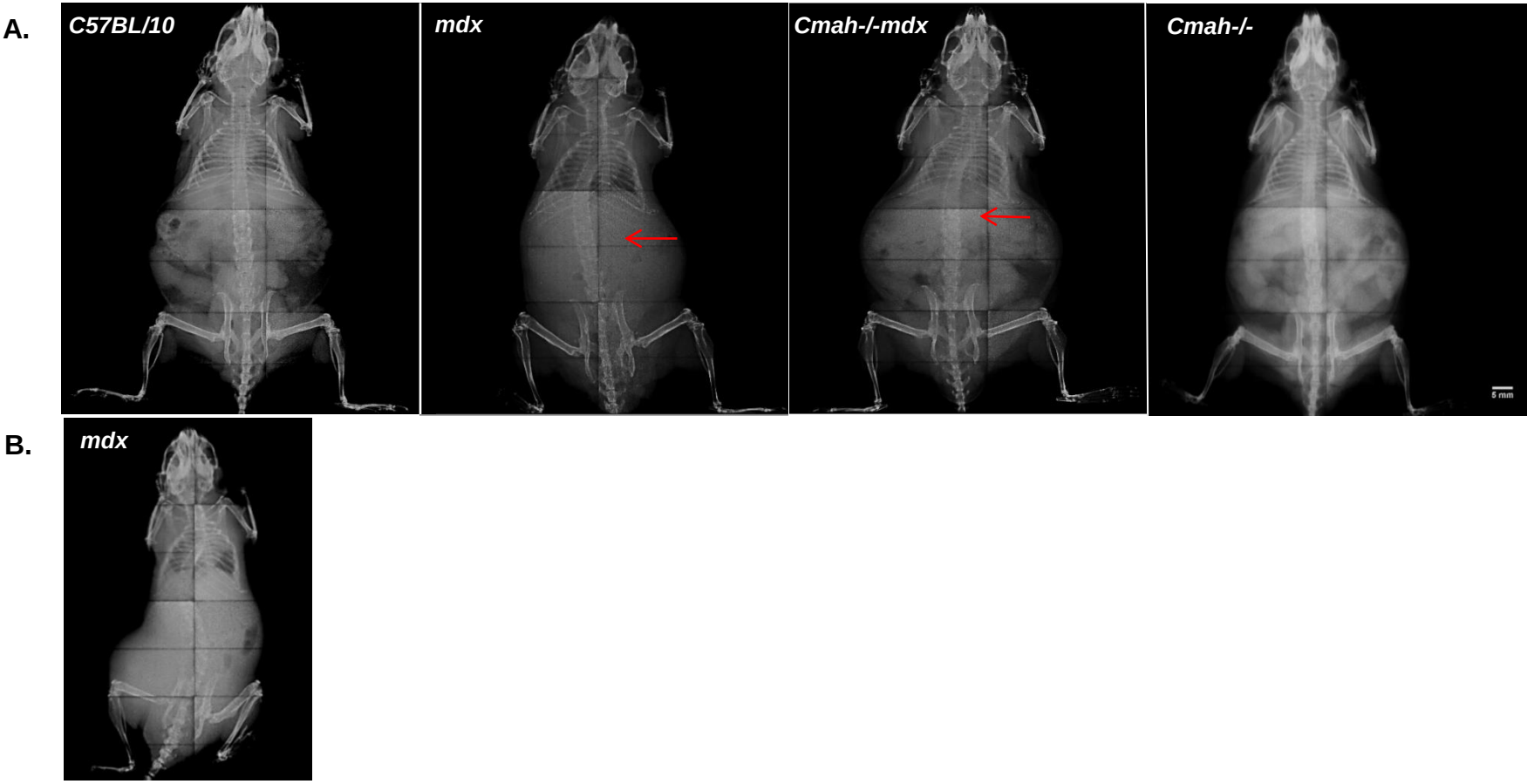

Figure 3.23: Examples of mouse whole body radiographs at 18 months old. **A**. DMD mice exhibit scoliosis (red arrows) which is not present in control *C57BL/10* or *Cmah-/-* mice (n=4 mice/ genotype). **B.** Radiograph of an *mdx* mouse at 18 months showing a large spontaneous rhabdomyosarcoma leading to excessive spinal deformities observed in 3/8 *mdx* mice. Scale bar= 5 mm in part A.

3.4.2 Changes in mouse body weights

Prior to MRI scanning each mouse was weighed and their body weights recorded. A repeated measures ANOVA revealed that there was a significant interaction between age and genotype on body weight ($F_{3, 27}$=10.62, p<0.01). At 4 months old all mice had a similar body weight of approximately 30 g regardless of genotype (Figure 3.24). Body weight steadily increased in all genotypes between 4 and 6 months old with an average body weight of 36 g recorded. However, by the time the mice reach 12 months old the *mdx* mice weighed considerably less than the other genotypes (Figure 3.24). At 12 months old *mdx* mice had an average body weight of 37 g whereas control *C57BL/10*, *Cmah-/-mdx,* and *Cmah-/-* mice body weights averaged between 41-43 g. Additionally at 18 months old both DMD mouse models weighed substantially less than aged matched control *C57BL/10* and *Cmah-/-* mice. At 18 months old *mdx* mice averaged a body weight of 36 g and *Cmah-/-mdx* mice weighed on average 41 g (Figure 3.24). Whereas at 18 months old the control *C57BL/10* mice weighed 48 g and the *Cmah-/-* mice weighed 52 g. Interestingly, it has previously been reported that mice lacking dystrophin often weigh more than age matched controls due to muscular pseudohypertrophy at young ages. This study has demonstrated that old DMD mice begin to lose weight particularly from 12 months onwards when disease symptoms are becoming increasingly evident in these models. The weight loss may be as a result of increasing spinal deformities causing restricted movement (Figure 3.22 and Figure 3.23).

These findings are particularly important for studies of age related changes and extra consideration needs to be accounted for when using old mice for long-term experiments. For example, issues arise when MRI scanning a mouse as the scanner is built to optimally house a mouse weighing ~35 g, therefore positioning the mouse correctly in the isocentre of the magnet takes considerably longer. This means the mice are exposed to a higher amount of anesthetic and scanning protocols become increasingly more difficult.

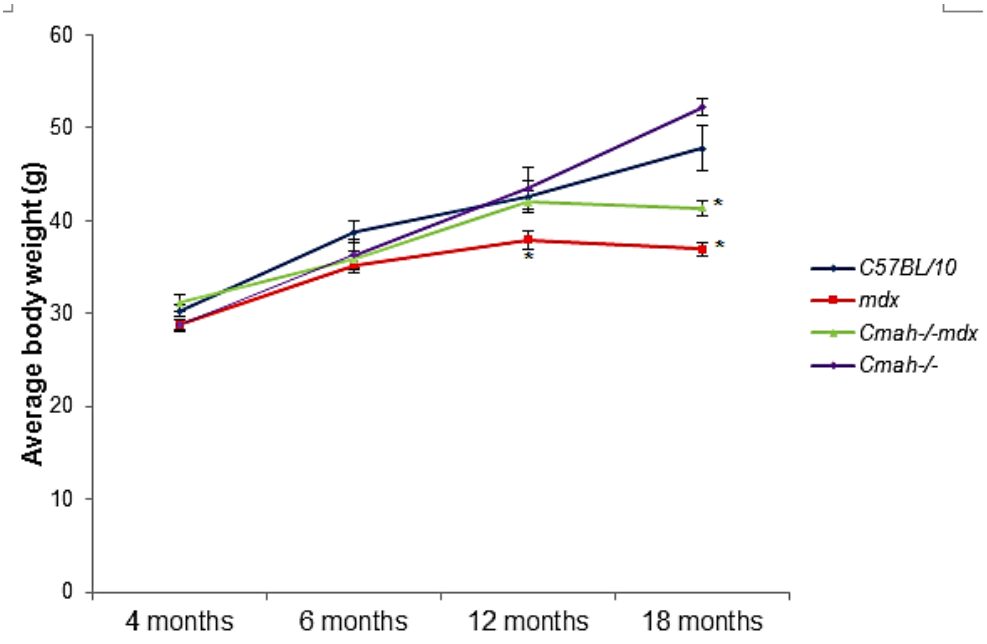

Figure 3.24: Bar graph showing average body weights of the same mice used for the longitudinal MR imaging study. At 4 months old all mice had a comparable body weight. Between 12-18 months DMD mice begun to lose weight, whereas control *C57BL/10* and *Cmah-/-* mice gained weight. Data presented as mean ± SEM, *p<0.05 compared to control *C57BL/10* mice (n=8 mice per genotype at each time point).

3.4 Voxel-based morphometry validation

Voxel-based morphometry (VBM) describes the automated process of analysing morphological differences between images of brains by performing voxel-wise statistics comparing groups of animals. Images are registered into the same stereotactic space and usually segmented into grey matter (GM), white matter (WM) and CSF. VBM has wide spread applications in human imaging, forming the basis for detection of changes in brain morphometry, but has rarely been applied to mouse brain imaging. To the best of our knowledge Voxel-based morphometry (VBM) has not been applied in the *mdx* brain, therefore we applied the VBM approach to our previously acquired MRI data sets to determine if VBM was a useful tool for detecting changes in grey matter (GM) volume.

VBM investigates focal differences in brain morphology. Traditional methods for morphometry analysis are calculated by drawing ROIs to determine the TBV or the volume of its sub regions on acquired MR images and calculating the volume enclosed. However, this method is time consuming and can only provide information on volume measurements from larger areas, thus smaller differences in volume can be overlooked. VBM registers all brains to a relevant template, which helps to eliminate the large differences in brain anatomy among subjects. The brain images are then smoothed such that each voxel represents the average of itself and its neighbours. Ultimately, this allows the image volume to be compared across brains at every voxel.

3.4.1 *Pre-processing*

The steps involved in VBM as illustrated in Figure 3.25 and discussed in more detail below.

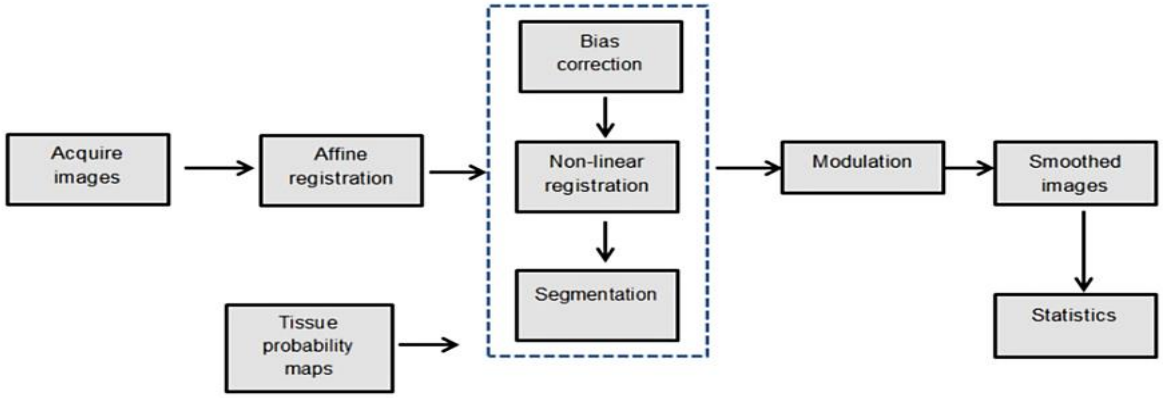

Figure 3.25: Steps involved in voxel based morphometry (VBM). Blue box highlights unified segmentation.

Following acquisition of images voxel-wise statistics need to be calculated. Images are first registered into the same stereotactic space and then segmented to give tissue probability maps provided by SPMMouse (http://www.spmmouse.org/).

Affine registration refers to a global geometric transformation applied identically to each part of the image which preserves parallel lines. Non-linear registration provides a finer match between images by allowing local transformations that adjust different parts of the image in different ways.

Before images were processed in statistical parametric mapping software version 12 (SPM12) (Wellcome Department of Clinical Neurology, London; http://www.fil.ion.ucl.ac.uk), the skull needed to be removed, leaving a mask of the brain and this was performed manually in ImageJ (Figure 3.26).

3.4.3 Affine registration

The SPMMouse package was used as a reference providing tissue probability maps for main tissue types. SPMMouse is a plug-in package for SPM created by calculating the distribution of affine parameters from a large number of ex-*vivo* mouse scans. Utilization of this package has previously been shown to improve the quality of affine registration (Sawiak *et al.*, 2009).

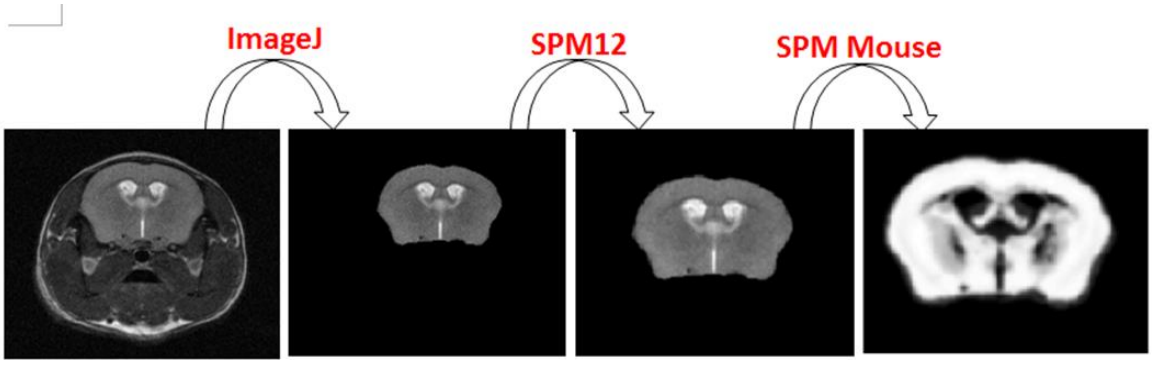

Figure 3.26: Representative images depicting the pre-processing steps for voxel based morphometry (VBM) carried out in ImageJ and statistical parametric mapping (SPM12) using SPMMouse plugin.

3.4.4 Non-linear registration and segmentation

VBM normally considers the brain to consist of 4 classes including GM, WM, CSF, and 'everything else'. SPM models each voxel as a weighted sum of each tissue type based on a mixture of (typically two) Gaussian distributions. This helps deal with partial volume effects which confound the segmentation process. The SPMMouse interface allows templates to be created with smoothing parameters, commensurate with the scale differences between human and mouse brains so that these more advanced algorithms can be used readily with the mouse brain.

3.4.5 Image smoothing and modulation

If parameters encoding morphological difference are considered as a signal that can be obtained amongst the noise of a random field, then the matched filter theorem suggests the optimal spatial smoothing kernel has the same scale as the signal to be found (Sawiak *et al.*, 2013). In addition, smoothing confers benefits on the normality of the statistics and reduces the impact of misregistration between images. According to standard methodologies a spatial smoothing was applied to all images (Sawiak *et al.*, 2013).

3.4.6 Statistics

Following pre-processing, structural measures were modelled in a general linear model (GLM) to test hypotheses. An appropriate model for our mutant mouse study was a two-sample Student's t-test between the mutant (*mdx*, *Cmah-/-mdx* and *Cmah-/-*) and the control *C57BL/10*. The images of this longitudinal brain study were acquired *in-vivo* with a relatively short scan time per mouse (15 minutes for a T_2-weighted image) and as such the image quality was lower than the *ex-vivo* SPMMouse brain template used for the segmentations steps. With such a large number of tests, correction for multiple comparisons was necessary and we used the false-discovery rate (FDR) technique (Genovese *et al.*, 2002) with a threshold of $p \leq 0.05$ for statistical significance.

3.4.7 Problems with VBM

Problems arose whilst performing the VBM analysis due to the misalignment of images, which provided a large amount of false positives either indicating that there was a reduction/increase in GM posterior or anterior of the SPMMouse GM template (Figure 3.27). The segmented GM volume from our mouse brains did not properly align to the GM template provided in the SPMMouse plugin. This was because the mice were positioned via a bite bar inside the MRI scanner, but given the previously reported spinal deformities (Figure 3.19 and Figure 3.22) and larger size of control *C57BL/10* and *Cmah-/-* (from 12 months onwards), the mice did not always lie in the same position whilst fixed by the bite bar.

In order to circumvent this issue, prior to segmentation, images were realigned individually to the GM template using the SPM12 software package and images reoriented using the roll, pitch, and yaw functions (Figure 3.27 and Figure 3.28). Once all mouse brains had been correctly angulated the usual VBM approach was followed (Figure 3.25).

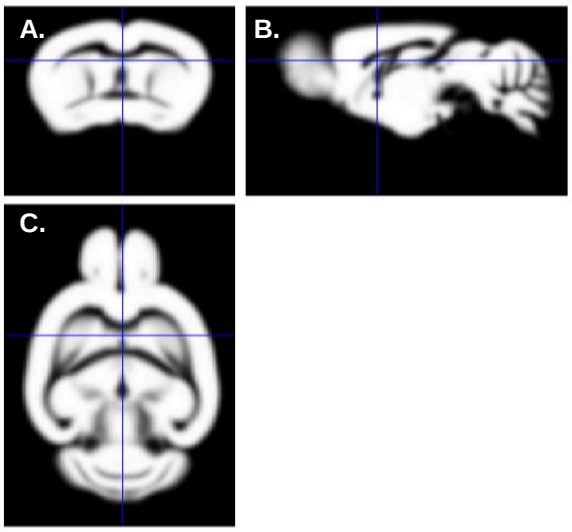

Figure 3.27: SPMMouse tissue probability map for mouse brain grey matter (GM) (Sawiak *et al.*, 2013). **A.** Coronal GM, **B.** sagittal GM, and **C.** axial GM. Blue cross represents the same point in the mouse brain across all orthogonal planes. This SPMMouse template was used to separate the GM from our T_2-w MR images.

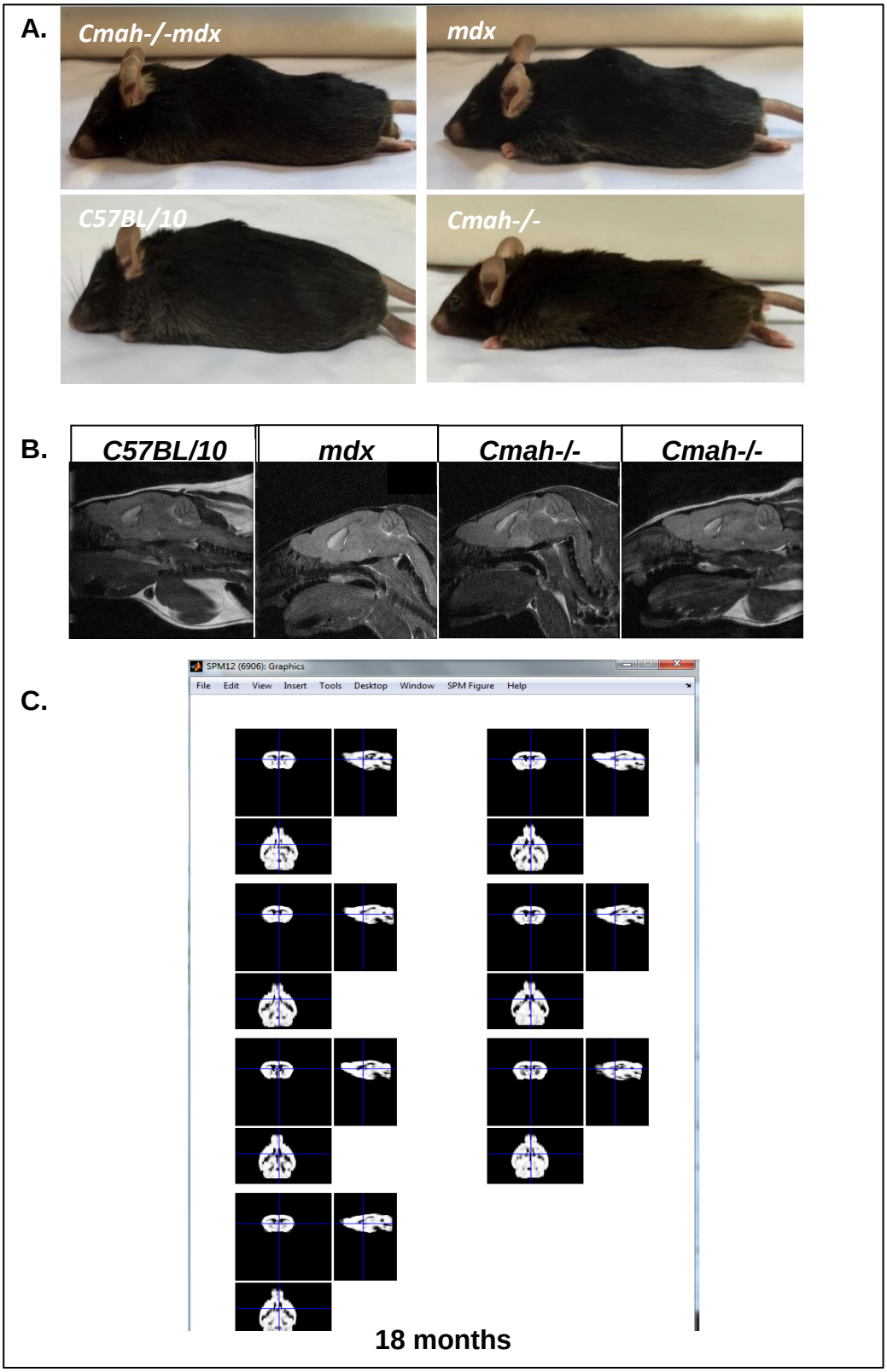

Figure 3.28: Problems with voxel based morphometry (VBM). A. Photographs of mice showing overt spinal deformities in DMD mice. **B.** Representative T_2-*w* sagittal MR images of mouse heads. Note the downward angulation of the DMD mouse model heads compared to the more horizontal positioning of the control *C57BL/10* and *Cmah-/-* mice. **C.** Example screenshot of SPM12 displaying the orientation of control *C57BL/10* mouse brains at 18 months old following realignment to the SPMMouse grey matter (GM) template.

3.4.8 Maximum intensity projections

Maximum intensity projections were created using SPM12 and SPMMouse to demonstrate changes identified following statistical analysis (two tailed student's t-test for control *C57BL/10* vs mutant mouse brains) (Figure 3.29).

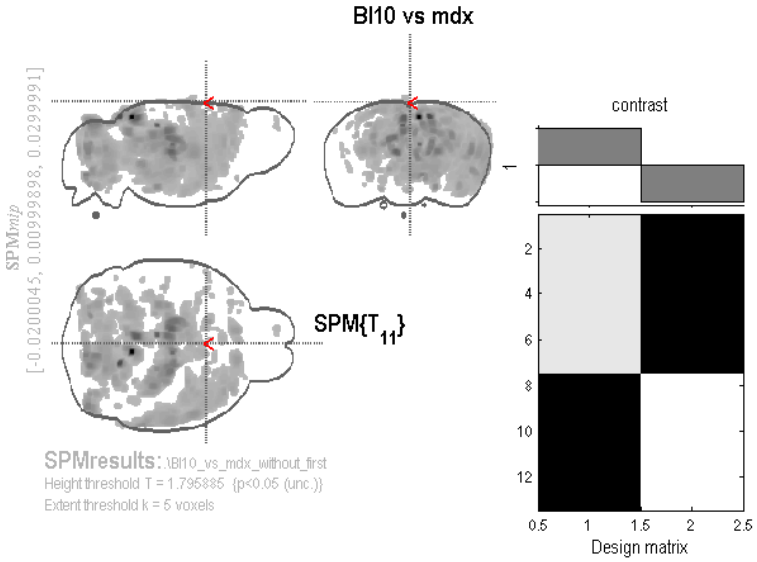

Figure 3.29: Presentation of the voxel based morphometry (VBM) results produced by the SPM software with the SPMMouse plugin. An example of a maximum-intensity projection (MIP) of the results for grey matter (GM) of control *C57BL/10* vs *mdx* mice at 18 months old is shown in sagittal, coronal, and axial planes and the corresponding design matrix for the study. The grey overlay indicated areas of changes detected between the two genotypes.

3.4.9 VBM in control C57BL/10 vs mutant mouse brains

3.4.9.1 VBM in control vs mdx mice brains

VBM registered all mice into the same stereotaxic space accounting for differences in overall brain size and shape and then detected morphological changes regardless of changes in the overall TBV. VBM was first applied to the *mdx* mouse brain between 6 and 18 months old. At 6 months old there was little difference between the GM of control *C57BL/10* and *mdx* mice, with changes observed mainly around the lateral ventricles and hippocampus, as well as the vermal cerebellum (Figure 3.30).

Interestingly, by 12 months old the number and extent of differences observed between control *C57BL/10* and *mdx* mouse brains had drastically increased.

The control *C57BL/10* mouse brain was larger compared to the *mdx* in regions of the caudate putamen (striatum), the prefrontal cortex, and the olfactory bulbs. On the other hand, the *mdx* mouse was larger than the control *C57BL/10* mouse primarily in the cingulate cortex, primary somatosensory cortex, and cortical amygdaloid nucleus (Figure 3.31).

Furthermore, at 18 months old the control *C57BL/10* and *mdx* mouse brains displayed the largest number of differences detected by VBM. The control *C57BL/10* mice were larger in numerous regions including the thalamus, the inferior colliculus, the somatosensory cortex, and the hippocampus (Figure 3.32). In contrast, the *mdx* mouse brain was larger than the control *C57BL/10* in various regions, mainly the cortex (lower layers), basal lateral amygdala nucleus, and the cingulate cortex.

This data suggests that there are progressive changes occurring in the *mdx* mouse brain structures with age. Interestingly, the brain structures showing the highest level of changes between 6 and 18 months old are those known to dystrophin-rich (the hippocampus, cerebellum, and amygdala).

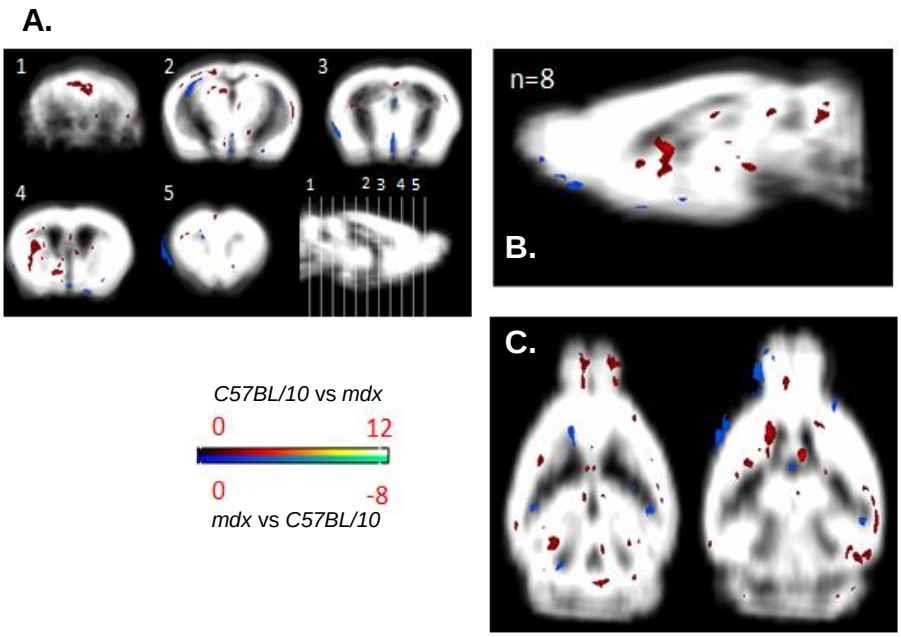

Figure 3.30: Presentation of the voxel based morphometry (VBM) results produced by the SPM12 software with the SPMMouse plugin for grey matter (GM) of *C57BL/10* vs *mdx* at 6 months old. The GM average shown is for the control *C57BL/10* mice and a coloured overlay showing the location of significant clusters. Red clusters indicate where the control *C57BL/10* mouse brain was larger than the *mdx* brain and blue indicates where the *mdx* brain is larger than the control *C57BL/10* brain (in terms of GM volume). Colour intensity on the scale bar refers to the level of significance with a lighter colour indicating a higher level of significance ($p<0.05$, student's t-test). **A.** Coronal images numbered 1-5 with a corresponding sagittal image detailing the image plane where the coronal image lies. **B.** Sagittal representation of VBM findings. **C**. Two coronal grey matter slices detailing VBM findings. Grey matter average is from 8 control *C57BL/10* mice. Few changes were detected using VBM in the *mdx* mouse brain at 6 months old. The asymmetry of findings could be as a consequence of incorrect positioning of the mouse in the MR scanner.

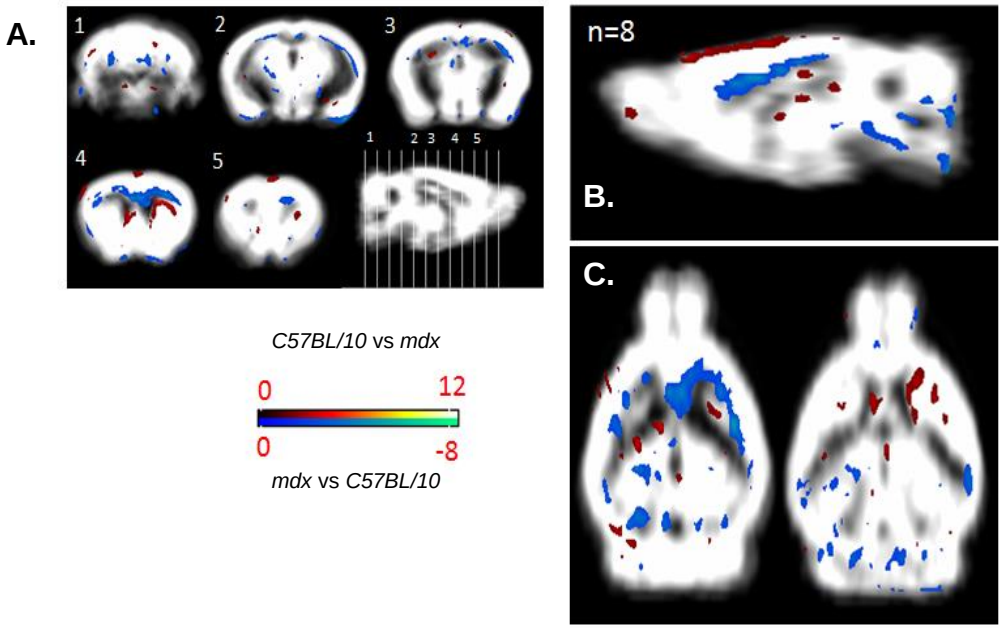

Figure 3.31: Presentation of the voxel based morphometry (VBM) results produced by the SPM12 software with the SPMMouse plugin for grey matter (GM) of *C57BL/10* vs *mdx* at 12 months old. The GM average shown is for the control *C57BL/10* mice and a coloured overlay showing the location of significant clusters. Red clusters indicate where the control *C57BL/10* mouse brain is larger than the *mdx* brain and blue indicates where the *mdx* brain is larger than the control *C57BL/10* brain (in terms of GM volume). Colour intensity on the scale bar refers to the level of significance, with a lighter colour indicating a higher level of significance ($p<0.05$, student's t-test). **A.** Coronal images numbered 1-5 with a corresponding sagittal image detailing the image plane where the coronal image lies. **B.** Sagittal representation of VBM findings. **C.** Two coronal grey matter slices detailing VBM findings. Grey matter average is from 7 control *C57BL/10* mice. Many more changes were detectable by VBM at 12 months old in the *mdx* mouse brain. Increased GM volume was detected in the cingulate cortex, primary somatosensory cortex, and cortical amygdaloid nucleus.

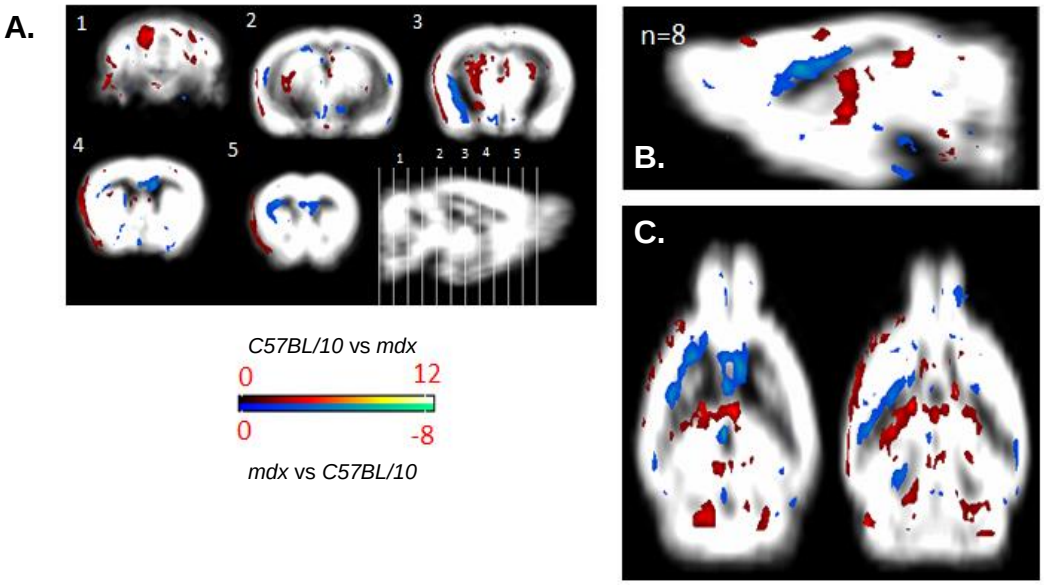

Figure 3.32: Presentation of the voxel based morphometry (VBM) results produced by the SPM software with the SPMMouse plugin for grey matter (GM) of *C57BL/10* vs *mdx* mice at 18 months old. The GM average shown is for the control *C57BL/10* mice and a coloured overlay showing the location of significant clusters. Red clusters indicate where the control *C57BL/10* mouse brain is larger than the *mdx* brain and blue indicates where the *mdx* brain is larger than the control *C57BL/10* brain (in terms of GM volume). Colour intensity on the scale bar refers to the level of significance with a lighter colour indicating a higher level of significance ($p<0.05$, student's t-test). **A.** Coronal images numbered 1-5 with a corresponding sagittal image detailing the image plane where the coronal image lies. **B.** Sagittal representation of VBM findings. **C.** Two coronal grey matter slices detailing VBM findings. Grey matter average is from 7 control *C57BL/10* mice. The largest amount of changes were detected at 18 months old in the *mdx* mouse brain with the control *C57BL/10* mice having a higher GM volume in the thalamus, the inferior colliculus, the somatosensory cortex, and the hippocampus.

3.4.9.2 VBM in control vs Cmah-/-mdx mice brains

VBM was next applied to the control *C57BL/10* vs *Cmah-/-mdx* mice brains between 6 and 12 months old. Similarly there was an increase in the number of changes detected using VBM in the older *Cmah-/-mdx* mice compared to the younger mice. At 6 months old changes between the genotypes were seen in

the vermal cerebellum, the caudate putamen (striatum), the primary and secondary motor cortices, and the primary somatosensory cortex, all of where the control *C57BL/10* mice were had a larger GM volume than the *Cmah-/-mdx* mice (Figure 3.33). Remarkably at 12 months old there were more changes in the cerebellum, hippocampus and the lateral septal nucleus surrounding the lateral ventricles (Figure 3.34). Again the *Cmah-/-mdx* mice showed more GM in the lower cortical layers, similar to that observed in *mdx* mice.

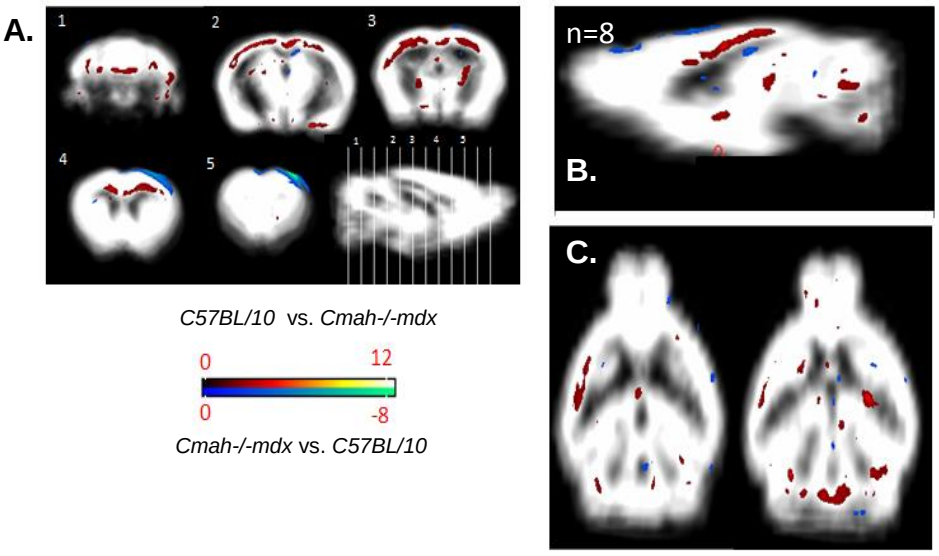

Figure 3.33: Presentation of the voxel based morphometry (VBM) results produced by the SPM software with the SPMMouse plugin for grey matter (GM) of *C57BL/10* vs *Cmah-/-mdx* mice at 6 months old. The GM average shown is for the control *C57BL/10* mice and a coloured overlay showing the location of significant clusters. Red clusters indicate where the control *C57BL/10* mouse brain is larger than the *Cmah-/-mdx* brain and blue indicates where the *Cmah-/-mdx* brain is larger than the control *C57BL/10* brain (in terms of GM volume). Colour intensity on the scale bar refers to the level of significance with a lighter colour indicating a higher level of significance ($p<0.05$, student's t-test). **A.** Coronal images numbered 1-5 with a corresponding sagittal image detailing the image plane where the coronal image lies. **B.** Sagittal representation of VBM findings. **C.** Two coronal grey matter slices detailing VBM findings. Grey matter average is from 8 control mice. Few changes were detected using VBM in the *Cmah-/-mdx* mouse brain at 6 months old. The asymmetry of findings could be as a consequence of incorrect positioning of the mouse in the MR scanner.

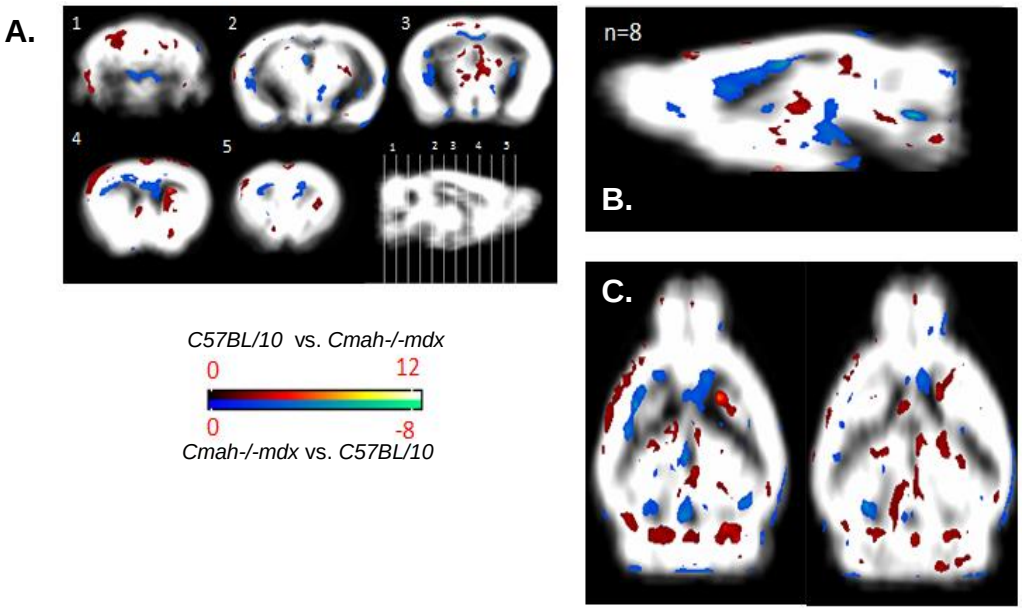

Figure 3.34: Presentation of the voxel based morphometry (VBM) results produced by the SPM software with the SPMMouse plugin for grey matter (GM) of *C57BL/10* vs *Cmah-/-mdx* mice at 12 months old. The GM average shown is for the control *C57BL/10* mice and a coloured overlay showing the location of significant clusters. Red clusters indicate where the control *C57BL/10* mouse brain is larger than the *Cmah-/-mdx* brain and blue indicates where the *Cmah-/-mdx* brain is larger than the control *C57BL/10* brain (in terms of GM volume). Colour intensity on the scale bar refers to the level of significance with a lighter colour indicating a higher level of significance. ($p<0.05$, student's t-test). **A.** Coronal images numbered 1-5 with a corresponding sagittal image detailing the image plane where the coronal image lies. **B.** Sagittal representation of VBM findings. **C.** Two coronal grey matter slices detailing VBM findings. Grey matter average is from 8 control mice. Many more changes were detectable by VBM at 12 months old in the *Cmah-/-mdx* mouse brain. Increased GM volume was detected in the Control *C57BL/10* mice compared to the *Cmah-/-mdx* mice at 12 months old in the cerebellum, hippocampus and the lateral septal nucleus surrounding the lateral ventricles

3.4.9.3 VBM in control C57BL/10 vs Cmah-/- mice brains

VBM was applied to *Cmah-/-* mice brains between 6 and 18 months old. In the *Cmah-/-* mouse brains, the greatest differences in GM were detected with VBM compared to any other genotype. The *Cmah-/-* mouse brain had larger GM volume than the control *C57BL/10* mouse brain in numerous brain regions including the cerebellum, the hippocampus, and the somatosensory cortex (Figure 3.35). The largest differences at 6 months old detected by VBM were changes in the GM surrounding the third ventricle (including the dorsal third

ventricles) and the lateral ventricles, which is not surprising given the aforementioned change in ventricle volume detected by T_2-weighted imaging (Figure 3.9).The only region that was larger in GM volume in the control *C57BL/10* mice at 6 months old was the olfactory bulbs (Figure 3.35).

At 12 months old the control *C57BL/10* mice had numerous brain regions where their volume was larger than that of the *Cmah-/-* mice, including the somatosensory cortex (primary and secondary), cingulate cortex, and the cerebellum (simple lobule). Again, the *Cmah-/-* mice had larger GM brain regions compared to the control *C57BL/10* mice surrounding the lateral ventricles in particular (Figure 3.7).

By 18 months old the control *C57BL/10* mice had the highest number of regions where the brain regional GM volume was larger than the *Cmah-/-* mice. These regions included the somatosensory cortex and the caudate putamen (Figure 3.37). Given that the total brain volume of the *Cmah-/-* mice decreased with increasing age (Figure 3.3) it was interesting to also detect reduced GM volume in the same mice.

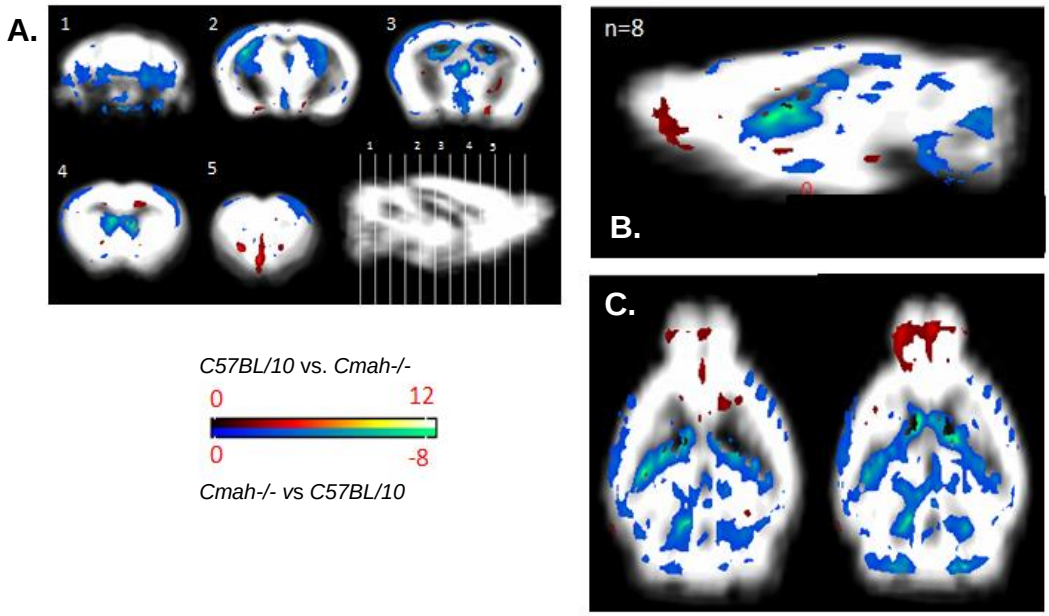

Figure 3.35: Presentation of the voxel based morphometry (VBM) results produced by the SPM software with the SPMMouse plugin for grey matter (GM) of *C57BL/10* vs *Cmah-/-* mice at 6 months old. The GM average shown is for the control *C57BL/10* mice and a coloured overlay showing the location of significant clusters. Red clusters indicate where the control *C57BL/10* mouse brain is larger than the *Cmah-/-* brain and blue indicates where the *Cmah-/-* brain is larger than the control *C57BL/10* brain (in terms of GM volume). Colour intensity on the scale bar refers to the level of significance with a lighter colour indicating a higher level of significance. ($p<0.05$, students t-test). **A.** Coronal images numbered 1-5 with a corresponding sagittal image detailing the image plane where the coronal image lies. **B.** Sagittal representation of VBM findings. **C.** Two coronal grey matter slices detailing VBM findings. Grey matter average is from 8 control mice. The largest amount of changes detected by VBM were found in the *Cmah-/-* mouse brain. At 4 months old the *Cmah-/-* mice had larger GM volume in many brain regions, particularly the regions surrounding the brain ventricles.

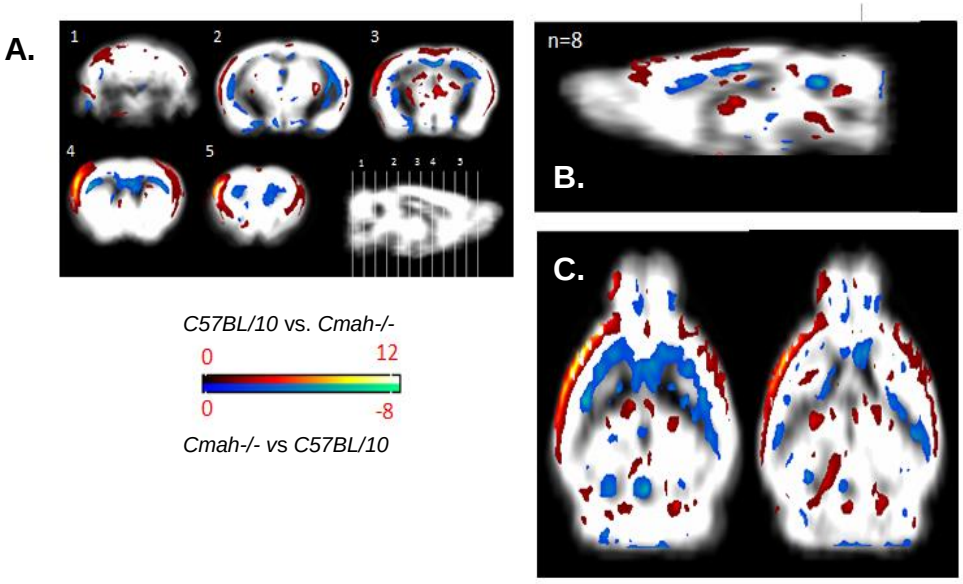

Figure 3.36: Presentation of the voxel based morphometry (VBM) results produced by the SPM software with the SPMMouse plugin for grey matter (GM) of *C57BL/10* vs *Cmah-/-* mice at 12 months old. The GM average shown is for the control *C57BL/10* mice and a coloured overlay showing the location of significant clusters. Red clusters indicate where the control *C57BL/10* mouse brain is larger the than *Cmah-/-* brain and blue indicates where the *Cmah-/-* brain is larger than the control *C57BL/10* brain (in terms of GM volume). Colour intensity on the scale bar refers to the level of significance with a lighter colour indicating a higher level of significance. ($p<0.05$, students t-test). **A.** Coronal images numbered 1-5 with a corresponding sagittal image detailing the image plane where the coronal image lies. **B.** Sagittal representation of VBM findings. **C.** Two coronal grey matter slices detailing VBM findings. Grey matter average is from 8 control mice. At 6 months old the *Cmah-/-* mice continued to have a larger GM volume in areas surrounding the brain ventrcicle but additionally control *C57BL/10* mice had an increased GM volume in layers of the cortex.

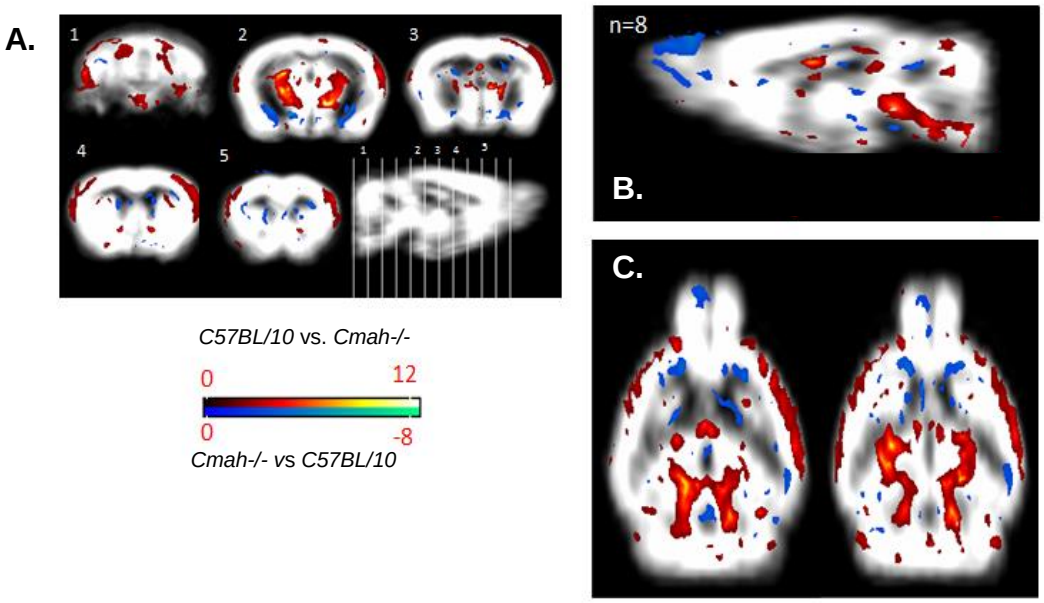

Figure 3.37: Presentation of the voxel based morphometry (VBM) results produced by the SPM software with the SPMMouse plugin for grey matter (GM) of *C57BL/10* vs *Cmah-/-* mice at 18 months old. The GM average shown is for the control *C57BL/10* mice and a coloured overlay showing the location of significant clusters. Red clusters indicate where the control *C57BL/10* mouse brain is larger than the *Cmah-/-* brain and blue indicates where the *Cmah-/-* brain is larger than the control *C57BL/10* brain (in terms of GM volume). Colour intensity on the scale bar refers to the level of significance with a lighter colour indicating a higher level of significance. ($p<0.05$, students t-test). **A.** Coronal images numbered 1-5 with a corresponding sagittal image detailing the image plane where the coronal image lies. **B.** Sagittal representation of VBM findings. **C.** Two coronal grey matter slices detailing VBM findings. Grey matter average is from 8 control mice. At 18 months old the control *C57BL/10* mice had a larger GM volume in many brain regions, which is the opposite effect to that seen at 6 months old.

3.4.10 Grey matter volume comparison

Cross animal mean GM volume images were generated using the SPMMouse template and SPM12 and were compared between the genotypes at 18 months old. Figure 3.38 shows that the highest difference in GM was between the control *C57BL/10* and the *Cmah-/-* mice. The DMD mouse models display changes in GM structure particularly around the lateral ventricles.

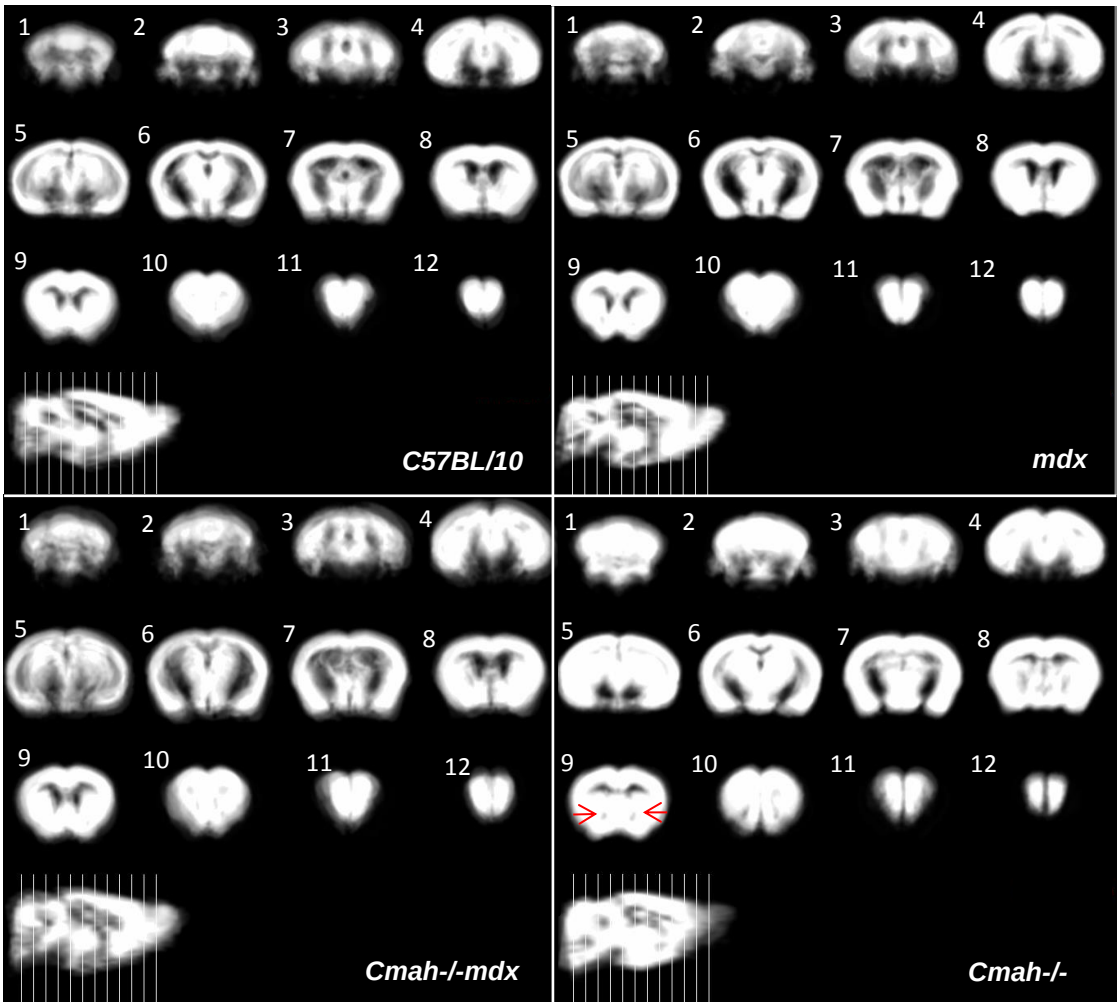

Figure 3.38: Average grey matter (GM) volume for control *C57BL/10*, *mdx*, *Cmah-/-mdx,* and *Cmah-/-* at 18 months old generated using the SPMMouse plugin and SPM 12. (n=8/genotype). The *Cmah-/-* mice showed the largest change in grey matter volume compared to control C57BL/10 mice. Red arrows indicate reduced lateral ventricle spaces.

3.5 Discussion

MRI provides invaluable information about the brain as a whole, identifying many malformations in a non-invasive manner. This was the first study investigating longitudinal changes in DMD mouse brains, scanning the same mouse at each time point. A major finding of this study was that at all time points investigated (4 months, 6 months, 12 months and 18 months old) the *Cmah-/-mdx* mice had a statistically significant increase in their TBV compared to all other genotypes. This was an interesting finding as the original assumption was that the *Cmah-/-mdx* double mutant mice would serve to exacerbate the *mdx* brain phenotype, as they have already demonstrated a more severe muscle phenotype to that exhibited by *mdx* mice (Chandrasekharan *et al.*, 2010). This assumption may in part be true, given that the *mdx* mouse TBV was significantly larger than that of control *C57BL/10* mouse brain from 12 months onward (Figure 3.3) and this effect of increased TBV volume might be enhanced in *Cmah-/-mdx* mice from 4 months onwards.

A particularly interesting finding of the study was the increase in TBV in control *C57BL/10* mice, which was not an expected result. We observed significant, progressive, whole brain and regional volume increases (brain ventricle system) in mature control *C57BL/10* mice, where the increase began at 4 months old and brain growth slowed down from 12 months onward (Figure 3.4). In contrast, the human brain grows significantly between birth until our mid-teens, when brain growth begins to plateau, followed by a prolonged period of stability in brain size before a very slow decline (atrophy) in later life (Giedd *et al.*, 1999; Courchesne *et al.*, 2000). In rodents, the closure of the growth plates is long delayed, which is opposite to that in humans (Kilborn *et al.*, 2002). The synchondroses of the neocranium permits skull enlargement in mice (Lobe *et al.*, 2006), especially the basisphenoid, basioccipital, presphenoid and supraoccipital bones, up to at least 60 days of age (Vilmann, 1969), but most likely even longer. In the mature normal mouse brain, there is no literature reporting neurocranial changes. If in fact the mouse neurocranium can expand with maturity to accommodate an increase in TBV in control mice (5.29±0.68 % between 4 and 18 months old), this could account for the presence of an increased ventricle volume with increasing age. Since the mouse skull does not

provide a ‘rigid box’ like the human skull does, the brain and brain regions are able to expand, and any uncompensated increase in regional tissue volume should result in a balanced reduction in CSF and/or other tissue volume, which was not observed in this study (Figure 3.10). This finding is important when using transgenic mice to model human brain diseases at the macroscopic level; the brain and skull growth could be the underlying ontological feature which should be considered.

It has been previously reported that thicker temporal muscles are associated with a more ovoid head shape in DMD patients compared to age matched controls (Straathof *et al.*, 2014). We also observed a thickening of the temporal muscle in our DMD mouse models and a rounder head shape (Figure 3.20). In addition, skeletal preparation of the skull and X-rays of the cranium detected a shorting of the nasal plate and a widening of the squamosal bones, particularly in the *Cmah-/-mdx* mice, but also in the *mdx* mice (at 4 months and 18 months old respectively). Taken together, this could suggest that the weaker, hypertrophic cranial muscles, including the temporal muscles, influence the development of the skull, resulting in a rounder shape. The majority of DMD patients in whom this effect has been reported have been taking long-term corticosteroids and authors suggested they could have an impact on muscle hypertrophy. However, the mice in this study did not receive any corticosteroids and hence we hypothesise that this effect is due to the loss of full length dystrophin. The skull size is also known to directly correlate with brain volume and there was 25-27% increase in whole brain and intracranial volume between early childhood and adolescence (Reiss *et al.*, 1996; Courchesne *et al.*, 2000). It could therefore be possible that the change in skull shape observed in the *Cmah-/-mdx* and *mdx* mice could facilitate the further expansion of the brain, given the aforementioned change in skull bone fusion between mice and humans, and could account for the extensive increased TBV observed in the DMD mice.

In this study we found that brain regions increased in volume, but normalising the region to TBV allowed us to better understand their relative trajectories. In humans there is a pattern of progressive, maturity-onset, relative grey matter (GM) loss, but white matter (WM) and ventricular gain with aging (Giedd *et al.*,

1999; Bartzokis *et al.*, 2001). We have demonstrated an increased ventricular volume with increasing age in the control *C57BL/10* and interestingly also in the *Cmah-/-* mice, which have a more similar glycoprofile to that of humans, and suggest a similar aging effect on the brain occurs between these two species. The LV appeared to dilate significantly more in the DMD mouse models, relative to TBV increases, suggesting that this is a pathological feature associated with full-length dystrophin loss. The cerebral ventricle system is a specialised series of connected cavities which are filled with CSF and surrounded by neuroepithelium (Lowery and Sive, 2009). The adult brain consists of four connected ventricles: two LV within the cerebrum, a 3V within the diencephalon, and a 4V lying between the cerebellum and pons (Lowery and Sive, 2009). The LV are connected to the 3V, which is linked to the 4V via the cerebral aqueduct. In turn, the 4V joins to the spinal cord canal and the subarachnoid space that envelops the brain. The choroid plexus (CP) consists of epithelial tissue masses highly vascularised with fenestrated blood vessels of which there are four within the brain, located in each ventricle and in turn produce two thirds of the CSF in the brain. The remaining third of CSF is thought to be produced by the surface of the ventricles and the lining of the subarachnoid space (Liddelow, 2015). This fluid circulates in the ventricular system, subarachnoid spaces, and spinal canal, where the plexuses are essential for controlling the homeostasis of its composition through regulation of movement of essential ions and molecules into, and metabolites out of the CSF (Liddelow, 2015). The blood cerebrospinal fluid barrier (BCSFB) is compromised predominately of the choroid plexus (CP) with other contributions from the arachnoid and arachnoid villi on the outer surface of the brain. Within the CP the basolateral membrane utrophin A and colocalises with dystrophin to control structural stability, transmembrane signalling, and ion/water homeostasis (Johanson *et al.*, 2011).The loss of full-length dystrophin in these mice could potentially alter the structural stability of the BCSFB and cause abnormalities in osmotic regulation leading to an increase in CSF circulating in the ventricle system causing dilation of the lateral ventricles (LV).

Furthermore, the enlargement of brain ventricles has been described for various brain disorders with cognitive impairment, including multiple sclerosis (Bakshi *et al.*, 2002), Klinefelter syndrome (Itti *et al.*, 2006) and fragile X mental retardation

(Reiss *et al.*, 1995). Moreover, several studies have described correlations between the degrees of ventricular enlargement and the level of the cognitive dysfunction or mental retardation (Reiss *et al.*, 1995). Although obstruction of the 4V and/or the cerebral aqueduct has been known to cause ventricular expansion (Ishihara *et al.*, 2010) this was not evident on any of the MR images acquired for the DMD mice. Enlargement of the ventricular system may also be caused by a failure of absorption or an overproduction of CSF, structural or functional impairments of cilia, and impaired cell proliferation around ventricles (Garton and Piatt, 2004).

The *Cmah-/-mdx* mice displayed further potentially pathological abnormalities in their ventricular system. A hypoplastic septum was present in 2/8 *Cmah-/-mdx* mice participating in the longitudinal scanning and this effect has also been reported in a platelet-derived growth factor C (PDGFC) deficiency mouse model, where the study identified abnormalities in the ependymal layer of the ventricle system (Fredriksson *et al.*, 2012). The ependymal cells of DMD mice were not investigated in this study, but future studies could investigate this to determine whether dystrophin is necessary for the development of normal cerebral ventricles and neuroependymal integrity. Furthermore, mice participating in the *in vivo* BBB study (chapter five) displayed extreme hydrocephalus manifested as an abnormal accumulation of CSF and enlargement of the LV.

The *Cmah-/-* mice had an enlarged TBV at 4 months old compared to control *C57BL/10* mice, but surprisingly the TBV decreased with increasing age (Figure 3.4). This effect was similar to that of humans in terms of brain size and aging and it was unusual that given these mice also express Neu5Ac and not Neu5Gc like the control *C57BL/10* and *mdx* mice, where the largest amounts of TBV increase occurred between 4 -18 months old, it may be that this change in sialyation capacity has an influence on brain size. Contrasting with other organs that express varying ratios of Neu5Gc and Neu5Ac, depending on the variable expression of *Cmah*, Neu5Gc expression in the brains of all vertebrae is extremely low, suggesting that neuronal expression may be detrimental to animals (Okerblom and Varki, 2017). Focal atrophy was clearly evident on the MR images acquired from 2/8 *Cmah-/-* mice at 18 months old, where the atrophy was not present in the same animal at 12 months old and was

additionally observed via VBM analysis. The effect of reduction in brain volume in the *Cmah-/-* mice is most likely a global TBV reduction as these focal areas of atrophy were not enough to account for the significant reduction in TBV overserved in all 8 *Cmah-/-* mice investigated in this longitudinal study.

Interestingly, the *Cmah-/-* mice have previously been reported to show other signs of 'normal human aging' not exhibited by wild type mice, including age related hearing loss. By 9 months of age, *Cmah-/-* mice displayed reduced hearing sensitivities across all frequencies, increased outer hair cell degeneration throughout the cochlea, and collapse of the outer organ of Corti, compared to wild type control mice (Kwon *et al.*, 2015). Since the *Cmah-/-* mice have a more similar glycoprotein to that of humans, it could therefore be possible that this effect on brain tissue and on the hearing are two effects seen in the *Cmah-/-* mice as a consequence of Neu5Gc loss, although the biochemical mechanisms in this phenotype have not been characterised or described. Only a small number of *Cmah-/-* mice participated in this study and diet was not controlled for and this is the first time *Cmah-/-* mice on a *C57BL/10* background have been investigated utilising MRI. Many additional studies will be needed to be pursued in these, and other phenotypic features resulting from this human-like genetic defect.

Voxel-based morphometry (VBM) is routinely applied to the human brain to aid in the diagnosis of neurological disorders but its application in mouse brain is limited. VBM has been successfully applied in various brain disorders including mouse models of Huntington's disease (Sawiak *et al.*, 2009), where it has proved instrumental in determining underlying differences in brain morphology.

This is the first study to demonstrate VBM in the DMD mouse brain. We identified numerous changes with VBM in the *mdx* mouse brain where, the complexity of these changes increased between 6 and 18 months old. Interestingly, the *mdx* and *Cmah-/-mdx* mice almost identically demonstrated enlargements in GM volume in the lower layers of the cortex. The DMD mice also showed reduced GM volume in the cerebellum and hippocampus, regions known to be rich in dystrophin, where the decreased in GM volume of these regions increased with age. These changes in the GM volume of the

hippocampus and cerebellum could be linked to the cognitive dysfunction observed in DMD. The increased GM volume in the amygdala may be linked to the increased anxiety related behaviour which we observed in older *mdx* mice (see chapter four for details).

The *Cmah-/-* mice displayed the highest number of changes detectable by VBM, which is not surprising given how different their brains appeared during T_1 and T_2 weighted imaging (Figure 3.5). The GM was larger in the *Cmah-/-* mice surrounding the LV and 3V, which was not surprising given the huge reduction ventricular volume we have previously observed (Figure 3.10). Additionally, since the *Cmah-/-* mice were the only genotype to demonstrate a TBV reduction between 4 and 18 months old, the VBM analysis illustrated a reduction in GM volume in various brain regions in comparison to the control *C57BL/10* mice.

In accordance with studies investigating the brain in patients with DMD we did not observe any gross structural abnormalities of regions known to be rich in dystrophin (cerebellum, hippocampus, cerebral cortex) (Dubowitz and Crome, 1969a; Doorenweerd *et al.*, 2014). We did however observe changes in the ventricles of DMD mice, particularly increased LV volume in relation to TBV which has also been reported in mouse models of autism (Bertram *et al.*, 2016). We observed an increased TBV in *mdx* mice from 12 months old and *Cmah-/- mdx* mice at all time points (Figure 3.4). Autism is a heterogeneous disorder with multiple behavioural and biological phenotypes and has been strongly associated with DMD where a deficiency in dystrophin expression is believed to be the key etiological factor of this comorbidity (Hendriksen *et al.*, 2016a). The term “dystrophin associated neurodevelopmental syndrome” was recently coined (Ricotti *et al.*, 2016) relating to autism spectrum disorders (ASD) and attention deficit hyperactivity disorder (ADHD). One striking feature of autistic patients is an enlarged brain compared to healthy aged matched control subjects (Sparks *et al.*, 2002; Courchesne *et al.*, 2003). GM is gradually pruned in favour of higher WM density in normal brain development. In ASD changes in cortical pruning have been reported such that children with ASD have shown a thickened cortex in regions associated with ASD relating to behavioural changes and social difficulties (Mensen *et al.*, 2017). Additionally, mouse models of ASD have shown changes in TBV, including increased TBV.

Although there are reports of decreased TBV the changes in TBV appear to be related to the underlying genetic cause (Ellegood *et al.*, 2015).

Overall, this chapter has demonstrated that MRI is useful and sensitive technique to monitor changes in the same DMD mouse brains longitudinally. We have identified an increase in total brain volume (TBV) in the *mdx* mouse and increased ventricular volume with age. Voxel-based morphometry (VBM) identified changes in grey matter (GM) volume, where larger changes in GM volume were detected in older *mdx* mice. The data presented in this chapter suggests that morphologically the *mdx* mouse brain changes with age, and therefore this provides the first piece of evidence to suggest that dystrophin-deficiency leads to progressive brain changes. The increase in ventricular volume with age could be used as an outcome measure to monitor treatment effect in *mdx* mice.

We observed various differences between the *mdx* and *Cmah-/-mdx* mouse brains. The *Cmah-/-mdx* mice had a larger TBV at all time points, larger total ventricular volume at all time points, and a hypoplastic septum (CSP) was present in 2/8 *Cmah-/-mdx* mice. Additionally, in the *Cmah-/-* mice we observed various differences in brain size and morphology, in comparison to both the control *C57BL/10* and *Cmah-/-mdx* mice, including: decreased TBV with age, focal brain atrophy, and reduced ventricular volume. These findings suggest that the loss of the *Cmah* gene, from mice, has an impact on brain morphology and consequently we would not recommend studying the *Cmah-/-mdx* mouse brain to determine the effect of dystrophin-deficiency on brain structure.

Observation	*mdx*	*Cmah-/-mdx*	*Cmah-/-*	*Cmah+/-*
Increased TBV	✓	✓		✓
Decreased TBV			✓	
Enlarged ventricles	✓	✓		
Reduced ventricles			✓	✓
Focal brain atrophy			✓	
Morphological abnormalities		✓		
Thoracolumbar Kyphosis	✓	✓		
Scoliosis	✓	✓		
Temporalis muscle hypertrophy	✓	✓		
Skull size changes	✓	✓		
Hippocampal volume changes	✓	✓	✓	
Cerebellum GM volume reduction with age	✓	✓		
Hippocampal GM volume reduction with age	✓	✓		
Increased GM volume in cortex	✓	✓		

Figure 3.39: Summary of findings, in comparison to control *C57BL/10* mice, from longitudinal brain magnetic resonance imaging (MRI) investigations. GM= grey matter, **TBV=** total brain volume.

Chapter 4. Monitoring the progression of cognitive dysfunction in mouse models for Duchenne muscular dystrophy

4.1 Introduction

The dystrophin-deficient *mdx* mouse has been studied for over twenty years and is the most common and best characterised mouse model of DMD (Bulfield *et al.*, 1984). The *mdx* mouse has also been extensively investigated for the detection of cognitive dysfunction associated with DMD (Muntoni *et al.*, 1991; Vaillend *et al.*, 2004; Grounds *et al.*, 2008; Vaillend and Chaussenot, 2017).

DMD patients often exhibit psychiatric abnormalities including self-depreciation, marginalisation, minor depression, signs of insecurity, hypochondria, poor adaptation to the environment, and high levels of anxiety (Komoto *et al.*, 1984; Fitzpatrick *et al.*, 1986; Zwaigenbaum and Tarnopolsky, 2003; Wu *et al.*, 2005). DMD patients display a varying degree of memory impairments, which have been attributed to the loss of dystrophin in brain structures involved in cognition, including the neocortex and hippocampus (Anderson *et al.*, 2002). A more specific comorbid diagnosis of autism was also strongly associated with DMD and BMD, with dystrophin and other members of the DGC now being proposed as new candidate risk loci for autism spectrum disorder (ASD) (Komoto *et al.*, 1984; Hinton *et al.*, 2009; Sekiguchi *et al.*, 2009). The phenotypic heterogeneity in dystrophinopathies is likely due to individual genetic background differences with a variety of mutation profiles linked to differing levels of cognitive impairment, either due to the loss of Dp427 or the cumulative loss of shorter dystrophin brain isoforms (Dp140 and Dp71), likely resultant from internal promotor mutations (Taylor *et al.*, 2010). While approximately one-third of DMD patients demonstrate a varying degree of cognitive impairment, there have been recent suggestions of a genotype-phenotype relationship with mutations affecting C-terminal forms of dystrophin showing higher correlation with cognitive dysfunction (Hinton *et al.*, 2007; Hinton *et al.*, 2009). However, there still remains no concrete genotype-phenotype relationship (Pagnamenta *et al.*, 2011) and flaws exist in this theory. One patient with DMD and autism was shown to carry a submicroscopic deletion encompassing exons 12–25 of the dystrophin transcript, suggesting that the loss of Dp427 is sufficient to induce

vulnerability to autism and learning difficulties (Erturk *et al.*, 2010). The *mdx* mouse is therefore a relevant model to study the effect of the loss of Dp427 on cognitive abilities.

Brain alterations associated with a lack of Dp427 are predominately located at the synaptic level and involve impaired GABAergic function, including the excitation/inhibition balance which is also a key mechanism thought to be involved in ASD (Zikopoulos and Barbas, 2013). The autism-associated trans-synaptic neurexin-neuroligin complex interacts with dystroglycan, which has a central role in the DGC implying a putative mechanism underlying the alteration in social behavioural or communication seen in DMD (Craig and Kang, 2007; Südhof, 2008).

Male *mdx* mice aged between 3-5 months old have shown abnormal behaviour and communication on behavioural and bioacoustic measures, validated to identify autistic traits in mice (Miranda *et al.*, 2015). In particular when *mdx* mice were confronted with an intruder in their home cage they displayed an increased freezing response during physical contacts, only reverting to normal exploratory activity upon interruption of social contact. This is suggestive that enhanced fear-related responses could contribute to altered social behaviour in *mdx* mice, with such behaviour confirming that executive functions enabling adaptation of behaviour to distinct contexts are also affected (Miranda *et al.*, 2015). Moreover, *mdx* mice also showed altered ultrasonic communication. In particular adult male mice used an abnormal vocal repertoire when exposed to anesthetised females showing a reduction in expression of peak and composite calls (Miranda *et al.*, 2015). Importantly, studies investigating autism-like behaviour in *mdx* mice reported a lack of stereotypic behaviours often observed in mouse models of autism, such as altered patterns of grooming activity or repetitive jumping (Silverman *et al.*, 2010).

Previous studies have identified dystrophin expression in the hippocampus (CA1 – CA4 fields, but not the DG), cerebral cortex, and cerebellum (Lidov *et al.*, 1990; Lidov *et al.*, 1993). The brain stem (with the exception of the facial nucleus and trigeminal complex), thalamus, hypothalamus, basal ganglia and spinal cord are thought to be devoid of dystrophin (Lidov, 1996). A recent study

in *mdx* mice found emotional defensive behaviours; fear-motivated unconditioned and conditioned defensive responses were altered, which was linked to the expression of dystrophin in the amygdala (Sekiguchi *et al.*, 2009). The amygdala was important for association learning, which is necessary for conditioned fear learning. Abnormal GABAergic synaptic activity observed in the amygdala was linked to the alteration of fear-motivated unconditioned and conditioned defensive response in *mdx* mice (Sekiguchi *et al.*, 2009). The study found attenuation of GABAergic inhibition in the basolateral nucleus of the amygdala (BLA) correlated with enhancement of conditioned fear memory, as local GABAergic inhibition is one of the crucial factors regulating amygdala neuronal circuit activity (Sah *et al.*, 2003). Fear conditioning responses have highlighted the importance of efferent projection of the amygdala to the periaqueductal grey (PAG) freezing response (Brandao *et al.*, 1999). Projections from the CA1 field and subiculum of the central hippocampus to the BLA are involved in contextual fear (Maren and Fanselow, 1995). The CA1 field and BLA are connected with each other and this interaction is known to be important for contextual fear memory, and hippocampal synaptic plasticity (Nakao *et al.*, 2004).

Cognitive assessment in *mdx* mice has utilised both male and female mice and focused upon one time point. Studies have shown that a rodent's biological response to stress is affected by gender differences. Chronic stress has been shown to have a direct effect on brain plasticity and function with an emphasis on morphological changes in the hippocampus, prefrontal cortex, and amygdala, characterised by dendritic arborisation. These brain structures, known to be dystrophin–rich, are highly interconnected and sensitive to stress and gonadal hormones and influence a variety of cognitive abilities (McLaughlin *et al.*, 2009). For example, when researching other neurodevelopmental disorders the mouse model for Down's Syndrome (DS), showed gender differences in defensive behaviour to predator exposure (Martinez-Cue *et al.*, 2006). In the case of *mdx* mice, female mice showed a reduced but significant freezing response to a brief restraint with the duration of freezing shorter than that of males (Yamamoto *et al.*, 2010). Interestingly female wild type mice did not show any freezing response suggesting that the freezing response occurs with the loss of dystrophin in both male and female mice, although male mice

are more susceptible. Heterozygous females did not show a freezing response at all, given that they express near 50% levels of dystrophin this is suggestive that this amount is enough to avert the abnormal freezing response induced by restraint (Yamamoto *et al.*, 2010).

Previous studies in the *mdx* mice have also shown deficits in passive avoidance learning (Muntoni *et al.*, 1991), impairments in memory consolidation (both spatial and non-spatial learning) (Vaillend *et al.*, 2004), and retention deficits at long delays in spontaneous alteration and bar pressing tasks (Vaillend *et al.*, 1995). One major caveat of the cognitive assessment testing in *mdx* mice is the lack of monitoring of potential progressive cognitive defects. Recent studies have alluded to worsening cognitive performance with increasing age in DMD patients (Suzuki *et al.*, 2017) and there is now an increasing need for a behavioural assessment to test cognitive function of *mdx* mice at different ages. Additionally, assessing the cognitive/behavioural profile of male *mdx* mice at both young and old time points will provide a better understanding regarding the level of cognitive dysfunction and how this may decline with age.

4.1.1 Aims:

The experiments described in this chapter aim to monitor if the cognitive deficits seen in DMD mice are progressive utilising male mice only. Specifically, this chapter aims to:

- Verify if the Barnes maze test and Novel object recognition (NOR) task; which measures hippocampal spatial learning and non-spatial recognition memory respectively, are sufficiently sensitive to detect a cognitive impairment in DMD mice.
- Monitor behavioural changes in control *C57LBL/10* and mutant mice between 4 and 12 months old using the Barnes maze test and NOR task.
- Assess the cognitive profile of mice lacking the *Cmah* gene. There is currently no data regarding the cognitive abilities of *Cmah-/-mdx* mice and studies in the *Cmah-/-* mice remain ambiguous.

.

4.2 Barnes maze testing

4.2.1 Overview of procedure

Mice were trained during a four day period to learn the location of the target box associated with a target hole and target shape (square, triangle, circle or cross). Habituation to the maze was carried out on day one before the acquisition phase began (Figure 4.1). The first probe trial measured short-term memory (day five), whereas long-term memory was assessed during the second probe trial (day twelve). Primary latency to locate the target hole served to measure learning during the acquisition phase (day 1-4). During the first probe trial (day five) the target box was removed and mice were given 90 seconds to explore the maze. Short-term memory was monitored by measuring the time spent in the target quadrant, primary latency, and a success score (number of head pokes x hole value). Mice received no training between probe trial 1 and probe trial 2. During the second probe trial long-term memory was assessed by measuring the time spent in the target quadrant, primary latency, and a success score (number of head pokes x hole value).

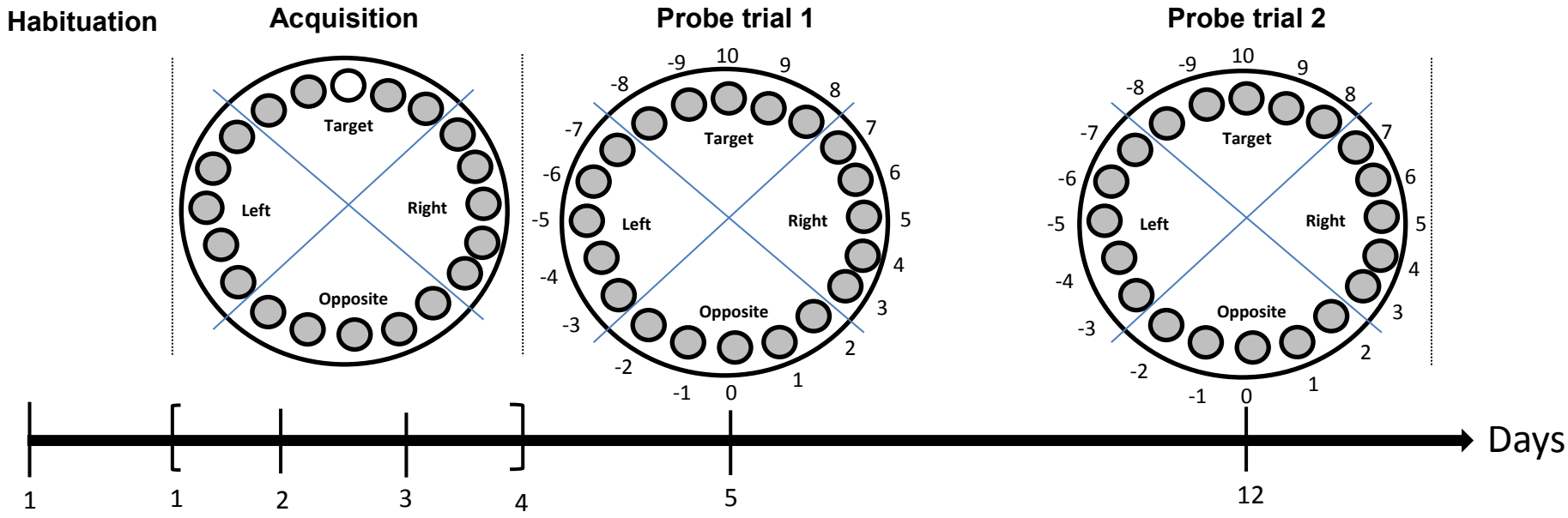

Figure 4.1: Overview of Barnes maze test.

Habituation occurred on day one to familiarise the mouse with the test. Training occurred between days 1-4 where there are four trails per day per mouse, with an inter-trial interval of 15 minutes. During training days mice are given 3 minutes to explore the maze and locate and enter a target box, under a target hole, associated with a target shape. Primary latency, total latency, primary errors, total errors, and search patterns were recorded during training sessions. On day 5 short-term memory was assessed (probe trial 1). The target box was removed and the mouse had 90 seconds to explore the maze. Long-term memory was assessed on day 12 (probe trial 2) and there was no training between days 5 and 12. The memory probe trails calculate a success score which is the hole value x number of nose pokes. A higher success score indicated a good short- or long-term memory in relation to remembering the location of the target hole. The percentage of time the mice spent in the quadrants (target, left, right, and opposite) was also recorded.

4.2.2 Primary latency

During Barnes maze testing, primary latency (the time it takes to find the target hole regardless of the time it takes to enter the target hole), was used as the primary measure. A repeated measures ANOVA revealed that all mice showed significant spatial acquisition (learning) across all four days of testing at 4 months old ($F_{3,84}$ = 20.9, p<0.01). On day 4 (the last day of training) the control *C57BL/10* mice had an average primary latency of 15±3 seconds whereas *mdx* mice had an average primary latency of 52±15 seconds. Although this was significantly longer (p<0.05), *mdx* mice performed similarly to the control *C57BL/10* mice on the other days of training at 4 months old, for example on day 2 the control *C57BL/10* mice average primary latency was 37±8 seconds and the *mdx* mice average primary latency was 43±8 seconds. The average primary latency was comparable between all genotypes at 4 months old (Figure 4.2A). Interestingly, the *Cmah-/-mdx* mice had the lowest recorded primary latencies on all four days of training compared to all other genotypes.

A repeated measures ANOVA revealed that all mice showed significant spatial acquisition (learning) across all four days of testing at 6 months old ($F_{3,81}$=25.3, p<0.01). However, by the 6 months old time point a significant difference in performance on the Barnes maze test was observed between control *C57BL/10* and *mdx* mice in terms of primary latency measurements. On day 4 of training *mdx* mice took considerably longer to find the target hole compared to control mice (40±8 seconds average primary latency for control *C57BL/10* mice compared to 80±20 seconds for *mdx* mice) (Figure 4.2B). Again, the *Cmah-/-mdx* mice had a performance similar to that of control *C57BL/10* mice and better than that of *Cmah-/-* and *mdx* mice.

A repeated measure ANOVA revealed that all mice showed significant spatial acquisition (learning) across all four days of testing at 12 months old ($F_{3,84}$=16.8, p<0.01). At 12 months old the *mdx* mice showed a severe cognitive deficit in the ability to locate the target hole compared to control *C57BL/10* mice during all four days of training (Figure 4.2C). The 12 months old *mdx* mice also took far longer to locate the target hole than they did at 4 and 6 months old. For example on day 4 of training 6 months old *mdx* mice had an average primary

latency of 56±15 seconds and at 12 months old 150±25 seconds ($p<0.05$) compared to control *C57BL/10* mice, whose average primary latency at 6 months old was 15±3 seconds and at 12 months 20±8 seconds.

Mixed measures repeated ANOVA revealed that there was no significant interaction between day, genotype and age with respect to average primarily latency during the Barnes maze test ($F_{18, 249} = 1.32$, $p=0.1$).

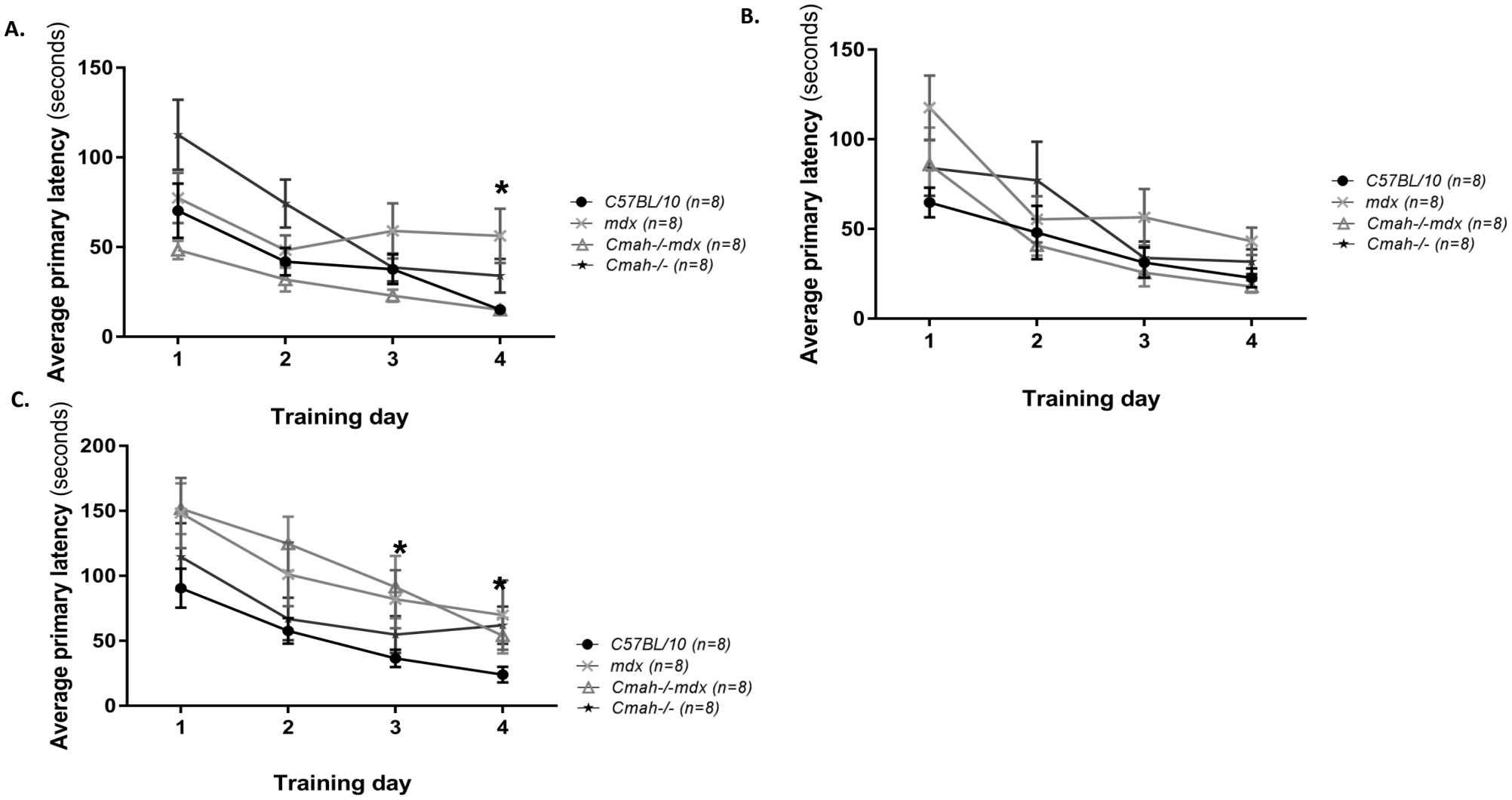

Figure 4.2: Spatial acquisition times for all mice across the four days of training. Primary latency is the time it takes to find the target hole regardless of the time that it takes to enter the target hole. **A.** Average primary latency at 4 months old. **B.** Average primary latency at 6 months old. **C.** Average primary latency at 12 months old. Data presented as mean ± SEM, *p<0.05 vs control *C57BL/10* mice.

4.2.3 Total latency

Total latency is the time it takes for the mouse to enter the target hole regardless of the time it took the mouse to locate the target holes. There was a significant interaction between day and total latency with all mice demonstrating learning of the task by entering the target hole faster each day (mixed measures repeated ANOVA, $p<0.01$).

A repeated measures ANOVA revealed that all mice showed increased learning by entering the target hole faster between days 1-4 of training at 4 months old ($F_{3,84} = 14.61$, $p<0.01$). At 4 months old the average total latency was comparable between all four genotypes (Figure 4.3A) during initial training. However, by day 4 of training *mdx* mice had shown a reduced ability to enter the target hole and had an average total latency of 168±30 seconds compared to control *C57BL/10* mice, who had an average total latency of 86±36 seconds. On the whole, *mdx* mice had the longest average total latency compared to the other genotypes during all four days of training at 4 months old. Interestingly the lowest average total latency was observed was in the *Cmah-/-*mdx mice who on day 4 of training had an average total latency of 69±16 seconds whereas, control *C57BL/10* mice had an average total latency of 86±36 seconds, and *Cmah-/-* mice had an average total latency of 87±26 seconds (Figure 4.3A).

A repeated measures ANOVA revealed that all mice showed increased learning by entering the target hole faster between days 1-4 of training at 4 months old ($F_{3,81} = 12.6$, $p<0.01$). At 6 months old there was a significant difference in the performance of all genotypes with all genotypes demonstrating an increase in the average total latency to enter the target hole (Figure 4.3B) The *mdx* mice took longer to enter the target hole than they did at 4 months old during the first two training days. However, by day 4 of training the *mdx* mice had a comparable average total latency to that of 4 months old, with an average total latency of 56±15 seconds and 43±7 seconds respectively. *Cmah-/-mdx* mice displayed a large deficit in average total latency between 4 and 6 months old by taking longer to enter the target hole during all four days of training and having an average total latency of 70±16 seconds and 122±27 seconds respectively (on day 4 of training).

A repeated measures ANOVA revealed that all mice showed increased learning by entering the target hole faster between days 1-4 of training at 4 months old ($F_{3,84}$ = 23.8, p<0.01). At 12 months old both DMD mouse models had a considerably reduced performance than control *C57BL/10* mice in terms of average total latency during the Barnes maze test. The *mdx* mice had the largest increase in average total latency with a performance of 147±25 seconds compared to control *C57BL/10* mice at 61±15 seconds on day 4 of training (p<0.05) (Figure 4.3C). The average total latency on day 4 of training at 12 months was more than twice the latency recorded at 6 months old for *mdx* mice (43±7 seconds vs 147±25 seconds, p<0.05). Interestingly, at 12 months old 2/8 *mdx* mice exhibited a 'total freezing response', whereby they sat in the centre of the maze for a total of 3 minutes. Other *mdx* mice showed a similar freezing response, remaining immobile for a minute or more, but eventually began searching the maze. This total freezing response, seen only in the *mdx* mice at 12 months old, may account for the sudden difference in average total latency between 4 and 12 months old. The control *C57BL/10* mice showed little change in their average total latency (65± 25 seconds at 4 months old and 62±19 seconds at 12 months old on day 4 of training). *Cmah-/-mdx* mice also demonstrated an increase in average total latency at 12 months old (144±28 seconds, on day 4 of training), showing a similar time to that of *mdx* mice. The *Cmah-/-* mice did not differ significantly from the control *C57BL/10* mice between 4 and 6 months old, showing comparable average total latency times (e.g. at 4 months old on day 4 of training control *C57BL10* mice had an average total latency of 65±25 seconds and *Cmah-/-* mice had an average total latency of 73±13 seconds). However, at 12 months old the *Cmah-/-* mice had a poor performance with a huge increase in their average total latency to 138±19 seconds (day 4 of training).

Mixed measures repeated ANOVA revealed that there was a significant interaction between day, genotype and age with respect to average total latency during the Barnes maze test ($F_{16, 220}$ =1.72, p<0.05).

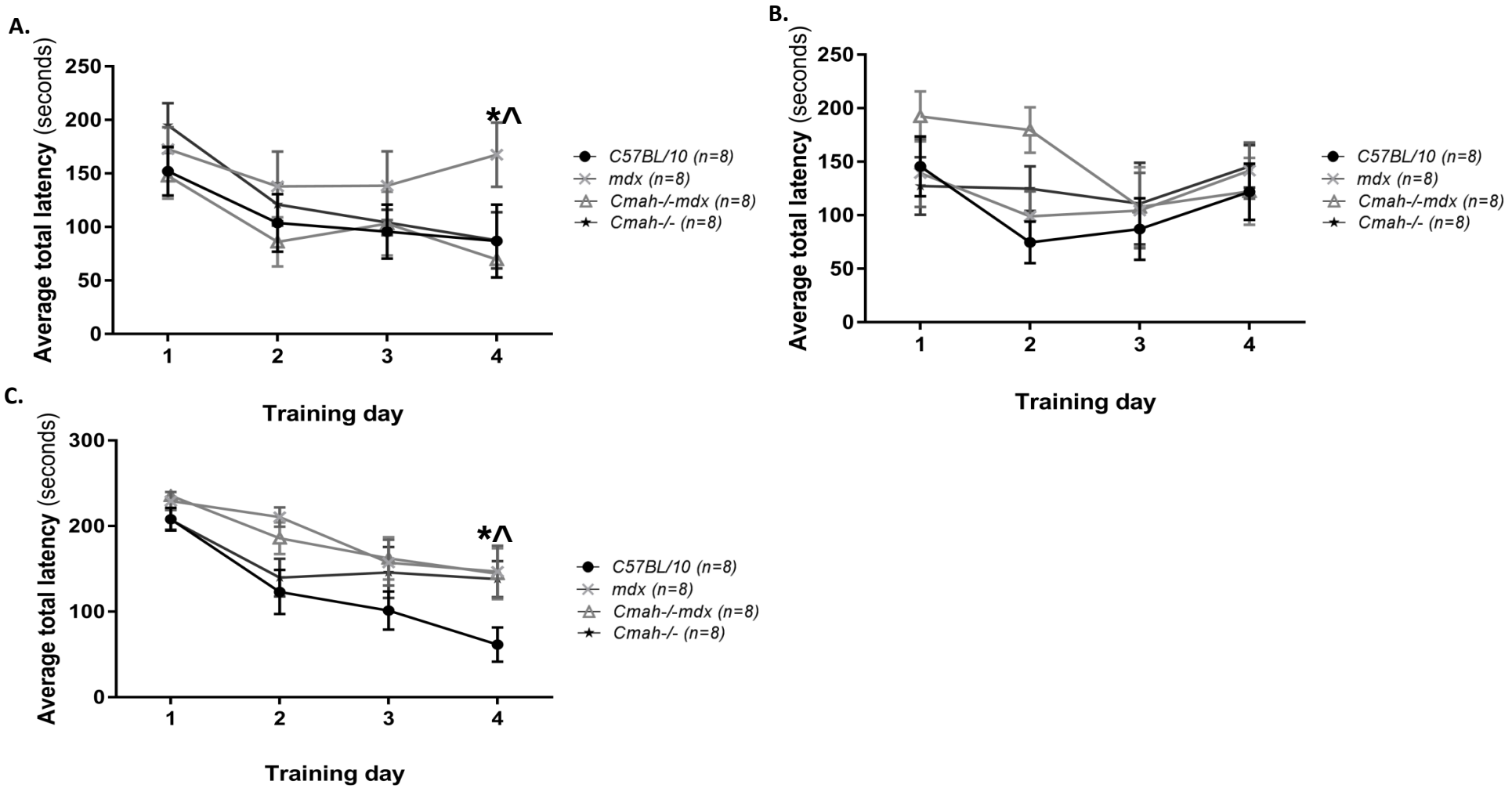

Figure 4.3: Spatial acquisition times for all mice across the four days of training. Total latency is the time it takes to enter the target hole regardless of the time it takes to locate the target hole . **A.** Average total latency at 4 months old. **B.** Average total latency at 6 months old. **C.** Average total latency at 12 months old. Data presented as mean ± SEM, *p<0.05 vs control *C57BL/10* mice, ^p <0.05 vs *mdx* mice.

4.2.4 Mean primary errors

The primary error is the number of nose pokes that the mouse has until it reaches the target hole regardless of entering the target hole. At 4 months old there was a significant interaction between genotype and day showing that all mice made fewer mistakes as they learnt the position of the target hole (mixed measures repeated ANOVA, $p<0.05$) (Figure 4.4A). However, by day 4 of training the *mdx* mice had the largest number of primary errors at 8±2 errors compared to control *C57BL/10* mice, who made the fewest primary errors of 3±1 error. Overall all mice, regardless of genotype, made the fewest number of errors at 4 months old.

At 6 months old all mice, regardless of genotype, showed a comparable number of primary errors (Figure 4.4B). Interestingly, the *mdx* mice displayed an unusually high number of errors on day 3 of training with mean primary errors of 8±1 error, which was double that of control *C57BL/10* mice with a mean primary error of 4±0.5 errors (Figure 4.4B).

At 12 months old both DMD mouse models took longer to learn where the target hole was located by displaying a high number of errors on day 1 of training which were much higher than at 4 and 6 months old (Figure 4.4C). On day 1 of training *mdx* mice had a primary number of errors of 10±1 error compared to control *C57BL/10* mice that had a primary number of errors of 6±1 error.

Mixed measures repeated ANOVA revealed that there was a significant interaction between day, genotype and age with respect to mean primary errors made during the Barnes maze test ($F_{18, 249} = 14.1$, $p<0.05$).

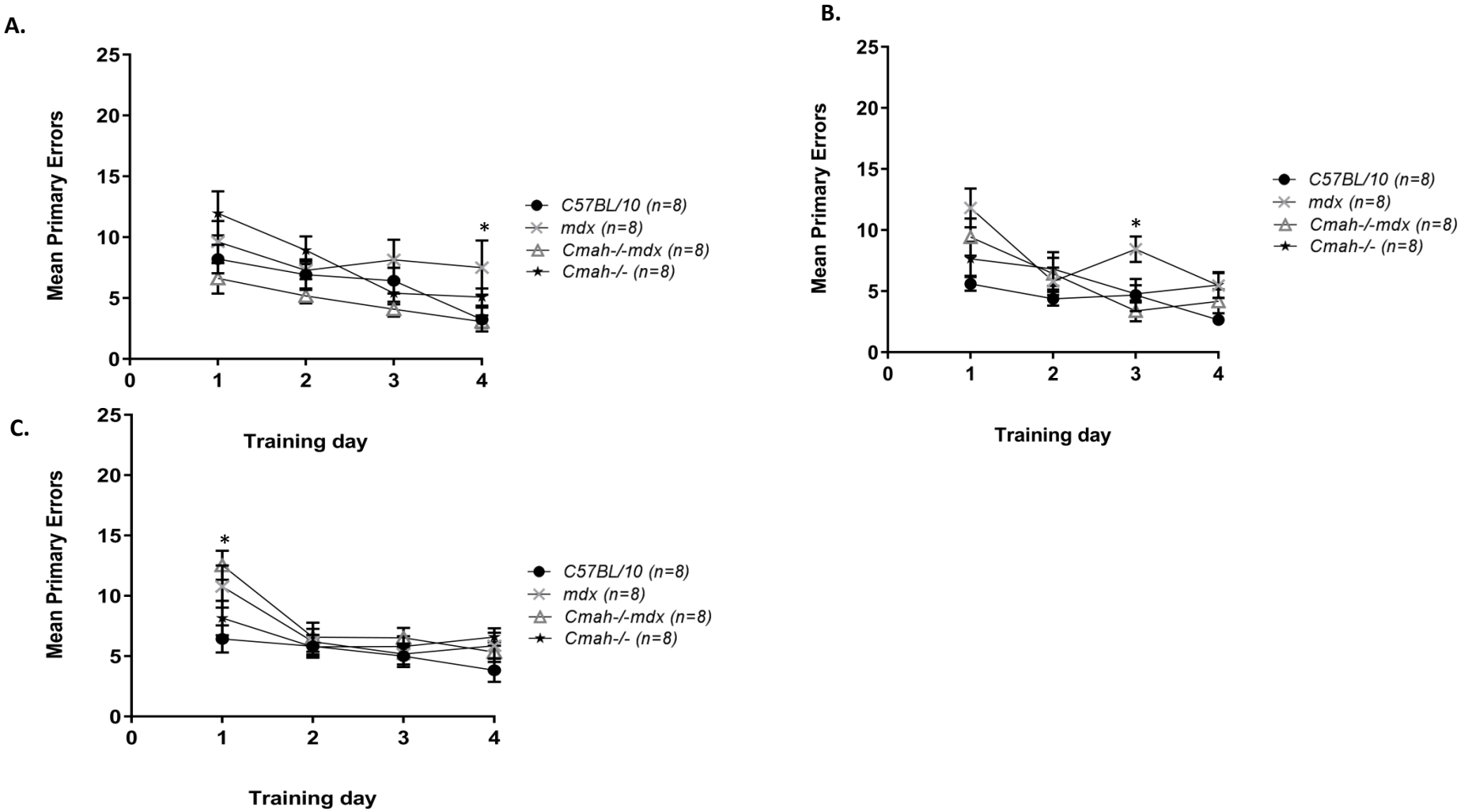

Figure 4.4: Mean number of primary errors (locating the target box for the first time) in the Barnes maze test acquisition phase are shown for each day of the trial. The performance improved in all genotypes at all time points during the course of training. **A.** Mean primary errors at 4 months old. **B.** Mean primary errors at 6 months old. **C.** Mean primary errors at 12 months old. Data presented as mean ± SEM, *p<0.05 vs control *C57BL/10* mice.

4.2.5 Mean total errors

The mean total number of errors is defined as the number of nose pokes the mouse makes into any hole before it enters the target hole. At 4 months old there was a significant interaction between genotype and day showing that all mice made fewer mistakes as they learnt the position of the target hole (mixed measures repeated ANOVA, $p<0.05$) (Figure 4.5A). On day 4 of training the *mdx* mice displayed the highest number of total errors compared to control *C57BL/10* mice (13±3 errors for *mdx* mice compared to 9±3 errors for control *C57BL/10* mice). Surprisingly, at 4 months old the *Cmah-/-mdx* mice had the lowest number of mean total errors out of all four genotypes with 6±3 errors on day 4 of training.

At 6 months old all genotypes showed a comparable number of mean total errors to that at 4 months old except for day 3 of training (Figure 4.5B). On day 3 of training the *Cmah-/-mdx* mice had the fewest mean total errors with 3±0.5 errors and *mdx* mice had the largest number of mean total errors with 13±2 errors compared to control *C57BL/10* with 7±1 mean total errors.

At 12 months old both DMD mouse models took longer to learn where the target hole was located by displaying a much higher number of errors on day 1 of training than at 4 and 6 months old (Figure 4.5C). On day 1 of training *mdx* mice had a total number of errors of 17±2 errors compared to control *C57BL/10* mice, who had a primary number of errors of 12±2 errors. The *mdx* mice had a comparable number of errors to that of control *C57BL/10* mice during training days 3 and 4 at 12 months old. The control *C57BL/10* mice displayed an increased number of errors with increasing age, but the numbers of errors was always higher in the *mdx* mice.

Mixed measures repeated ANOVA revealed that there was no significant interaction between day, genotype and age with respect to mean total errors made during the Barnes maze test ($F_{18, 249}=0.8$, $p<0.6$). However, there was a

significant interaction between genotype and day with respect to mean total errors made during the Barnes maze test ($F_{9, 249}$ =2.03, p<0.05).

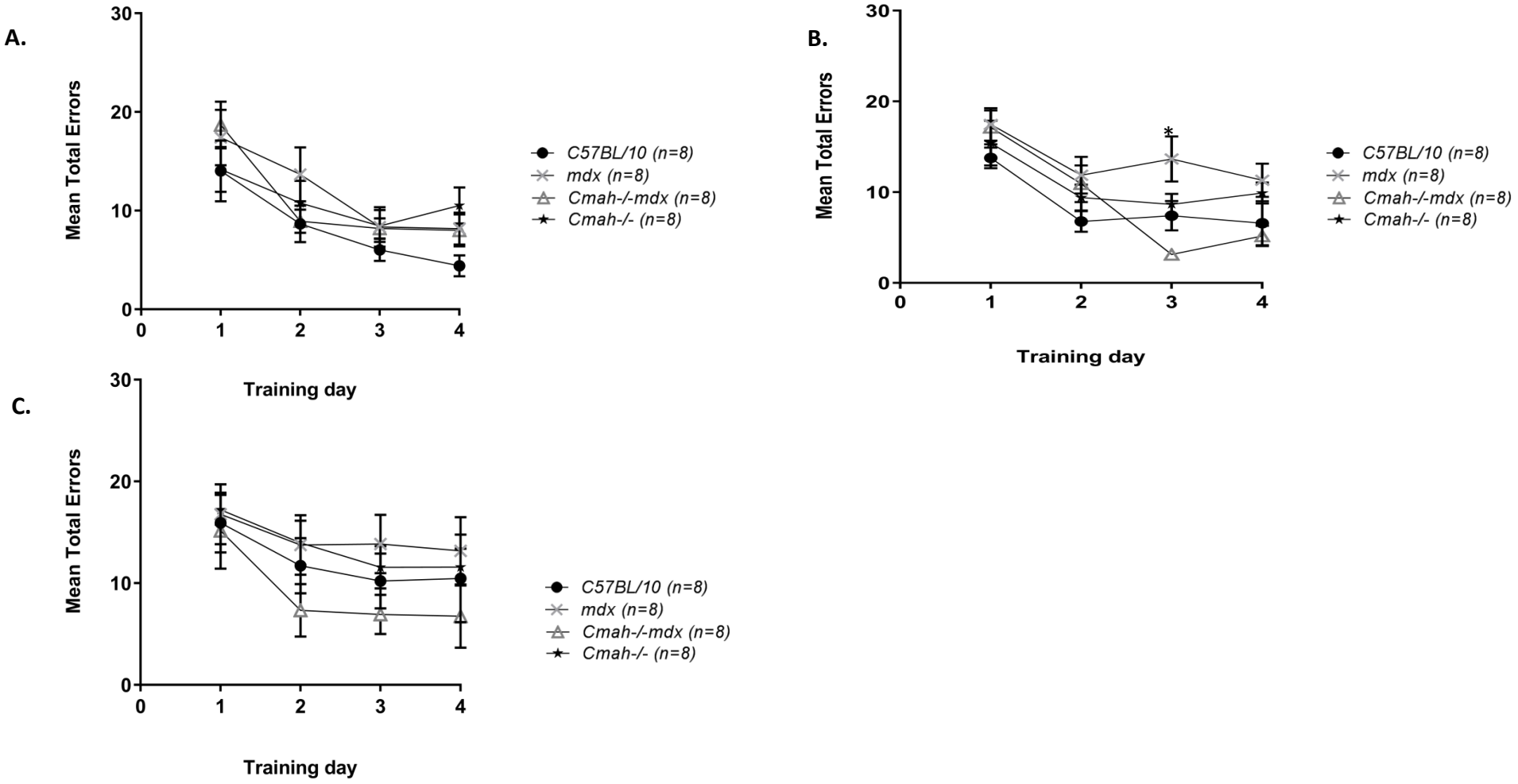

Figure 4.5: Mean number of total errors (entry into the escape box) in the Barnes maze test acquisition phase are shown for each day of the trial. The performance improved in all genotypes at all time points during the course of training. **A.** Mean total errors at 4 months old. **B.** Mean total errors at 6 months old. **C.** Mean total errors at 12 months old. Data presented as mean ± SEM, *p<0.05 vs control *C57BL/10* mice.

4.2.6 Short and long-term memory assessment

4.2.6.1Mean latency to target hole

Probe trails 1 and 2 were carried out to measure short- and long-term memory respectively (Figure 4.1). The target box was removed from the target hole and mice were given 90 seconds to explore the maze. There was no training between days 5 (short-term memory) and day 12 (long-term memory). The *mdx* mice had the longest mean latency to find the target hole for both short- and long-term memory between 4 and 12 months old (Figure 4.6). At 4 months old there was no significant difference between control and *mdx* mice with regard to short-term memory ($F_{3,28} = 1.9$, p=0.1). At 12 months old the short-term memory of *mdx* mice was impaired compared to at 4 months old, when the mean latency was recorded as 50±14 seconds and 21±0.5 seconds respectively ($p<0.05$). The long-term memory of *mdx* mice was also impaired between 4 and 12 months old with a mean latency of 26±2.5 seconds and 59±13 seconds recorded respectively ($p<0.05$). The control *C57BL/10* mice also showed a small decline in their short- and long-term memory abilities with a 10 second increase in the mean latency to target for both short- and long-term memory between 4 and 12 months old.

Surprisingly the *Cmah-/-mdx* mice had a shorter mean latency to locate the target hole for short-term memory between 4 and 6 months old compared to control *C57BL/10* mice. However, by 12 months old the *Cmah-/-mdx* mice had a substantial increase both in their short- and long-term mean latency to target. Interestingly, the *Cmah-/-* mice exhibited a similar effect at 12 months old with a huge increase in mean latency to find the target hole during both short- and long-term memory.

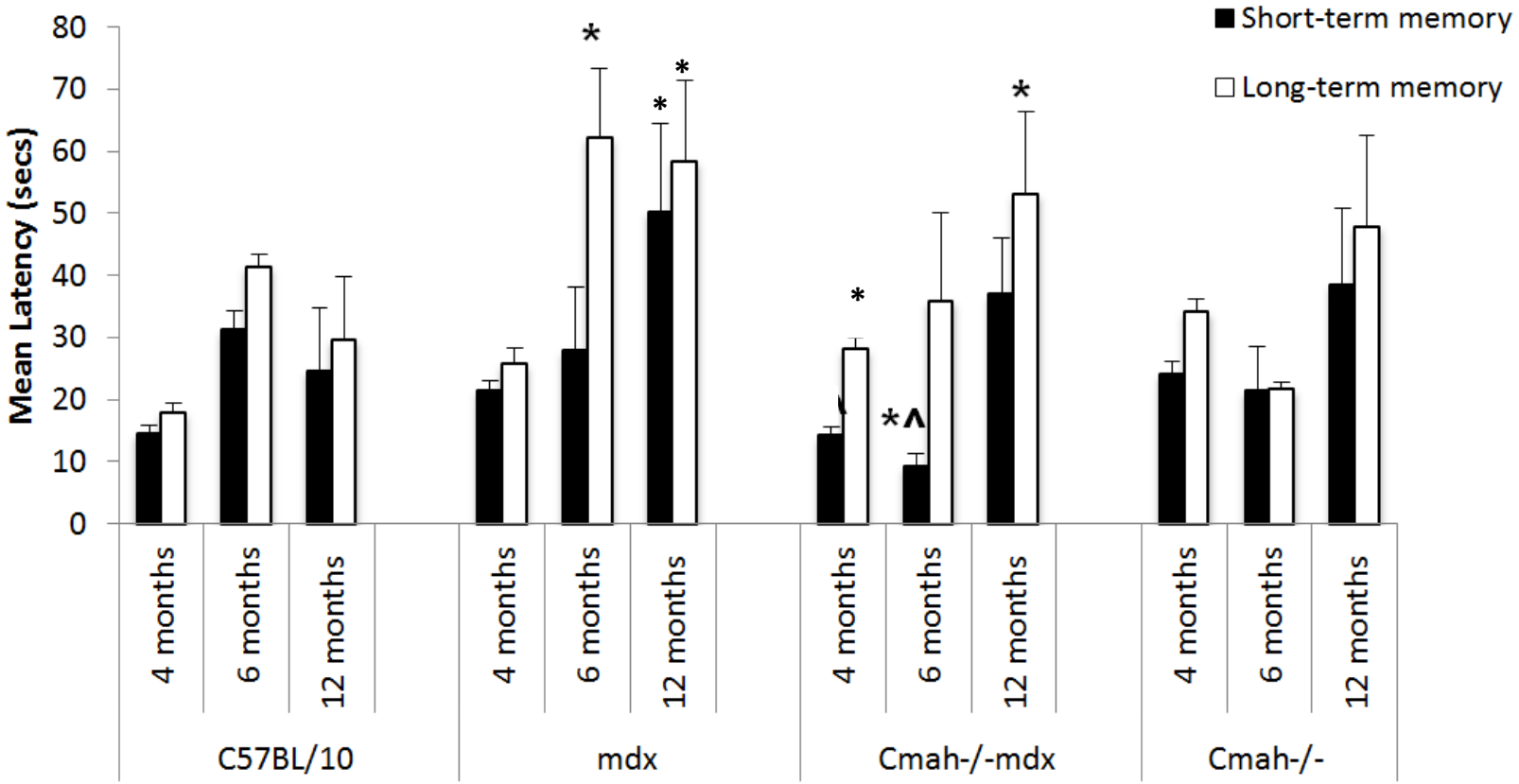

Figure 4.6: Short- and long-term memory retention on the Barnes maze test. Short-term and long-term memory were assessed on day five (probe trail 1) and day twelve (probe trial 2) respectively. A single trial was given to each mouse on the Barnes maze test and the primary and total latency, to find the target hole, were evaluated. Data are presented as mean ± SEM, *p<0.05 vs control *C57BL/10* mice, ^p<0.06 vs *mdx* mice. For each time point n=8 mice/genotype.

4.2.6.2 Mean number of errors before locating the target hole

The number of errors, before the mouse located the target hole, was measured for short- and long-term memory trials. The *mdx* mice had the largest mean number of errors between 4 and 12 months old, when locating the target hole, compared to all other genotypes for both short- and long-term memory. The number of errors also increased with increasing age in the *mdx* mice (Figure 4.7). In the *mdx* mice the number of errors declined between 6 and 12 months old (for long-term memory assessment, 23±3 errors and 16±2 errors respectively) ($p>0.05$); this may be due to the increased freezing response exhibited by *mdx* mice at 12 months old, resulting in reduced exploration of the maze. An increase in the number of errors was seen in the *Cmah-/-mdx* mice between 4 and 12 months old, for both short- and long-term memory. On average the *Cmah-/-* mice made the fewest errors between 4 and 12 months old, for both short- and long-term memory (Figure 4.7) during the Barnes maze test.

Control *C57BL/10* mice showed a slight increase in the number of errors between 4 and 12 months old for short-term memory, 3±4 errors and 8±1 error respectively. This was not seen for long-term memory, where the number of errors decreased between 4 and 12 months old, 10±4 errors and 9±1 error respectively (Figure 4.7).

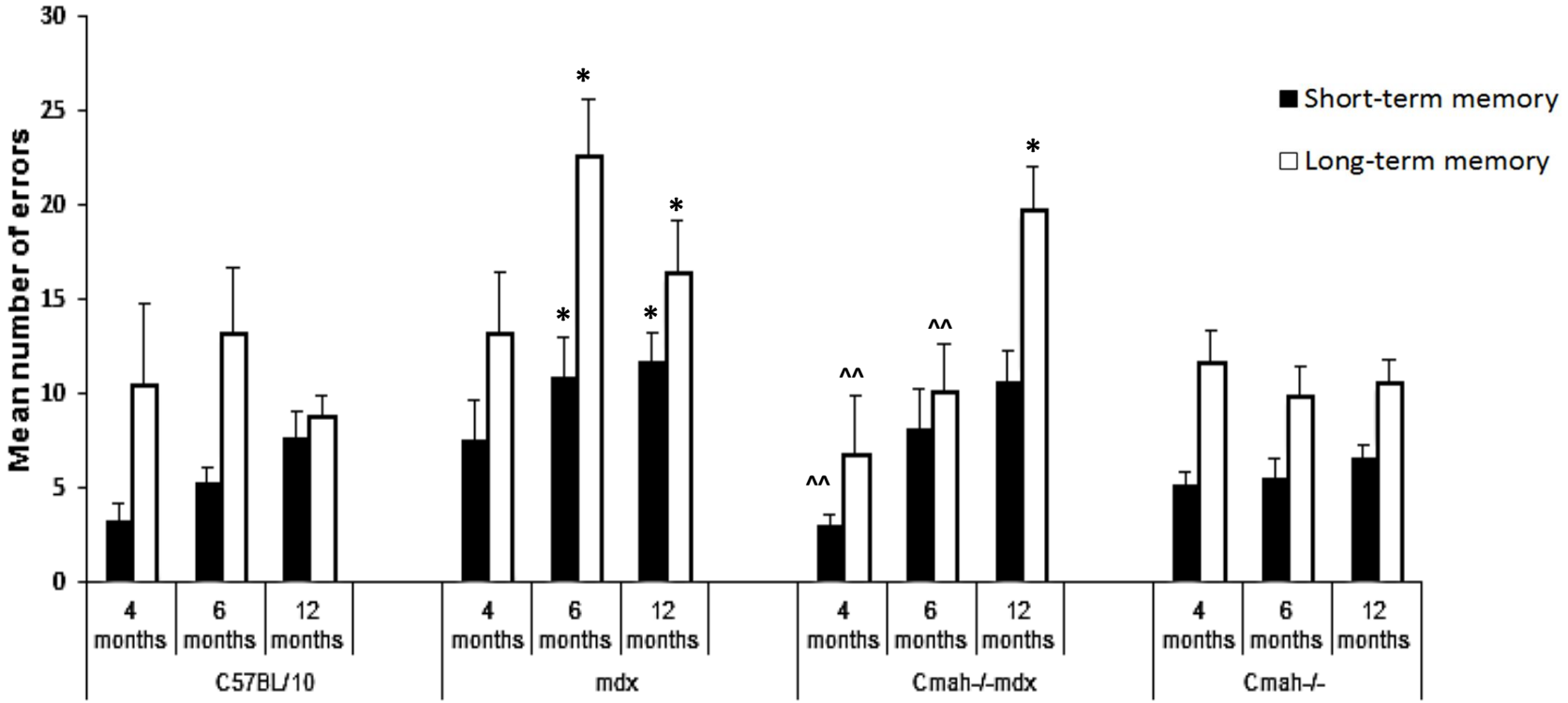

Figure 4.7: Bar graph displaying mean number of errors, during short- and long-term memory trails, between 4 and 12 months old. The *mdx* mice had the largest number of errors between 4 and 6 months old for both short- and long-term memory assessment during the Barnes maze test. At 12 months old both DMD mouse models displayed increased numbers of errors compared to control *C57BL/10* and *Cmah-/-* mice for short- and long-term memory. Data presented as mean ± SEM, *p<0.05 vs control *C57BL/10* mice, ^p<0.05, ^^P<0.01 vs *mdx* mice. For each time point n=8 mice/genotype.

4.2.6.3 Success score

The success score is calculated by multiplying the hole value by the number of nose pokes (Figure 4.1). The highest success score was recorded during the short-term memory probe trial for all genotypes (Figure 4.8). The *mdx* mice had the lowest recorded success score for both short- and long-term memory at all time points. The success score in the *mdx* mice decreased between 4 and 12 months old for both short- and long-term memory. At 4 months old, the *mdx* mice had a short-term memory success score of 99±3 and 83±1 for long-term memory (Figure 4.8). Whereas at 12 months old the *mdx* mice had a shot-term memory success score of 75±1.5 and 53±1 for long-term memory ($p<0.05$). In contrast, the control *C57BL/10* mice had a success score of 136±3 for short-term memory and 105±2 for long-term memory. Interestingly the *Cmah-/-mdx* mice had the highest success score for short-term memory between 4 and 6 months old, higher than that recorded for control *C57BL/10* mice (146±4 and 136±1, respectively) (Figure 4.8). The *Cmah-/-* mice had slightly lower success scores to those of control *C57BL/10* mice between 4 and 12 months old (125±2 and 80±1 for short-term memory).

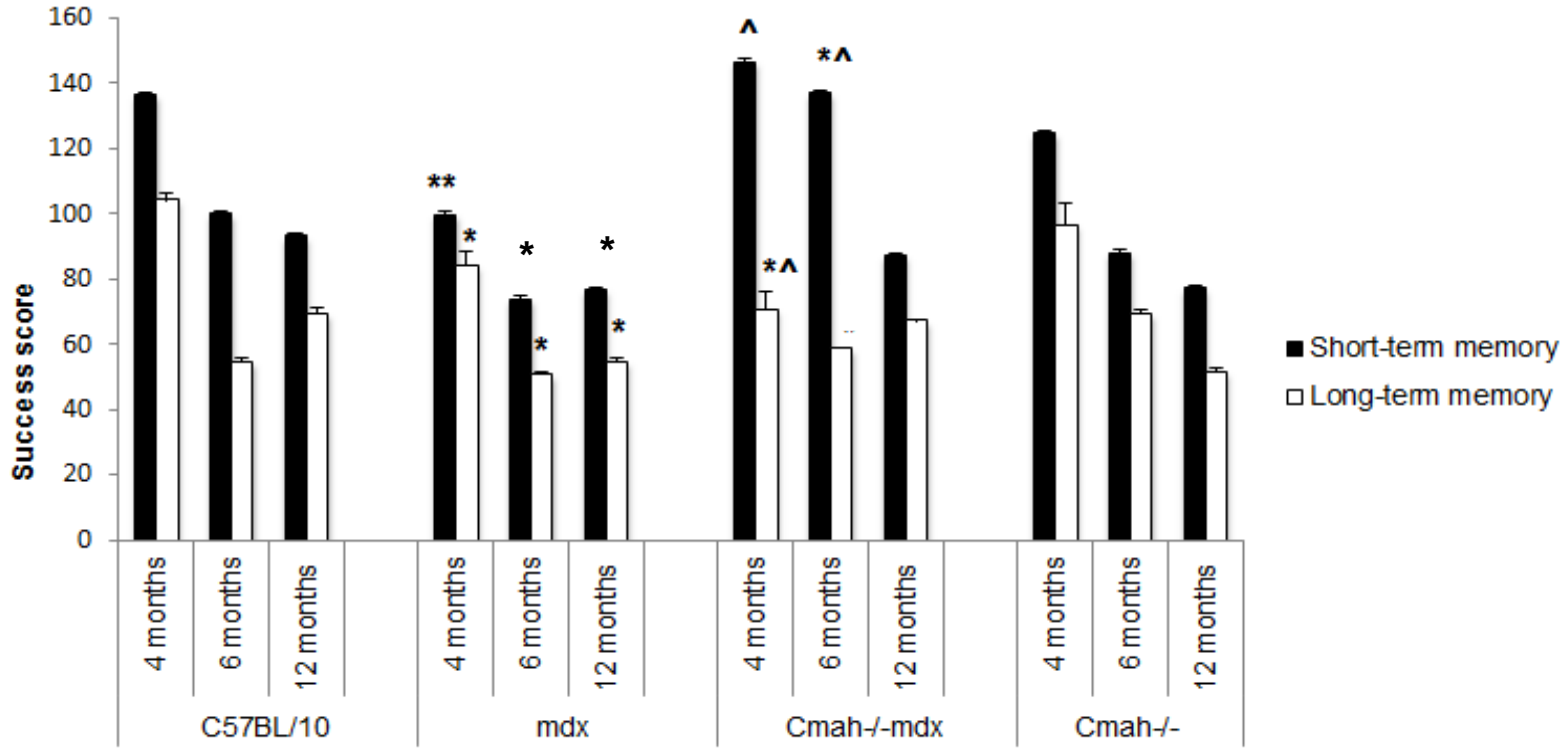

Figure 4.8: Success score (hole value multiplied by the number of head pokes) observed during short- and long-term memory retention trials. The highest success scores were observed during the short-term memory retention trials across all genotypes on the Barnes maze test. The mdx mice had the lowest success score, at all time points, for both short- and long-term memory. Data are presented as mean ± SEM, p*<0.05, **p<0.01 vs control *C57BL/10* mice, ^p<0.05 vs *mdx* mice. For each time point n=8 mice/genotype.

4.2.6.4 Preference for the target hole

During the probe trials a preference for the target hole was measured by recording the number of nose pokes the mice made into the target and other holes (Figure 4.1). At 4 months old during the short-term memory assessment the *Cmah-/-mdx* mice had the highest preference for the target hole, although the other genotypes also showed a significant preference for the target hole (Figure 4.9). At 4 months old the mdx mice showed the lowest preference for the target hole during the long-term memory assessment (Figure 4.9). At 6 months old control *C57BL/10* mice had the largest preference for the target hole. *Mdx* mice showed the lowest number of nose pokes into the target hole during both the short- and long-term memory assessment (Figure 4.10). At 12 months old, again the control *C57BL/10* mice showed the highest preference for the target hole, *mdx* and *Cmah-/-mdx* mice showed a reduced preference for the target hole (Figure 4.11). During the long-term memory assessment the *mdx* mice were least active at 12 months old, due to increased anxiety-related behaviour and freezing response, and had the fewest number of nose pokes into the target hole (Figure 4.11).

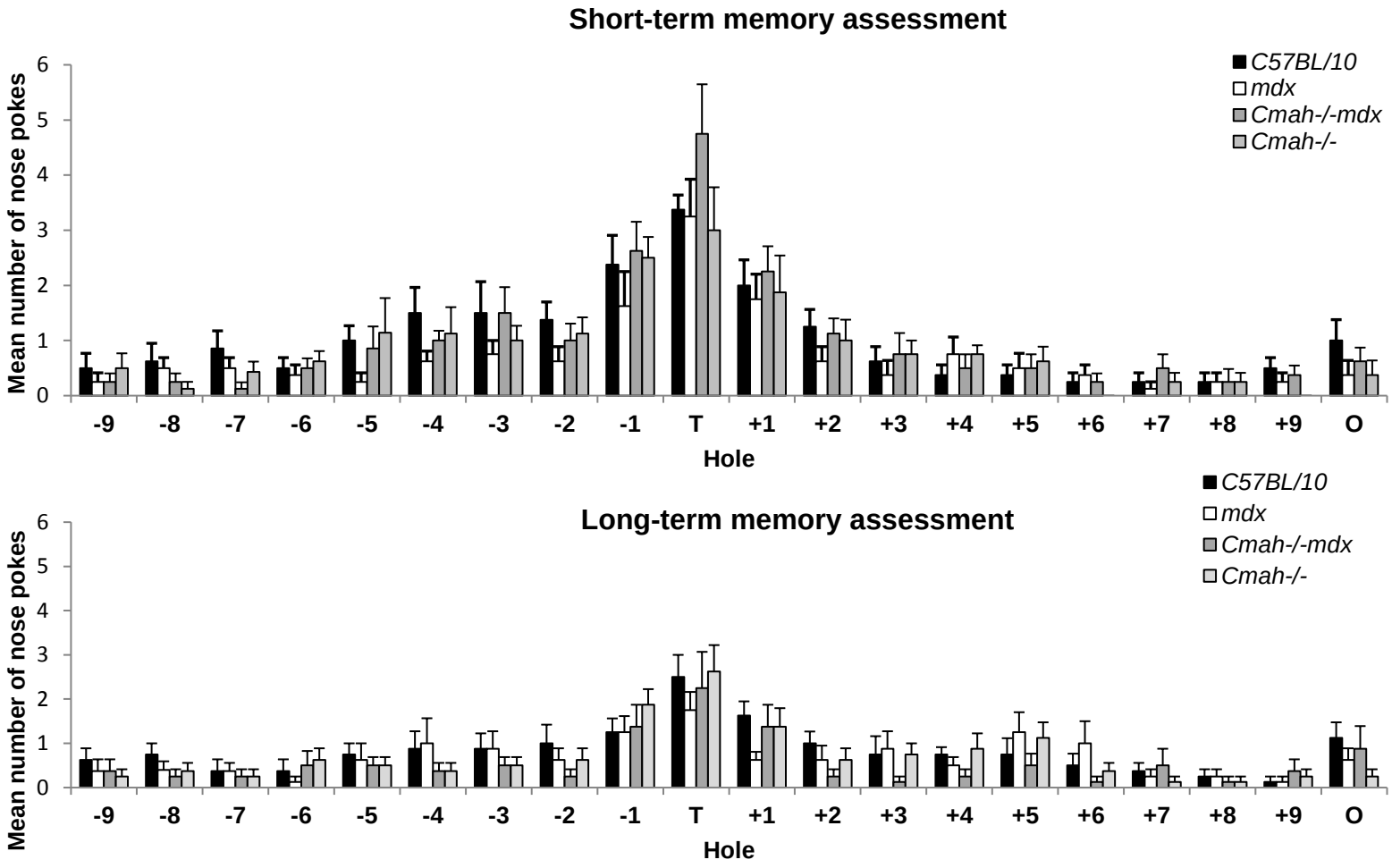

Figure 4.9: Short- and long-term assessment for mean number of nose pokes into the target hole at 4 months old. The *mdx* mice displayed the lowest number of target nose pokes during both short- and long- term memory assessment, (n=8 mice per genotype). Data presented as mean ± SEM.

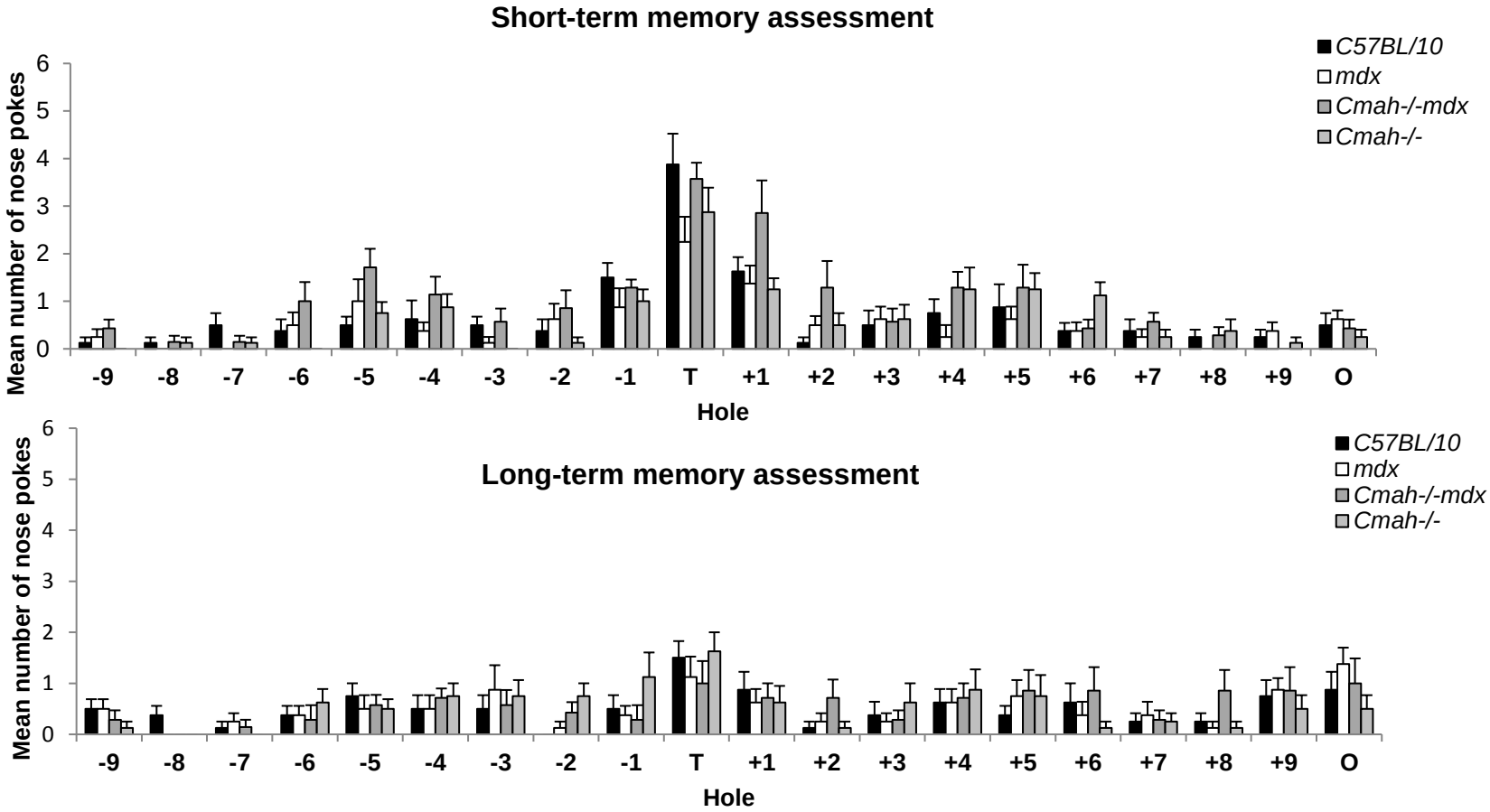

Figure 4.10: Short- and long-term assessment for mean number of nose pokes into the target hole at 6 months old. The *mdx* mice displayed the lowest number of target nose pokes during both short- and long- term memory assessment, (n=8 mice per genotype). Data presented as mean ± SEM.

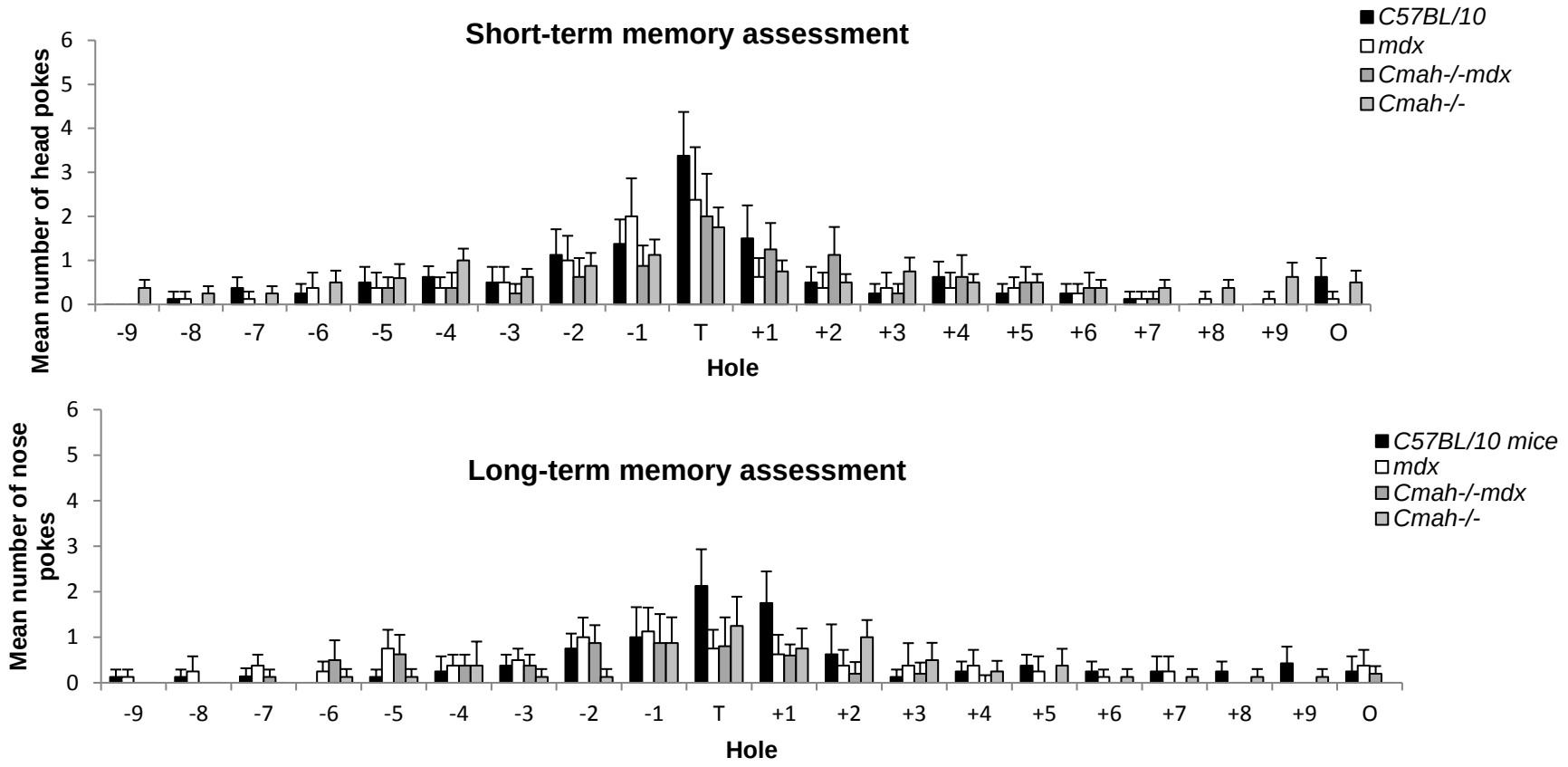

Figure 4.11: Short- and long-term assessment for mean number of nose pokes into the target hole at 12 months old. The *mdx* mice displayed the lowest number of target nose pokes during long- term memory assessment, (n=8 mice per genotype). Data presented as mean ± SEM.

4.2.7 Search strategy

During training days 1-4 the search strategy used to locate the target hole was recorded for each mouse. A direct strategy was when the mouse moved directly to the target hole or adjacent hole before visiting the target hole (≤2 errors). A serial search strategy was where the target hole was located by searching holes adjacent to one another in a clockwise or counter clockwise direction. A mixed search strategy was where the hole searches were separated by crossing through the centre of the maze or unorganised searching.

The direct search strategy was employed the most by the control *C57BL/10* mice between 4 and 12 months old (Figure 4.12). The *mdx* mice utilised the direct search strategy the least between 4 and 12 months old and favoured the mixed search strategy (Figure 4.12). The serial search strategy was used the most at the 12 month old time point across all genotypes. Interestingly at 6 months old the *Cmah-/-mdx* mice favoured a direct search strategy (Figure 4.12). This is also when the *Cmah-/-mdx* mice had the lowest mean latency to target for both short- and long-term memory.

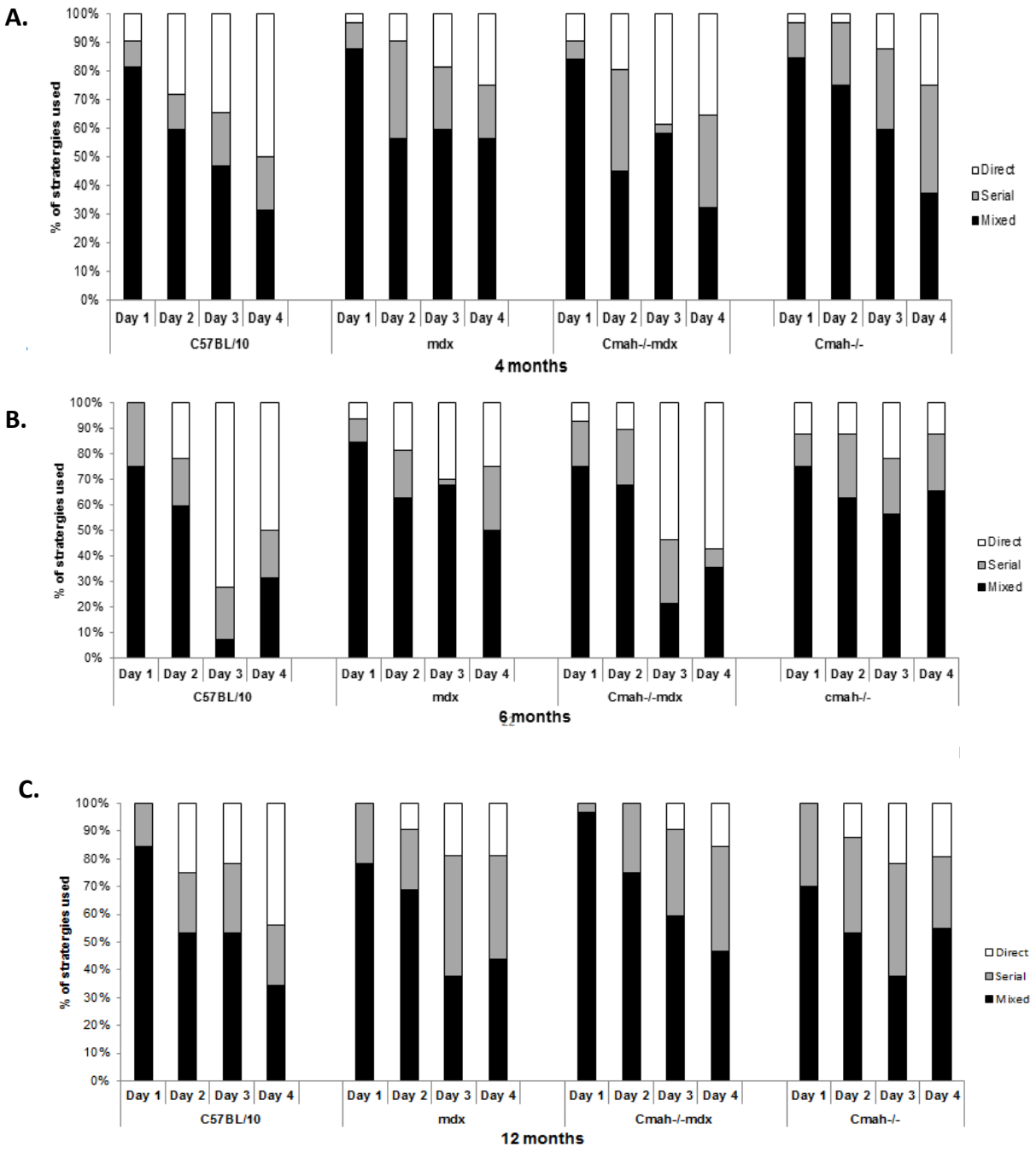

Figure 4.12: Search strategies used during the acquisition phase of the Barnes maze test. Each trial was categorised into different search strategies (1) direct- moving directly to the target hole or adjacent hole before visiting the target hole (≤2 errors); (2) serial- target hole was located by searching holes adjacent to one another in a clockwise or counter clockwise direction; (3) mixed- hole searches separated by crossing through the centre of the maze or unorganized searching. Data are shown as total percentage of trials in which each strategy was used. **A.** Search pattern at 4 months old. **B.** Search pattern at 6 months old and **C.** Search pattern at 12 months old. At all ages n=8 mice per genotype. Overall, younger mice favoured a direct search strategy, whereas older mice employed a mixed search strategy more often.

4.2.7.1 Time spent in target quadrant

During the short-term memory probe trial the time spent in the target quadrant (TQ) was recoded for each mouse between 4 and 12 months old (Figure 4.13). The *mdx* mice spent less time in the TQ as they got older (55±9 seconds at 4 months old, 36±4 seconds at 6 months old and 32±5 seconds at 12 months old). The control *C57BL/10* mice spent a similar amount of time in the TQ between 4 and 6 months old (46±4 seconds and 41±6 seconds, respectively) and an increased amount of time in the TQ at 12 months old (59±6 seconds) (Figure 4.13). This was the same for the *Cmah-/-mdx* mice, who spent 69±4 seconds in the TQ at 12 months old. The *Cmah-/-* mice also spent less time in the TQ between 4 and 6 months old, however, this was not found to be significant until 12 months old (27±7 seconds).

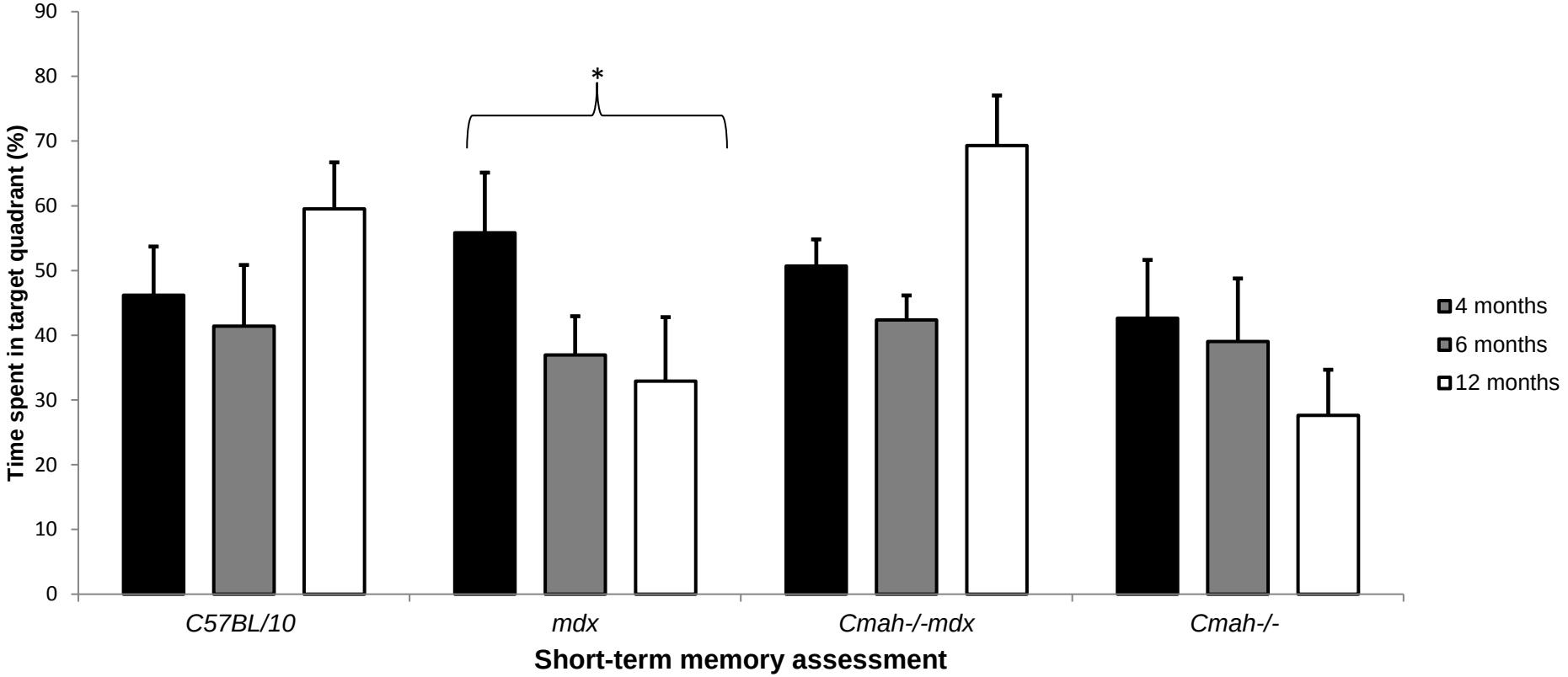

Figure 4.13: Bar graph displaying the percentage of time that mice spent in the target quadrant (TQ) during short-term memory assessment between 4 and 12 months old. The *mdx* mice spent considerably less time in the TQ as they got older. Interestingly control *C57BL/10* mice spent a much longer time in the TQ as they got older. Data presented as mean ± SEM, *p<0.05 (n=8 mice per genotype at each time point).

4.3 Novel object recognition

4.3.1 Basis for novel object recognition (NOR) task

Ennaceur and Delacour provided the preliminary development for the basis of the NOR task (Ennaceur and Delacour, 1987) (Ennaceur and Delacour, 1988), (Ennaceur *et al.*, 2005). The NOR task is based on the natural propensity of animals to explore new environments (Ennaceur and Delacour, 1987). In brief, mice explore two identical objects (for 3 minutes), before a delay for memory consolidation of these objects (where mice are placed back into their home cage, in this case for 15 minutes). One of the objects is then replaced by a novel object and a familiar object remains. The natural response of animals is to then recognise the novel object and thus exhibit a preference for this object, depicted by more time spent with the novel object compared to the familiar object (in the 3 minute allocated time period) (Figure 4.14). More specifically, the task measures visual memory recognition abilities of animals (Ennaceur and Delacour, 1987). Cognitively impaired animals will not recognise the novel object as novel and thus show no preference for this object (no visual recognition memory). The same time points used in Barnes maze testing were also employed for the NOR task (4, 6, and 12 months old).

4.3.2 Novel object recognition at 4 months old

The NOR task was first performed on mice aged 4 months old. During the sample phase all mice spent equal amounts of time with the two identical objects regardless of genotype (Figure 4.15). Interestingly, overall *mdx* mice spent less time with the objects when compared to the other genotypes who showed comparable amounts of time spent with the two identical objects (Figure 4.15). During the choice phase of the NOR task the *mdx* mice showed significant preference for the familiar object (11±2 seconds) and spent significantly longer exploring the familiar object compared to the novel object (6±1 second) (Figure 4.16).

In contrast the control *C57BL/10*, *Cmah-/-mdx,* and *Cmah-/-* mice all showed a preference for the novel object with the *Cmah-/-* mice showing the highest preference for the novel object (15±2 seconds). The D2 ratio, calculated based

on the amount of time the mouse spent with the novel and familiar objects during the choice phase, showed that control *C57BL/10*, *Cmah-/-mdx*, and *Cmah-/-* mice spent considerably longer with the novel object than they did with the familiar object (positive D2 ratio), whereas the *mdx* mice spent significantly longer exploring the familiar object (negative D2 ratio) (Figure 4.17). Surprisingly the *Cmah-/-mdx* mice were most active at 4 months old, spending the highest amount of time with the objects compared to both control *C57BL/10* and *Cmah-/-* mice.

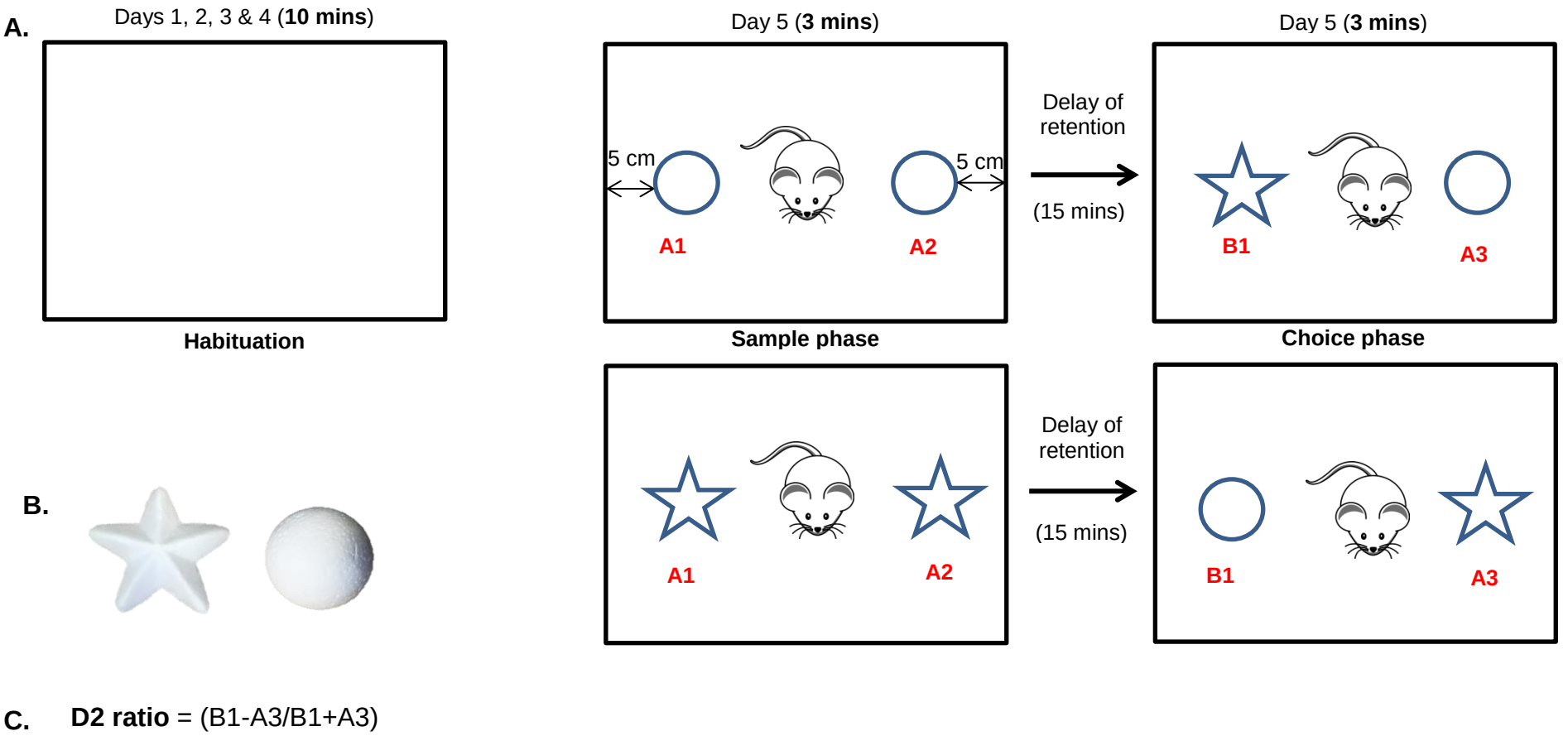

C. **D2 ratio** = (B1-A3/B1+A3)

Figure 4.14: A: Summary of the orientation of the objects in the novel object recognition (NOR) task. A. The diagram shows two possible sample phases and two possible choice phases. The orientation and choice of objects varied between all four genotypes at all three time points. **B.** The two polystyrene objects used during the test phase. **C.** Formula for calculating the D2 ratio recorded on the test day. Adapted from (Ennaceur *et al.*, 2005).

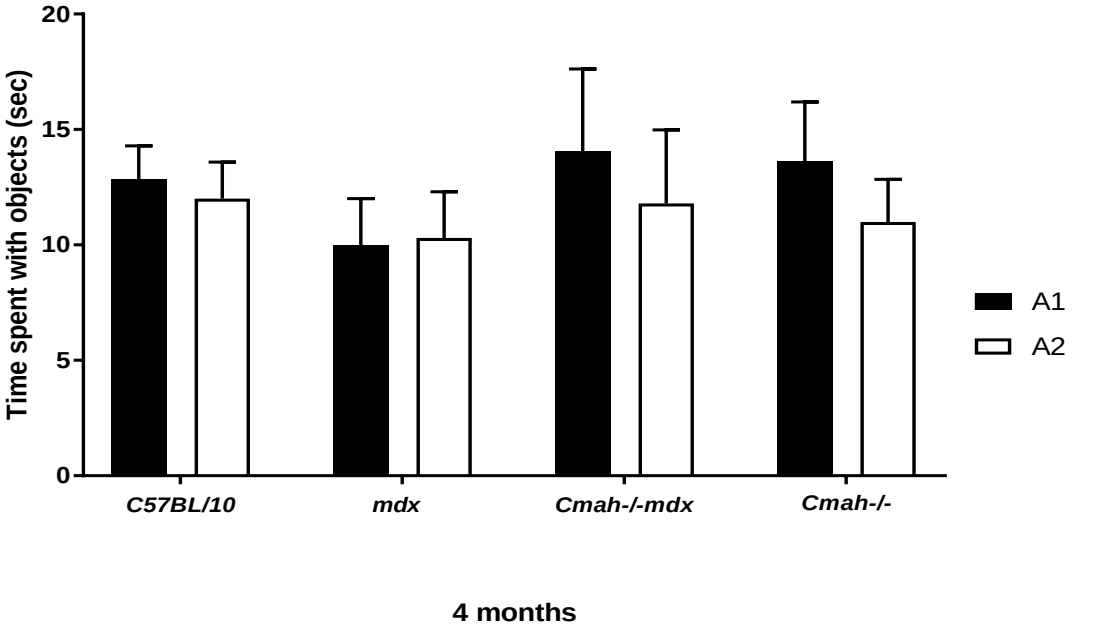

Figure 4.15: Time spent with objects in the sample phase of the novel object recognition (NOR) task at 4 months old. Graph shows that in all genotypes, mice showed no preference for either of the identical objects at 4 months old, n=8/genotype. Data presented as mean ± SEM.

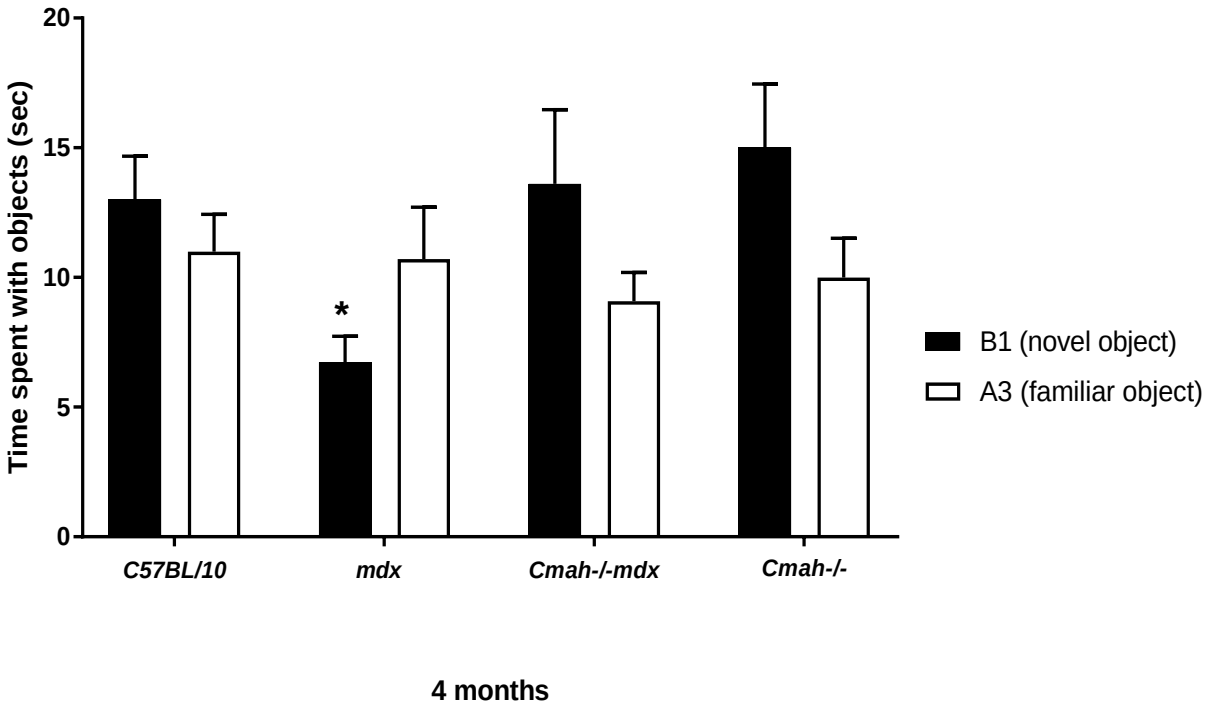

Figure 4.16: Times spent with familiar and novel objects in the choice phase of the novel object recognition (NOR) task at 4 months old. Control *C57BL/10*, *Cmah-/-mdx,* and *Cmah-/-* mice showed a preference for the novel object whereas *mdx* mice showed a higher preference for the familiar object, n=8/genotype. Data presented as mean ± SEM, *p<0.05 vs control *C57BL/10* mice.

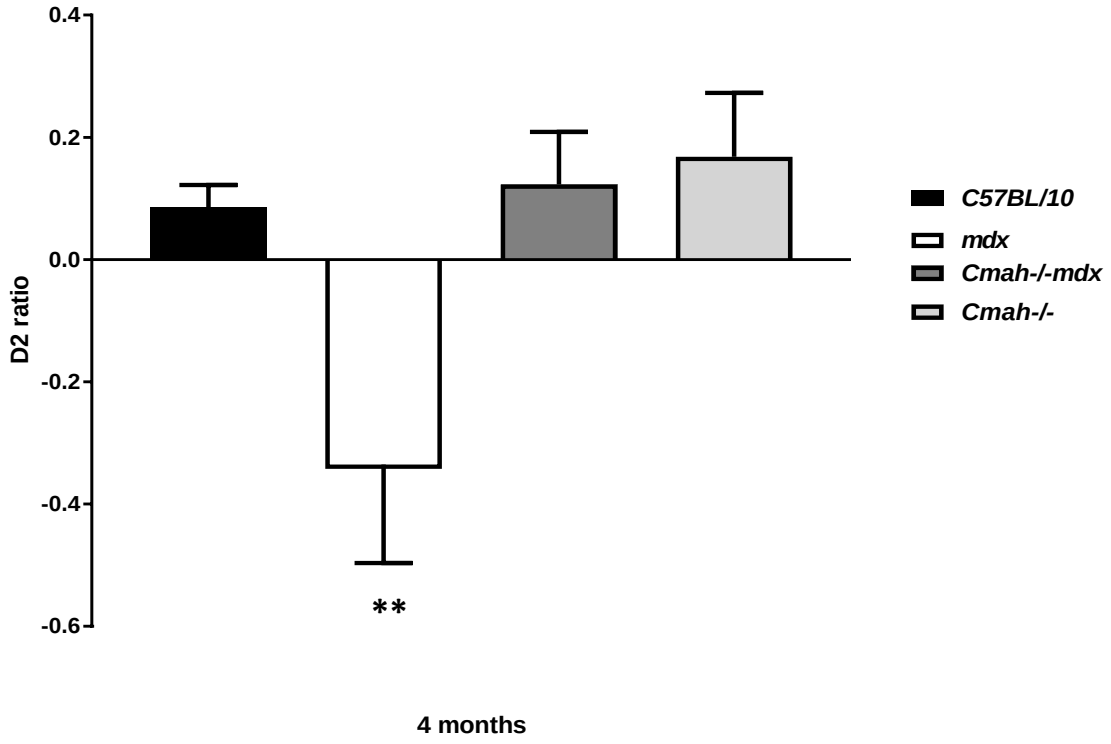

Figure 4.17: D2 ratios expressing preference for the novel and familiar objects in the choice phase of object recognition task at 4 months old. With the exception of the *mdx* mice, all mice showed a significant preference for the novel object at 4 months old, n=8/genotype. Data presented as mean ± SEM, *p<0.05, **p<0.01 vs control *C57BL/10* mice.

4.3.3 The novel object recognition task at 6 months old

The NOR task was also performed on mice aged 6 months old. During the sample phase all mice spent equal amounts of time with the two identical objects regardless of genotype (Figure 4.18), as was the case at 4 months old. Again the *mdx* mice spent less time with the objects when compared to the other genotypes, who showed comparable amounts of time spent with the two identical objects (Figure 4.18). The *Cmah-/-mdx* mice again were the most active mice, spending the highest amount of time exploring the identical objects. During the choice phase of the NOR task the *mdx* mice showed a significant preference for the familiar object (17±5 seconds) and spent significantly longer exploring the familiar object compared to the novel object (7±1.5 seconds) (Figure 4.19). In contrast, the control *C57BL/10*, *Cmah-/-mdx*, and *Cmah-/-* mice all showed preference for the novel object with the *Cmah-/-* mice showing the highest preference for the novel object (23±3 seconds). The D2 ratio showed that control *C57BL/10*, *Cmah-/-mdx,* and *Cmah-/-* mice spent considerably longer with the novel object than they did with the familiar object (positive D2 ratio), whereas the *mdx* mice spent significantly longer exploring the familiar object (negative D2 ratio) (Figure 4.20). The control *C57BL/10* mice had the highest D2 ratio, thus showing the best overall object recognition memory at 6 months old (Figure 4.20).

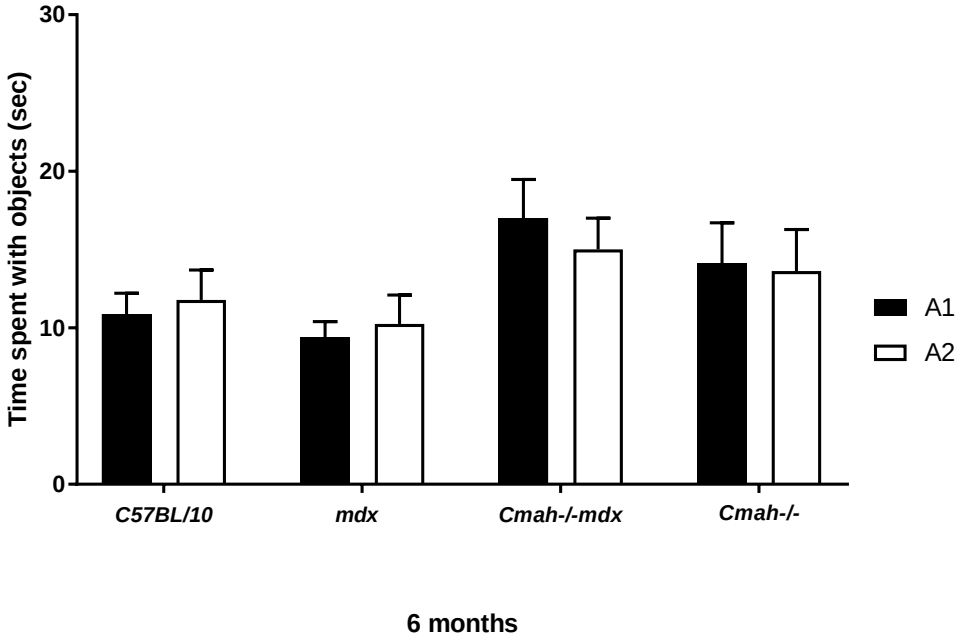

Figure 4.18: Time spent with objects in the sample phase of the novel object recognition (NOR) task at 6 months old. Graph shows that in all genotypes, mice showed no preference for either of the identical objects at 6 months old, n=8/genotype. Data presented as mean ± SEM.

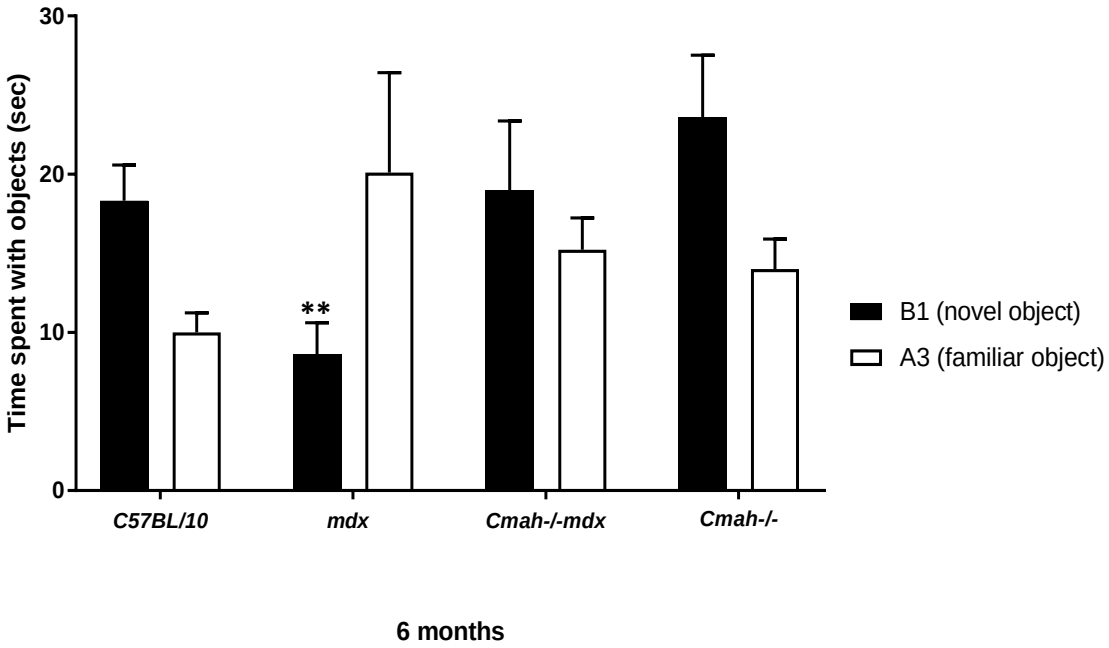

Figure 4.19: Times spent with familiar and novel objects in the choice phase of the novel object recognition (NOR) task at 6 months old. Control *C57BL/10*, *Cmah-/-mdx,* and *Cmah-/-* mice showed a preference for the novel object whereas *mdx* mice showed a higher preference for the familiar object, n=8/genotype. Data presented as mean ± SEM, *p<0.05, **p<0.01.

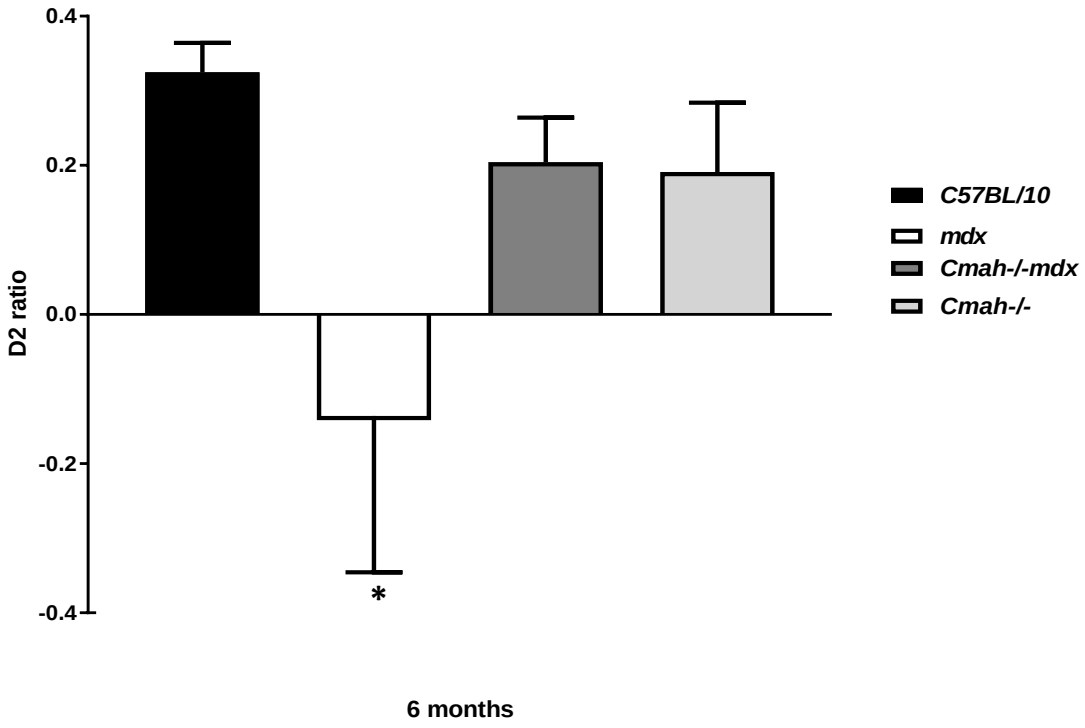

Figure 4.20: D2 ratios expressing preference or no preference for the novel and familiar objects in the choice phase of object recognition task at 6 months old. With the exception of the mdx mice, all mice showed a significant preference for the novel object at 6 months old. Objects were either polystyrene sphere or star and varied to avoid condition place preference effects, n=8/genotype. Data presented as mean ± SEM, *p<0.05 vs control *C57BL/10* mice.

4.3.4 Novel Object Recognition task at 12 months old

Finally, the NOR task was performed on mice aged 12 months old. During the sample phase all mice spent equal amounts of time with the two identical objects regardless of their genotype (Figure 4.21). This was the same effect as seen at 4 and 6 months old. Although the *Cmah-/-mdx* mice spent slightly longer with the A1 object than the A2 object, this was not found to be significant ($p>0.05$) (Figure 4.21). Interestingly, the *Cmah-/-mdx* mice did not display the increased activity for exploring the objects like they did at 4 and 6 months old. During the choice phase of the NOR task, the *mdx* mice showed a significant preference for the familiar object (9±2 seconds) (Figure 4.22). This effect was the same as that seen at 4 and 6 months old, but at 12 months old the *mdx* mice spent considerably less time exploring any of the objects.

In contrast to the *mdx* mice, the control *C57BL/10*, *Cmah-/-mdx,* and *Cmah-/-* mice all showed a preference for the novel object, with the control *C57BL/10* mice showing the highest preference for the novel object (24±2 seconds). The D2 ratio showed that control *C57BL/10*, *Cmah-/-mdx,* and *Cmah-/-* mice spent considerably longer with the novel object than they did with the familiar object (positive D2 ratio) whereas the *mdx* mice spent significantly longer exploring the familiar object (negative D2 ratio) (Figure 4.23). The control *C57BL/10* mice had the highest D2 ratio, showing the best overall object recognition memory. The *Cmah-/-mdx* and *Cmah-/-* mice both showed a reduced D2 ratio compared to those at 4 and 6 months old (Figure 4.23). The anxiety of the *mdx* mice had increased significantly at 12 months old, as represented by the reduced amount of time the mice spent exploring the objects and the increased amount of time the animals sat in the corners of the NOR arena (Figure 4.24 and Figure 4.25). This effect, of increased anxiety-related behaviour, was the same as that observed on the Barnes maze test at 12 months old, resulting in a reduced performance (Figure 4.8).

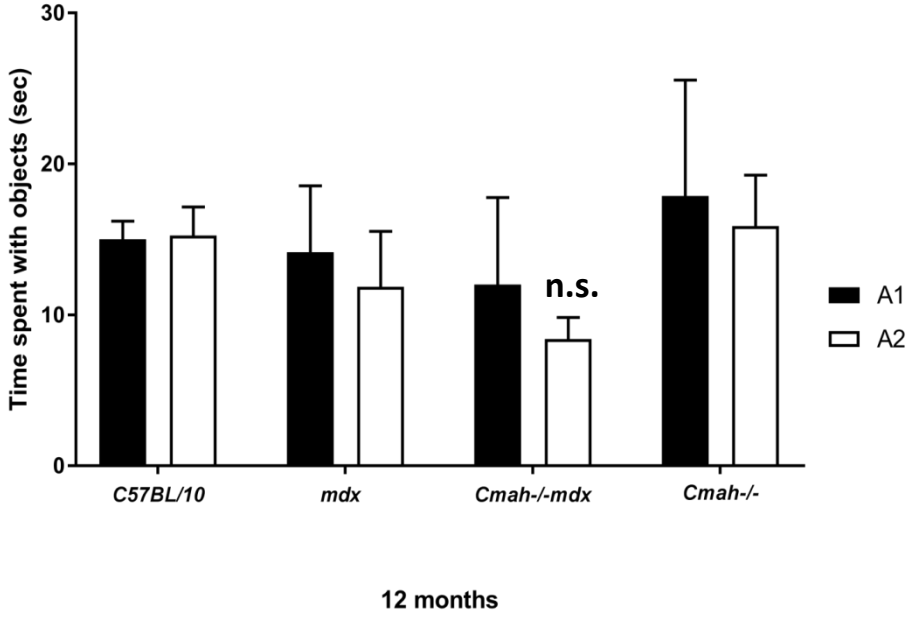

Figure 4.21: Time spent with objects in the sample phase of the novel object recognition (NOR) task at 12 months old. Graph shows that in all genotypes mice showed no preference for either of the identical objects at 12 months old. Data presented as mean ± SEM.

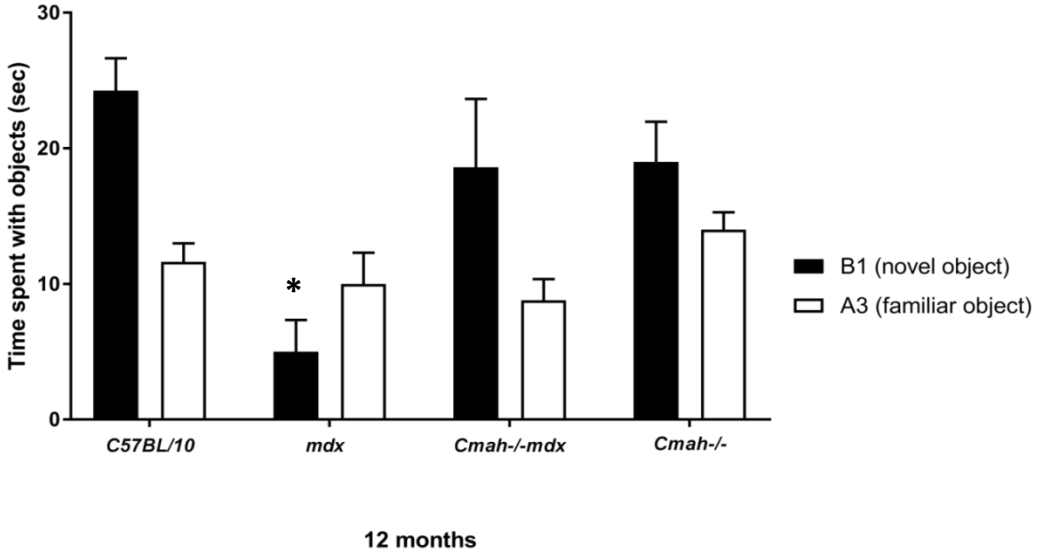

Figure 4.22: Times spent with familiar and novel objects in the choice phase of the novel object recognition (NOR) task at 12 months old. Control *C57BL/10*, *Cmah-/-mdx*, and *Cmah-/-* mice showed a preference for the novel object whereas *mdx* mice showed a higher preference for the familiar object, n=8/genotype. Data presented as mean ± SEM, *p<0.05.

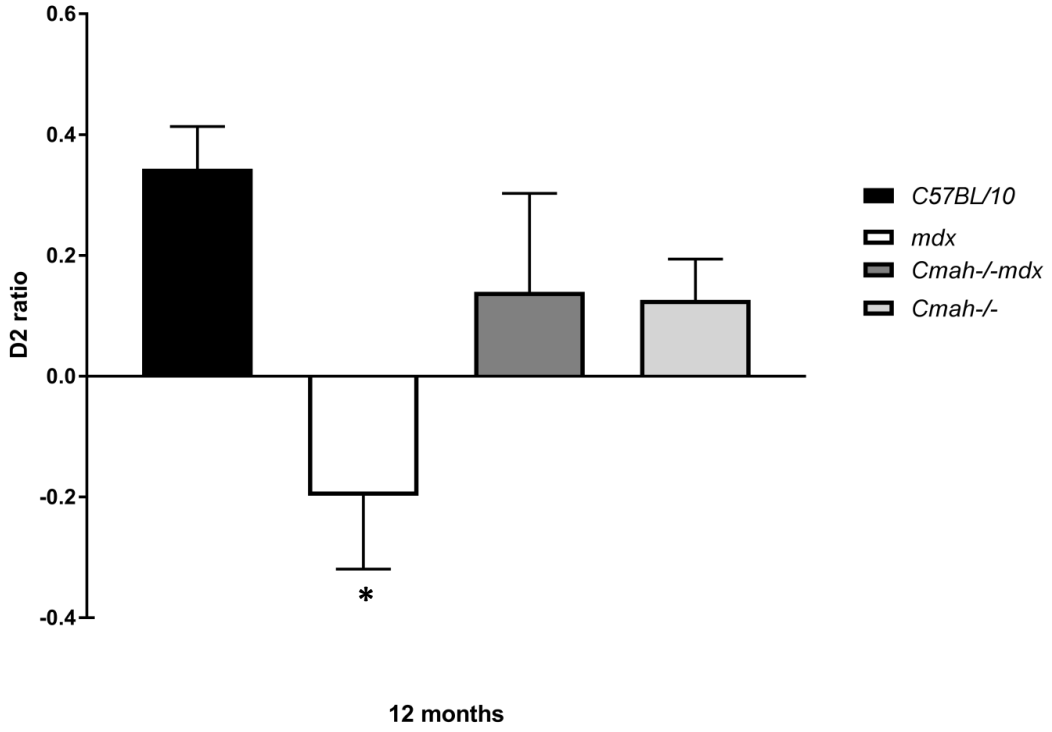

Figure 4.23: D2 ratios expressing preference or no preference for the novel and familiar objects in the choice phase of object recognition task at 12 months old. With the exception of the *mdx* mice, all mice showed a significant preference for the novel object at 12 months old. Objects were either polystyrene sphere or star and varied to avoid condition place preference effects, n=8/genotype. Data presented as mean ± SEM, *p<0.05 vs control *C57BL/10* mice.

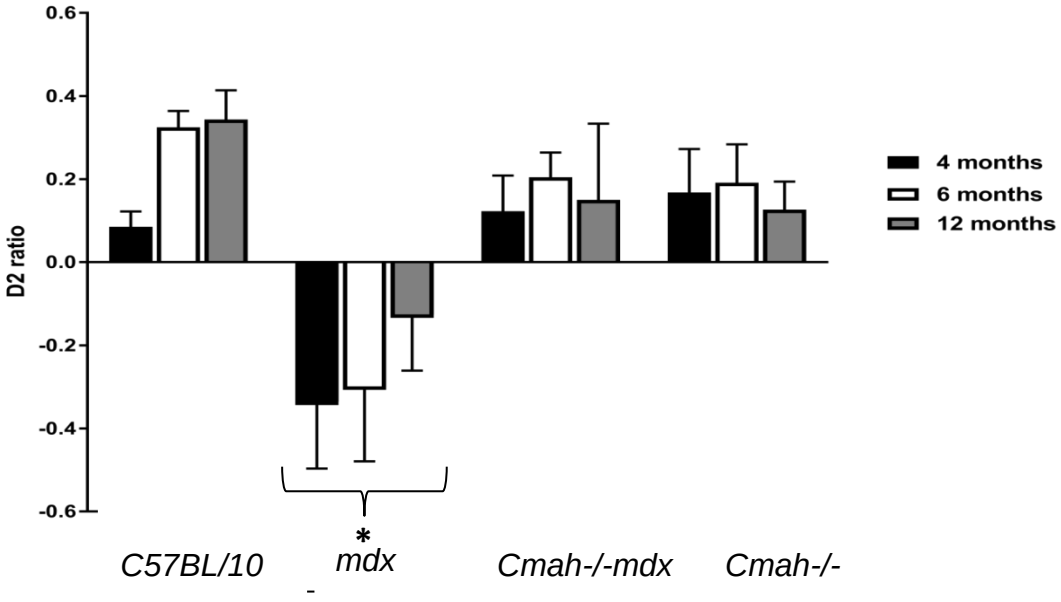

Figure 4.24: Comparison of D2 ratios between 4 and 12 months old. The control *C57BL/10* mice had an increasing D2 ratio between 4 and 12 months old, demonstrating an increased preference for the novel object. The *mdx* mice showed an increased preference for the familiar object at all time points; however, the D2 ratio increased over time, as the mice spent less time exploring the object in total. Data presented as mean ± SEM, *p<0.05, vs control *C57BL/10* mice.

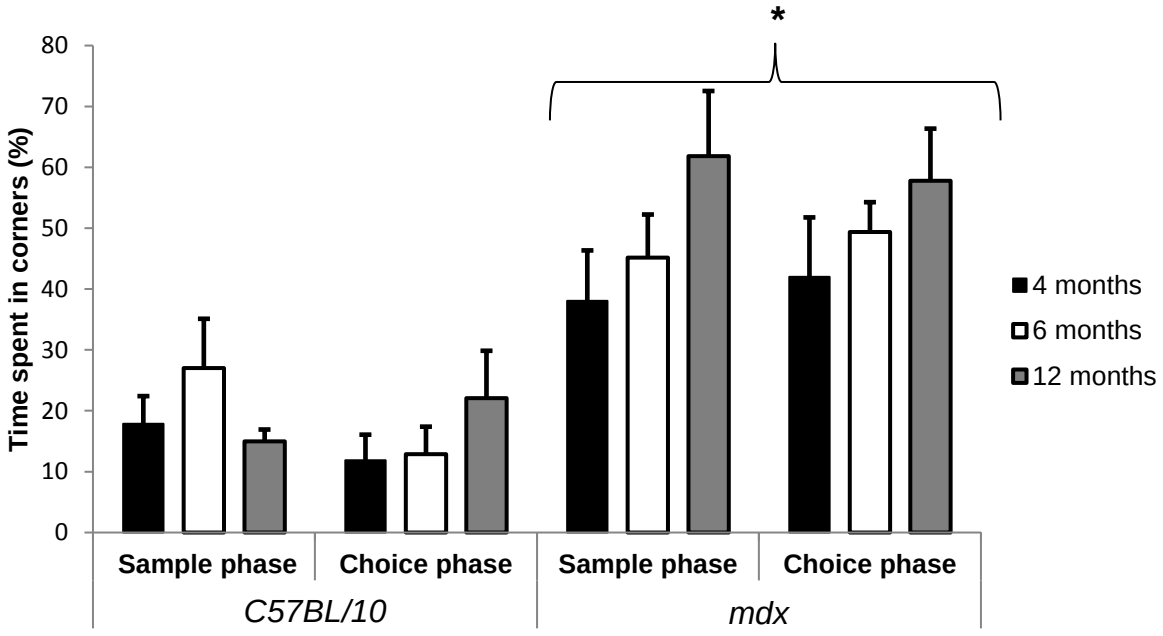

Figure 4.25: Bar graph displaying the amount of time that mice spent in the corners of the novel object recognition (NOR) arena between 4 and 12 months old. The control *C57BL/10* mice spent considerably less time in the corners of the NOR arena during both the sample and choice phase compared to the *mdx* mice. The *mdx* mice spent significantly longer in the corners of the NOR arena during the sample and choice phases of the NOR task and this time increased with increasing age. Data presented as mean ± SEM, *p<0.05 vs control *C57BL/10* mice.

4.4 Discussion

Memory tests are important indices of brain functions that control for rodents' behaviour. Many memory tasks require external forces (e.g. electric shocks) or intrinsic forces (e.g. hunger and thirst) to trigger the responses, potentially affecting the natural behaviour. High levels of anxiety have previously been reported in *mdx* mice (Sekiguchi *et al.*, 2009), consequently no aversive stimulus was employed in either of our behavioural studies.

Unlike DMD patients, adult *mdx* mice do not show obvious impairments in motor ability, presumably as a consequence of differences between mice and men regarding body size/architecture and a better regenerative muscle capacity in mice (Turk *et al.*, 2005). Only when the endurance of *mdx* mice is challenged does muscle impairment become apparent, for example during the endurance hanging test (van Putten *et al.*, 2012). The Barnes maze test and the NOR task are not described as strenuous activity tests, and thus were deemed acceptable behavioural assays to employ for the monitoring of a potential progressive cognitive dysfunction in DMD mouse models up to 12 months old. Although we did not use equipment necessary to directly measure mouse speed to reach the target hole, we do not think that the muscle weakness of DMD mice would considerably impair their ability to perform the Barnes maze test. In addition, the *Cmah-/-mdx* mice outperformed the control mice in multiple parameters and they are supposed to have a more severe muscle pathology to that of the *mdx* mouse (Chandrasekharan *et al.*, 2010).

On the cellular level, dystrophin loss causes alterations in calcium homeostasis and hippocampal neuronal function (Mehler *et al.*, 1992), particularly hippocampal alterations in long-term potentiation (LTP), a form of plasticity widely believed to be critical for memory formation (Vaillend *et al.*, 2002). It is not yet clear whether *mdx* mice have deficits in memory retention. Some studies describe no deficits (Vaillend *et al.*, 1998), but other studies outline some memory retention impairment (Muntoni *et al.*, 1991). One study described how altered expression of full length dystrophin or C-terminal dystrophin proteins in the brain (Dp140 and Dp71) did not markedly affect hippocampus-dependent spatial learning and CA1 hippocampal LTP in *mdx* and *mdx*^{3cv} mice aged 3-4

months old (Vaillend *et al.*, 1998). However, recent studies have emphasised that long-term but not short-term hippocampal spatial learning was affected in *mdx* mice (aged 3-5 months) using the water maze (Vaillend *et al.*, 2004), suggesting a normal acquisition of spatial learning but impaired long-term memory capabilities. Studies in female *mdx* mice at 6 months old did not show a memory deficit during the Barnes maze test, as during the initial learning probe trial female *mdx* mice performed similar to control *C57BL/10* mice (Remmelink *et al.*, 2016). The female *mdx* mice did however display an inflexible search strategy during the Barnes maze probe trial reversal learning and a profound impairment in cognitive flexibility during an automated home-cage task (between 15 and 21 weeks old). However, this study did not investigate long-term memory retention ability and investigated female *md*x mice at one time point only (Remmelink *et al.*, 2016). Given the previously established effect of gender difference on cognition in *mdx* mice, our studies investigated the loss of Dp427 on male mouse behaviour only.

In this present study we utilised the Barnes maze test and numerous parameters (primary latency, total latency, primary errors, total errors, search pattern, and time spent in target quadrants) to monitor if cognitive impairment is progressive in DMD mice. It is only with a combination of these parameters that the progressive cognitive dysfunction becomes apparent. The aging control *C57BL/10* mice showed a reduction in their success score (calculated during probe trials) between 4 and 12 months old with the largest reduction detected in long-term memory ability. The number of errors (primary and total errors) also increased with increasing age in control *C57BL/10* mice, but time spent in the target quadrant remained relatively constant between 4 and 12 months old during probe trials. These findings are consistent with previously published data regarding the effect of aging on control mice (*C57BL6J*) behaviour (Shoji *et al.*, 2016), which suggested that impaired spatial and learning memory on the Barnes maze test is evident with increasing age, and further indicates that relatively narrow age differences can produce significant behavioural differences during adulthood in mice. In the *mdx* mice these parameters (success score, number of errors, time spent in the target quadrant) were affected to a greater extent. In particular, the time spent in the target quadrant, during short-term memory probe trial, was significantly reduced between 4 and

12 months old, as was the short-term memory (as shown by a decreasing success score and an increased number of errors). The long-term memory of *mdx* mice appears to show the highest deficit between 4 and 12 months old compared to long-term memory defect of control *C57BL/10* mice.

Long-term memory impairment in DMD has recently been reported (Vaillend *et al.*, 2004) (Chamova *et al.*, 2013). Dp427 appears to play a role in acquisition of associated learning as well as in general processes involved in memory consolidation following the assessment of DMD mice in this current study. Furthermore, it has been reported that long-term spatial memory is a function of the CA1 hippocampal sub-region and that this area has less of a role in short term memories (Vago *et al.*, 2007). Given that the Barnes maze test we performed, highlighted in particular a reduction in long-term memory ability in the *mdx* mice between 4 and 12 months old (and the *Cmah-/-mdx* mice at 12 months), it is likely down to abnormalities in the CA1 field of the hippocampus. A recent study demonstrated a reduced neuronal density in the anterior dorsal hippocampus (CA1 field), highlighting a reduction in pyramidal neurons in the *mdx* mouse, associated with Dp427 loss (Miranda *et al.*, 2016). The CA1 dorsal hippocampus is known to be especially vulnerable to hypoxic insults, which may selectively damage neurons in this subfield, while sparing neurons in the CA3 and DG (Schmidt-Kastner, 2015). *Mdx* mice have also been shown to be more susceptible to hypoxic induced hippocampal damage (Mehler *et al.*, 1992). The long-term memory impairments in *mdx* mice suggest a direct link with the loss of full length dystrophin, therefore affecting all DMD patients. However, previous studies in the *mdx* identified that loss of Dp427 has no effect on perception and gating of sensory input and does not impair spatial working memory performance (*mdx* mice aged 3-4 months old) (Vaillend *et al.*, 2004). Our study has highlighted that whilst at 4 months old spatial learning and memory in the *mdx* mice is comparable to that of control mice as the *mdx* mice age (6 months onwards), spatial learning and memory becomes significantly impaired.

With respect to learning during the Barnes maze test, at 4 months old, the *mdx* mice had a tendency to make an increased number of errors during the first two days of training compared to the control *C57BL/10* mice. However, by day 4 of training at 4 months old the *mdx* mice had comparable parameters (primary and

total errors, primary and total latency) to that of the control *C57BL/10* mice. Interestingly this initial delay in performance has previously been reported in *mdx* mice (Chaussenot *et al.*, 2015). During the first 3 days on the water maze task 4 month old male *mdx* mice had an initial delay in locating the platform, suggesting a transient deficit in procedural learning that could be linked to reduced motor coordination (Chaussenot *et al.*, 2015). Performance (aged 4 months) was comparable during additional training sessions between genotypes, with performance optimisation in the *mdx* mice found to be less efficient, suggesting that defective control processes that normally enable performance optimisation in cognitive tasks is affected by the loss of dystrophin (Chaussenot *et al.*, 2015). The authors suggested that qualitative alterations in learning and memory processes could be masked by these apparently normal/borderline cognitive performances.

Novelty and behaviour has gained much attention and interest from researchers. Novelty can be defined as an alteration from the expected likelihood of an event on the basis of both previous information and internal estimates of conditioned probabilities (Antunes and Biala, 2012). A novel stimulus can affect an animals' behaviour and the NOR task relies on the rodents' innate exploratory behaviour in the absence of externally applied rules or reinforcement (Ennaceur and Delacour, 1987). The preference for the novel object means that presentation of the familiar object exists in the animals' memory (Antunes and Biala, 2012). The recognition of novelty requires more cognitive skills from the subject, relative to tasks measuring exploration of novel environments. The NOR paradigms have been shown to be influenced by both hippocampal and cortical lesions (Buckmaster *et al.*, 2004). It is widely accepted that within the rodent brain the perirhinal cortex plays an important role in object recognition memory, i.e. the ability to evaluate a previously encountered item as familiar depends on the integrity of the medial temporal lobe (Hammond *et al.*, 2004). Other studies in rodents have highlighted the importance of the parahippocampal regions for visual object recognition memory (Antunes and Biala, 2012).

For half the mice the novel object was the sphere and the familiar object was the star, while for the other half the novel object was the star and the familiar

object was the sphere. These modifications were made to reduce object and place preference effects (Ennaceur *et al.*, 2005). These objects have no natural significance for the mice and had never been associated with reinforcement. The *mdx* mice displayed a preference for the familiar object, and were opposed to the novel object, at all time points, which indicates that the *mdx* mice have an impaired recognition memory. Additionally, DMD patients have also demonstrated impairments in visual recognition memory (during Peabody picture vocabulary test) (Anderson *et al.*, 1988). Interestingly, the time spent with the familiar object did not increase over time but the amount of time that the mice spent with the objects in total decreased between 4 and 12 months old. The amount of time the *mdx* mice spent in the corners (frozen) of the NOR arena increased between 4 and 12 months old and is indicative of increased anxiety-related behaviour. The *mdx* mice often sat in the corners of the NOR arena and displayed elevated freezing, sniffing, and rearing compared to the other genotypes. Complete immobilisation of the mouse, except for respiration, was regarded as a freezing response and was most prominent in the *mdx* mice at 12 months old. Interestingly, at 12 months old during the Barnes maze test 2/8 *mdx* mice displayed a complete freezing response (no movement on the maze during the test) during both training and probe trials. This freezing behaviour has previously been reported in *mdx* mice, but this is the first time this anxiety-like behaviour has been observed to increase with increasing age in *mdx* mice. The *mdx* mice have previously been reported to demonstrate an unimpaired startle reflex to auditory threshold testing, suggesting that auditory, cochlea, and brain stem function are largely unaffected by the loss of dystrophin. The amygdala is therefore the main candidate responsible for the fear conditioning and enhanced defensive behaviour in *mdx* mice. Interestingly, we observed increased grey matter volume in the *mdx* amygdala with age (see chapter 3 for details), changes to amygdala volume in rodents is linked to anxiety levels (Yang *et al.*, 2008) . The control *C57BL/10* mice showed an increased preference for the novel object with increasing age and these findings are in congruence with previous literature examining the effects of aging on rodents performance during the NOR tasks (Ilay *et al.*, 2013).

Remarkably, *mdx* mice also displayed repetitive behaviour, consistent with autistic-like traits in mice (Silverman *et al.*, 2010). At 12 months old 3/8 *mdx*

mice displayed stereotypical behaviours associated with autistic traits in mice including spontaneous motor stereotypes: circling the inside walls of the arena and jumping repeatedly. These characteristics were most obvious in *mdx* mice at 12 months old.

Previous studies assessing cognitive functioning of *Cmah* null mice described a battery of tests (fear conditioning, passive avoidance, and water maze testing) and reported that no statistically significant differences were observed in gross physical assessment, sensorimotor reflexes, nociception, and learning and memory, compared to aged matched controls (Hedlund *et al.*, 2007). *Cmah* null mice did however display an age related hearing loss, similar to that seen in humans, which is associated with hair cell loss causing late-onset deafness (Hedlund *et al.*, 2007). Authors emphasised the need to pursue additional studies to assess both cognitive ability and hearing abnormalities. During both our Barnes maze test and NOR task the *Cmah-/-* mice performed similarly to control *C57BL/10* mice. During the Barnes maze probe trials the *Cmah-/-* mice displayed similar success scores to that of control *C57BL/10* mice for both short- and long-term memory between 4 and 12 months old. During the NOR task the *Cmah-/-* mice displayed a preference for the novel object and opposed the familiar object between 4 and 12 months old. Only at 12 months old did the *Cmah-/-* mice spend less time in the target quadrant during the short-term Barnes maze assessment than control *C57BL/10* mice. Additionally, at 12 months old the *Cmah-/-* mice had a reduced D2 ratio compared to control *C57BL/10* mice. Taken together these two findings are suggestive of a change in memory and learning capabilities of *Cmah-/-* mice at 12 months old where a decline in memory was observed.

To the best of our knowledge, this is the first behavioural study to assess if cognitive impairment is progressive in the *mdx* mouse model of DMD. This study has highlighted a progressive cognitive deficit in the *mdx* mice using the Barnes maze test between 4 and 12 months old, with the highest impairment in long-term memory performance. Moreover, the NOR tasks outlined an increase in anxiety-related behaviour in *mdx* mice, with the highest levels of anxiety evident at 12 months old. Interestingly, no other genotype exhibited these anxiety and autistic-like traits. In this study we have identified an increased

latency to locate the target hole and a reduced success score for *mdx* mice during the Barnes maze test from 6 months old onwards. These two parameters could be used as outcome measures to non-invasively measure changes over time in relation to brain pathology in the *mdx* mice. However, the mice would need to be a certain age as we did not observe obvious cognitive dysfunction until *mdx* mice were 6 months old utilising the Barnes maze test.

Additionally, this is the first study to employ behavioural assays in the *Cmah-/-mdx* mice and given their unusual performance on the Barnes maze test and NOR tasks at 4 and 6 months old, further investigations and increased number of mice tested are necessary to confirm these findings.

Chapter 5. Alterations of blood-brain barrier permeability in dystrophin deficient mice

5.1 Introduction

5.1.1 The blood-brain barrier (BBB) formation

The blood- brain barrier (BBB) development and differentiation is a gradual process that leads the embryonic vessels to acquire barrier properties, by selectively and progressively decreasing permeability and expression of specific endothelial transporters and antigens (Nico *et al.*, 2005). Formed by specialised vascular endothelial cells, the BBB is tightly controlled by pericytes, embedded in the vascular basement membrane, perivascular microglial cells, astrocytes, and neurons; all of these elements contribute to the formation of the neurovascular unit (NVU) (Heye *et al.*, 2014). A primary function of this specialised brain region is to regulate the ionic composition of the extracellular milieu by controlling local cerebral blood flow and transport across the BBB (Wilcock *et al.*, 2009). BBB endothelial cells display a unique phenotype characterised by the presence of tight junctions (TJs) and the expression of specific polarised transport systems. TJs are composed of TJ proteins (occludin, claudins, zonula occludens (ZO)-1, ZO-2, ZO-3, cingulin, AF6, 7H6), adherent junctions (AJ) composed of cadherins, catenins, vinculin, and actinin, and junctional adhesion molecules (JAMs) (Abbott *et al.*, 2010). Additionally, the BBB controls water transport, which has a pivotal role in the CNS physiology as it is involved in CSF production, fluid transport across the endothelium, and osmolarity compensation in potassium siphoning (Filippidis *et al.*, 2017). The BBB allows the passage of water, various gases, and lipid-soluble molecules via passive diffusion, in addition to the selective transport of molecules such as glucose and amino acids, which are pivotal for correct neural functioning (Abbott *et al.*, 2010). Disruption of the BBB is reported in numerous neurological conditions and leads to various pathogenic effects (Figure 5.1).

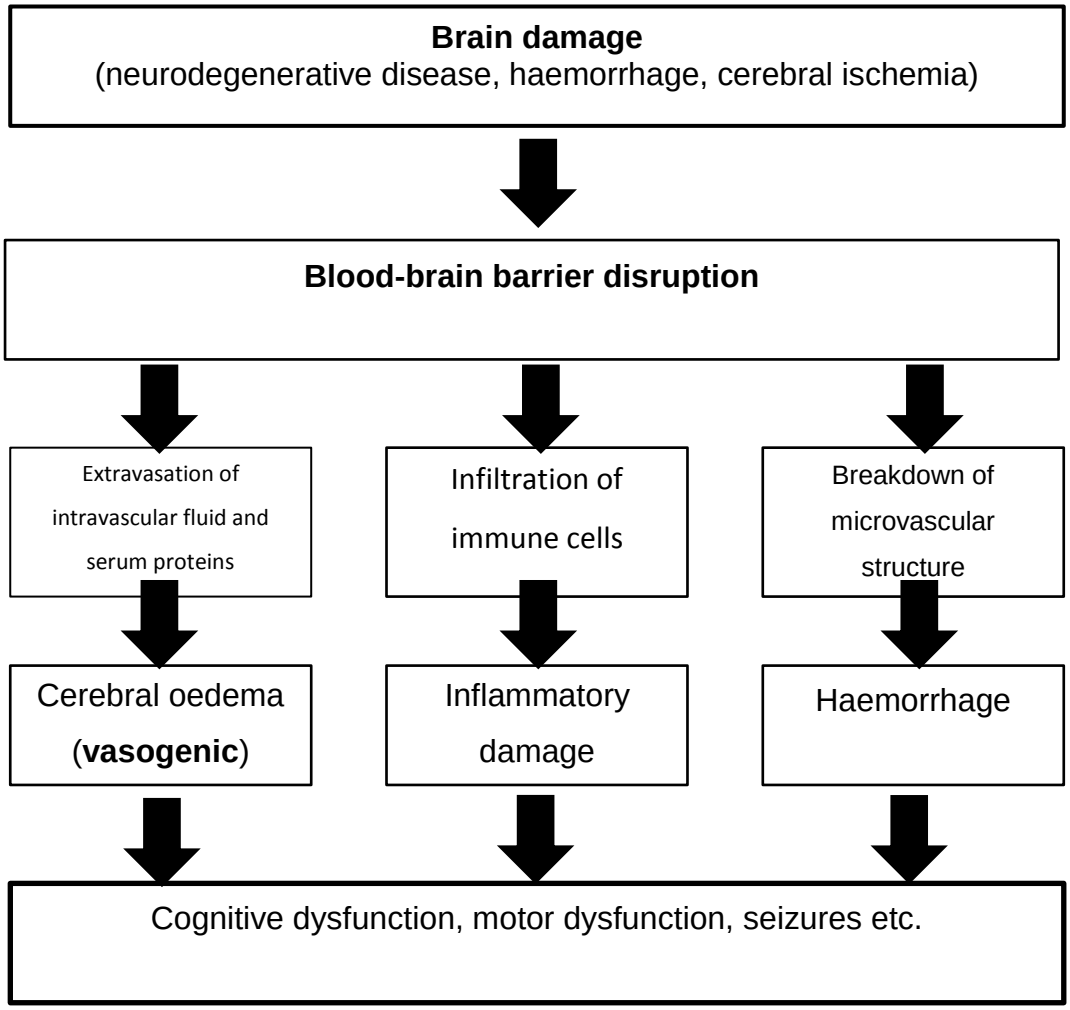

Figure 5.1: Pathophysiological outcomes by blood-brain barrier (BBB) disruption after damage. BBB disruption leads to several conditions including brain oedema, inflammatory damage, and haemorrhage. (Figure adapted from: (Michinaga and Koyama, 2017)).

5.1.2 The role of AQP4 at the BBB

Astrocytes control the neuronal microenvironment by direct or indirect regulation of the ionic flux occurring during neuronal activity (Iacovetta *et al.*, 2012). In addition, astrocytes regulate the rate of water flow by means of a specific water channel, namely AQP4. AQP4 is considered to be an important marker for glial cells and is normally strongly expressed in perivascular processes, where it regulates both CSF production at the cerebral ventricle level and water permeability at the BBB (Iacovetta *et al.*, 2012). Moreover, AQP4 proteins are associated with the DGC in the brain (Qiu *et al.*, 2015). Syntrophins are members of the DGC and mice null for α-syntrophin show a mislocalisation of AQP4 on glial membranes, which suggests that proteins of the DGC are

necessary for correct localisation of AQP4 in the brain (Hoddevik *et al.*, 2017). Vasogenic cerebral oedema occurs when the BBB is disrupted due to the breakdown of tight endothelial junctions and mainly affects the white matter through leakage from capillaries (Papadopoulos *et al.*, 2004; Papadopoulos and Verkman, 2007). This is in contrast to cytotoxic cerebral oedema, where the BBB remains intact but the sodium and potassium pump in the glial cell membrane is impaired due to a disruption in cellular metabolism, causing cellular retention of sodium and water (Szu and Binder, 2016). Studies of cytotoxic oedema have shown that mice that are AQP4 deficient have protection against cellular swelling and improved neurological outcome (Verkman, 2005), whilst vasogenic oedema was worse in the absence of AQP4 (Papadopoulos *et al.*, 2004).

5.1.3 Alterations of the BBB in mdx mice

Dystrophin and other members of the DGC are expressed in brain microvessels (Lidov *et al.*, 1995), and in astrocyte perivascular endfeet (Blake *et al.*, 1999) where dystrophin proteins play a role in BBB functions. Dystrobrevin, a DGC-associated protein discovered by immunoelectron microscopy, was localised not only in the astrocytic endfeet around blood vessels and under the pia mater, but also in endothelial cells and plays a role in BBB functions as a component of the DGC complex (Ueda *et al.*, 2000). Numerous members of the DGC are localised in the endothelial and glial cells, and are reduced in dystrophin deficiency (Nico *et al.*, 2005).

Ultrastructural alterations of the blood vessel wall have been reported in the *mdx* brain. The *mdx* mice endothelial cells demonstrated an increase in vesicles and vacuoles involved in transcellular transport in addition to a detachment of the TJ (Nico *et al.*, 2005). Moreover, ZO-1 colocalises with α-actin in the wild type mouse brain and ZO-1 protein content was decreased and its expression pattern strongly modified in the *mdx* vessels (Nico *et al.*, 2005). Using immunogold electron microscopy researchers found that α-actin was expressed in both pericytes and endothelial cells of the control vessels, where α-actin gold particles were concentrated along the cytoplasmatic face of the TJ in the form of an electron dense peripheral band. Conversely, in the *mdx* vessels α-actin

particles were scattered throughout the endothelial cytoplasm and not located at the inner aspect of the TJ, which appeared devoid of dense peripheral bands (Nico *et al.*, 2005). The authors hypothesised that alteration of cytoskeletal actin, induced by dystrophin deficiency, caused alteration of ZO-1 anchoring to the TJ membranes (Nico *et al.*, 2005), therefore impairing BBB integrity (Figure 5.2).

AQP4 is developmentally expressed during BBB differentiation. Its expression occurs in a polarised way at the perivascular glial processes facing the vessels (Nico *et al.*, 2001). AQP4 glial expression is reduced in a damaged BBB (Filippidis *et al.*, 2017). A reduction in AQP4 expression in the brains of *mdx* mice has been reported and is also associated with swollen astrocyte processes, suggesting that its function is related to the reabsorption of water from the extracellular fluid to the blood and CSF (Nico *et al.*, 2010). Thus, a reduction of AQP4 expression in *mdx* mouse brain could cause a slower drainage of water out of the brain, astrocyte swelling, and cellular cerebral oedema (Nico *et al.*, 2005). Another theory is that the reduction of AQP4 protein in the brain may be a consequence of an altered vascular permeability of the BBB (Nico *et al.*, 2005).

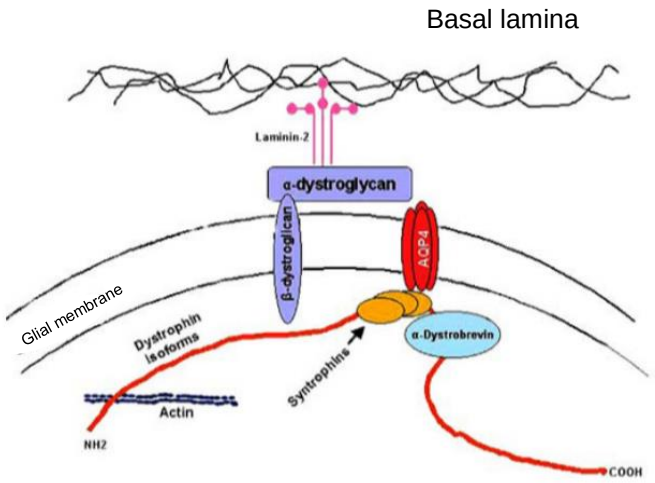

Figure 5.2: Schematic representation of endothelial junction plasma membrane. Mutations in the *DMD* gene lead to the dissociation of the relationship between cytoskeleton actin and the ZO-1 complex with cytoplasmic translocation of tight junction (TJs) proteins. (Figure adapted from:(Nico *et al.*, 2005)).

5.1.4 Measuring BBB disruption

A disruption in the BBB can enable the extravasation of low-molecular weight MRI contrast agents. This accumulation of contrast material in the extravascular extracellular space (EES) of affected tissues leads to an decreased longitudinal relaxation rate, and therefore increased signal intensity in T_1-weighted MR images (Heye *et al.*, 2014), which can evaluate and detect regions of BBB impairment. In the brain, MR signal changes caused by contrast agent extravasation are determined by several factors including tissue perfusion and capillary permeability (Heye *et al.*, 2014).

A more traditional method to assess BBB integrity is by Evans blue dye (EBD) extravasation. EBD binds to serum albumin which cannot cross the BBB therefore neural tissue remains unstained. However, when the BBB has been compromised serum-bound EBD can enter the CNS (Hawkins and Egleton, 2006). However, this is an *in vitro* method and cannot be used for monitoring BBB impairments longitudinally.

5.1.5 Measuring brain water content and environment

Quantitative MRI acquisition and analysis techniques allow investigations beyond conventional qualitative interpretation and provide further insights into brain pathologies. Quantifying tissue specific characteristics enables the detection of reproducible parameters that mirror the underlying biological systems (Leppert *et al.*, 2009). Relaxometry, for instance, combines acquisition and analysis techniques to generate MR relaxation time constants that directly reflect the local environment of water. Since the transverse relaxation time, T_2, is a quantitative measure of a basic biophysical property, which leads to signal contrast on MRI, it can provide a quantitative monitoring tool in both healthy and disease states (Leppert *et al.*, 2009).

A more common technique to measure brain water content is the wet:dry brain method. This conventional method is easy to perform and widely used, but is associated with multiple limitations including: the requirement of large sample sizes, variations in oven temperature and drying times, and the heating process which changes tissue morphology (Sebastiani *et al.*, 2017). Moreover, this method is an *in vitro* technique and cannot be used for monitoring brain water content longitudinally.

5.1.6 Aims

- To apply T_2 relaxometry to control *C57BL/10* mice and mutant mice brains to gain accurate data regarding brain water content and environment of numerous regions of interest and compare this *in vivo* method to the commonly used wet:dry brain ratio approach (*in vitro*).
- To compare Evans blue dye extravasation in the brain between control *C57BL/10* and mutant mice between 6 and 18 months old.
- To quantify the effects of age on BBB disruption utilising a contrast enhanced T_1 mapping approach in control *C57BL/10* mice and mutant mice between the ages of 6 and 14 months old.

5.2 Changes in brain water content

Brain edema is a major pathological feature associated with neurological defects. Small percentage changes in brain water content can reflect much bigger changes in brain swelling. The characteristic pathophysiological conditions caused by BBB disruption are brain oedema resulting from an excessive increase of brain water content, inflammatory damage caused by infiltrating immune cells, and haemorrhage caused by the breakdown of microvessel structures (Michinaga and Koyama, 2017). We investigated the brain water content and environment of mutant mice by utilising quantitative MRI (T_2 relaxometry) and the wet:dry brain method.

5.2.1 T_2 relaxation time at 7T

We recorded the T_2 relaxation times at 7T for numerous ROIs, including the cerebral cortex, corpus callosum, hippocampus, cerebellum and caudate putamen, in mutant and control C57BL/10 mouse brains at 6 and 18 months old (Figure 5.3). At 6 months old, no observation of change in T_2 relaxation time was found in any ROI of either the control *C57BL/10* or mutant mouse brains ($F_{3, 60}$ = 1.11, p=0.35) (Figure 5.4). There was no significant main effect for any ROI within the genotype ($F_{1, 24}$= 4.8, p=0.07).

Remarkably, at 18 months old the *Cmah-/-mdx* mice had a substantially longer T_2 relaxation time in all ROIs investigated compared to the control *C57BL/10*, *mdx* and *Cmah-/-* mice brains (Figure 5.5). There was a significant difference in the T_2 relaxation rates between control *C57BL/10* mice and *Cmah-/-* mice ($F_{3, 24}$ = 219, p<0.01). The largest difference in T_2 relaxation time was observed in the hippocampus, with *Cmah-/-mdx* mice having a T_2 relaxation time of 59±0.7 ms and control *C57BL/10* mice displaying a T_2 relaxation time of 51±0.3 ms (p<0.01). Interestingly, there was an elevation in T_2 relaxation time of the caudate putamen in the *mdx* mice (50±0.5 ms) compared to control *C57BL/10* mice (48±0.7 ms) at 18 months old and this was the only ROI investigated where there was a difference in T_2 relaxation times between *mdx* and control *C57BL/10* mice at 18 months old.

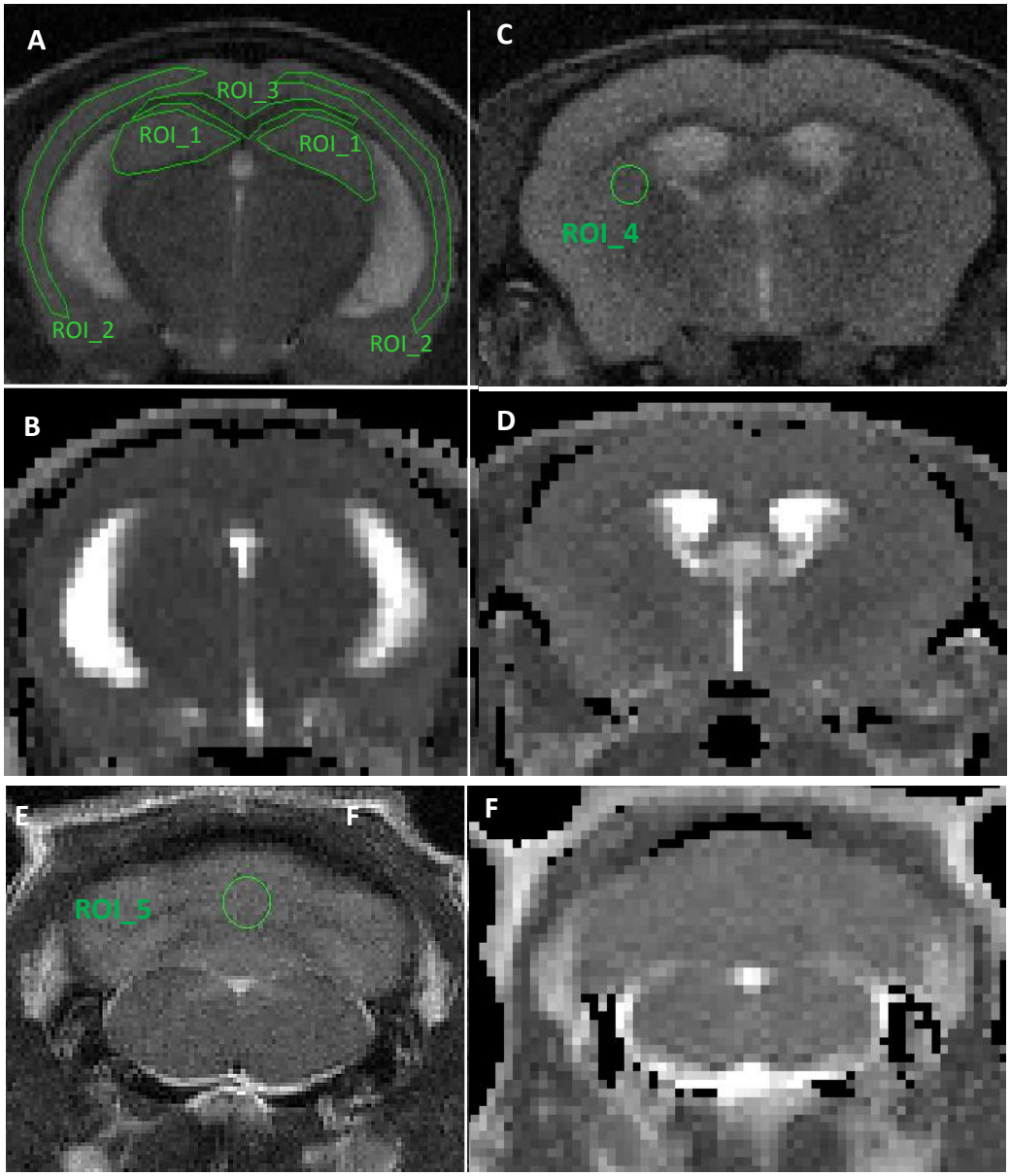

Figure 5.3: Regions of interest (ROIs) for T_2 measurements. A. 1. Hippocampus, 2. Cerebral Cortex and 3. Corpus Callosum, defined on a T_2-weighted coronal image. **B.** Corresponding coronal T_2 map. **C.** ROI 4. Caudate Putamen, defined on a T_2-weighted coronal image **D.** Corresponding coronal T_2 map **E.** ROI 5 in the cerebellum. **F.** Corresponding T_2-weighted coronal image. Images shown are from 18 month old mice.

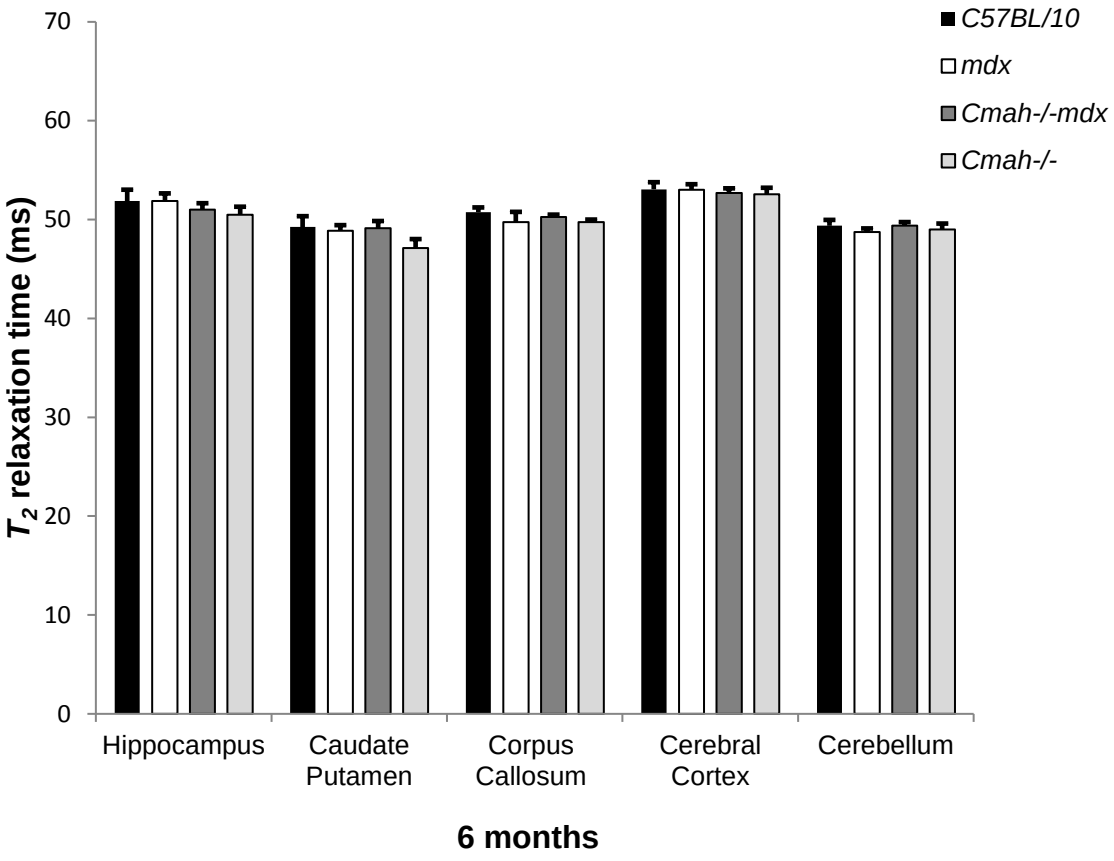

Figure 5.4: Comparison of T_2 relaxation times of each region of interest (ROI) between control *C57BL/10, mdx, Cmah-/-mdx* mice, and *Cmah-/-* mice aged 6 months old. No difference in T_2 relaxation rates was observed in any ROI between each genotype (n=4 mice/genotype). Data presented as mean ± SEM.

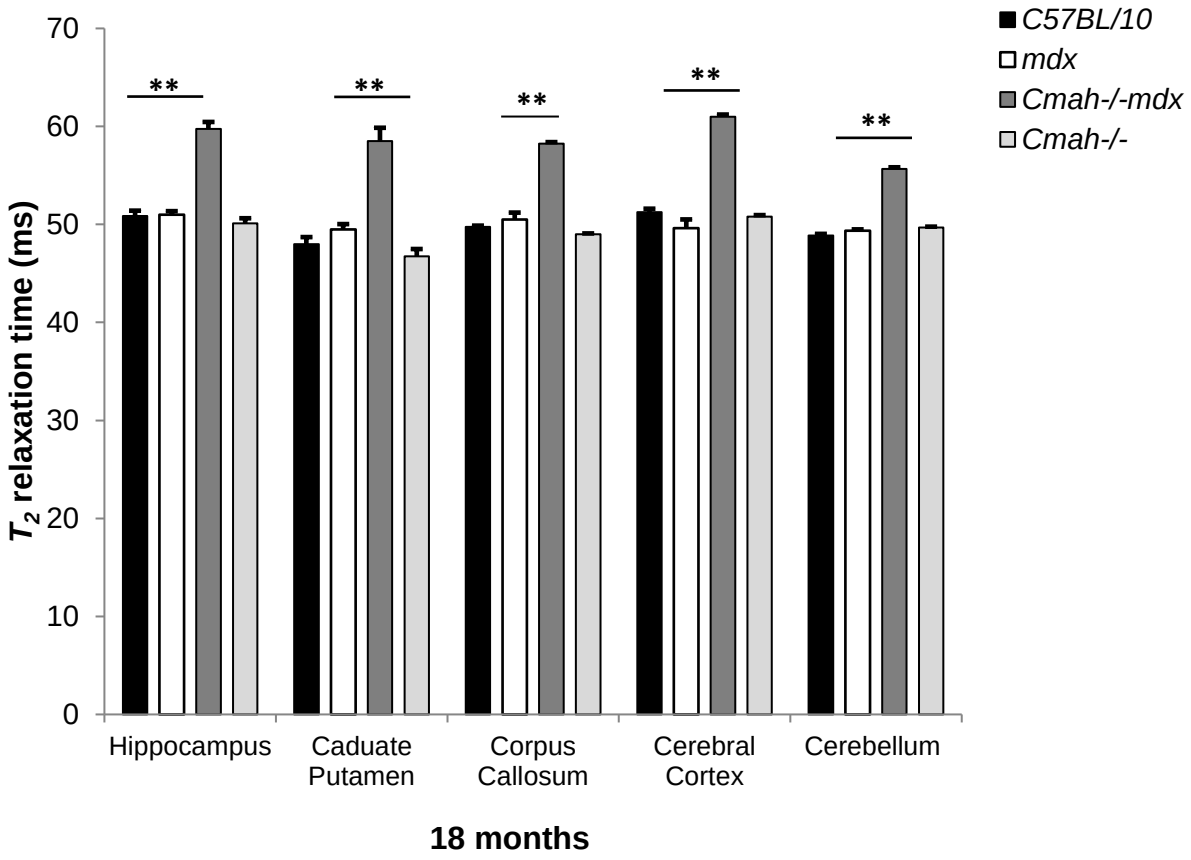

Figure 5.5: Comparison of T_2 relaxation times of each selected brain region between control *C57BL/10, mdx, Cmah-/-mdx*, and *Cmah-/-* mice aged 18 months old. The *Cmah-/-mdx* mice exhbited a higher T_2 relaxation time in all regions of interest (ROI's) compared to both control *C57BL/10* and *mdx* mice (n=4 mice per genotype). The *mdx* mice exhbited similar T_2 relaxtion rates to those of control *C57BL/10* mice in all ROIs investigated. Data presented as mean ± SEM, p*<0.05, p**<0.01 vs control *C57BL/10*.

5.2.2 Wet:dry brain water content measurements

The most common method used to measure brain water content is the wet:dry brain measurement. These measurements were performed in mice aged six months old and there was no main effect on genotype ($F_{3, 24} = 1.89$, p=0.16), indicating that there was no significant difference in the brain water content between control *C57BL/10* mice (76.6 ±0.89 %), *mdx* mice (75.7±0.86 %), *Cmah-/-mdx* mice (78.2±0.84 %) and *Cmah-/-* mice (76.19±0.86 %) at 6 months old (Figure 5.6). There was a main effect for brain region (cortex and cerebellum) ($F_{1, 24} = 4.8$, p=0.03), demonstrating that the cortex (77.8±0.6 %) contained significantly more water than the cerebellum (75±0.5 %), which is expected given their differences in size. These findings are consistent with our T_2 relaxation times for the ROIs investigated (Figure 5.4).

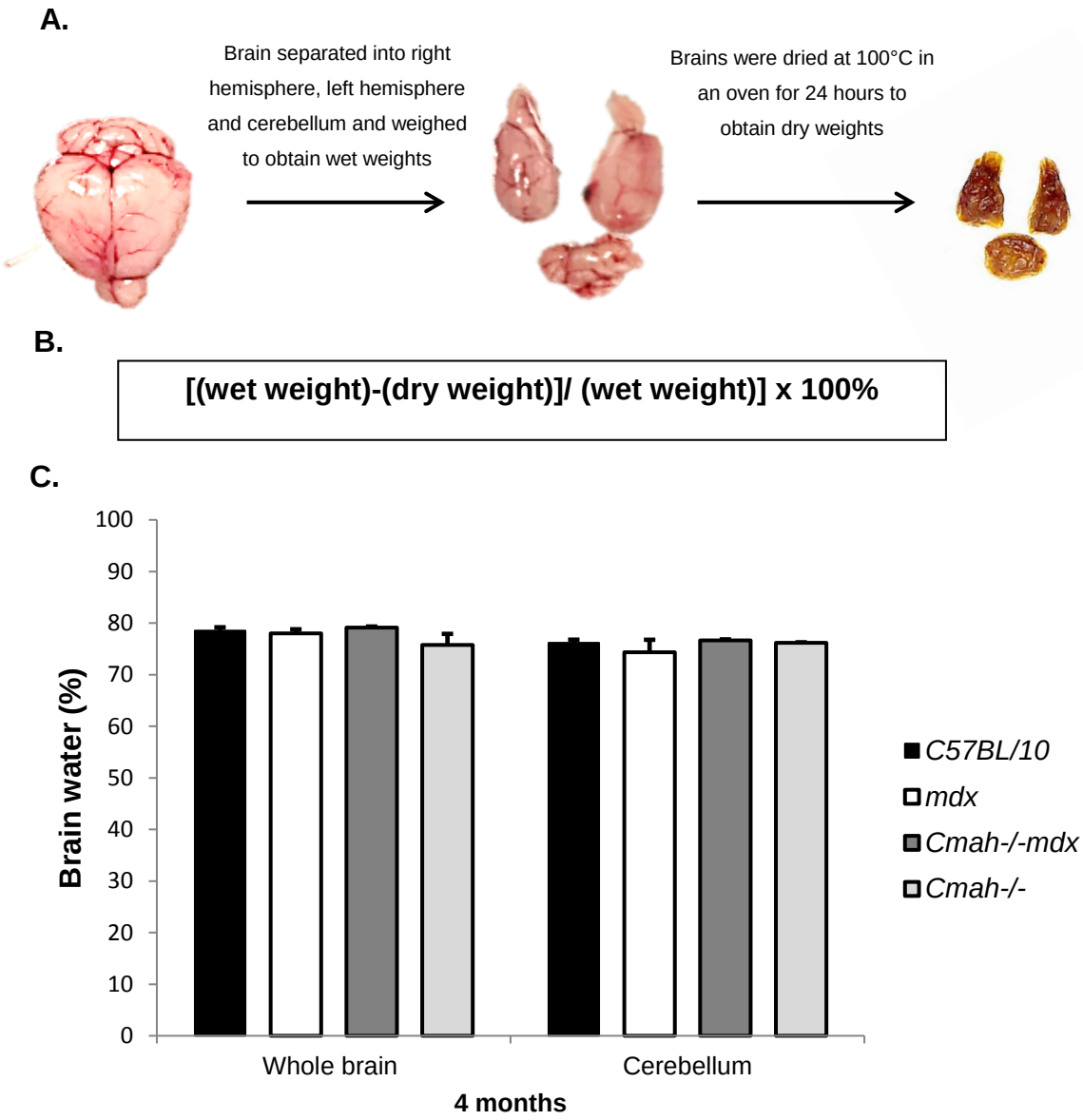

Figure 5.6: Brain wet:dry measurements. A. Outline of the method used for determining brain water content. **B.** Formula used for calculating brain water content. **C.** Bar graph showing the evaluation of brain water content in mice aged 4 months old. Data presented as mean ± SEM. No difference was observed in the brain water content between any genotype in either the whole brain or the cerebellum (n=4/genotype), which is consistent with previous findings.

5.3 Extravasation of Evans blue dye (EBD)

To investigate the integrity of the BBB in the absence of full length dystrophin, we examined the extravasation of EBD from blood vessels following an intraperitoneal injection of a bolus of EBD into mice aged 6 months and 18 months old. Successful uptake of EBD was considered when mice extremities appeared blue (Figure 5.7). There was a substantial leakage of EBD into the cerebrum of both mdx and *Cmah-/-mdx* mice at 6 months old as demonstrated in Figure 5.8. There were no vessels demonstrating EBD extravasation in control *C57BL/10* mice and *Cmah-/-* mice brains at 6 months old. At 18 months old mdx and *Cmah-/-mdx* mice portrayed a significant leakage of EBD, more so than at the 6 months old time point (Figure 5.9) into the cerebrum but control *C57BL/10* mice again showed no EBD leakage.

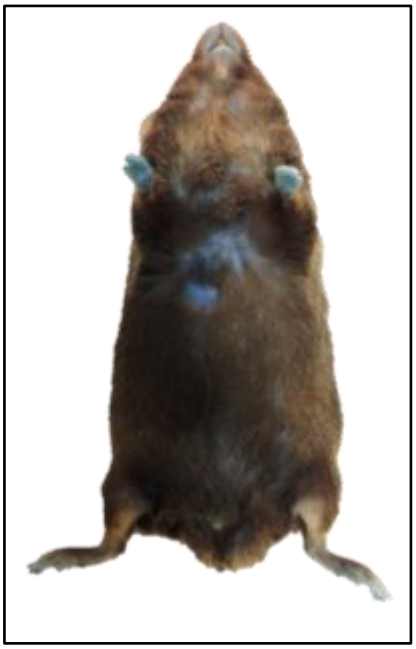

Figure 5.7: Mouse 24 hours after intraperitoneal injection of Evans blue dye (EBD). Successful EBD is evident from blue appearance of the mouse.

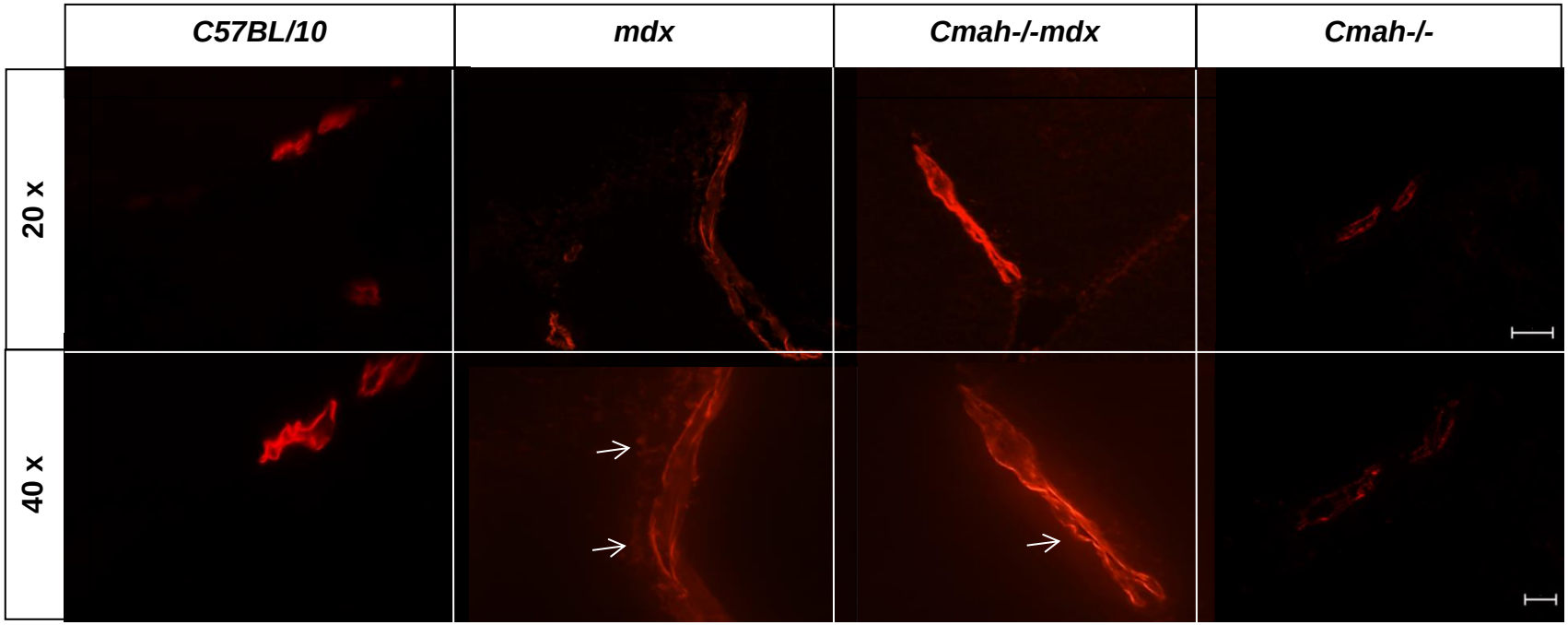

Figure 5.8: Representative images of Evans blue dye (EBD) fluorescence on coronal cyrosections of 6 month old frozen mouse brain (20 µm) (n=4 mice per genotype). The extravasation of EBD can be seen in the *mdx* and *Cmah-/-mdx* mice (white arrows). Scale bar = 20 µm at 20 x magnification and 50 µm at 40 x magnification. There were few vessels demonstrating EBD extravasation in either the control *C57BL/10* or the *Cmah-/-* mouse brain at 6 months old.

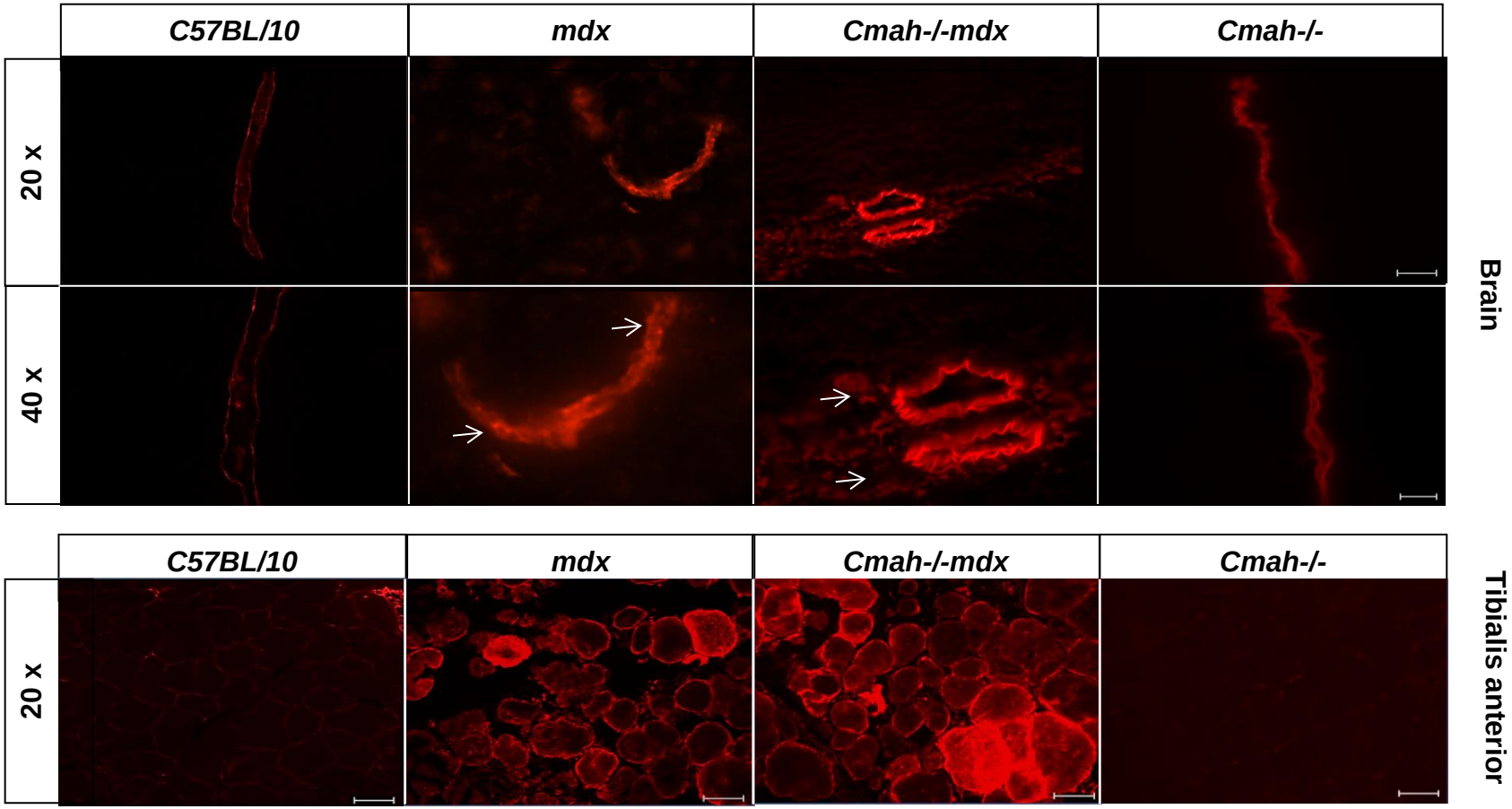

Figure 5.9: Representative images of Evans Blue dye (EBD) fluorescence on coronal cyrosections of 18 month old frozen mouse brains (20 µm) (n=4 mice per genotype). The extravasation of EBD can be seen in the *mdx* and *Cmah-/-mdx* mice (white arrows). Tibialis anterior muscle served as a control tissue. Scale bar = 20 µm at 20 x magnification and 50 µm at 40 x magnification for brain images and 50 µm at 20 x magnification for muscle images. There were few vessels demonstrating EBD extravasation in either the control *C57BL/10* or the *Cmah-/-* mouse brain at 18 months old.

5.4 Western blot analysis of brain aquaporin's

Aquaporins are a family of proteins that function as water channels in the brain. There are two main aquaporins in the CNS: AQP1 and AQP4. AQP1 was found to be localised at the apical membrane of the choroid plexus, whereas AQP4 is located in the astrocyte foot processes that surround capillaries in the CNS in addition to its location at the basolateral membrane of the ventricular ependymal cells. AQP1 has previously been implicated in choroidal CSF secretion, driven mainly by carbonic anhydrase and Na^+/K^+ ATPase.

5.4.1 Aquaporin-1

Western blot analysis of whole brain tissue lysates from control *C57BL/10*, *mdx*, *Cmah-/-mdx and Cmah-/-* mice was performed at 1 month, 4 months and 12 months old, and confirmed there was no difference in expression of the AQP1 (~30 kDa) levels between either control or mutant brains (Figure 5.10). Glyceraldehyde 3-phosphate dehydrogenase (GAPDH) (~38 kDa) was used as a loading control.

5.4.2 Aquaporin-4

Western blot analysis of whole brain tissue lysates from control *C57BL/10*, *mdx*, *Cmah-/-mdx and Cmah-/-* mice was performed at 1 month, 4 months and 12 months old, and demonstrated a progressive reduction of AQP4 in DMD mouse brains. Interestingly, there was also a reduced level of AQP4 present in the *Cmah-/-* mouse brain at 1 and 6 months old (Figure 5.11). However, by 12 months old expression levels were comparable to that of control *C57BL/10* mouse brains.

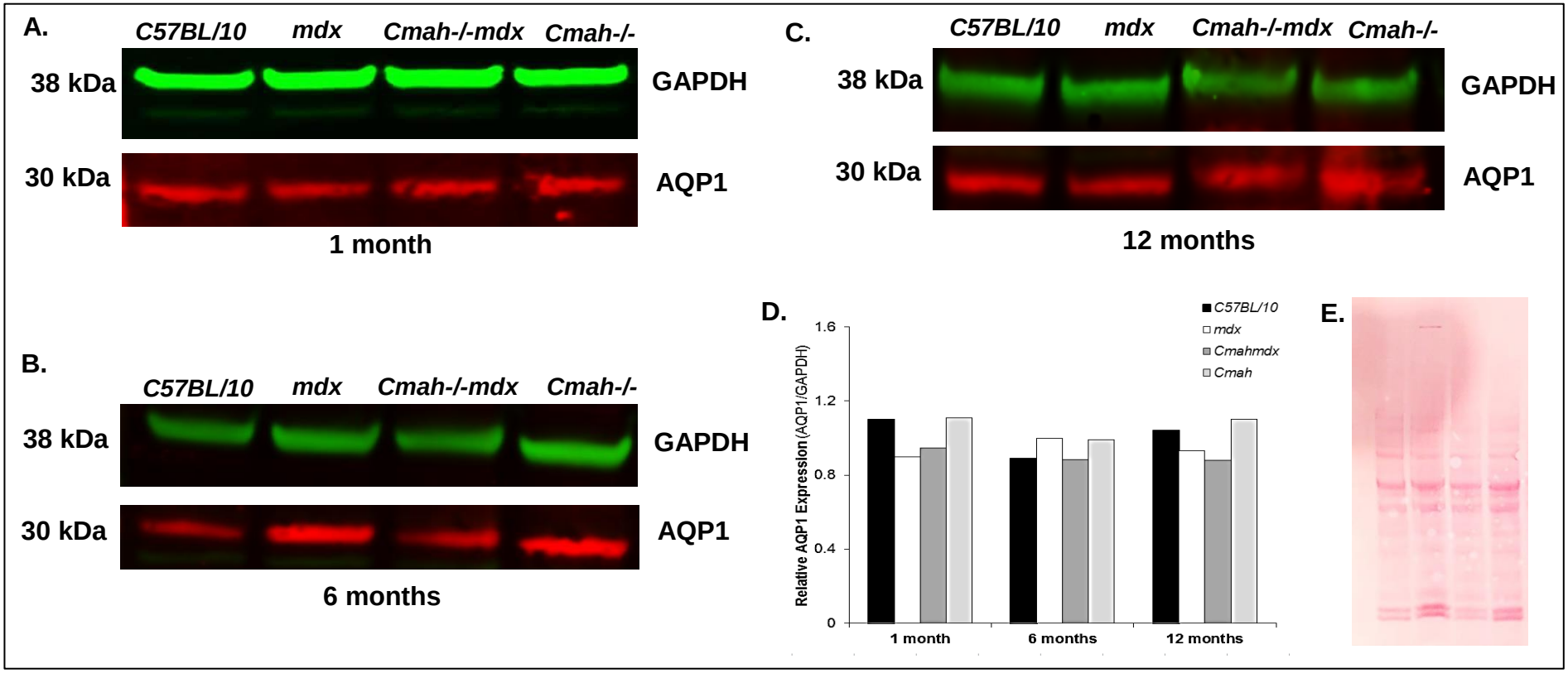

Figure 5.10: Representative western blot analyses of brain tissue from control *C57BL/10*, *mdx*, *Cmah-/-mdx,* and *Cmah-/-* mice at **A.** one month old, **B.** four months old and, **C.** twelve months old. There was no change in expression of AQP1 (30 kDa). Membranes were incubated with rabbit ploYclonal AQP1 antibody (Abcam,ab15080) at a dilution of 1/500, GAPDH (Abcam, ab6276) was used as a loading control (1/1000), **D.** quantification of AQP1 expression at various time points where expression levels normalised to their corresponding GAPDH loading controls, **E.** example Ponceau stain to verify equal sample loading.

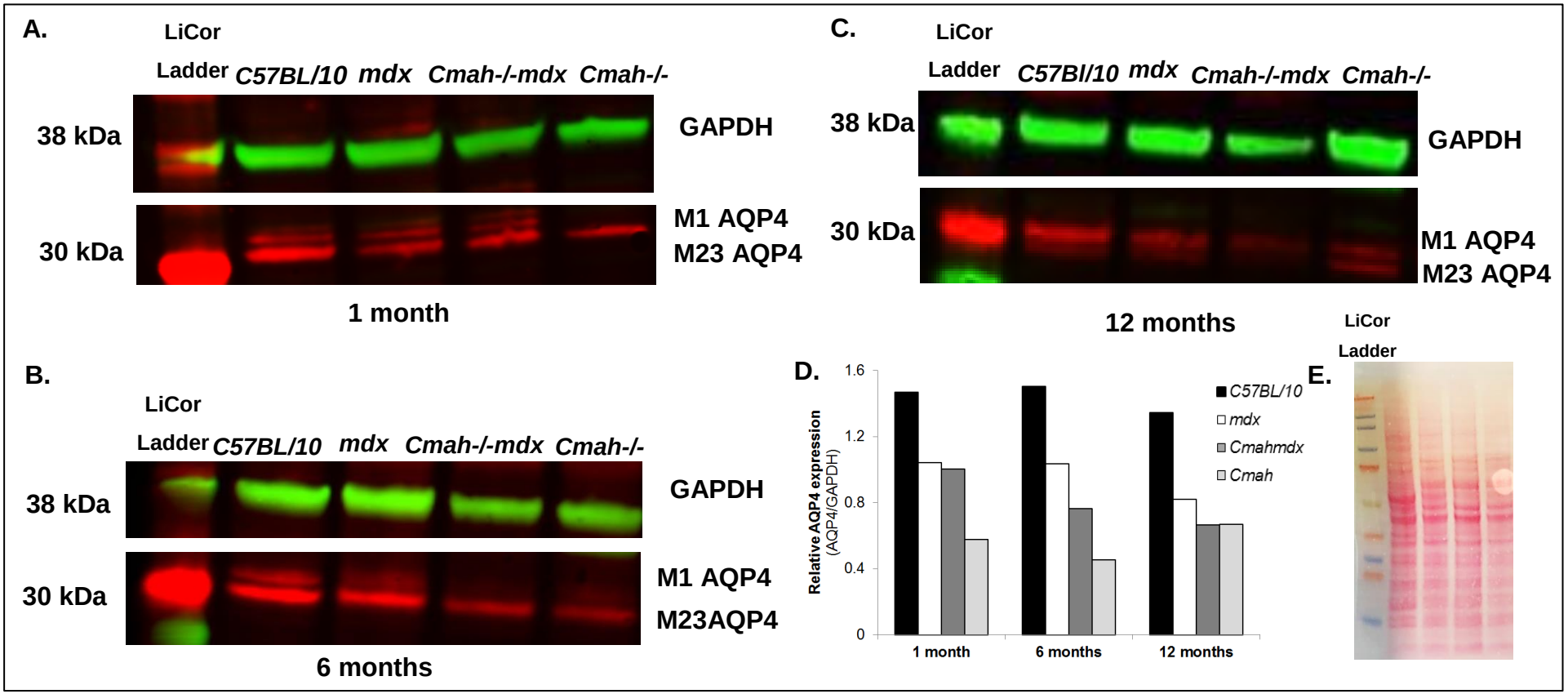

Figure 5.11: Representative western blot analyses of brain tissue from control *C57BL/10*, *mdx*, *Cmah-/-mdx,* and *Cmah-/-* mice at **A.** one month old, **B.** four months old and, **C.** twelve months old. There was a progressive reduction in the expression of both AQP4 M1 and M23 isoforms (~30 kDa) in DMD mouse models with increasing age. Membranes were incubated with rabbit ploYclonal AQP4 antibody (Abcam,ab4182) at a dilution of 1/500. GAPDH (Abcam, ab6276) was used as a loading control (1/1000), **D.** quantification of AQP4 expression at various time points where expression levels normalised to their corresponding GAPDH loading controls, **E.** example Ponceau stain to verify equal sample loading.

5.4.3 T_1- mapping with Gadolinium enhancement

Loss of BBB integrity has previously been reported in *mdx* mice, yet no study to date has assessed BBB permeability *in vivo* in DMD mice. MRI offers the further possibility of monitoring the evolution of BBB modifications in the same animal. Gadolinium (Gd) is a paramagnetic MRI contrast agent used routinely for diagnosing BBB lesion in patients; the agent works by shortening tissue T_1 after extravasation into brain parenchyma. Tissue infiltration of the tracer can be assessed using T_1 mapping and T_1-*w* images to assess contrast agent uptake overtime. We investigated five ROIs, including brain regions known to be rich in dystrophin, to determine the extent of potential BBB disruption throughout the brain including: cerebellum, hippocampus, ipsilateral (right) hemisphere, contralateral (left) hemisphere and the caudate putamen (Figure 5.12).

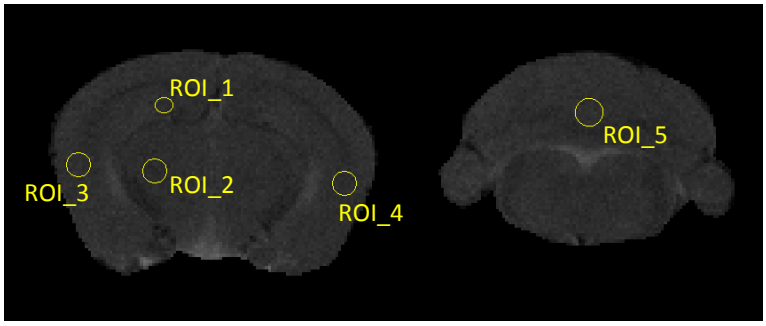

Figure 5.12: Regions of interest (ROI) for T_1 mapping measurements. 1. Hippocampus, **2.** Caudate Putamen, **3.** Ipsilateral Cortex, **4.** Contralateral Cortex, and **5.** Cerebellum, defined on T_1-weighted coronal images.

A temporal series of eight T_1-*w* images were acquired for each mouse at 6 (Figure 5.13) and 14 months old (Figure 5.14). The series of T_1-*w* images were split into two parts: pre- and post-Gd administration, where two T_1-*w* images were acquired pre-Gd administration and six T_1-*w* images were acquired post-Gd administration. Successful uptake of Gd, via a tail vein cannula, was confirmed when the vasculature appeared bright and the sagittal sinus lit up. It is important to confirm the uptake of the contrast agent as it is possible for a blood clot to form in the cannula, preventing the injection of contrast agent. Contrast enhancement of the temporalis muscle was also observed in some *mdx* mice as indicated by a brightening of the image (Figure 5.14).

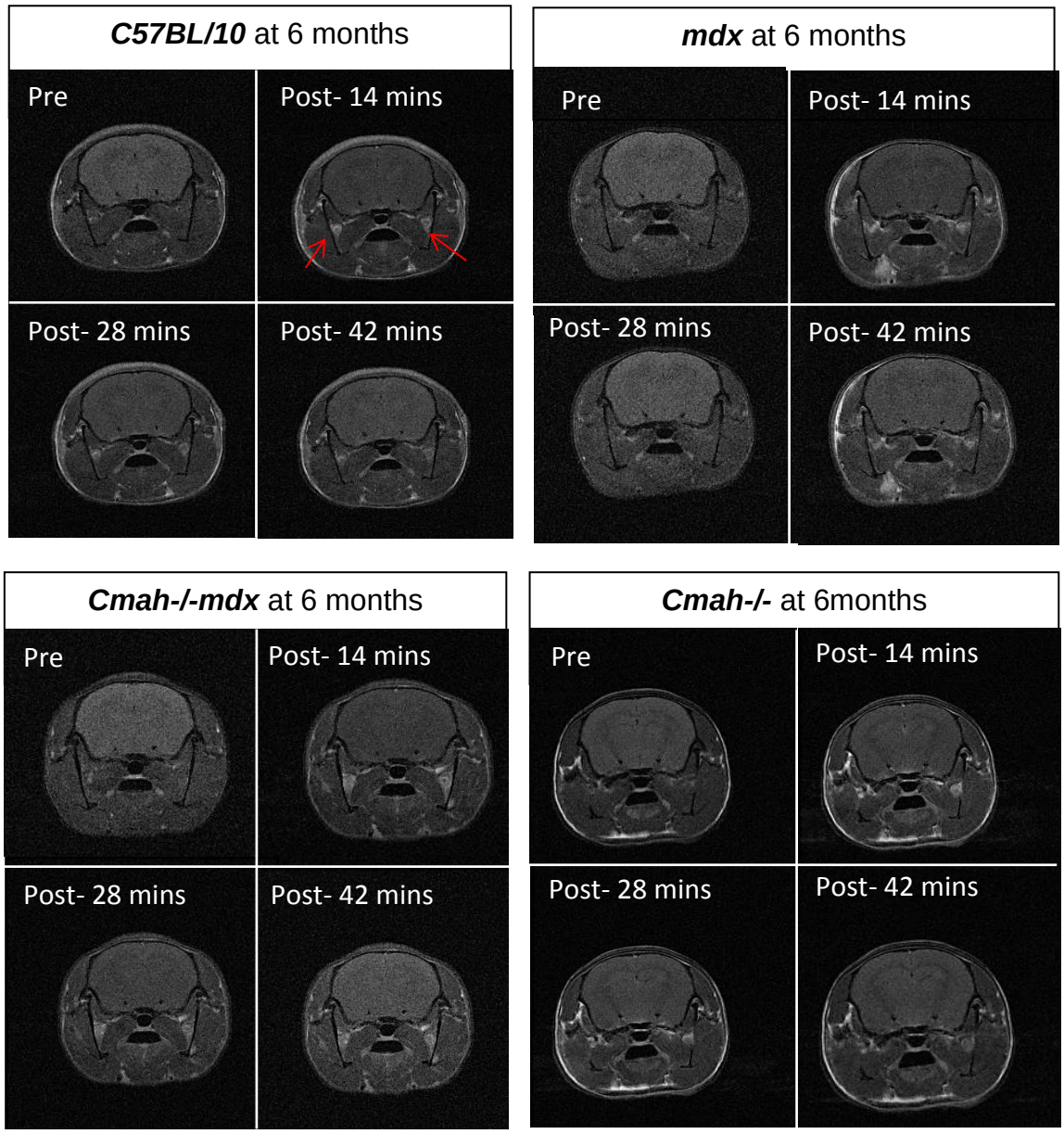

Figure 5.13: Representative T_1-w images from control *C57BL/10*, *mdx*, *Cmah-/-mdx* and *Cmah-/-* mice at 6 months old pre-gadolinium (Gd) injection (0 minutes) and 14, 28, and 42 minutes post-Gd injection (n=6-8 mice per genotype). Successful Gd injection was determined when the sagittal sinus and the vasculature (red arrow) appeared bright and was evident on post-Gd injected images.

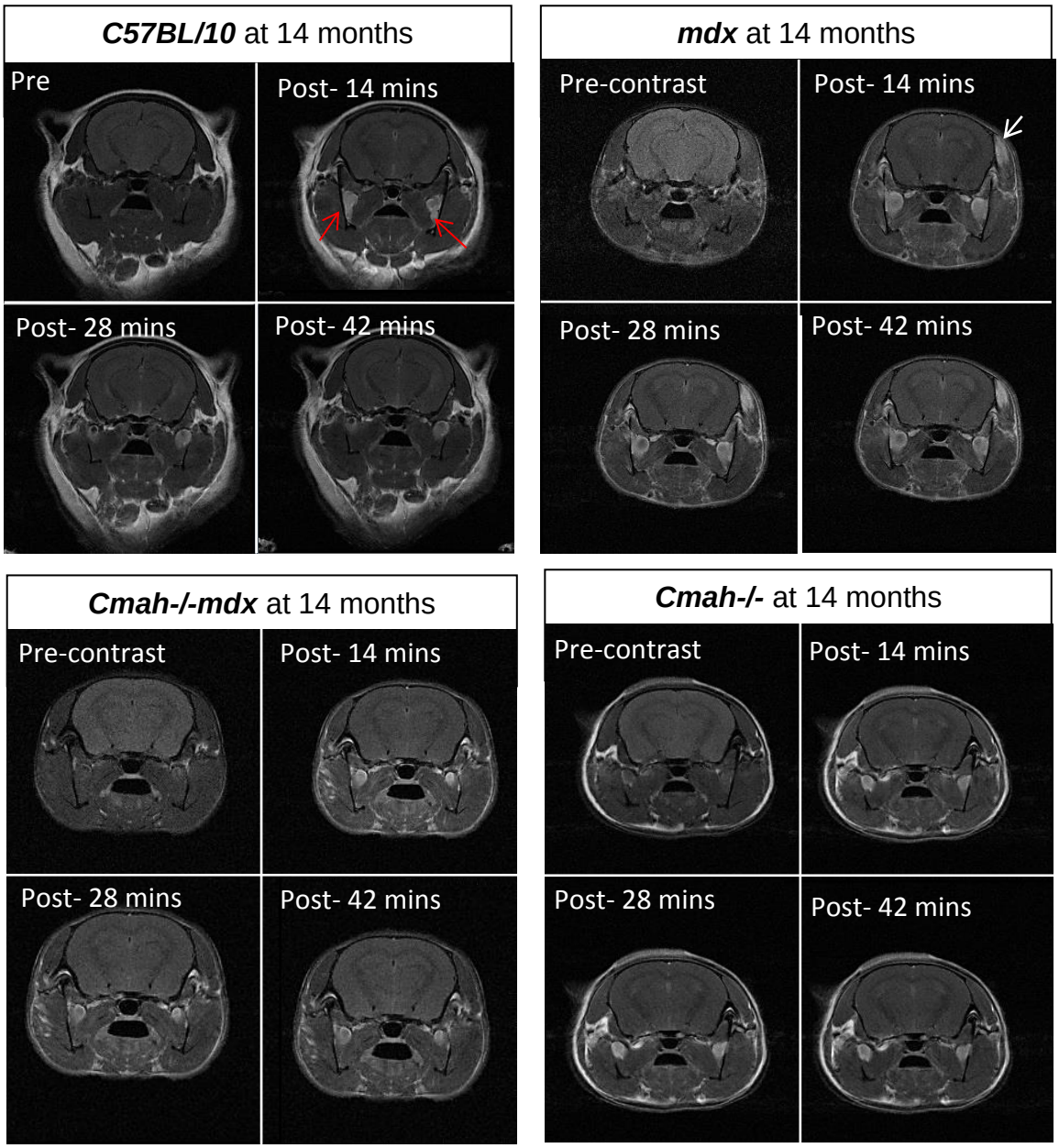

Figure 5.14: Representative T_1-w images from control *C57BL/10*, *mdx*, *Cmah-/-mdx,* and *Cmah-/-* mice at 14 months old pre-gadolinium (Gd) injection (0 minutes) and 14, 28, and 42 minutes post-Gd injection (n=6-7 mice per genotype). Successful Gd injection was determined when the sagittal sinus and the vasculature (red arrow) appeared bright and was evident on post-Gd injected images. Contrast uptake into temporal muscle tissue was observed in *mdx* mice (white arrows) where infiltration of Gd into muscle tissue appeared bright. Note also the change in head shape between genotypes as detailed in chapter 3.

Quantification of the concentration of Gd in brain tissue *in vivo* is possible using both the T_1 mapped values and the following formula:

$$R_{1post} = R_{1pre} + r_1[Gd] \text{ , where } r = 1/T_1$$

Where R_1post and R_1pre are the relaxation rates of the tissue post- and pre- Gd injection, [Gd] is the concentration of contrast agent and r_1 is the relaxivity of the contrast agent at 7T. (See Chapter 2 for further details regarding the methods used).

The r_1 relaxation rates before and after contrast enhancement were measured from the T_1 maps in the brain, which in turn could be used to calculate the concentration of contrast agent in each ROI.

The *mdx* mice displayed increased Gd uptake in the cerebellum at 6 months old compared to all other genotypes (Figure 5.15) at 42 minutes post-Gd injection (56 minutes of the scan protocol). The *mdx* mice had the highest concentration of Gd measured in the cerebellum at 12±1.4 µM compared to control *C57BL/10* mice at 1.8±2.7 µM. However, at 14 months old the concentration of Gd within the mdx cerebellum, at 42 minutes post-Gd injection, increased considerably up to 21.6±3.9 µM, whereas the concentration of Gd within the control *C57BL/10* mice cerebellum increased slightly to 11.4±1.4 µM (Figure 5.15). Additionally, at 42 minutes post Gd injection, the concentration of Gd in the mdx cerebellum appeared to be rising still, whereas in the control *C57BL/10* there was a decline in Gd concentration by this point. We expected to detect small levels of Gd in the brains of all mice since Gd is taken up into the vasculature and will contribute to a transient increase in T_1 signal until it is cleared and excreted by the liver and kidneys. The 6 month old control *C57BL/10* mice demonstrated this effect (Figure 5.15 and Figure 5.20). At 42 minutes post-Gd injection the level of Gd detected in the brain should be minimal unless Gd is ‘trapped’ due to decreased BBB integrity, which was clearly visible in numerous ROIs for mdx and *Cmah-/-mdx* mice (Figure 5.21 and Figure 5.22).

The *Cmah-/-mdx* mice displayed a similar concentration of Gd in the cerebellum at 6 months old compared to control *C57BL/10* mice with 10.3±3.9 µM recorded, but by 14 months old the concentration of Gd within the cerebellum had increased similar to that of control *C57BL/10* mice to 13.6±1.7 µM. Interestingly, the *Cmah-/-* mice showed little to no difference in Gd concentration in the cerebellum, 42 minutes post injection, between 6 and 14 months old, with a detection level of 7.7±2.7 µM Gd and 5.8±2.4 µM Gd at 6 and 14 months respectively.

In the cortex, *mdx* mice showed similar levels of Gd uptake in both the ipsilateral and contralateral hemispheres, with 11.9±1.4 µM Gd and 10.6±0.9 µM Gd recorded respectively at 6 months old 42 minutes post-Gd injection (Figure 5.16 and Figure 5.17). The control *C57BL/10* mice had significantly less Gd in the ipsilateral and contralateral hemispheres (42 minutes post Gd injection) compared to mdx mice at 6 months old with concentrations of 1.76±1.7 µM and 1.18±1.6 µM Gd recorded respectively. The *Cmah-/-mdx* mice displayed similar levels of Gd uptake in the ipsilateral and contralateral hemispheres to that of *mdx* mice at 6 months old, with a concentration of 10.7±3.2 µM Gd and 10.2±2.4 µM Gd recorded. Again, the *Cmah-/-* mice had the lowest concentration of Gd detected with 6.7±2.3 µM and 7±1.4 µM Gd in the contralateral and ipsilateral hemispheres respectively at 42 minutes post-Gd injection. By 14 months old the concentration of Gd had increased in the *mdx* cortex (42 minutes post-Gd injection) to 21.8±4.1 µM Gd in the ipsilateral hemisphere and 17.1±2.7 µM Gd in the contralateral hemisphere. There was also a slight increase in the concentration of Gd detected in the control *C57BL/10* mice cortex at 42 minutes post-Gd injection, but the increase was smaller than that observed in the *mdx* mice cortex at 14 months old, with 12.7±4.1 µM Gd and 13.3±1.9 µM detected in the ipsilateral and contralateral hemisphere respectively. The *Cmah-/-mdx* and *Cmah-/-* mice displayed similar levels of Gd uptake in the cortex at 14 months to that detected at 6 months old at 42 minutes post-Gd injection.

In the hippocampus at 6 months old all mice, regardless of genotype, displayed similar levels of Gd uptake at 42 minutes post-Gd injection (Figure 5.18). However, mdx mice did have the highest level of Gd in the hippocampus

recorded at 11.4±3.7 μM, whereas control *C57BL/10* mice had a concentration of 2.8±1.4 μM, *Cmah-/-mdx* mice had a concentration of 3.0±0.5 μM, and *Cmah-/-* mice a concentration of 3.3±1.1 μM, by 42 minutes post-Gd injection. By 14 months old the concentration of Gd detected in the hippocampus had increased slightly for all genotypes at 42 minutes post-Gd injection except for the *Cmah-/-* mice, with 1±3.4 μM Gd recorded. The concentration of Gd in the *mdx* hippocampus at 14 months old was similar to that detected at 6 months old, with a concentration of 17.3±1.3 μM Gd recorded, as was the concentration of Gd in the hippocampus of control *C57BL/10* and *Cmah-/-mdx* mice of 13.3±1.9 μM Gd and 17.1±2 μM Gd detected respectively.

Within the caudate putamen the *mdx* mice displayed the highest concentration of Gd at 6 months old, 42 minutes post-Gd injection, with a concentration of 12.2 ±4.1μM Gd recorded, compared to control *C57BL/10* mice with a concentration of 1.3±3.5 μM Gd (Figure 5.19). Focal areas within the *mdx* caudate putamen showed obvious signs of Gd uptake (Figure 5.21) The *Cmah-/-mdx* mice had a similar level of Gd in the caudate putamen compared to that of control *C57BL/10* mice, with a concentration of 9±3.8 μM detected. Again the *Cmah-/-* mice had the lowest levels of Gd detected at 42 minutes post injection, with a concentration of 3.3±1.9 μM Gd in the caudate putamen. At 14 months old there was an increase in Gd concentration in the caudate putamen of control *C57BL/10*, *mdx,* and *Cmah-/-mdx* mice, but the *mdx* mice still had the highest concentration of Gd detectable, 42 minutes post Gd-injection, at 18.6±2.8 μM Gd, and the *Cmah-/-mdx* mice and control *C57BL/10* mice had comparable levels to each other with 13.3±5.1 μM Gd and 13.6±0.8 μM Gd detected. The *Cmah-/-* mice displayed similar levels of Gd uptake in the caudate putamen at 14 months to that detected at 6 months old with a level of 3.2±3.4 μM Gd with no focal areas of Gd uptake detected unlike that seen for the other genotypes (Figure 5.23).

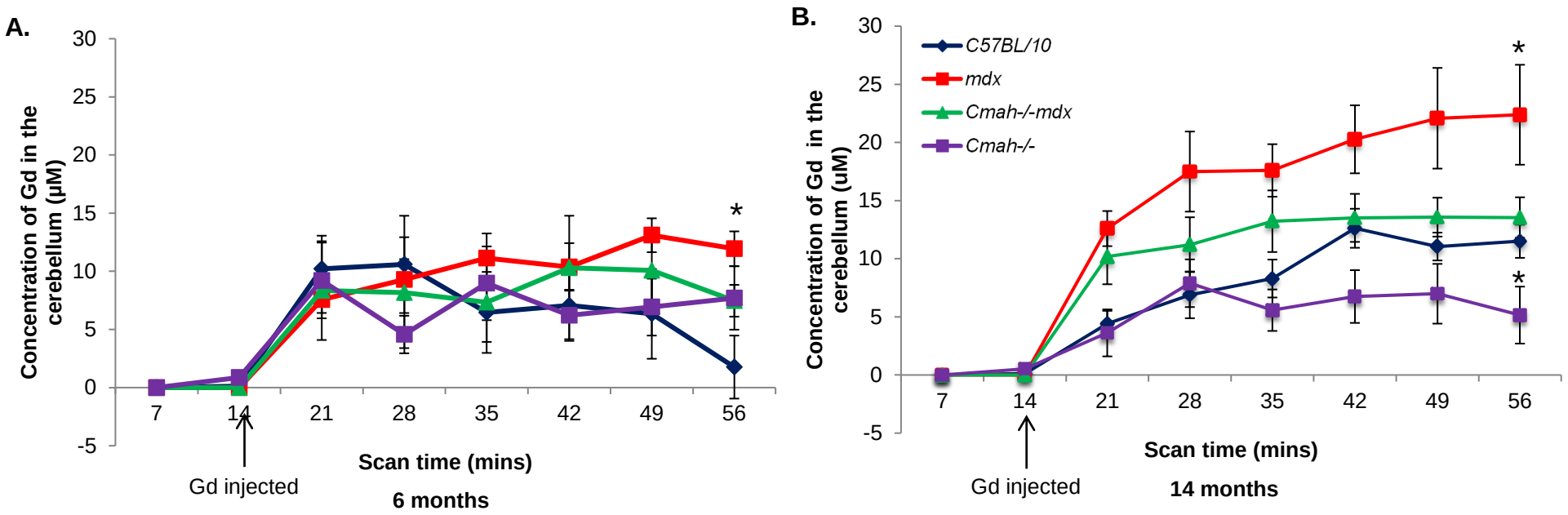

Figure 5.15: Line graphs displaying the concentration of gadolinium (Gd) within the cerebellum. A. The concentration of Gd within the cerebellum at 6 months old (n=4 mice per genotype). The *mdx* mice displayed the highest concentration of Gd within the cerebellum, which persisted up to 42 mins post Gd injection. **B.** The concentration of Gd within the cerebellum at 14 months old (n=6-7 mice per genotype). The *mdx* mice again displayed the highest concentration of Gd within the cerebellum, which appeared to be increasing still beyond 42 mins post Gd injection. The concentration of Gd within the *mdx* cerebellum was higher at 14 months than at 6 months old whereas all other genotypes displayed a similar level of Gd within the cerebellum at 6 and 14 months old. Data presented as mean ± SEM, *p<0.05 vs control *C57BL/10* mice.

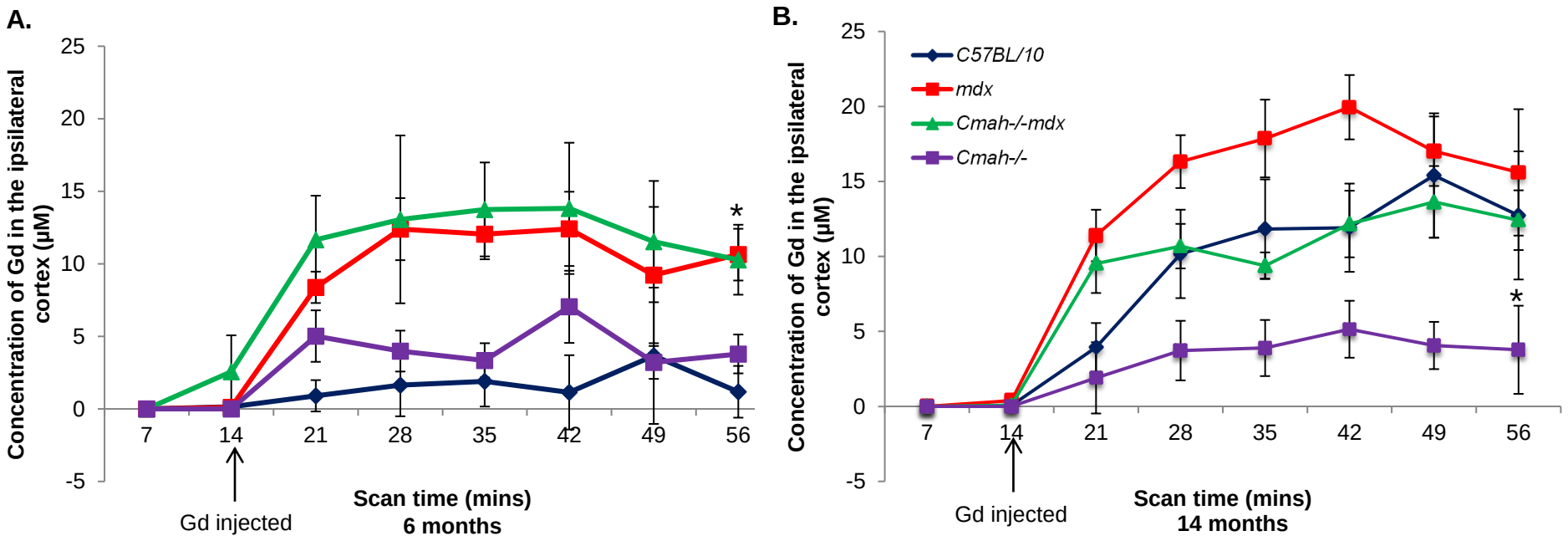

Figure 5.16: Line graphs displaying the concentration of gadolinium (Gd) within the ipsilateral cortex. A. The concentration of Gd within the ipsilateral cortex at 6 months old (n=4 mice per genotype). The DMD mice displayed the highest concentration of Gd within the ipsilateral hemisphere, which persisted up to 42 mins post Gd injection. **B.** The concentration of Gd within the ipsilateral hemisphere at 14 months old (n=6-7 mice per genotype). The *mdx* mice displayed the highest concentration of Gd within the ipsilateral hemisphere but there was also an increase in Gd concentration in the control *C57BL/10* mice ipsilateral hemisphere. The *Cmah-/-* mice showed comparable levels of Gd within the ipsilateral hemisphere at 6 and 14 months old. Data presented as mean ± SEM, *p<0.05 vs control *C57BL/10* mice.

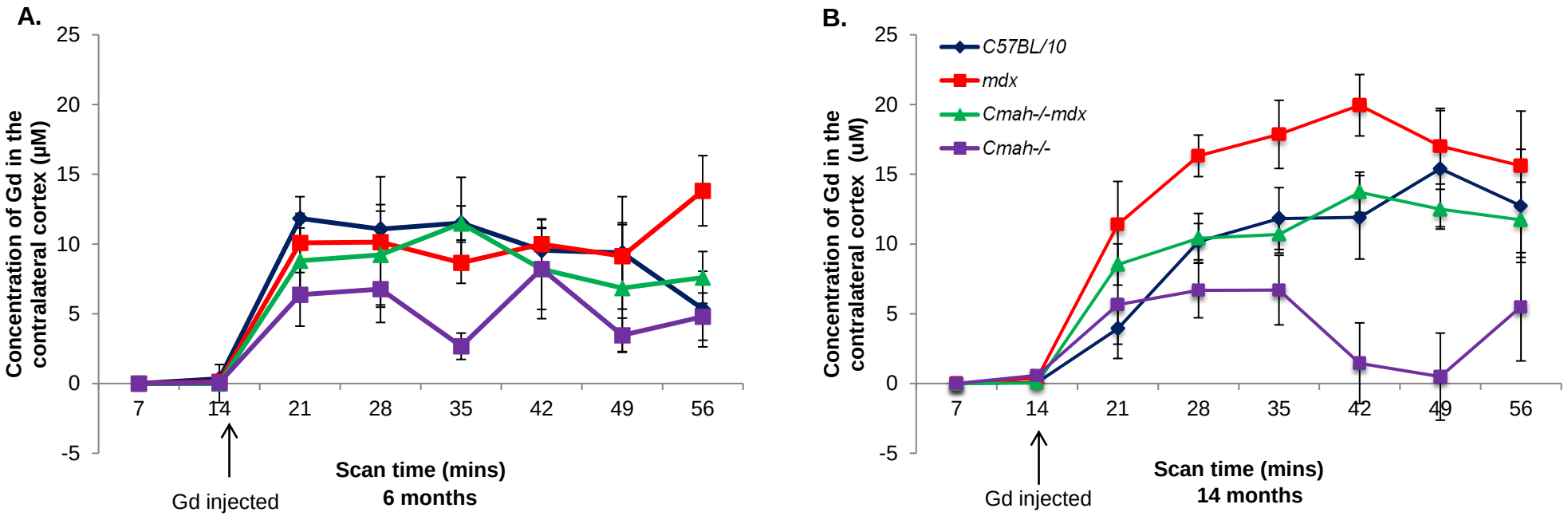

Figure 5.17: Line graphs displaying the concentration of gadolinium (Gd) within the contralateral cortex. A. The concentration of Gd within the contralateral hemisphere at 6 months old (n=4 mice per genotype). At 6 months old all mice, regardless of genotype, displayed comparable amounts of Gd within the contralateral hemisphere, except the *mdx* mice at 42 minutes post-Gd injection where there appeared to be a sharp increase in Gd concentration. **B.** The concentration of Gd within the contralateral hemisphere at 14 months old (n=6-7 mice per genotype). The *mdx* mice displayed the highest concentration of Gd within the contralateral hemisphere, but there is also an increase in Gd concentration in the control *C57BL/10* mice contralateral hemisphere. The *Cmah-/-mdx* and *Cmah-/-* mice showed comparable levels of Gd within the contralateral cortex at 6 and 14 months old. Data presented as mean ± SEM.

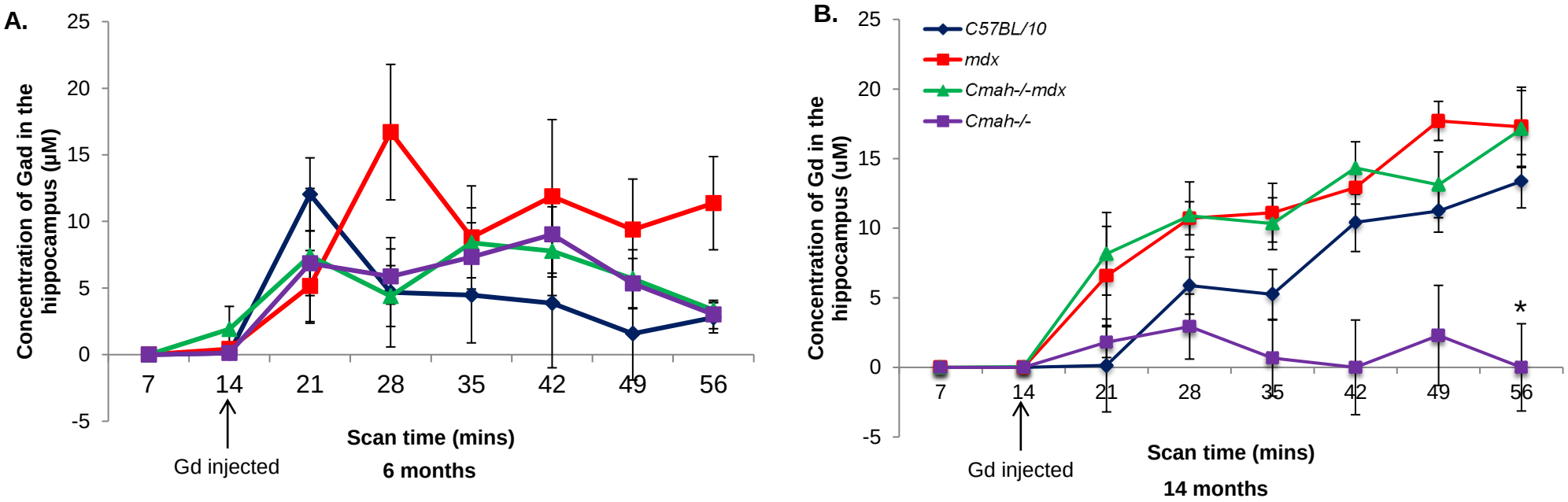

Figure 5.18: Line graphs displaying the concentration of gadolinium (Gd) within the hippocampus. A. The concentration of Gd within the hippocampus at 6 months old (n=4 mice per genotype). At 6 months the *mdx* mice appeared to have a slight increase in the concentration of Gd within the hippocampus, all other genotypes display comparable amounts of Gd within the hippocampus. **B.** The concentration of Gd within the hippocampus at 14 months old (n=6-7 mice per genotype). The DMD mice displayed the highest concentration of Gd within the hippocampus at 14 months old, but there was also an increase in Gd concentration in the control *C57BL/10* mice hippocampus. The *Cmah-/-* mice showed comparable levels of Gd within the hippocampus at 6 and 14 months old. Data presented as mean ± SEM, *p<0.05 vs control *C57BL/10* mice.

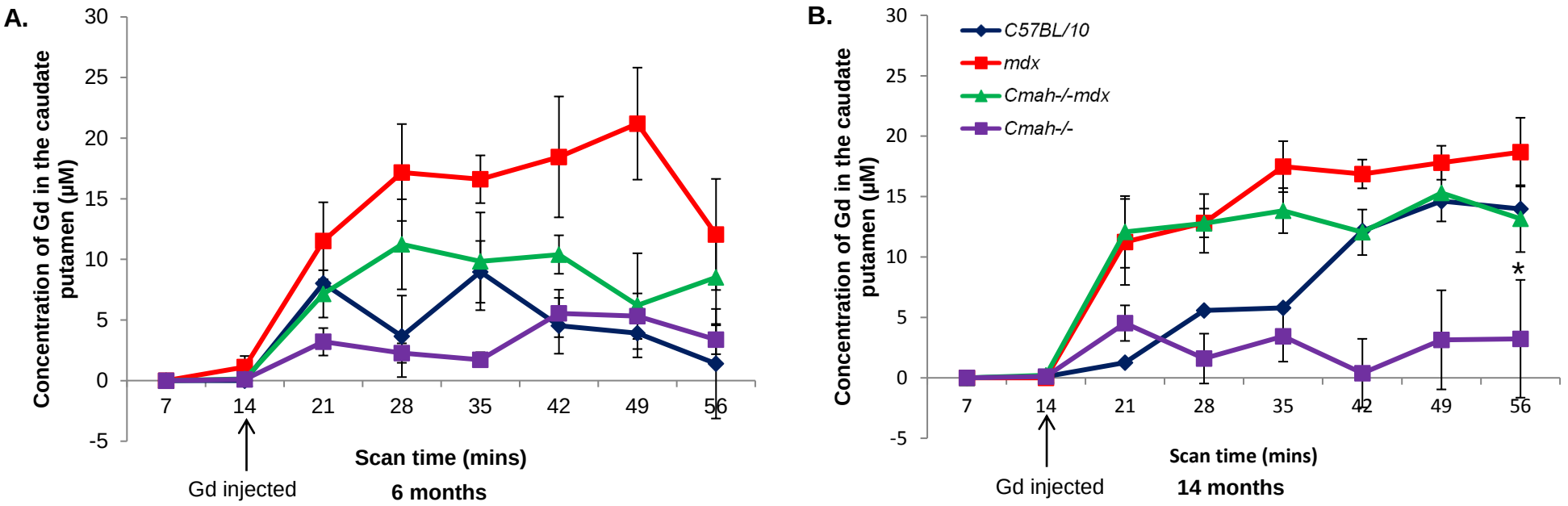

Figure 5.19: Line graphs displaying the concentration of gadolinium (Gd) within the caudate putamen. A. The concentration of Gd within the caudate putamen at 6 months old (n=4 mice per genotype). At 6 months the *mdx* mice appeared to have an increase in the concentration of Gd within the caudate putamen, all other genotypes displayed comparable amounts of Gd within the caudate putamen. **B.** The concentration of Gd within the caudate putamen at 14 months old (n=6-7 mice per genotype). The *mdx* showed a comparable level of Gd in the caudate putamen at 6 and 14 months old, except at 14 months old the concentration of Gd within the caudate putamen appeared to be increasing still beyond 42 mins post Gd injection There was an increase in Gd concentration in the control *C57BL/10* mice and *Cmah-/-mdx* mice caudate putamen between 6 and 14 months old. The *Cmah-/-* mice showed comparable levels of Gd within the caudate putamen at 6 and 14 months old. Data presented as mean ± SEM, *p<0.05 vs control *C57BL/10* mice.

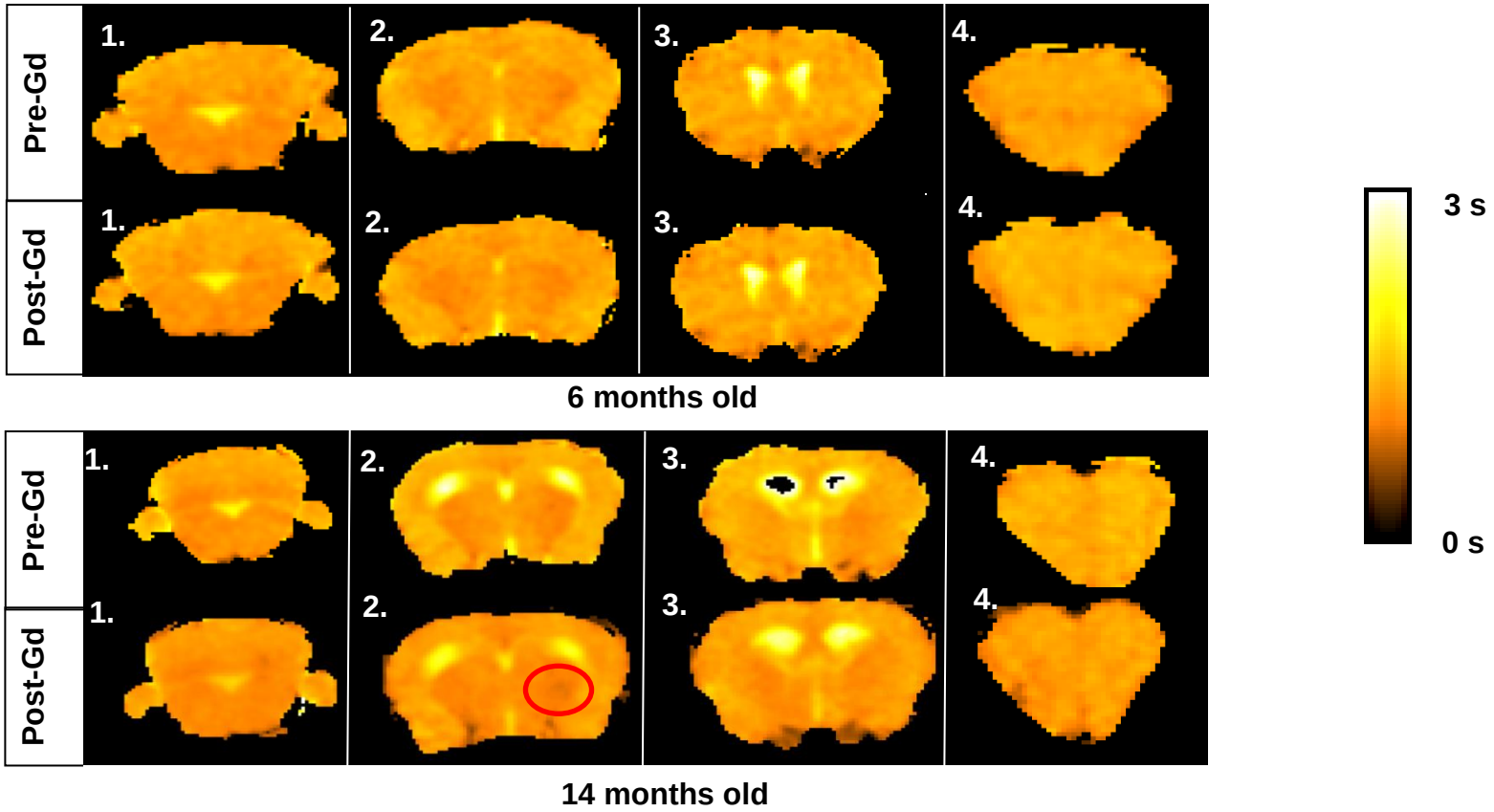

Figure 5.20: Representative T_1 maps for control *C57BL/10* mice pre- and post-gadolinium (Gd) enhancement at 6 and 14 months old. Image 1 represents the cerebellar region, image 2 represents the hippocampus and caudate putamen, image 3 represents the brain ventricles and the caudate putamen, and image 4 represents the cortex. The intensity was measured between 0 and 3 seconds, where a darker red indicates areas of increased change in T_1 signal (increased Gd detected) and therefore a shortening of tissue relaxation time. Red circle indicates focal areas of enhancement within the brain. At 6 months old there was little enhancement in any brain region but at 14 months old an increase in Gd was detected in the caudate putamen in particular (red circle).

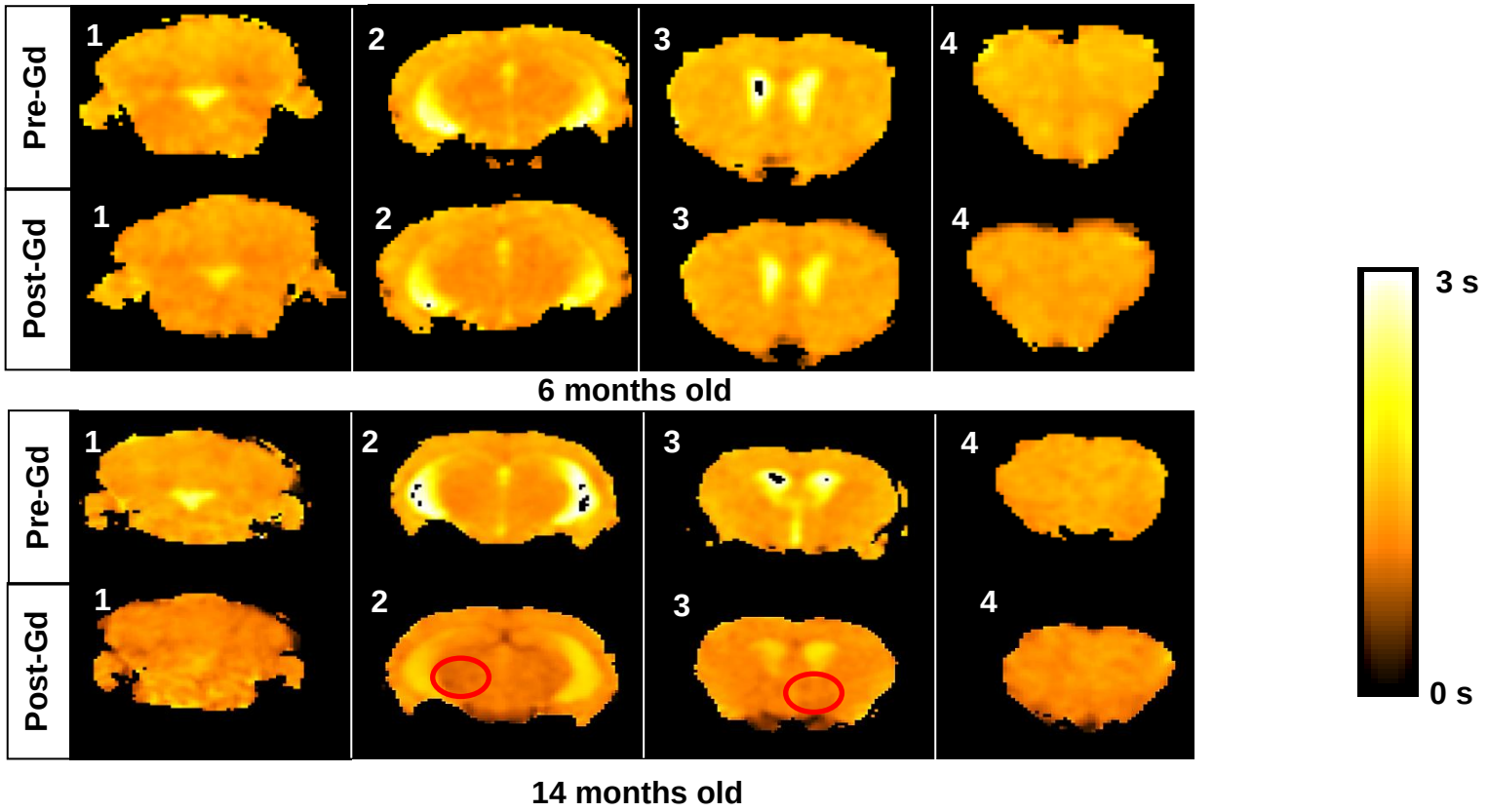

Figure 5.21: Representative T_1 maps for *mdx* mice pre- and post-gadolinium (Gd) enhancement at 6 and 14 months old. Image 1 represents the cerebellar region, image 2 represents the hippocampus and caudate putamen, image 3 represents the brain ventricles, and the caudate putamen, and image 4 represents the cortex. The intensity was measured between 0 and 3 seconds, where a darker red indicates areas of increased change in T_1 signal (increased Gd detected) and therefore a shortening of tissue relaxation time. Red circle indicates focal areas of enhancement within the brain. At 6 months old there was some enhancement in the caudate putamen and cerebellum but at 14 months old there was an increase in Gd detected in these regions. The ventricles were harder to distinguish in the post-Gd maps at 14 months old in *mdx* mice. These findings suggest increased blood-brain barrier impairment with age in *mdx* mice.

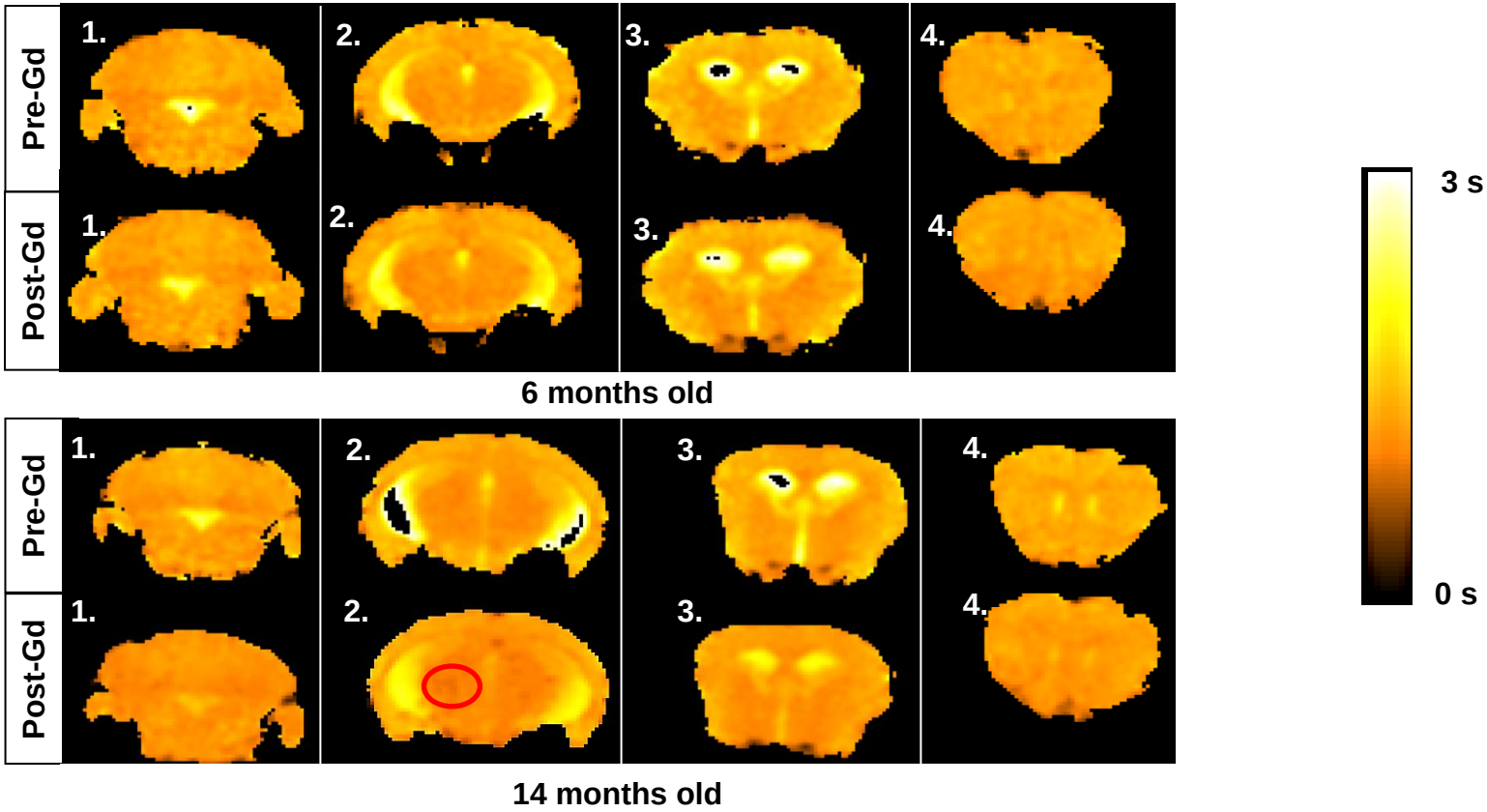

Figure 5.22: Representative T_1 maps for *Cmah-/-mdx* mice pre- and post-gadolinium (Gd) enhancement at 6 and 14 months old. Image 1 represents the cerebellar region, image 2 represents the hippocampus and caudate putamen, image 3 represents the brain ventricles and the caudate putamen, and image 4 represents the cortex. The intensity was measured between 0 and 3 seconds, where a darker red indicates areas of increased change in T_1 signal (increased Gd detected) and therefore a shortening of tissue relaxation time. Red circle indicates focal areas of enhancement within the brain. At 6 months old there was some enhancement in the brain but at 14 months old there was an increase in Gd detected. The ventricles were harder to distinguish in the post-Gd maps at 14 months old.

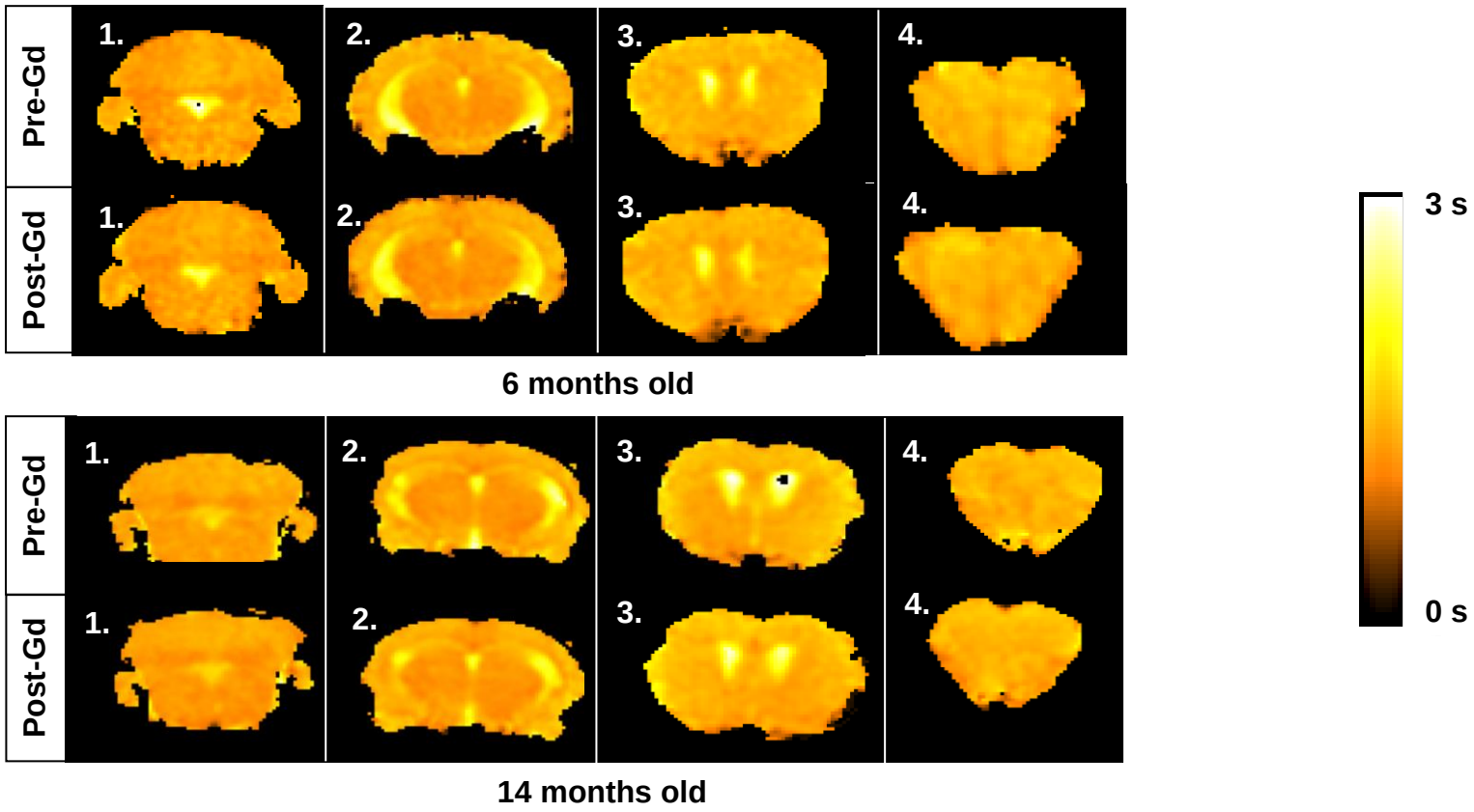

Figure 5.23: Representative T_1 maps for *Cmah-/-* mice pre- and post-gadolinium (Gd) enhancement at 6 and 14 months old. Image 1 represents the cerebellar region, image 2 represents the hippocampus and caudate putamen, image 3 represents the brain ventricles and the caudate putamen, and image 4 represents the cortex. The intensity was measured between 0 and 3 seconds, where a darker red indicates areas of increased change in T_1 signal (increased Gd detected) and therefore a shortening of tissue relaxation time. Red circle indicates focal areas of enhancement within the brain. Between 6 and 14 months old there was little difference in contrast enhancement in the *Cmah-/-* brain, with *Cmah-/-* mice demonstrated consistently very low to no levels of Gd in any ROI.

During this study we identified additional brain abnormalities in both the control *C57BL/10* and *mdx* mice. At the 14 months old time point one control *C57BL/10* and one *mdx* mice were identified with extreme hydrocephalus where the hydrocephalus was worse in the *mdx* than the control *C57BL/10* brain (Figure 5.24). This was only observed through MR imaging and the mice otherwise appeared healthy and did not display any abnormalities in head shape. As a consequence of this hydrocephalus the mice were not included in the analysis.

Furthermore, it was interesting to observe and compare the control *C57BL/10* mice brains to the mutant mice brains following Gd administration, as the control *C57BL/10* mice brain ventricles appeared bright, whereas the mutant mouse brain ventricles did not (Figure 5.25).

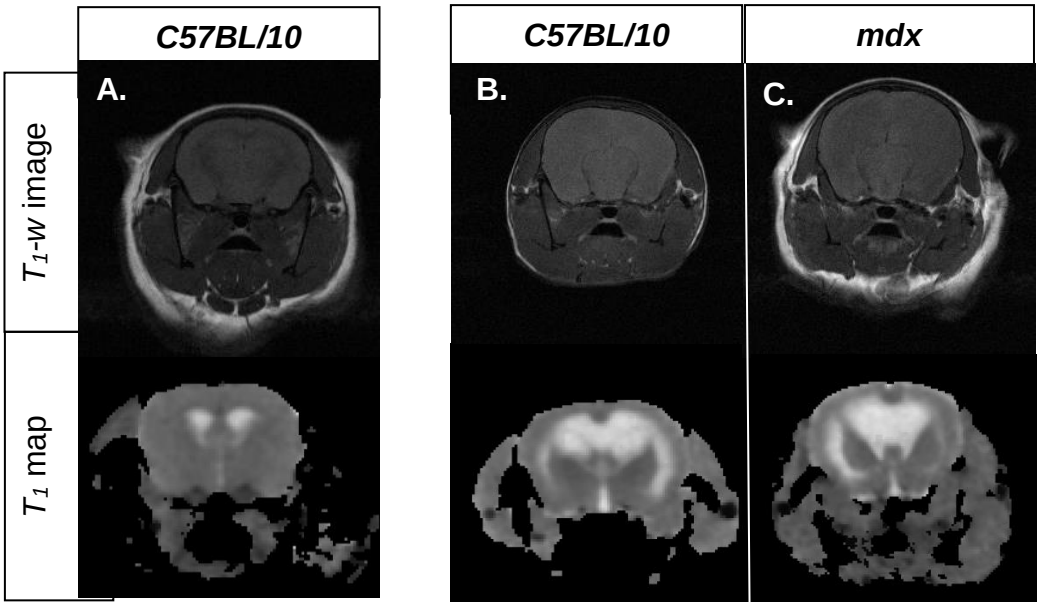

Figure 5.24: Representative T_1-w images and T_1 maps from control *C57BL/10* and *mdx* mice at 14 months old displaying normal brain structure vs. hydrocephalus. A. Representative T_1-w coronal image and T_1 map from a control *C57BL/10* mouse brain displaying the normal mouse brain structure, where the ventricles appeared bright on the T_1 map and were small in volume. **B.** Representative T_1-w coronal image and T_1 map from a control *C57BL/10* mouse brain displaying hydrocephalus. Note the larger size of the brain in the T_1-w image. The T_1 map image showed large ventricles which occupy the majority of brain tissue. **C.** Representative coronal T_1-w image and T_1 map from *mdx* mouse brain displaying hydrocephalus. The brain appeared even larger to that of control *C57BL/10* mouse brain with hydrocephalus and the T_1 map showed ventricles which are abnormally large.

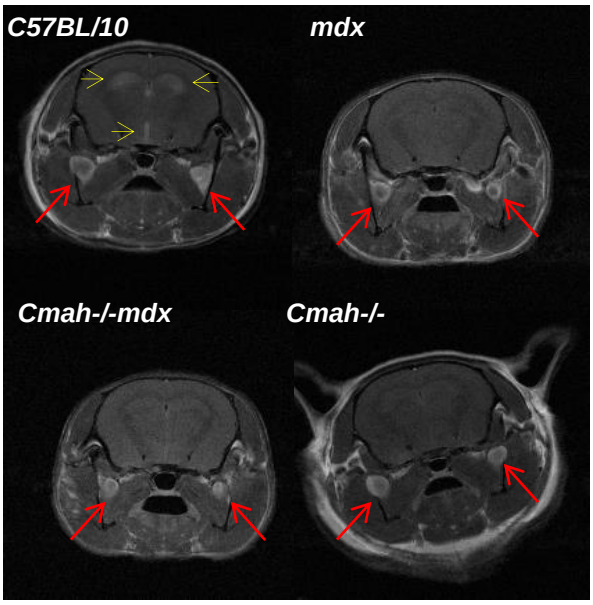

Figure 5.25: Representative *T_1-w* coronal images from control *C57BL/10*, *mdx*, *Cmah-/-mdx* and *Cmah-/-* mice displaying brain ventricles and vasculature following administration of gadolinium (Gd) at 14 months old. Successful uptake of Gd was confirmed when the vasculature appeared bright (red arrows). In the control *C57BL/10* mice the ventricles (lateral and third ventricles on image) appeared bright as well (yellow arrows). This effect was not observed in mutant mouse brains.

5.5 Discussion

The *mdx* mouse has previously been shown to exhibit dysfunction of the vascular compartment of the brain including brain oedema, alterations of the BBB, decreased levels of TJ - associated protein ZO-1, and reduced levels of AQP4, a glial protein (Frigeri *et al.*, 2001; Laws and Hoey, 2004; Nico *et al.*, 2005; Tamma *et al.*, 2013). AQP4 mediates the bidirectional transport of water molecules in brain tissue and is known to play a role in traumatic brain oedema (Iacovetta *et al.*, 2012). Under normal conditions, water moves in a bidirectional manner across the BBB, obeying the rules of osmosis, into the CNS and away via the CSF and venous circulation. A reduction or loss of AQP4 expression in the brain is found after trauma, stroke, haemorrhage and tumours, resulting in oedema and impaired ability to maintain ionic balance between cells and interstitial fluid (ISF) (Badaut *et al.*, 2014). Vasogenic brain oedema occurs when the BBB is disrupted due to the breakdown of tight endothelial junctions and mainly affects the white matter through leakage out of capillaries. Therefore we sought to determine the consequence of dystrophin deficiency on BBB function *in vitro* and *in vivo* in DMD mice, between the ages of 6 and 18 months old, to determine if this pathological aspect is progressive.

5.5.1 Changes in brain water content

As a non-invasive method, MRI has been used for evaluating brain oedema in patients and experimental animals. The *in vivo* T_2 of brain tissue is related to the local water environment and free-to-bound water ratio, which may change in response to cellular and axonal loss or membrane breakdown. The *Cmah-/-mdx* mice showed higher brain water content, reflected by an increase in the T_2 relaxation time, at 18 months old compared to all other genotypes. The *mdx* mice only showed a slight elevation in the T_2 relaxation times in the caudate putamen compared to control *C57BL/10* mice but other ROIs investigated showed a comparable T_2 relaxation time to that of control *C57BL/10* mice. Additionally the *Cmah-/-* mice showed a reduced T_2 relaxation time in the caudate putamen at both 6 months and 18 months old compared to all other genotypes.

The increase in T_2 relaxation time in the *Cmah-/-mdx* mouse brain at 18 months old is particularly interesting, as this suggests that it is a combination of the loss of full length dystrophin and Neu5Gc from the brain, which causes changes in the brain water content associated with vasogenic brain oedema, potentially causing the cognitive dysfunction we observe. The T_2 relaxation times in the *Cmah-/-mdx* mouse brain were comparable to that of the other genotypes at 6 months old; at 6 months old we did not observe any cognitive impairment on the Barnes maze or NOR task (see Chapter 4 for details). However, by 12 months old we found a huge increase in the time it took the *Cmah-/-mdx* mice to locate the target hole, suggesting that hippocampal spatial learning and memory was impaired at this age, which is consistent with the development of vasogenic oedema at an older age.

5.5.2 Evans blue dye (EBD) extravasation

Traditional EBD confirmed an interruption at the BBB, in both the 6 and 18 month old DMD mice with an increase in EBD extravasation observed at 18 months old. BBB disruption in *mdx* mice due to reduced expression of tight junction proteins has been reported previously (Nico *et al.*, 2001). We have also demonstrated a reduction in AQP4 expression by western blot analysis, in the DMD mice brains between 1 and 12 months old, where both the M1 and M23 isoforms were reduced with increasing age.

The lack of properly functioning AQP4 channels at the BBB in *mdx* mice may impair water clearance from the cerebrum and worsen cellular oedema. Consequently, the osmotic influx of water into the cell causes cellular oedema and a decrease in extracellular space. Alternatively, a leaky BBB may also lead to an increase of large molecules in the extracellular space in the *mdx* mouse brain and cause interruptions in the circulation. A recent study utilised EBD and a quantitative MRI technique to determine the extent of BBB impairment in *mdx* mice (aged 2-10 months old) (Goodnough *et al.*, 2014). The authors hypothesised that the reduction in water diffusivity in the *mdx* mouse brain was likely due to an increase in cerebral oedema or the existence of large molecules in the extracellular space, from a leaky BBB. Since we did not detect any noticeable changes in T_2 relaxation rates in any ROI of the *mdx* brain, we would suggest that a disruption of the BBB is likely causing an increase in large

molecules in the extracellular space and interruptions in the circulation, resulting in a cognitive defect.

5.5.3 T_1 mapping with gadolinium enhancement

There was a huge amount of variation between each mouse within a given genotype regarding the concentration of Gd for a particular ROI. It is already well established that there is variation in the *mdx* mouse muscle tissues, particularly in the extent of sarcolemma damage (Straub *et al.*, 1997). We saw the highest rate of variation between mice, regarding the concentration of Gd within a particular ROI, in the *mdx* mice, but the control *C57BL/10* mice also demonstrated a large amount of variation. Another obscure finding was the apparent uptake of Gd into the control *C57BL/10* mice brain ventricle system. In an intact BCSFB there should be no uptake of Gd into the brain ventricle system. These results therefore suggest that the control *C57BL/10* mice have a compromised blood-cerebrospinal fluid barrier (BCSFB), but since we did not observe any reduction in AQP1 expression it is therefore likely that the small reduction in AQP4 expression observed between 1 and 12 months old is allowing Gd to enter the ventricles. Interestingly the Gd uptake in the control *C57BL/10* mice brain ventricles was only evident at 14 months old. This effect could also be happening in DMD mouse brains, but since the reduction of AQP4 is much greater we did not see the uptake of contrast agent into the brain ventricles, as it is already diffusing into brain parenchyma.

The molecular weight of EBD is 961 g/mol whereas the molecular weight of gadolinium (Gadovist) is 604.7 g/mol therefore the Gd is smaller in size, which could account for why we did not see any extravasation of EBD in the control *C57BL/10* brain parenchyma, but we did observe small amounts of Gd extravasation into various brain ROIs.

The highest uptake of Gd in the *mdx* brain was observed in the cerebellum. The uptake of Gd into the *mdx* mouse cerebellum was higher at 6 months than at 14 months old, which suggests the integrity of the BBB decreases with increasing age. It was also higher than that observed in the control *C57BL/10* mice and in an ROI where dystrophin is enriched (Dp427p is lost from the *mdx* cerebellum). We also observed elevated levels of Gd in the *mdx* cortex (both ipsilateral and

contralateral hemispheres), which increased between 6 and 14 months old. Interestingly, the Gd concentration in the control *C57BL/10* mice cortex also increased between these two time points, suggesting that this could be an age related effect rather than a pathological result in the *mdx* mice. In the caudate putamen we also observed elevated levels of Gd uptake in the *mdx* mice. At 6 months old the *mdx* mice had the highest levels of Gd in the caudate putamen compared to all other genotypes. The levels of Gd remained consistent in the *mdx* mice caudate putamen at 14 months old, but increased in the *Cmah-/-mdx* mice between 6 and 14 months old. Other members of the brain DGC have been detected in the caudate putamen, β- and α-dystrobrevins were identified in subcortical structures of the caudate putamen (Blake *et al.*, 1998), which suggests (alongside these findings) that the brain DGC has a function within the mouse caudate putamen.

The *Cmah-/-* mice displayed the lowest uptake of Gd in any ROI investigated and the concentration of Gd detected did not increase between 6 and 14 months old, which was the opposite to what was identified in the other genotypes. The loss of the effect of the *Cmah* gene from mice at the BBB has not previously been reported, but it suggests that the loss of Neu5Gc expression confers resistance to BBB degradation. Consistent with this theory is that the *Cmah-/-mdx* mice did not display a higher concentration of Gd in any ROI to that of the *mdx* mice. From existing studies it cannot be established whether traces of Neu5Gc expression, in the brain are confined to endothelial and blood cells, or extend across the BBB. It was unusual to detect a reduced expression of AQP4 in the *Cmah-/-* mouse brain, which was lower than that detected in control *C57BL/10* mouse brain at corresponding time points. AQP4 null mice have shown similar features to those observed in other studies of the *Cmah-/-* mice, including impaired hearing (Kwon *et al.*, 2015) (Verkman, 2005). Additionally, we have demonstrated changes in brain ventricle volume in the *Cmah-/-* mice (see Chapter 3 for details) and it is therefore likely that the loss of Neu5Gc has an impact at the BCSFB too, but the mechanisms are yet to be defined. Further investigations into brain aquaporins in mice lacking the *Cmah* gene are necessary to determine the effects of Neu5Gc loss on brain function. Future studies should focus upon the characterization of the BBB in *Cmah-/-*

mice, as evolutionarily this could be a mechanism which was beneficial for human survival.

Interestingly, we also detected hydrocephalus in both the control *C57BL/10* and *mdx* mice at 14 months old. The level of hydrocephalus appeared to be exacerbated in the *mdx* mouse compared to the control *C57BL/10* mouse (larger brain and swollen brain ventricles). It is known that hydrocephalus occurs spontaneously in 1-3% of *C57BL/10* mice, but it was still unusual for the hydrocephalus to go unnoticed until 14 months old. Therefore, the genetic background of these mice may influence the development of hydrocephalus and this may not be a pathogenic consequence of the loss of neural Dp427.

5.5.3.1 Study limitations

The highest uptake of Gd into the *mdx* brain was observed in the cerebellum. The cerebellum consists of grey and white matter, which have different T_1 relaxation rates. The ROI was placed into a region of the cerebellum which contained both grey and white matter, since the structure of the cerebellum and the quality of the images does not allow for accurate delineation of an independent grey or white matter region. There is thus a small possibility that the ROIs in the different genotypes contained different ratios of grey and white matter tissue, although this should not affect the results drastically, it should be taken into consideration.

Unfortunately the caudate nucleus and putamen are not distinguishable in rodents. The myelinated fibres that penetrate the striatum to connect to the cerebral cortex and subcortical structures do not form an internal capsule, but are distributed throughout the striatum in the rodent brain. Thus, the rodent striatum is known as the ‘caudate putamen’ (Figure 5.26). Conversely, in humans it has two parts: the caudate nucleus and the putamen (Figure 5.26). The caudate nucleus encircles the putamen, separated from it by the internal capsule. Functionally the striatum co-ordinates multiple aspects of cognition in both rodents (Brovelli *et al.*, 2011) and humans (Grahn *et al.*, 2008). It is therefore possible that the differences in brain structure between mice and men give rise to the increased BBB permeability in the rodent caudate putamen.

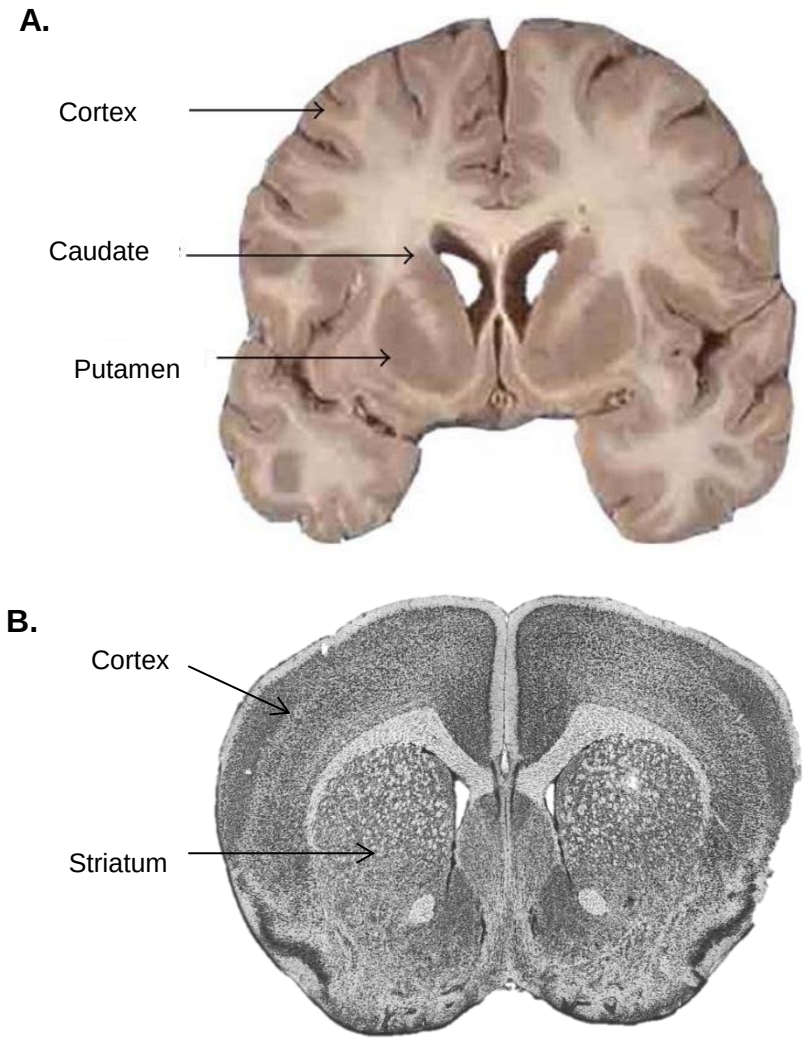

Figure 5.26: The caudate putamen in mice and men. A. Coronal section of a human brain showing the cortex, the caudate, and the putamen separately that when combined make up the striatum in comparison to **B.** caudal section of a nissl stained mouse brain showing the striatum as one structure and the cortex. Figure adapted from (Evans *et al.*, 2012) and (Paxinos, 2008).

Given the large amount of variation we observed between mice within a genotype, it is difficult to come to a concrete conclusion as to whether the T_1-mapping with Gd enhancement is a sensitive enough qualitative biomarker to monitor BBB integrity over time. Future studies should aim to optimise this technique by increasing the scanning protocol time, since it was evident that at 14 months old (and 6 months old for certain ROIs) the Gd had not completely been removed in the *mdx* mouse brain, as Gd concentrations were increasing at the last scan time (42 minutes post injection). The literature states that clearance of Gd based agents in wild type mice is very significant by 60-80

minutes (Senanayake *et al.*, 2017), which is why we opted to scan for 90 minutes total. The Gd also appeared to persist in the control *C57BL/10* mouse brains at 14 months old as the Gd concentration had not returned to baseline as it did in the 6 month old control *C57BL/10* mice. This suggests that there is a decline in kidney and liver function in older control *C57BL/10* mice, which is the clearance route of Gd, although we did not look specifically and kidney or liver function this would be interesting to address clearance rates in future studies. Increasing the number of mice studied would undoubtedly improve the findings, either by confirming that variation regarding Gd uptake is present in a larger sample of mice (including control mice), or by producing an overall effect in a genotype. Additionally, monitoring the same mouse over time to detect BBB impairment on an individual basis would be the gold-standard method; this was not possible in our study due to scanning related problems.

Overall, we have demonstrated a progressive decline in BBB integrity in DMD mice together with reduced AQP4 expression, increased EBD extravasation, and increased Gd concentration in various ROIs. A close relationship between AQP4 and the BBB integrity has been demonstrated, as AQP4 protein is developmentally expressed during BBB differentiation. Replacement of AQP4 at the BBB could be one potential target to ameliorate BBB dysfunction in DMD mice and subsequently improve cognitive functioning.

Chapter 6. Proteomic profiling in the *mdx* mouse cerebellum

6.1 Introduction

Proteomics is a reliable, powerful and very sensitive state of the art technique, which has become an important tool in the field of neuromuscular disease research due to the unique ability to quantify thousands of proteins, in one approach, in an unbiased manner (Roos *et al.*, 2016). Biomedical surveys established on mass spectrometry-based proteomics can provide a comprehensive overview of molecular changes that underlie paediatric disorders and identify novel proteomic biomarker candidates for improving predictive, diagnostic, prognostic and therapy-monitoring processes (Murphy *et al.*, 2015).

Numerous studies to date have argued that the cognitive abnormalities associated with DMD could be classified as a cerebellar disorder due to the absence of full-length dystrophin (Dp427-p) in the cerebellum (Cyrulnik and Hinton, 2008). The cerebellum contains four times more cells than the cerebral cortex and houses a staggering number of neurons (Andersen *et al.*, 1992). These neurons are arranged uniformly in self-contained units consisting of a Purkinje cell (PCs) and the associated molecular and granular cell neurons. The PC is the primary output neuron of the cerebellum and it is thus likely that disruption of the PC structure will have a widespread impact on signalling efficiency (Elizabeth and Molliver, 2001).

The cerebellum has a predominant role in controlling motor coordination (Snow *et al.*, 2013) and more recently studies have confirmed the importance of the cerebellum in non-motor functions including cognitive processing (Yoshihara *et al.*, 2003). The major anatomical subdivisions of the cerebellum include the flocculonodular lobe, which receives information on balance and equilibrium (Tokarz *et al.*, 1998), and the lateral and vermal hemispheres. It has been widely documented that damage to the vermal hemisphere results in impaired motor behaviour, affecting equilibrium (Glickstein and Doron, 2008). Damage to the lateral hemisphere, which has received less attention, indicates this as

being the cerebellar region involved in cognition (Akshoomoff and Courchesne, 1992).

Dp427-p, the third full length dystrophin gene product, is expressed in the PCs, and in the wild type mouse dystrophin expression was found to be limited to the puncta on somatic and dendritic membranes of both the vermal and lateral cerebellum (Snow *et al.*, 2013). Furthermore, the density of dystrophin expression was greatest in the lateral cerebellum, associated with cognitive ability, compared with vermal dystrophin expression (Snow *et al.*, 2013). Dystrophin loss has also been associated with the dysfunction of signalling at the GABA synapses on PCs, potentially by destabilisation of $GABA_A$ receptor clusters ($GABA_A$ –R's) (Snow *et al.*, 2014). Intrinsic electrophysiological properties have recently been investigated and demonstrated that the membrane potential of PCs from the vermal region of wild type mice exhibited a significant hyperpolarisation, along with a concurrent reduction in the frequency of spontaneous action potentials compared with PCs from the lateral region (Snow *et al.*, 2014). This regional hyperpolarisation and concurrent reduction in frequency was abolished in *mdx* mice, indicating a difference in electrophysiological properties in the absence of full length dystrophin (Snow *et al.*, 2014). Furthermore, firing frequency in the lateral cerebellum was also reduced in PCs of *mdx* mice relative to wild type mice (Snow *et al.*, 2014).

Within the cerebellum, a decrease in the number of PCs has been reported in DMD patients at autopsy. In the only Golgi-staining study of dendritic morphology in DMD patients (Koenig *et al.*, 1988) investigators noted decreased dendritic length and decreased dendritic branching in brains of all patients examined, although the visual cortex was the only region investigated (Jagadha and Becker, 1988). Moreover, the post-mortem studies are limited in number and often consist of a small number of cases of multiple myopathies that are not always restricted to DMD patients.

The current literature highlights that cognitive impairments associated with DMD may be mediated by the loss of dystrophin predominantly associated with the lateral portion of the cerebellum. Given the varied nature and occurrence of cognitive abnormalities seen within the DMD patient cohort, numerous

questions arise regarding the origin of the molecular and cellular pathogenesis of these brain abnormalities. Unbiased comparative proteome profiling has the potential to identify complex global changes within cellular systems compared to individual and hypothesis-driven biochemical, cell biological or physiological investigations.

Previous systematic proteomic studies have demonstrated a number of changes in proteins involved in energy metabolism, cellular signalling, the extracellular matrix, cytoskeletal networks, and the cellular stress response in dystrophic skeletal and cardiac muscles (Holland *et al.*, 2013). More recently, a label-free mass spectrometric analysis revealed complex changes in the brain proteome from the *mdx*^{4cv} (transgenic mouse lacking any dystrophin isoforms) model of DMD. These included an increase in expression of glial fibrillary acidic protein (GFAP), the neuronal Ca^{2+} binding protein calretinin, annexin A5, vimentin, the neuron-specific enzyme ubiquitin carboxyl-terminal hydrolase isozyme L1, the dendritic spine protein drebrin, the cytomatrix protein bassoon of the nerve terminal active zone, and the synapse-associated protein SAP97 (Murphy *et al.*, 2015). Additionally, the *mdx*^{4cv} serum reveals highly elevated levels of the inflammation-induced plasma marker haptoglobin, using a comparative proteomic approach (Murphy *et al.*, 2017).

6.1.1 Aims

The aim of this chapter is to identify the molecular nature of pathophysiological processes caused by dystrophin deficiency in the cerebellum of *mdx* mice at 6 months old using comparative proteomic techniques. Previous literature (Huard and Tremblay, 1992; Kueh *et al.*, 2011; Snow *et al.*, 2013; Snow *et al.*, 2014) and results presented in chapters of this thesis have established changes in the cerebellum of *mdx* mice; hence we chose to investigate the *mdx* cerebellum at the biochemical level.

Different therapeutic approaches for DMD not only target restoration of dystrophin expression, but also modulation of pathophysiological cellular cascades in order to antagonise the detrimental molecular effects caused by dystrophin deficiency. The principal goal of this chapter is to provide an understanding of the biochemical processes contributing to cognitive impairment in the genesis of DMD. This will not only provide a better understanding of the nature of cognitive impairment in DMD, but will potentially identify biomarkers in the brain which are suitable for therapeutic intervention.

As membrane proteins are notoriously underrepresented in a normal shotgun proteomic approach, we aimed to further enrich membrane proteins via carbonate extraction and subjected these to protein profiling utilising mass spectrometry. This additional procedure helped to enable a more accurate and robust detection of direct targets of loss of Dp427 as a membrane associated protein. The differential expression patterns of identified proteins was confirmed through immunoblotting and/or immunofluorescence (IF) microscopy.

6.2 Identification of proteome wide changes in the CNS

The workflow for global protein extraction and membrane enriched protein extraction is outlined in Figure 6.1. Within the CNS, dystrophin expression is highest in the cerebellum, where it is localized as discrete puncta along the somatic and dendritic membranes of PCs (Yoshida *et al.*, 1994) in both mouse (Lidov *et al.*, 1990) and human studies. The protein, visualised by immunogold electron microscopy, is predominantly expressed at postsynaptic sites (Lidov *et al.*, 1990), including dendritic spines (Jancsik & Hajos, 1998). Dystrophin is extensively colocalised with a subset of $GABA_A$-R's clusters in the typical brain, including in the cerebral cortex, hippocampus, and cerebellum (Knuesel *et al.*, 1999), our preliminary data shows reduced abundance of membrane-resident AQP4 in DMD mouse brains (chapter 5), putting an increased emphasis on membrane proteins. However, it is well known that these proteins are underrepresented in protein lysates generated with common extraction methods. In order to overcome this problem, we used carbonate extraction methods to separate cytosolic and membrane proteins and analyse both fractions separately via liquid chromatography-mass spectrometry (LC-MS/MS). The "Tissue Omics" group of the Leibniz-Institute of Analytical Science (ISAS e.V.) in which the proteomic investigations were performed, has substantial experience in the application of the strategy (Labisch *et al.*, 2017). Assays for protein content and plasma membrane markers allow calculation of the yield and extent of plasma membrane enrichment by 70%. This parallel investigation of membrane and cytosolic proteins combined with faithful pathway analyses has enabled this study to better assess the question of how loss of dystrophin affects both, membrane and cytosolic/cytoskeletal proteins, and how these proteins are functionally interconnected in neuronal maintenance

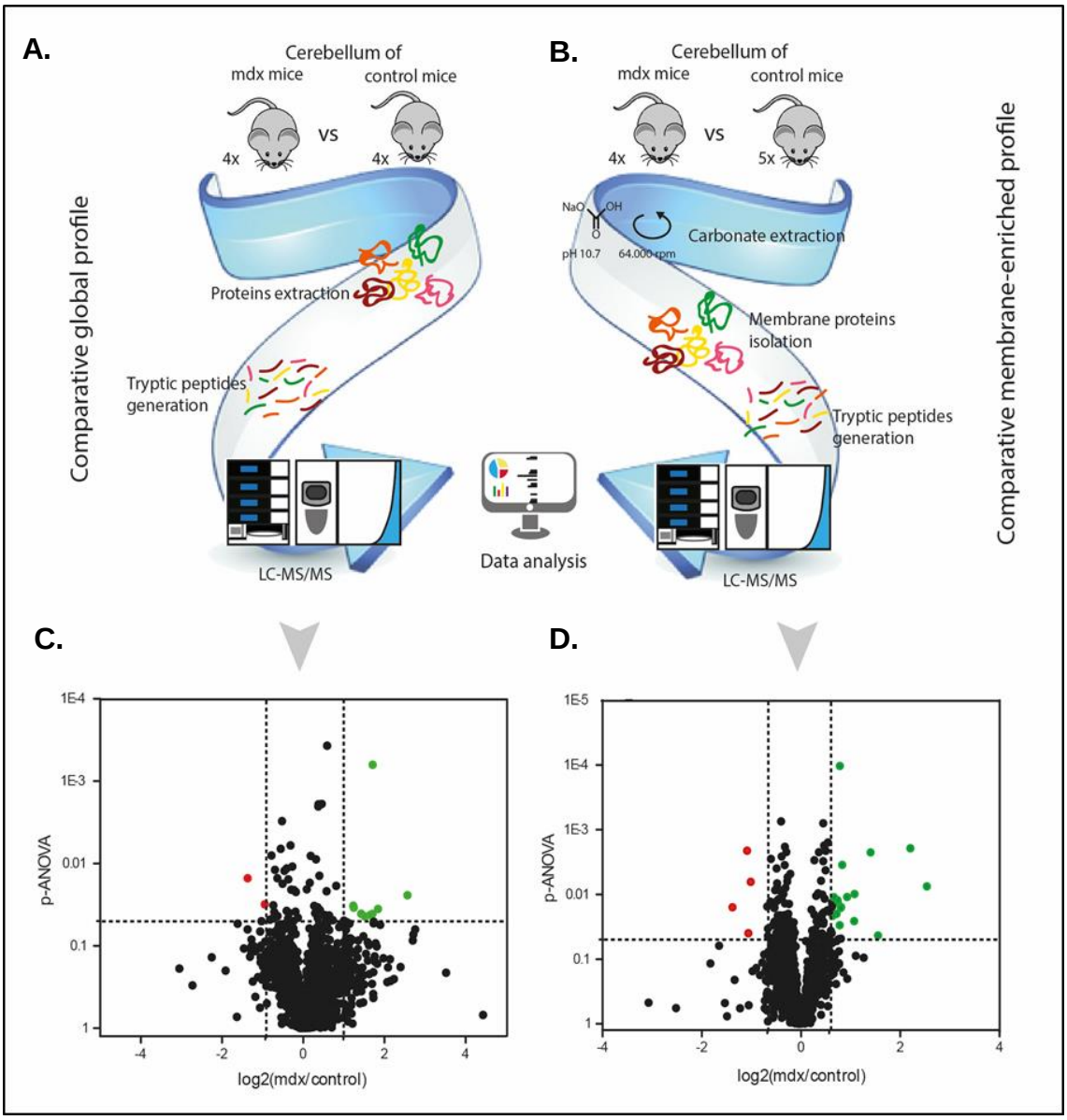

Figure 6.1: Proteomic studies on *mdx* and control (*C57BL/10*) mouse cerebella. **A.** Workflow for global proteome profiling. **B.** Workflow to enrich membrane proteins followed by subsequent liquid chromatography – mass spectrometry (LC-MS/MS). **C.** Volcano plot of proteomic findings obtained from global protein extracts derived from *mdx* and control *C57BL/10* mice cerebella. **D.** Volcano plot of proteomic findings obtained in protein extracts enriched for membrane proteins derived from *mdx* and control *C57BL/10* mice cerebella. In both volcano plots, proteins with decreased abundances are represented as red dots, whereas proteins with increased abundance are highlighted by green dots.

6.2.1 Cerebellar global protein extraction

Cerebellar proteins identified with an increased concentration, with two or more unique peptides, in the *mdx* mouse included: thrompospondin-1 (TSP-1), fibrinogen α and β chains, Ig kappa chain C region, acetyl-coenzyme thioesterase, peptidyl-prolyl cis-trans isomerase FKBP3, aspartoacylase, and NADH dehydrogenase 1 beta subcomplex subunit 3, 9 and 10 (Table 6.1). Proteins with an identified statistically significant decreased abundance in the *mdx* cerebellum included: the 60S acidic ribosomal protein P1, Rho GTPase-activating protein 21, and histone deacetylase 6 (Table 6.1).

Cerebellar proteins with an increased concentration, with one unique peptide, in the *mdx mice* included: SH3 and multiple ankyrin repeat domains protein 3, and synaptoporin (Table 6.2). Whereas proteins with a decreased abundance in the *mdx* cerebellum, identified with one unique peptide, included: bifunctional 3'-phosphoadenosine 5'-phosphosulfate synthase 1, U6 snRNA-associated Sm-like protein LSm8, and coiled-coil domain-containing protein 58 (Table 6.2).

.

Global protein extraction						
Accession number	**Protein name**	**Peptide count**	**Anova (p)**	**Fold change (Log_2)**	**Subcellular localisation**	**Protein function**
E9PV24	Fibrinogen alpha chain	11	0.03	**1.25**	Secreted	Cleaved by the protease thrombin to yield monomers which, together with fibrinogen beta (FGB) and fibrinogen gamma (FGG), polymerize to form an insoluble fibrin matrix. May also facilitate the immune response via both innate and T-cell mediated pathways.
P01837	Ig kappa chain C region	4	0.04	**1.71**	Membrane	Antigen activates B Cell Receptor (BCR) leading to generation of second messengers.
P35441	Thrombospondin-1	2	0.02	**2.57**	Endoplasmic reticulum, sarcoplasmic reticulum	Adhesive glycoprotein that mediates cell-to-cell and cell-to-matrix interactions.
P47955	60S acidic ribosomal protein P1	6	0.02	**-0.63**	Cytoplasm	Plays an important role in the elongation step of protein synthesis.
Q3UUI3	Acyl-coenzyme A thioesterase THEM4	2	0.00	**1.72**	Cytosol, mitochondrion	Inhibits AKT1 phosphorylation and activity. Interacts with AKT1. Expressed predominantly in skeletal muscle, testis, uterus, brain and kidney. Down-regulated in glioblastoma or glioma compared to non-neoplastic brain due to promoter hypermethylation.
Q62446	Peptidyl-prolyl cis-trans isomerase FKBP3	3	0.04	**0.64**	Cytoplasm, nucleus	Constitutes a family of receptors for the two immunosuppressants which inhibit T-cell proliferation by arresting two distinct cytoplasmic signal transmission pathways.
Q6DFV3	Rho GTPase-activating protein 21	2	0.05	**-0.73**	Golgi apparatus membrane, peripheral membrane protein, cell junction, cytoplasm, cytoskeleton	Functions as a GTPase-activating protein (GAP) for RHOA and CDC42. Downstream partner of ARF1 which may control Golgi apparatus structure and function.
Q8K0E8	Fibrinogen beta chain	6	0.02	**0.82**	Secreted	Cleaved by the protease thrombin to yield monomers which, together with fibrinogen alpha (FGA) and fibrinogen gamma (FGG), polymerize to form an insoluble fibrin matrix. May also facilitate the immune response via both innate and T-cell mediated pathways.

Q8R3P0	Aspartoacylase	5	0.04	**0.64**	Cytoplasm, nucleus	Catalyzes the deacetylation of N-acetylaspartic acid (NAA) to produce acetate and L-aspartate. NAA occurs in high concentration in brain and its hydrolysis NAA plays a significant part in the maintenance of intact white matter.
Q9CQJ8	NADH dehydrogenase 1 beta subcomplex subunit 9	4	0.04	**1.66**	Mitochondrion inner membrane	Accessory subunit of the mitochondrial membrane respiratory chain NADH dehydrogenase (Complex I), that is believed to be not involved in catalysis. Complex I functions in the transfer of electrons from NADH to the respiratory chain.
Q9CQZ6	NADH dehydrogenase 1 beta subcomplex subunit 3	2	0.04	**1.85**	Mitochondrion inner membrane	Accessory subunit of the mitochondrial membrane respiratory chain NADH dehydrogenase (Complex I), that is believed to be not involved in catalysis. Complex I functions in the transfer of electrons from NADH to the respiratory chain.
Q9DCL9	Multifunctional protein ADE2	5	0.05	**0.74**	Cell-cell adherens junctions, cytoplasm, extracellular exosome, membrane	This protein is involved in step 1 of the subpathway that synthesizes 5-amino-1-(5-phospho-D-ribosyl) imidazole-4-carboxamide from 5-amino-1-(5-phospho-D-ribosyl) imidazole-4-carboxylate.
Q9DCS9	NADH dehydrogenase 1 beta subcomplex subunit 10	6	0.03	**1.43**	Mitochondrion inner membrane	Accessory subunit of the mitochondrial membrane respiratory chain NADH dehydrogenase (Complex I), that is believed to be not involved in catalysis. Complex I functions in the transfer of electrons from NADH to the respiratory chain.
Q9Z2V5	Histone deacetylase 6	2	0.01	**-0.78**	Nucleus, cytoplasm, perikaryon	Responsible for the deacetylation of lysine residues on the N-terminal part of the core histones.

Table 6.1: Proteins altered in abundance in *mdx* cerebellar tissue as revealed by label-free liquid chromatography – mass spectrometry (LC–MS/MS) analysis following global protein extraction identified with two or more unique peptides. Proteins in green were elevated in the *mdx* (n=4) cerebellum compared to control C57BL/10 (n=4) cerebellum at 6 months old. Red proteins had decreased abundance in *mdx* cerebellum compared to control cerebellum. Information regarding protein function was obtained from UniPort (Pundir *et al.*, 2017).

Global protein extraction						
Accession number	**Protein name**	**Peptide count**	**Anova (p)**	**Fold change (Log_2)**	**Subcellular localisation**	**Protein function**
Q4ACU6	SH3 and multiple ankyrin repeat domains protein 3	1	0.05	**1.01**	Cytoplasm, cell junction, synapse, cell junction, synapse, postsynaptic cell membrane, postsynaptic density, cell projection, dendritic spine	Major scaffold postsynaptic density protein which interacts with multiple proteins and complexes to orchestrate the dendritic spine and synapse formation, maturation and maintenance. Interconnects receptors of the postsynaptic membrane including NMDA-type and metabotropic glutamate receptors. Plays a role in the structural and functional organization of the dendritic spine and synaptic junction. May be required at an early stage of synapse formation and be inhibited by IGF1 to promote synapse maturation.
Q60967	Bifunctional 3'-phosphoadenosine 5'-phosphosulfate synthase 1	1	0.02	**-1.36**		Bifunctional enzyme with both ATP sulfurylase and APS kinase activity, which mediates two steps in the sulfate activation pathway.
Q6ZWM4	U6 snRNA-associated Sm-like protein LSm8	1	0.03	**-0.94**	Nucleus	Binds specifically to the 3'-terminal U-tract of U6 snRNA and is probably a component of the spliceosome.
Q8BGN8	Synaptoporin	1	0.04	**1.52**	Cytoplasmic vesicle, secretory vesicle, synaptic vesicle membrane	Intrinsic membrane protein of small synaptic vesicles. Probable vesicular channel protein.
Q8R3Q6	Coiled-coil domain-containing protein 58	1	0.05	**-1.02**	Mitochondrion	

Table 6.2: Proteins altered in abundance in *mdx* cerebellar tissue as revealed by label-free LC–MS/MS analysis following global protein extraction identified with one unique peptide. Proteins in green were elevated in the *mdx* (n=4) cerebellum compared to control *C57BL/10* (n=4) cerebellum at 6 months old. Red proteins had decreased abundance in the *mdx* cerebellum compared to control *C57BL/10* cerebellum. Information regarding protein function was obtained from UniPort (Pundir *et al.*, 2017).

6.2.2 Cerebellar membrane enriched protein extraction

Following carbonate extraction methods, in order to enrich membrane proteins, numerous proteins were detected with increased abundance in the *mdx* cerebellum compared to control *C57BL/10* mice at 6 months old. Proteins with an increase concentration, identified with two or more unique peptides, in the *mdx* cerebellum included: syntaxin-1A, protein IMPACT, cytochrome c oxidase subunit 3, gelsolin, sodium- and chloride-dependent GABA transporter 3, Purkinje cell protein 4-like protein 1, uncharacterised protein C19orf52 homolog, brain acid soluble protein 1, and cadherin-13 (Table 6.3). In contrast, only one protein was identified with a reduced abundance in the *mdx* mice cerebellum compared to control *C57BL/10* mice cerebellum at 6 months old; CDGSH iron-sulfur domain-containing protein 2 (Table 6.3).

Cerebellar membrane enriched tissue-associated proteins with an increased concentration, with one unique peptide, in the *mdx* mice included: fibrinogen β chain, alpha-1-antitrypsin 1-5, peripherin, ubiquitin-like modifier-activating enzyme 5, poly(rC)-binding protein 2, guanine nucleotide-binding protein G(I)/G(S)/G(O) subunit gamma-4, membralin, aggrecan core protein, actin-related protein 10, gap junction gamma-2 protein, cystatin-C, receptor-type tyrosine-protein phosphatase S, and Ras-related protein Rab-31 (Table 6.4). In contrast, proteins with a decreased abundance (one unique peptide) in the *mdx* cerebellum following membrane protein enrichment included three proteins: catechol O-methyltransferase, protein FAM134C, and diacylglycerol kinase epsilon (Table 6.4).

Cerebellar membrane enrichment						
Accession number	**Protein name**	**Peptide count**	**Anova (p)**	**Fold change (Log_2)**	**Subcellular localisation**	**Protein function**
O35526	Syntaxin-1A	4	0.03	**0.78**	Cytoplasmic vesicle, secretory vesicle, synaptic vesicle membrane	Plays a role in hormone and neurotransmitter exocytosis (By similarity). Potentially involved in docking of synaptic vesicles at presynaptic active zones.
O55091	Protein IMPACT	2	0.01	**0.74**	Cytoplasm	Translational regulator that ensures constant high levels of translation upon a variety of stress conditions, such as amino acid starvation, UV-C irradiation, proteasome inhibitor treatment and glucose deprivation. May be required to regulate translation in specific neuronal cells under amino acid starvation conditions by preventing GCN2 activation and therefore ATF4 synthesis Through its inhibitory action on EIF2AK4/GCN2, plays a role in differentiation of neuronal cells by stimulating neurite outgrowth.
P00416	Cytochrome c oxidase subunit 3	2	0.0001	**0.79**	Mitochondrion inner membrane	Subunits I, II and III form the functional core of the enzyme complex.
P13020	Gelsolin	7	0.01	**0.63**	Cytoplasm, cytoskeleton	Calcium-regulated, actin-modulating protein that binds to the plus (or barbed) ends of actin monomers or filaments, preventing monomer exchange (end-blocking or capping). It can promote the assembly of monomers into filaments (nucleation) as well as sever filaments already formed.
P31650	Sodium- and chloride-dependent GABA transporter 3	4	0.03	**0.60**	Membrane	Terminates the action of GABA by its high affinity sodium-dependent reuptake into presynaptic terminals. Can also transport beta-alanine and taurine.

Q6W8Q3	Purkinje cell protein 4-like protein 1	2	0.053	**0.61**	Expressed in laminar and nuclear structures of the CNS	Expressed at early stages of development in the isthmus and in metencephalic and mesencephalic roof plates. At later stages of development, it is expressed in structures corresponding to circumventricular organs which in adult control the production of the cerebrospinal fluid.
Q8BGX2	Uncharacterised protein C19orf52 homolog	2	0.02	**0.72**	Mitochondrion inner membrane	Component of the TIM22 complex, a complex that mediates the import and insertion of multi-pass transmembrane proteins into the mitochondrial inner membrane.
Q91XV3	Brain acid soluble protein 1	10	0.003	**0.83**	Cell membrane	
Q9CQB5	CDGSH iron-sulfur domain-containing protein 2	2	0.02	**-0.67**	Endoplasmic reticulum membrane	Regulator of autophagy that contributes to antagonize BECN1-mediated cellular autophagy at the endoplasmic reticulum. Participates in the interaction of BCL2 with BECN1 and is required for BCL2-mediated depression of endoplasmic reticulum $Ca^{(2+)}$ stores during autophagy. Contributes to BIK-initiated autophagy, while it is not involved in BIK-dependent activation of caspases.
Q9WTR5	Cadherin-13	2	0.02	**0.64**	Cell membrane	Cadherins are calcium-dependent cell adhesion proteins. They preferentially interact with themselves in a homophilic manner in connecting cells; cadherins may thus contribute to the sorting of heterogeneous cell types. May act as a negative regulator of neural cell growth.

Table 6.3: Proteins altered in abundance in *mdx* cerebellar tissue as revealed by label-free LC–MS/MS analysis following membrane enriched extraction identified with two or more unique peptides. Proteins in green were elevated in the *mdx* mouse (n=5) cerebellum compared to control *C57BL/10* mouse (n=4) cerebellum at 6 months old. Red proteins had decreased abundance in *mdx* cerebellum compared to control *C57BL/10* cerebellum. Information regarding protein function was obtained from UniPort (Pundir *et al.*, 2017).

Cerebellar membrane enrichment						
Accession number	**Protein name**	**Peptide count**	**Anova (p)**	**Fold change (Log_2)**	**Subcellular localisation**	**Protein function**
Q8K0E8	Fibrinogen beta chain	1	0.008	**2.54**		Cleaved by the protease thrombin to yield monomers which, together with fibrinogen alpha (FGA) and fibrinogen gamma (FGG), polymerize to form an insoluble fibrin matrix. Fibrin has a major function in hemostasis as one of the primary components of blood clots. May also facilitate the immune response via both innate and T-cell mediated pathways.
Q00898	Alpha-1-antitrypsin 1-5	1	0.002	**2.21**	Secreted	Does not inhibit elastase or chymotrypsin. No target protease has been identified to date.
P15331	Peripherin	1	0.04	**1.55**		Class-III neuronal intermediate filament protein.
Q8VE47	Ubiquitin-like modifier-activating enzyme 5	1	0.002	**1.40**	Cytoplasm, nucleus	E1-like enzyme which activates UFM1 and SUMO2.
Q61990	Poly(rC)-binding protein 2	1	0.001	**1.08**		Single-stranded nucleic acid binding protein that binds preferentially to oligo dC. Major cellular poly(rC)-binding protein. Binds also poly(rU). Negatively regulates cellular antiviral responses mediated by MAVS signalling.
P50153	Guanine nucleotide-binding protein G(I)/G(S)/G(O) subunit gamma-4	1	0.03	**1.07**	Cell membrane	Guanine nucleotide-binding proteins (G proteins) are involved as a modulator or transducer in various transmembrane signaling systems. The beta and gamma chains are required for the GTPase activity, for replacement of GDP by GTP, and for G protein-effector interaction.
Q8CIV2	Membralin	1	0.01	**0.93**	Endoplasmic reticulum membrane	May have a role in the ERAD pathway required for clearance of misfolded proteins in the endoplasmic reticulum (ER). Promotes survival of motor neurons, probably by protecting against ER stress.
Q61282	Aggrecan core protein	1	0.02	**0.81**	Secreted, extracellular space, extracellular matrix	This proteoglycan is a major component of extracellular matrix of cartilagenous tissues. A major function of this protein is to resist compression in cartilage. It binds avidly to hyaluronic acid via an N-terminal globular region.
Q9QZB7	Actin-related protein 10	1	0.01	**0.76**		

Q8BQU6	Gap junction gamma-2 protein	1	0.01	**0.67**	Cell membrane	One gap junction consists of a cluster of closely packed pairs of transmembrane channels, the connexons, through which materials of low MW diffuse from one cell to a neighboring cell. May play a role in myelination in central and peripheral nervous systems.
P21460	Cystatin-C	1	0.01	**0.64**	Secreted	As an inhibitor of cysteine proteinases, this protein is thought to serve an important physiological role as a local regulator of this enzyme activity.
B0V2N1	Receptor-type tyrosine-protein phosphatase S	1	0.02	**0.64**	Membrane	Interacts with LAR-interacting protein LIP.1.
Q921E2	Ras-related protein Rab-31	1	0.02	**0.63**	Early endosome, Golgi apparatus	The small GTPases Rab are key regulators of intracellular membrane trafficking, from the formation of transport vesicles to their fusion with membranes. Rabs cycle between an inactive GDP-bound form and an active GTP-bound form that is able to recruit to membranes different set of downstream effectors directly responsible for vesicle formation, movement, tethering and fusion. Required for the integrity and for normal function of the Golgi apparatus and the trans-Golgi network. Plays a role in the internalization of EGFR from the cell membrane into endosomes.
O88587	Catechol O-methyltransferase	1	0.006	**-1.01**	Isoform Soluble: Cytoplasm Isoform Membrane-bound: Cell membrane	Catalyzes the O-methylation, and thereby the inactivation, of catecholamine neurotransmitters and catechol hormones.
Q9CQV4	Protein FAM134C	1	0.04	**-1.06**	Membrane	Mediates NRF1-enhanced neurite outgrowth.
Q9R1C6	Diacylglycerol kinase epsilon	1	0.002	**-1.08**	Membrane, cytoplasm	Highly selective for arachidonate-containing species of diacylglycerol (DAG). May terminate signals transmitted through arachidonoyl-DAG or may contribute to the synthesis of phospholipids with defined fatty acid composition

Table 6.4: Proteins altered in abundance in *mdx* cerebellar tissue as revealed by label-free LC–MS/MS analysis following membrane enriched extraction identified with one unique peptide. Proteins in green were elevated in the *mdx* (n=5) cerebellum compared to control *C57BL/10* cerebellum (n=4) at 6 months old. Red proteins had decreased abundance in *mdx* cerebellum compared to control *C57BL/10* cerebellum. Information regarding protein function was obtained from UniPort (Pundir *et al.*, 2017).

6.3 Confirmation of proteins identified following cerebellar proteomic profiling

NLD-Progenesis software, which was used for label-free comparison, generated 3D-montages, to provide a visual representation of the increases in the unique tryptic peptide for the protein of interest. Following ionisation and detection by MS, a tryptic peptide is blotted in an ion chromatogram by Progenesis software based on its mass/charge (m/z) and its retention time (RT). The numbers of each detected peptide, following normalisation with all the samples, was converted into sizes and represented by a big or small peak/s (Figure 6.2).

Following both investigation of global and membrane enriched protein fractions, we identified changes in the abundance of six proteins, which we determined had the greatest relevance to brain function (based on the current literature) and therefore we sought to confirm these finding by protein experiments.

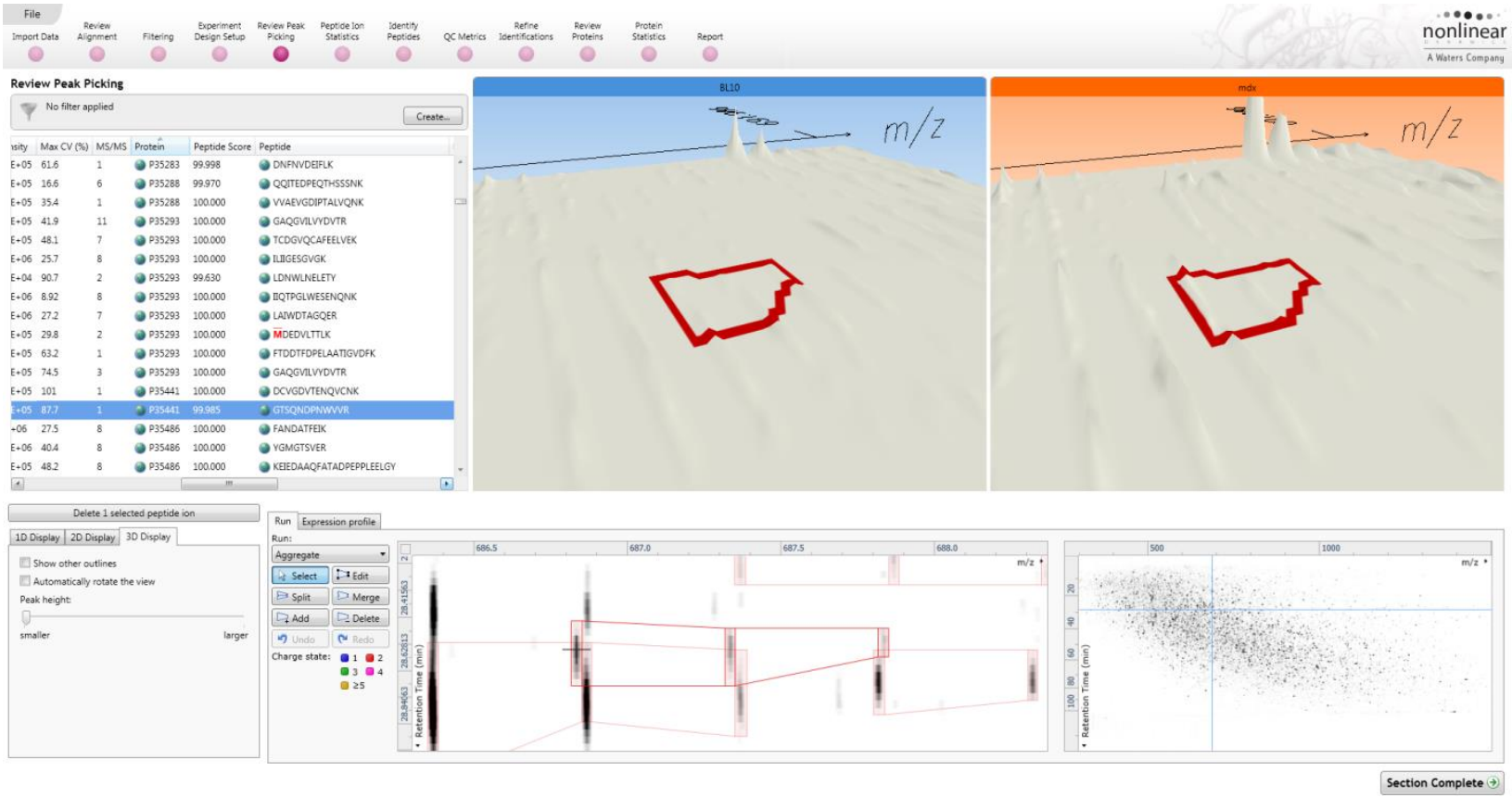

Figure 6.2: Screenshot of the NLD-Progenesis software. The NLD-Progenesis software was used to produce the 3D-montages of the unique tryptic peptide of a protein and provided a visual representation of the output following mass spectrometry (MS).

6.3.1 Elevated levels of thrombospondin-1 in the mdx mouse cerebellum

Astrocytes are the prominent glial cell population in the CNS, they are also the first cells of the brain parenchyma to encounter foreign molecules crossing the BBB (Chen *et al.*, 2011). In the developing CNS, soluble factors derived from astrocytes regulate synapse formation and neuronal survival (Chen *et al.*, 2011). Thrombospondins (TSPs) belong to the multimeric extracellular matrix glycoprotein (450 kDa) families, which are involved in the regulation of cell growth, motility, and differentiation (Risher and Eroglu, 2012). Astrocytes secrete TSP-1 and thrombospondin-2 (TSP-2), which have roles in promoting neurite outgrowth and synaptogenesis (Christopherson *et al.*, 2005).

TSP-1 was found to be elevated in the *mdx* cerebellum following global protein analysis (Figure 6.3). This increase in TSP-1 expression was confirmed via western blot analysis (Figure 6.3) and IF staining (Figure 6.3). In contrast, no difference in the expression levels of TSP-2 was detected in the *mdx* cerebellum at 6 months old following global protein profiling.

We performed immunoblotting analyses on cerebellar lysates from control *C57BL/10* (n=3) and *mdx* (n=3) *brain tissue*. Expression of TSP-1 in the cerebellum was examined by western botting using a polyclonal antibody against TSP-1. Results confirmed the overexpression of TSP-1 in the cerebellum of *mdx* compared to the control *C57BL/10* mice at 6 months old (Figure 6.3). Glyceraldehyde 3-phosphate dehydrogenase (GAPDH) (~38 kDa) was used as a loading control.

Additional confirmation of TSP-1 overexpression in the cerebellum of *mdx* mice was achieved using IF staining. We performed IF staining at two time points, 6 and 18 months old mice, to detect if TSP-1 overexpression was persistent. GFAP (mouse monoclonal antibody) was used as an accurate marker for astrocytes. The IF staining results demonstrated an increased expression of TSP-1 in the *mdx* cerebellum at 6 months old compared to age matched control *C57BL/10* mice (Figure 6.4 and Figure 6.5). Moreover, there was no difference in the expression levels of GFAP between *mdx* and control *C57BL/10* mice at 6 months old. An increased concentration of GFAP is an established indicator of

glial scar formation in the field of neuropathology (Kristjansdottir *et al.*, 2001). Increased expression of GFAP has previously been identified in *mdx*^{4cv} mouse brain (Murphy *et al.*, 2015), suggesting that loss of Dp427 does not affect GFAP expression levels in the *mdx* mouse cerebellum (Murphy *et al.*, 2015). Additionally, a reduced level of GFAP was found in the brains from embryonic and 30 day old *mdx* mice via western blot analysis, however this study measured levels of GFAP in the telencephalon (cerebrum) and did not provide results pertaining to the levels of GFAP in the cerebellum (Nico *et al.*, 2004). It could therefore be possible that GFAP is expressed developmentally in the *mdx* mouse brain in a region specific manner.

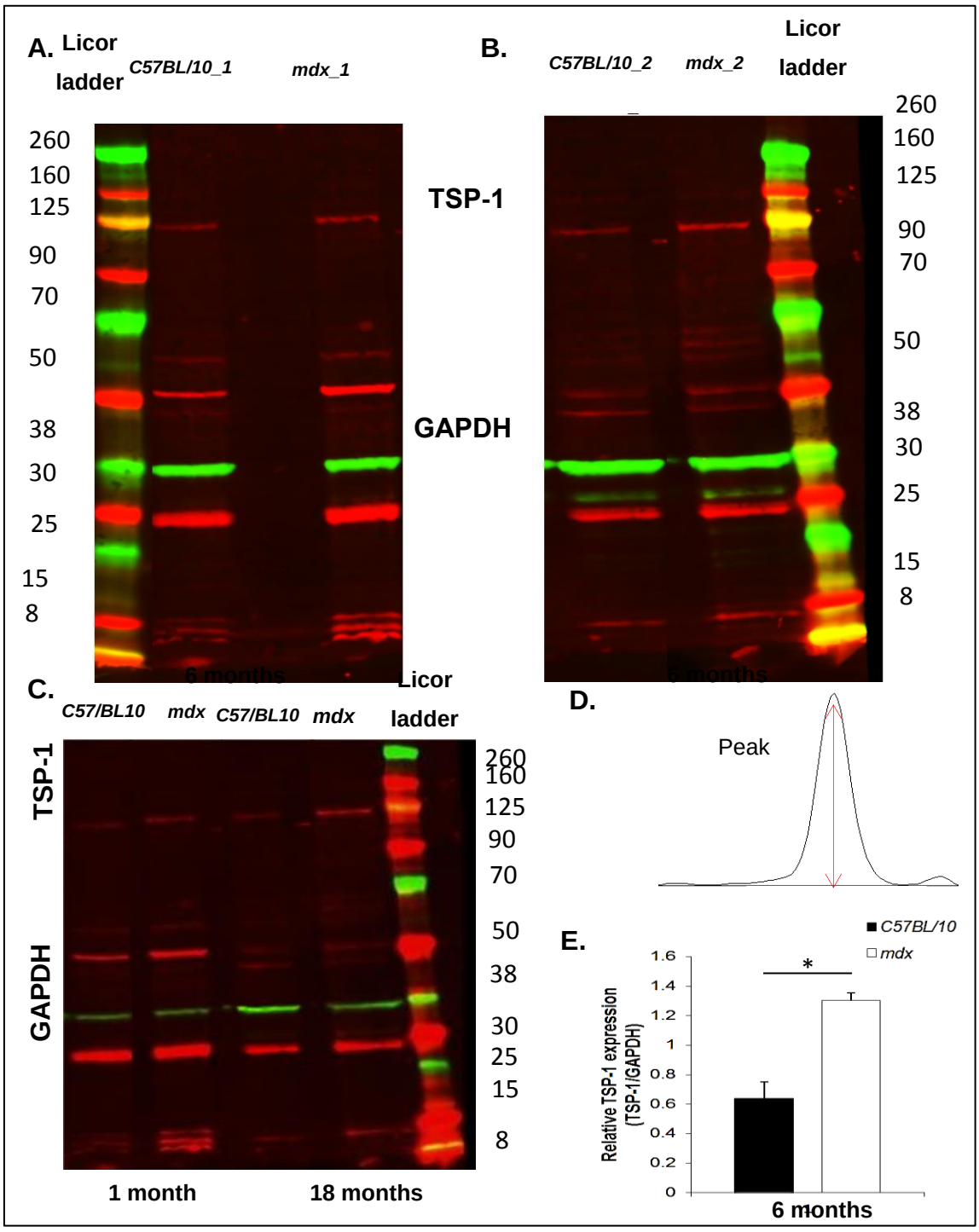

Figure 6.3: Western blot analysis of TSP-1 expression at various time points. A. Western blot analysis for TSP-1(125 kDa) at 6 months old on cerebellar lysates from control *C57BL/10* and *mdx* mice. **B.** Repeated TSP-1 western blot at 6 months old on cerebellar samples 2. **C.** Western blot analysis for TSP-1 at 1 month and 18 months old. All blots show TSP-1 overexpression in *mdx* mice cerebellum. **D.** Modified screenshot image of a profile plot demonstrating how band intensity was quantified using ImageJ gel analysis, calculated from area under the curve. **E.** Quantification of TSP-1 expression compared to loading control. In all blots GAPDH (38 kDa) was used as a loading control (mouse monoclonal, ab8245, at 1/10000). TSP-1 (rabbit polyclonal, ab85762, at 1/500).

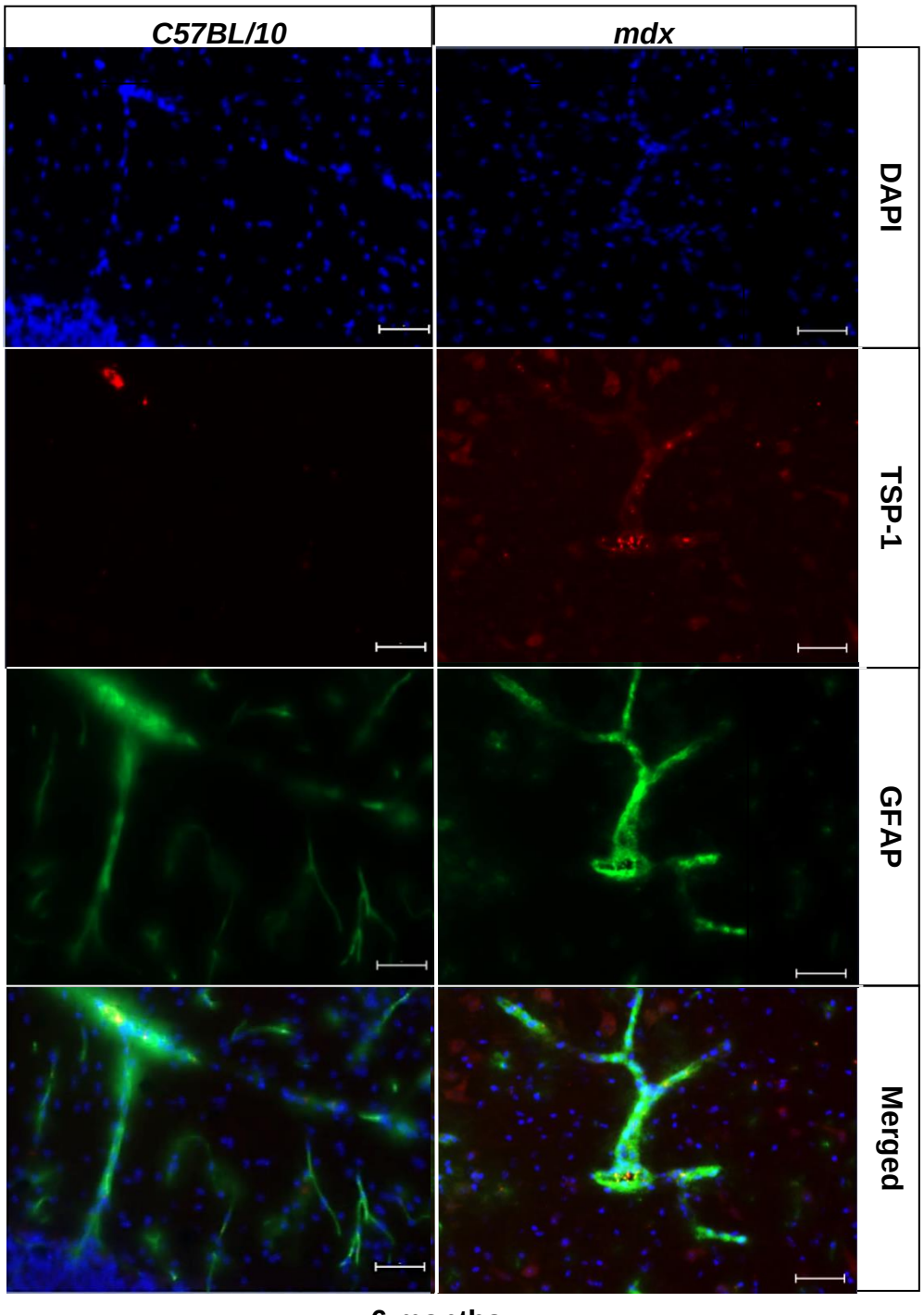

Figure 6.4: Immunofluorescence labelling of thrombospondin-1 (TSP-1) at 40x magnification. Double immunofluorescently labelled cryosections (10 µm) of control *C57BL/10* and *mdx* mouse cerebellum at 40x magnification, stained with (TSP-1) (red), the astrocytic marker glial fibrillary acidic protein (GFAP) (green) and DAPI (blue) used to locate cell nuclei. Overexpression of TSP-1, identified following proteomic analysis, is evident in the *mdx* mice cerebellum compared to aged matched control *C57BL/10* mice (6 months old). No difference in GFAP expression was observed. Scale bar= 20 µm. GFAP (mouse monoclonal, ab10062) (TSP-1 at 1/500 and GFAP at 1/1000).

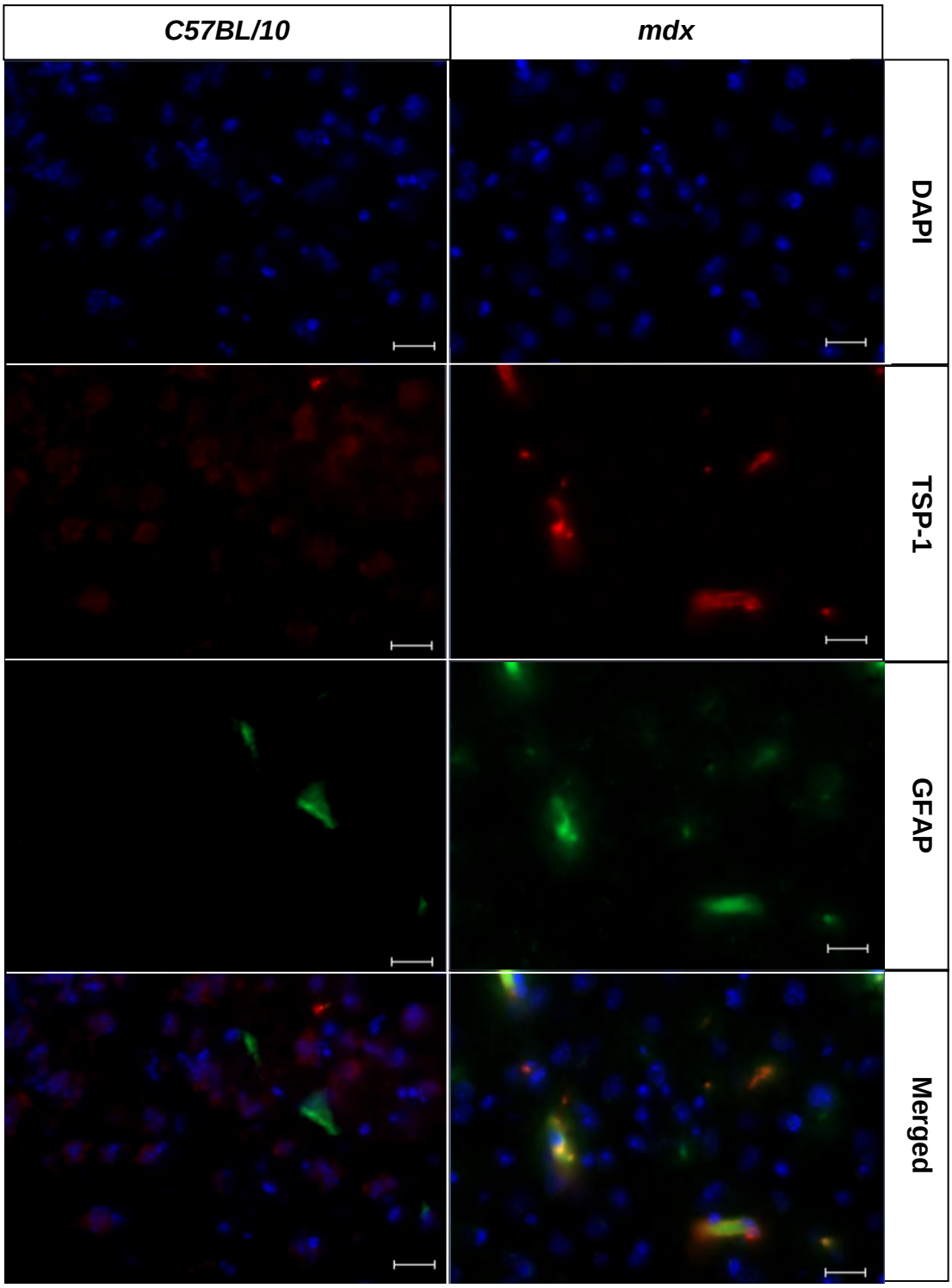

Figure 6.5: Immunofluorescence labelling of thrombospondin-1 (TSP-1) at 20x magnification. Double immunofluorescently labelled cryosections (10 µm) of control *C57BL/10* and *mdx* mouse cerebellum at 20x magnification, stained with TSP-1(red), the astrocytic marker GFAP (green) and DAPI (blue) used to locate cell nuclei. Overexpression of TSP-1, identified following proteomic analysis, was evident in the *mdx* mice cerebellum compared to aged matched control *C57BL/10* mice (6 months old). No difference in GFAP expression was observed. Scale bar= 50 µm. (TSP-1 at 1/500 and GFAP at 1/1000).

6.3.2 Elevation of gelsolin expression in the mdx cerebellum

Actin and its associated binding proteins play a critical role in cellular signalling (Basu *et al.*, 2008). Actin responds to extracellular signalling by converting from soluble to polymerised actin, under the control of gelsolin. Gelsolin is present intracellularly, in all cell types, and in the plasma/CSF as a secreted protein (Ji *et al.*, 2009). Intracellularly, gelsolin is a major actin-binding protein that caps the actin filaments growing end, stimulates its nucleation, and severs the actin filaments (Ji *et al.*, 2009). Both plasma/CSF and intracellular gelsolin originate from the alternative splicing of a single gene (Kwiatkowski *et al.*, 1988). Not only does gelsolin facilitate in controlling the formation of cytoplasmic actin filaments, but it also plays important roles in both apoptosis and amyloidosis (Antequera *et al.*, 2009).

Gelsolin levels were found to be elevated in the *mdx* cerebellum at 6 months old following the membrane protein enrichment extraction method (Table 6.3). We confirmed the increase of gelsolin via western blot analysis (Figure 6.6).

We performed immunoblotting analyses on cerebellar lysates from control *C57BL/10* (n=3) and *mdx* (n=3) brain tissue, using a polyclonal antibody against gelsolin. Results confirmed the overexpression of gelsolin in the cerebellum of *mdx* mice compared to the control *C57BL/10* mice at 6 months old (Figure 6.6). Multiple bands were possibly a consequence of posttranslational modification events. GAPDH (~38 kDa) was used as a loading control.

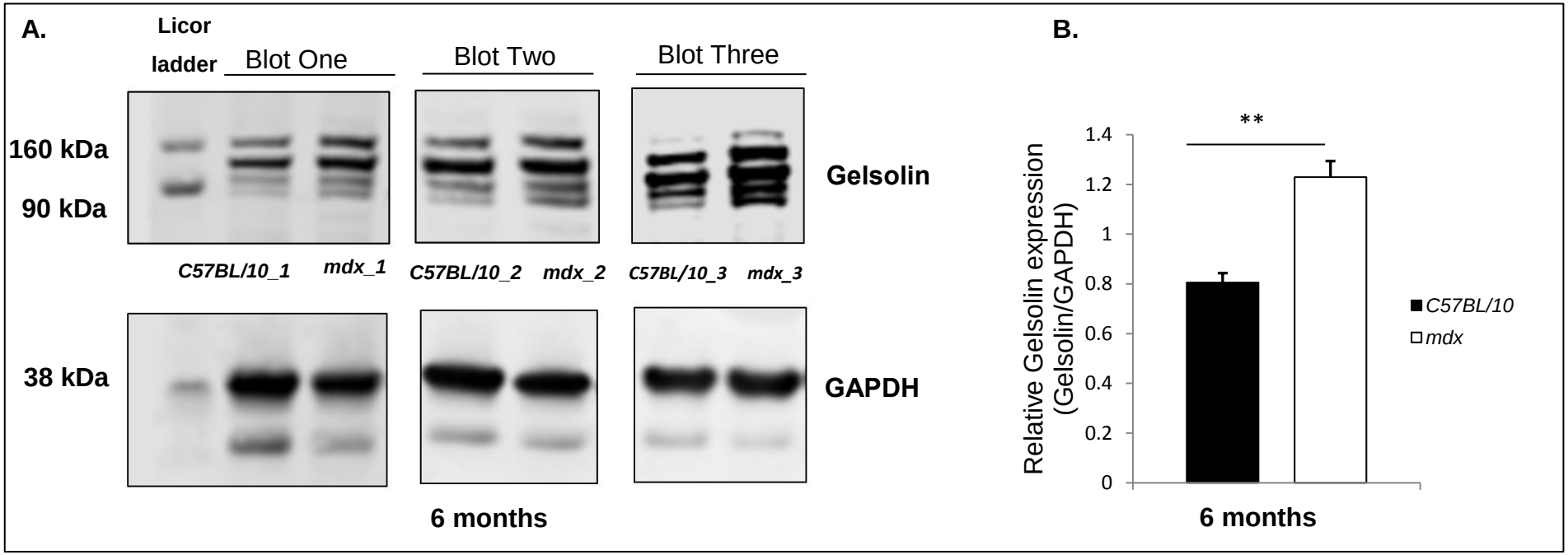

Figure 6.6: Immunoblot analysis showing relative expression levels of Gelsolin in *mdx* and aged match control *C57BL/10* mouse cerebellar lysates. A. Three separate blots using three independent cerebellar lysates from different mice per genotype represented by blots one, two and three. GAPDH was used as a loading control (1/1000). B. Graph showing relative Gelsolin expression calculated based on the results from the three blots. Gelsolin (rabbit polyclonal, ab74420, 1/1000). Data represented as ± SEM, p*<0.05, **p<0.01 vs control *C57BL/10.*

6.3.3 Detection of changes in GABA expression in mdx cerebellum

GABA is an inhibitory neurotransmitter in the CNS. The binding of GABA to specific transmembrane receptors in the plasma membrane, of both pre- and postsynaptic neuronal processes results in the opening of ion channels, allowing the flow of either negatively charged chloride ions into the cell or positively charged potassium ions out of the cell (Macdonald and Olsen, 1994). The result of this mechanism is a negative change in the transmembrane potential, usually causing hyperpolarisation. $GABA_A$ receptors are part of a ligand-gated ion channel complex, whereas $GABA_B$ metabotropic receptors are G-protein coupled receptors, which open or close ion channels via intermediates (Macdonald and Olsen, 1994; Borden, 1996).

It has previously been reported that there is a significant decrease in the number and size of $GABA_A$ receptor clusters immunoreactive for α_1 and α_2 subunits in the cerebellum and hippocampus of the *mdx* mouse (Knuesel *et al.*, 1999). The $GABA_A$ α_1 and α_2 subunit-containing receptors have also been implicated to have critical roles in working memory and cognition (Hashimoto *et al.*, 2009). Normally $GABA_A$ receptor subunit clusters are colocalised with dystrophin at the post-synaptic densities of cerebellar PCs and more recent reports suggest that there is no difference in expression of the gene for the $GABA_A$ receptor α_1 subunit in the cerebellum of young (3–4 month old) *mdx* mice compared to aged matched controls (Wallis *et al.*, 2004). Moreover, the latest reports hypothesise that the absence of dystrophin, from *mdx* Purkinje cells, reduces the number of post-synaptic $GABA_A$–R's and as a consequence causes an increase in extrasynaptic receptors. (Kueh *et al.*, 2011).

Following proteomic analysis in the *mdx* cerebellar membrane protein enriched fraction, GABA transporter type 3 (GAT3) was found to be elevated compared to age matched control *C57BL/10* mice. GAT1 and GAT3 are the two main subtypes of GATs responsible for the regulation of extracellular GABA levels in the CNS (Borden, 1996). GAT3 is highly expressed in the deep cerebellar nuclei and widely expressed in glial elements throughout the brain. Following the release of GABA from the pre-synaptic terminals it is rapidly removed from

the extracellular space by GATs, a regulatory mechanism that terminates inhibitory synaptic transmission maintaining GABA homeostasis to prevent excessive tonic activation of synaptic and extrasynaptic GABA-R's (Borden, 1996). It has recently been suggested that GATs modulation could play a critical role in maintaining homeostasis of GABAergic transmission (Jin *et al.*, 2012).

Firstly, we performed a western blot analysis for the $GABA_A$ receptor α_2 subunit to address potential changes in the expression levels of this protein with increasing age in *mdx* mice. Our findings demonstrate that $GABA_A$ receptor α_2 subunit protein levels remain unchanged in the *mdx* mice cerebellum between 6 and 12 months old (Figure 6.7). The western blots were carried out with the same antibody (rabbit polyclonal from Alomone labs) at the same concentration (1/500) but with two separate aliquots. The first aliquot only produced a band detectable at 30 kDa, whereas the second antibody aliquot produced a band at the correct 50 kDa position (Figure 6.7). GAPDH (~38 kDa) was used as a loading control. For further confirmation of these findings, the western blots should be performed with an additional antibody obtained from a different source.

A successful western blot was achieved and confirms overexpression of GAT3 in the *mdx* mice cerebellum (Table 6.3), but further investigations are necessary to gain a better understanding of how the GABAegic system in the cerebellum is affected in *mdx* mice (Figure 6.8). Nevertheless, these findings suggest a dysfunction in the GABAergic system in the cerebellum of *mdx* mice, due to the loss of Dp427.

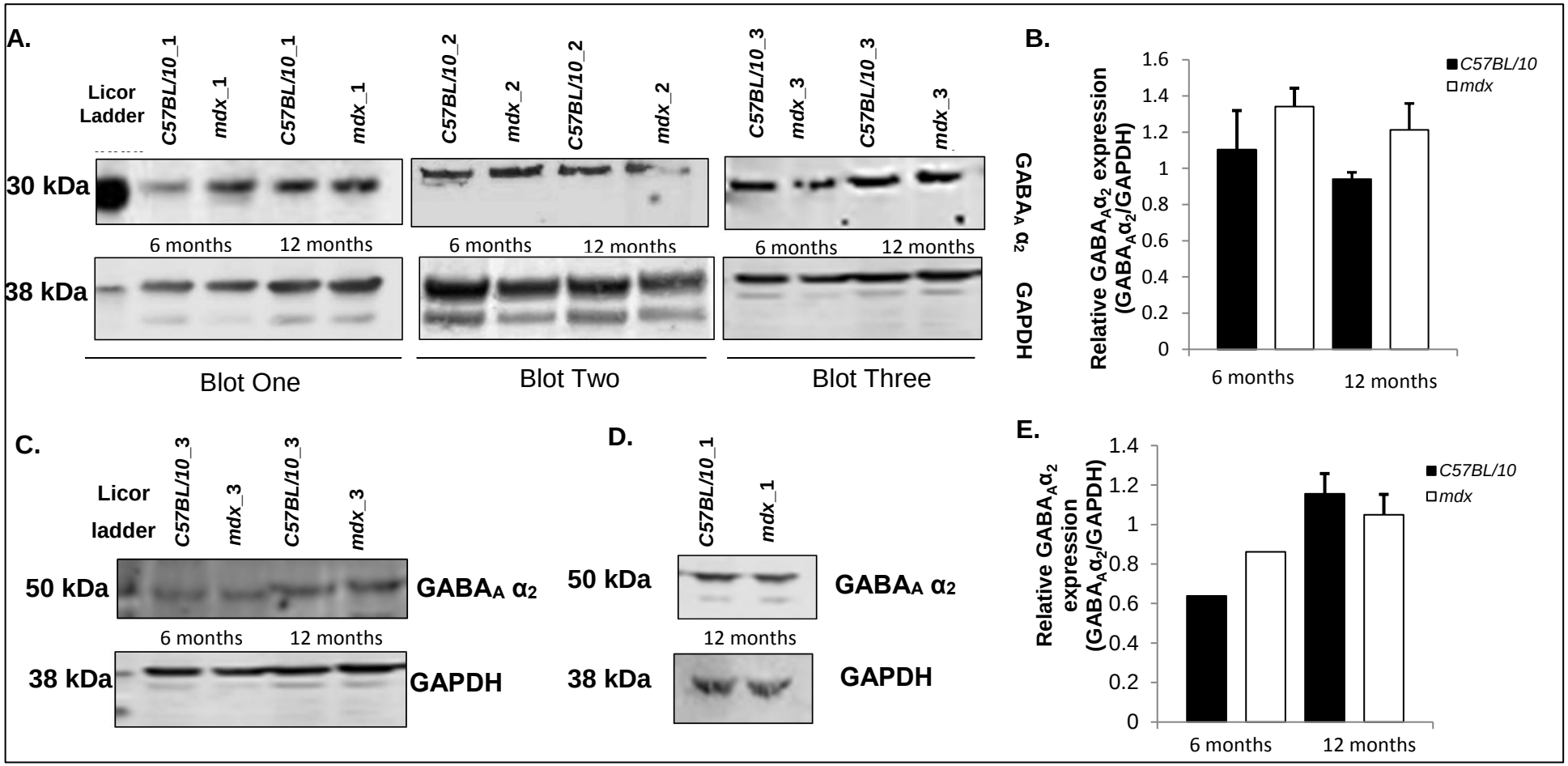

Figure 6.7: Western blot analysis for GABA$_A$ α$_2$ protein at 4 and 6 months old using *mdx* and control *C57BL/10* cerebellar lysates. A. Western blot performed with first aliquot of antibody at 6 and 12 months old**. B.** Quantification of GABA$_A$ α$_2$ protein at 4 and 6 months old. **C.** Western blot performed with a second aliquot of antibody at 4 and 6 months old. **D.** Repeated western blot at 12 months old with the second aliquot of antibody. **E.** Quantification of GABA$_A$ α$_2$ protein at 4 and 6 months old. Glyceraldehyde 3-phosphate dehydrogenase (GAPDH) (~38 kDa) was used as a loading control. GABA$_A$ α$_2$ (rabbit polyclonal, AGA-002, at 1/200).

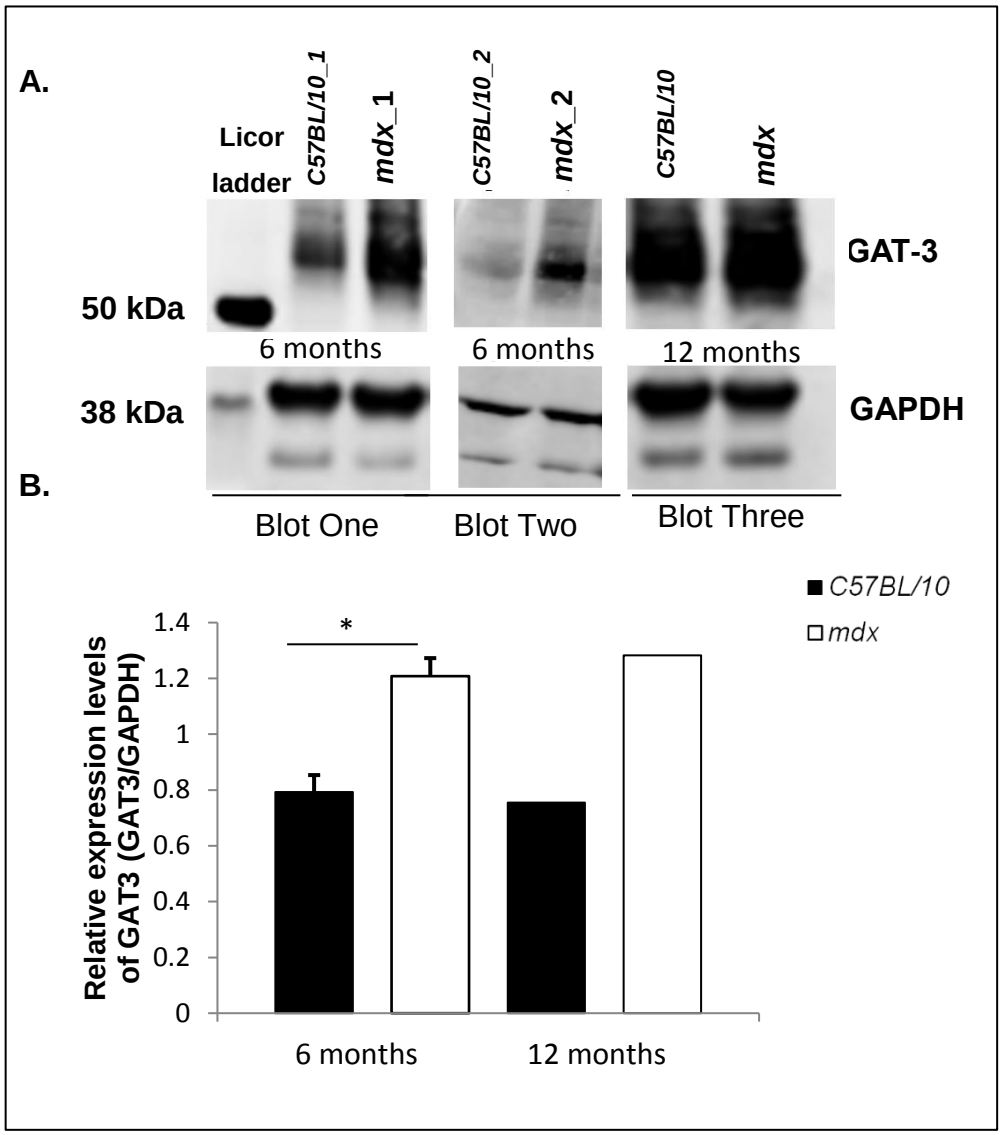

Figure 6.8: Western blot analysis for GAT-3 in *mdx* and control *C57BL/10* mouse cerebellum. A. Overexpression of GAT3 is detectable in *mdx* cerebellar protein lysate compared to control *C57BL/10* at 6 months old. Glyceraldehyde 3-phosphate dehydrogenase. **B.** Quantification of GAT3 expression in the cerebellum. Data presented as mean ± SEM, $p<0.05$ vs control C57BL/10 mice. (GAPDH) (~38 kDa) was used as a loading control. GAT3 (rabbit polyclonal, AGT-003, at 1/500).

6.3.4 Changes in mitochondrial proteins in the mdx cerebellum

Given the crucial roles for mitochondria in ATP energy supply, Ca^{2+} handling, and cell death, mitochondrial dysfunction has long been suspected to be an important pathogenic feature in DMD. In muscle, *mdx* mice have displayed significant uncoupling of oxidative phosphorylation and a reduction in maximal ATP synthesis capacity, which together resulted in decreased intramuscular

ATP levels (Percival *et al.*, 2013). The mitochondrial bioenergetic dysfunction in *mdx* skeletal muscle has been well document and its contributions to disease pathogenesis in dystrophin-deficient skeletal muscle investigated. However, changes in mitochondrial function in *mdx* mouse cerebellum as a consequence of Dp427 loss remain unknown.

Following both investigation of global and membrane enriched protein fractions, mitochondrial proteins were found to be elevated in the *mdx* cerebellum compared to control *C57BL/10* mice cerebellum at 6 months old (Table 6.1 and Table 6.3). NADH dehydrogenase was the most highly elevated mitochondrial protein in the *mdx* cerebellum (Figure 6.9). Prompted by this finding we performed a western blot analysis using the Oxphos 5 antibody (total OXPHOS rodent WB cocktail), which recognises all five mitochondrial complexes, and determined that complex III and complex II were significantly elevated in the *mdx* cerebellum compared to age matched control *C57BL/10* mice. Cytochrome C reductase (complex III) was found to be elevated following membrane enriched protein extraction methods and along with complex II form the functional core of the enzyme complex (Figure 6.10). The voltage-dependent anion channel (VDAC/Porin) (31 kDa) was used as a loading control.

Additionally, we sought to determine if the increased abundance of mitochondrial enzymes had an impact on the structural integrity of the mitochondria. Thus we performed electron microscopy of cerebellar sections derived from 6 and 12 month old mice, which revealed no ultrastructural changes in the mitochondria at either time point in the *mdx* cerebellum compared to age matched control *C57BL/10* mice (Figure 6.11).

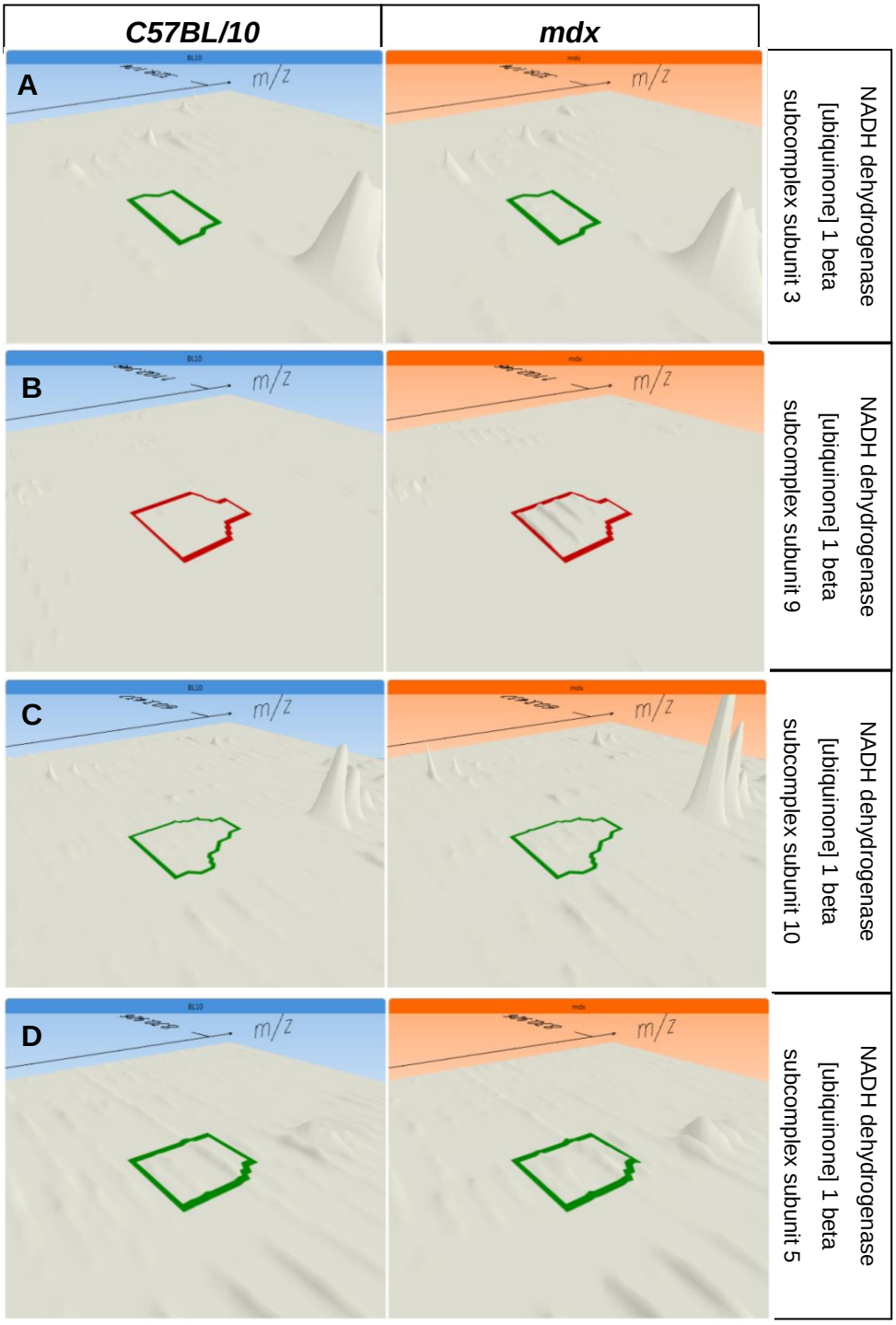

Figure 6.9: Representative 3D montages generated from NLD-Progenesis software following label free comparison. Each peak represents a unique tryptic peptide of the respective protein. **A.** 3D montage for NDUB3 protein from control and mdx cerebellar lystates. **B.** 3D montage for NDUB9 protein from control and mdx cerebellar lystates. **C.** 3D montage for NDUBA_mouse protein from control and mdx cerebellar lystates. **D.** 3D montage for NDUB5 protein from control and mdx cerebellar lystates. Green box indicates a tryptic peptide with a charge state of +3. Red box indicates a tryptic peptide with a charge state of +2.

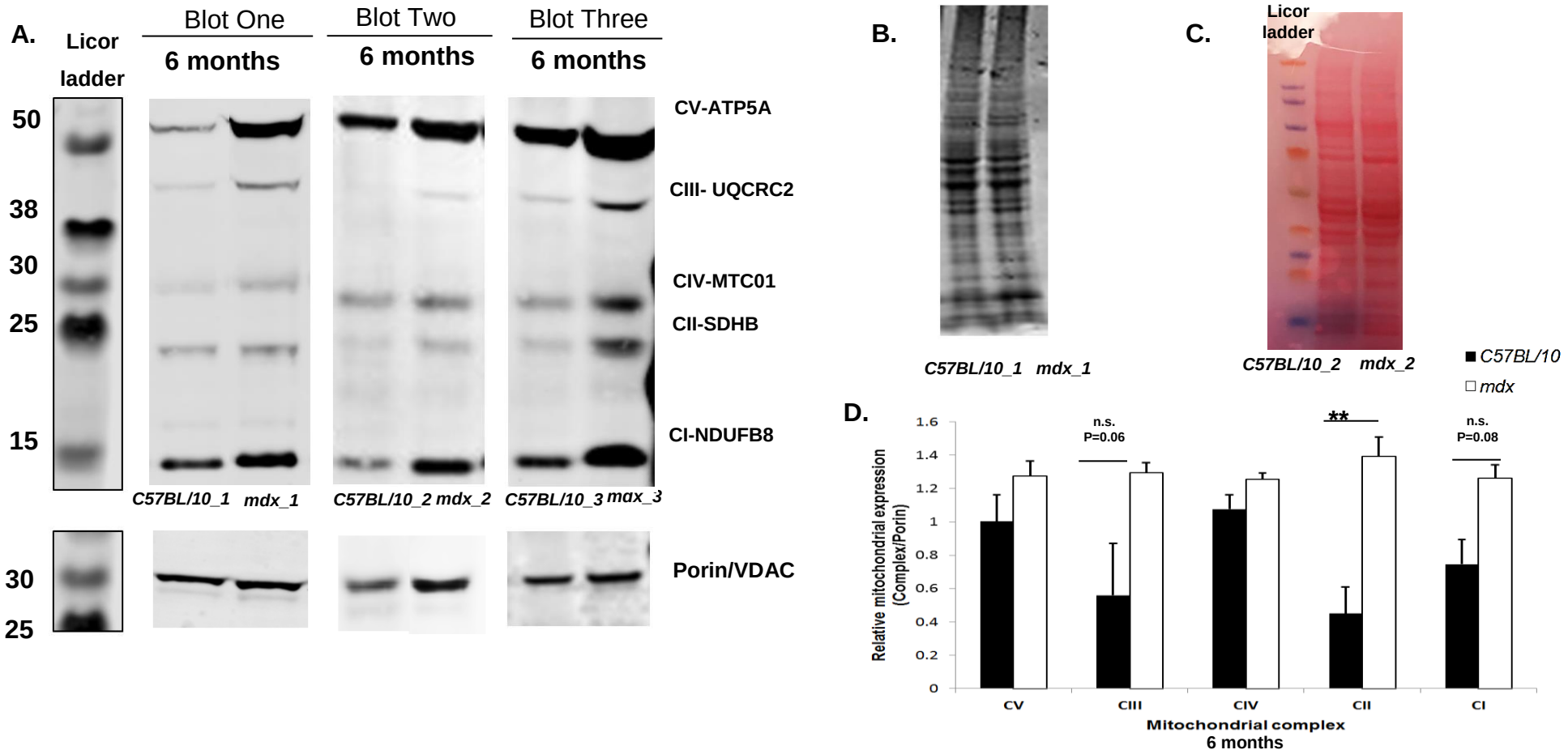

Figure 6.10: Western blot analysis for oxphos 5 antibody in control *C57BL/10* and *mdx* cerebellar protein lysates at 6 months old. A. Three blots with independent samples displaying overexpression of mitochondrial proteins in the *mdx* cerebellum. VDAC/Porin was used as a loading control. **B.** The Coomassie protein stain served as confirmation of equal protein loading. **C.** Ponceau stain to confirm western blot transfer and equal protein loading. **D**. Quantification of oxphos 5 levels in control *C57BL/10* and *mdx* cerebellar protein lysates at 6 months old. Oxphos 5 (ab110413, 1/1000). Porin/VDAC (mouse monoclonal, ab15895, 1/1000).

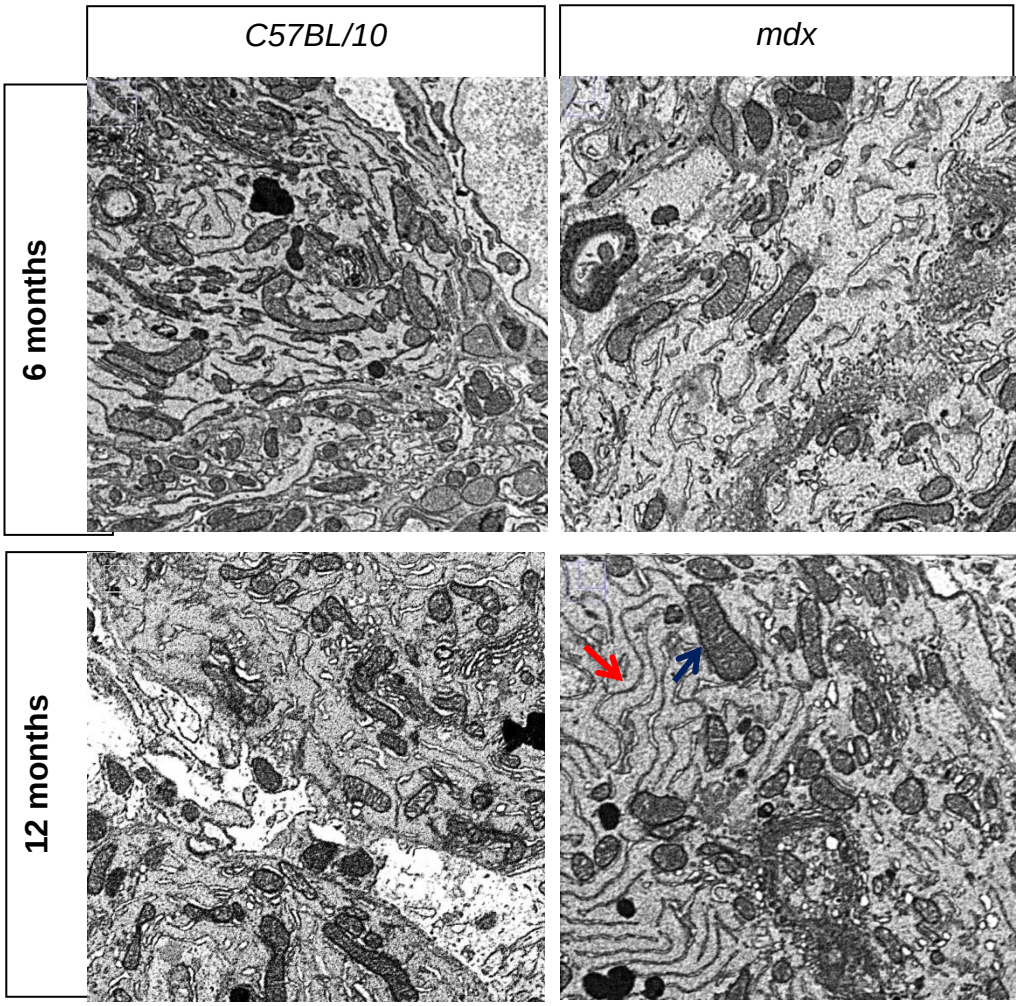

Figure 6.11: Representative Transmission electron micrographs (TEM) of control *C57BL/10* and *mdx* mouse cerebellum. Mitochondria were abundantly present at 6 and 12 months old in both genotypes. The mitochondria (blue arrow) appeared ultrastructurally normal with no abnormalities in membrane (inner and outer) integrity or cristae architecture and showed extensive surrounding by endoplasmic reticulum (ER) (mitochondria-ER-membrane sites) (red arrow). (n=2 mice/genotype at each time point). Images were captured by the Electron Microscopy facility at Newcastle University, UK.

6.3.5 Elevated levels of fibrinogen in the mdx cerebellum

Fibrinogen is a 340 kDa plasma glycoprotein that is converted by thrombin into fibrin during blood clot formation. Thrombin then converts the soluble fibrinogen into insoluble fibrin strands (Ryu *et al.*, 2015). These strands are then cross-linked by factor XIII to form a blood clot. Blood proteins such as fibrinogen, plasminogen and thrombin are therefore critical for the functional maintenance of integral vasculature homeostatic processes, which involve blood clotting (Palta *et al.*, 2014). However, rupture of the vasculature, due to pathological conditions and weakening of the BBB allows the entry of blood proteins into the brain and precedes subsequent oedema formation and neuronal damage (Abbott *et al.*, 2010). Recent studies have demonstrated fibrin deposition and damaged vasculature in transgenic mouse models of Alzheimer's disease (AD) (Paul *et al.*, 2007). It has been further identified that infiltration of fibrinogen into parenchymal regions acts to amplify and sustain chronic inflammatory microenvironments, which are proposed as toxic to bystander neurons (Ryu and McLarnon, 2009).

Following the proteomic analysis of global protein extracts and membrane enriched protein fractions, elevated levels of fibrinogen were detected in the *mdx* mouse cerebellum compared to control *C57BL/10* mouse cerebellum at 6 months old (Table 6.1 and Table 6.4). More specifically, the α and β fibrinogen chains were found to be overexpressed in the *mdx* cerebellum. We confirmed the increased abundance of fibrinogen using immunological techniques (Figure 6.12). Western blot analysis was performed on *mdx* and control *C57BL/10* mouse cerebellar lysates using a polyclonal antibody which detected fibrinogen-α chain at 95 kDa and confirmed the overexpression in the *mdx* cerebellar protein extracts (Figure 6.12). GAPDH (~38 kDa) was used as a loading control. For further confirmation of fibrinogen overexpression we also performed IF staining on cryosections of control *C57BL/10* and *mdx* mouse cerebellum (Figure 6.13).

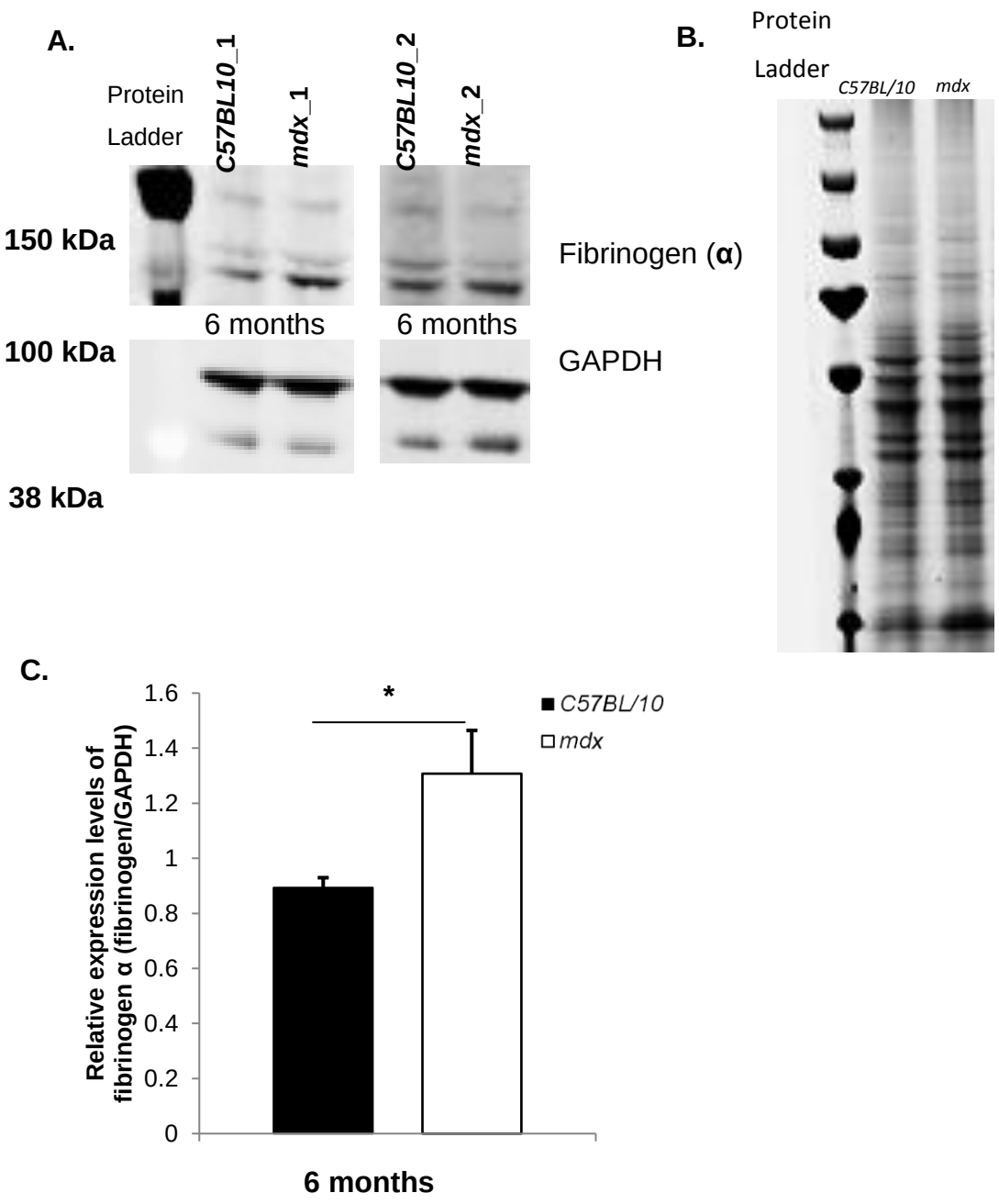

Figure 6.12: Analysis of fibrinogen expression. A. Western blot analysis for fibrinogen-α chain in the *mdx* and control *C57BL/10* cerebellar protein lysates at 6 months old. **B.** The Coomassie stained protein gel served as a verification of correct protein loading. C. Quantification of fibrinogen overexpression in the *mdx* cerebellum at 6 months old. GAPDH (~38 kDa) was used as a loading control. Fribrinogen-α chain (rabbit polyclonal, ab217931, at 1/1000).

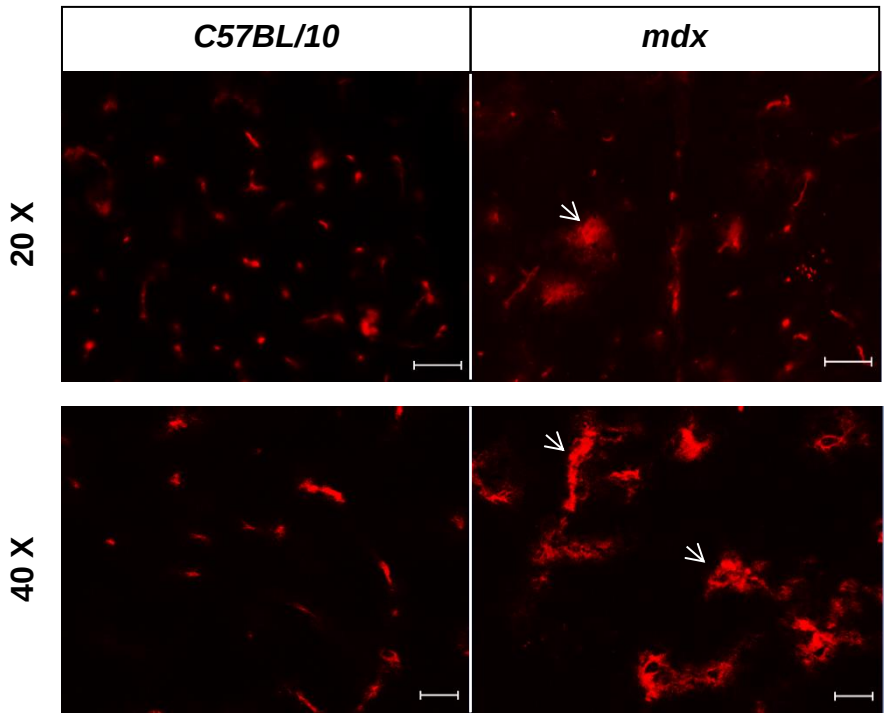

Figure 6.13: Immunofluorescently labelled cryosections (10 µm) of control *C57BL/10* and *mdx* mouse cerebellum at 20x and 40x magnification, stained with an antibody raised against the fibrinogen α chain. There appeared to be overexpression of fibrinogen in the *mdx* cerebellum compared to control C57BL10 cerebellum at 6 months old. The white arrows indicate extensive areas of diffuse fibrinogen deposition. Scale bar= 50 µm at 20x and 20 µm at 40x.

6.3.6 Further protein analysis

Enhanced proteins were analysed for enriched gene ontology (GO) terms using STRING (https://string-db.org/) software, which detected functional protein association networks from the proteins identified by both global and membrane enriched protein extraction methods. STRING highlighted two protein networks of interest (Figure 6.14). The first protein network highlighted was the known association between TSP-1, fibrinogen and the integrin beta-2 precursor, which are all proteins involved in an inflammatory response. The second protein network highlighted a link (co-expression) between NADH dehydrogenase and peptidyl-prolyl cis-trans isomerase (Figure 6.14). Panther (http://pantherdb.org/) bioinformatics software was also used to identify the protein class and molecular function of proteins which were found to have an increased abundance in the *mdx* cerebellum at 6 months old (Figure 6.15). Interestingly, the highest proportion of proteins identified were found to be functional binding proteins (50%) (Figure 6.15). The largest proportion of proteins identified with an increased abundance in the *mdx* cerebellum were either structural, cytoskeletal, or membrane trafficking proteins.

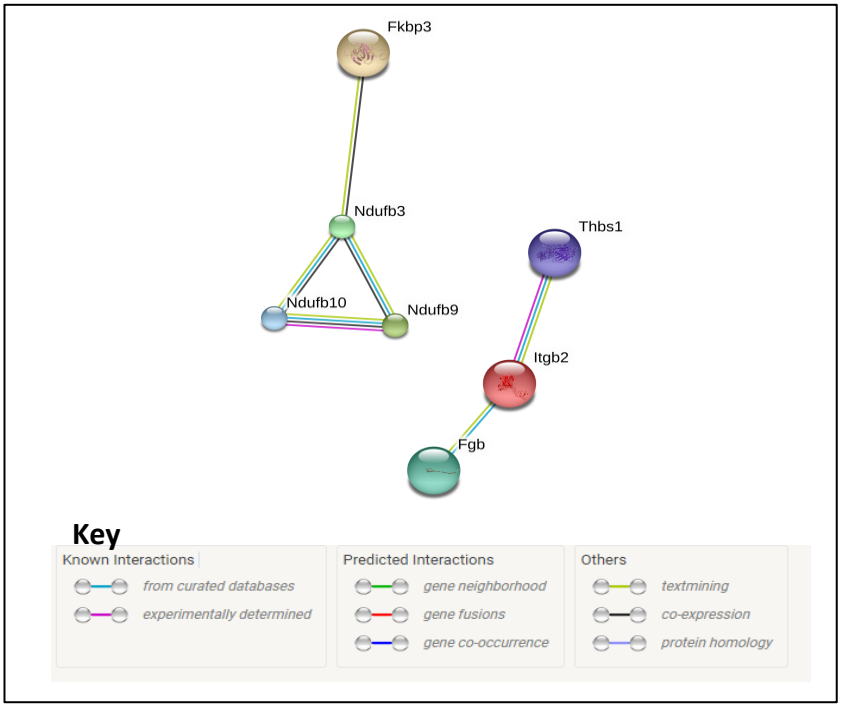

Figure 6.14: Analysis of protein interaction networks using STRING. Regulated proteins which have known interactions and predicted reactions are shown.

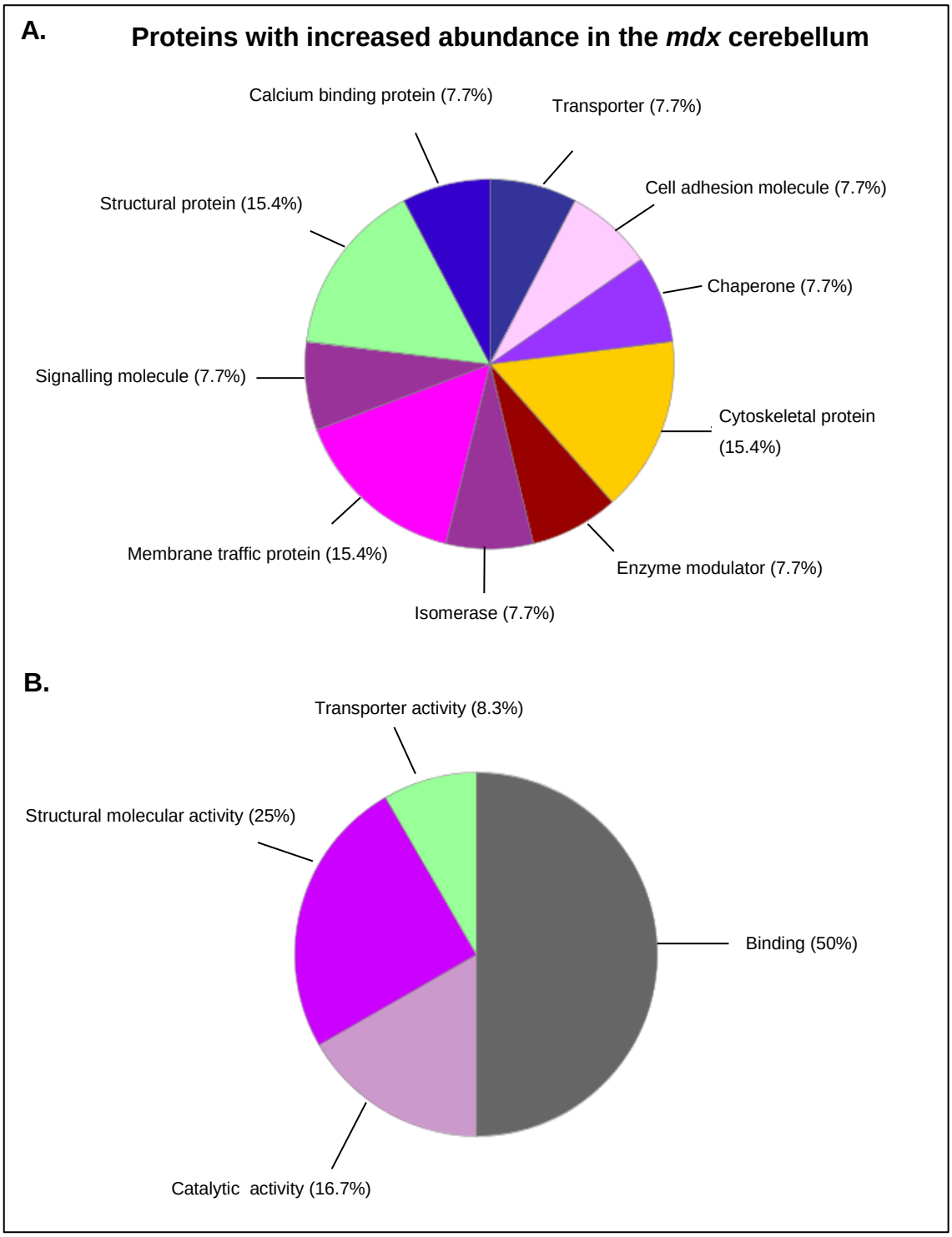

Figure 6.15: Protein class and molecular function identified with Panther software. A. Summary of increased protein classes in the *mdx* cerebellum following global protein extraction and membrane enrichment protein extraction compared to control *C57BL/10* mouse cerebellum. The bioinformatics software programme PANTHER was employed to establish the clustering of protein classes based on liquid chromatography- mass spectrometry (LC-MS/MS) analysis. B. Pie chart summarising the molecular function of proteins which were elevated in the *mdx* mouse cerebellum following LC-MS/MS analysis.

6.4 Discussion

Within the rodent cerebellum dystrophin (Dp427) is present in the molecular cell layer (MCL), the Purkinje cell layer (PCL) and the granular cell layer (GCL) (Hendriksen *et al.*, 2016b). Morphologically, dystrophin appears to be present around PCs, in astrocytes of both the MCL and GCL, and in blood vessels across all three cerebellar layers (Snow *et al.*, 2013; Hendriksen *et al.*, 2016b). Therefore, we sought to identify how the loss of full length dystrophin affected the *mdx* cerebellum utilising an unbiased proteomic profiling approach.

6.4.1 Elevated levels of thrombospondin-1 in the mdx mouse cerebellum

Elevated levels of TSP-1 were detected in the *mdx* cerebellum at 6 months old and this was confirmed using both western blot analysis and IF staining. Astrocytes are known to provide signals to guide synapse formation and neurite development, critical in both the developing and mature brain (Risher and Eroglu, 2012). Factors secreted by astrocytes are involved in the regulation of the stability, dynamics, and maturation of dendritic spines (Cheng et al., 2016). Changes in TSP expression can have direct impact on synapse function and development.

TSP's have also been implicated in the inflammatory response of the CNS. Nearly all neurological disorders are hallmarked by inflammation, characterised by the induction of microglia, monocytes, cytokines, and other mediators of injury (Wee Yong, 2010). In the immune system, TSP-1 modulates the adhesion and aggregation of monocytes/macrophages via interaction with CD36 and CD47 (Yamauchi et al., 2002b). Cytokines have recently been identified as having roles in synaptic plasticity and neurogenesis. For example IL-6 has been shown to modulate long-term potentiation (LTP) *in vitro* in the rat hippocampus (Yamauchi et al., 2002a). On the other hand TSP-1 can also suppress IL-10 release via interactions with latent TGF-β1 (Schultz-Cherry et al., 1994). TSP-1 and TGF-β1 may therefore play a role in cortical injury given their significant up regulation following brain injury (Schultz-Cherry et al., 1994). In the peripheral nervous system (PNS), TGF-β_1 is linked to multiple aspects of plasticity and synapse formation, particularly in Schwann cells (the major glial cell of the

PNS), where its release promotes synapse formation at the neuromuscular junction (Feng and Ko, 2008).

Previous studies in the skeletal muscles of *mdx* mice have also identified TSP-1 as a pathogenic biomarker. TSP-1 acts as a potent mediator of angiotensin-II-induced TGF-β via angiotensin-2. Control mice did not express significant amounts of TSP-1 in skeletal muscle but strong sarcolemma expression of TSP-1 was observed in the diaphragm (and other muscles) of *mdx* mice (Cohn *et al.*, 2007). Treatment with Lorstan, an angiotensin-II type 1 inhibitor, attenuated disease progression and reduced TSP-1 expression in the muscles of treated *mdx* mice.

6.4.1.1 Changes in thrombospondin-1 expression in other neurological disorders

TSP's have been identified as key disease regulators in numerous neurological diseases, for example, Fragile X-syndrome (FXS) is the most common form of intellectual disability and is a leading cause of ASD (Cheng et al., 2016). Both *in vitro* and *in vivo* studies have demonstrated the capacity of TSP's to increase synapse number, promote the localisation of synaptic molecules, and refine the pre- and post-synaptic alignment. For example hippocampal astrocytes were cultured from a FSX mouse model (Fmr1 KO) and displayed a significant decrease in TSP-1 expression compared to controls. Fmr1 hippocampal neurons also exhibited morphological dendritic spine deficits and altered long-term excitatory synapse formation (Cheng et al., 2016). Following the application of exogenous TSP-1, to the cultured astrocytes, spine and synaptic abnormalities were abolished. This work demonstrated an integral role of astrocyte-secreted signals in the establishment of neuronal communication.

Down's Syndrome (DS), a common form of genetic mental retardation, has recently been linked to decreased TSP-1 expression characterised by altered spine morphology and reduced synaptic density in DS astrocytes (Garcia et al., 2010). Additionally, in the progressive neurodegenerative disorder AD initial cognitive decline is characterised by a huge synaptic loss and TSP-1 expression is markedly decreased in vulnerable populations in AD patient brains, impairing correct repair of synapses (Terry et al., 1991; Buee et al.,

1992). Following stroke, TSP-1 and TSP-2 expression is drastically elevated where their upregulation is primarily driven by purinergic signalling in astrocytes (Tran and Neary, 2006).

Epilepsy is also characterised by synaptic disorganisation. Aberrant synaptogenesis following a seizure may influence hyper- excitability and worsen epileptic discharges. The 'matrix response' is a mechanism by which seizure activity induces widespread alteration in the localisation and synthesis of ECM molecules (Risher and Eroglu, 2012a). Gabapentin, the anticonvulsant drug, inhibits TSP induced synaptogenesis and could thus have direct implications on the drugs mechanism of action suggesting that the prevention of aberrant synaptic remodelling may be therapeutic (Eroglu et al., 2009). Interestingly, a higher incidence of epilepsy is reported in DMD patients (6.3%) compared to the normal population (1%) (Pane *et al.*, 2013).

It is therefore likely that elevation in TSP-1 in the cerebellum of *mdx* mice may be pathogenic, either by causing an increased inflammatory environment, or by altering synaptogenesis. Further investigations into TSP-1 overexpression in the cerebellum of *mdx* mice are required to confirm these findings.

6.4.1 Elevation of gelsolin expression in the mdx cerebellum

Elevated levels of gelsolin were detected in the *mdx* cerebellum at 6 months old and this was confirmed using western blot analysis. Gelsolin, a Ca^{2+} dependent actin-regulatory protein, which has been shown to modulate actin assembly and disassembly, is believed to regulate cell motility through modulation of the actin network (Basu *et al.*, 2008). Gelsolin contains six homologous domains (G1-6), each of which has a discrete function. More precisely, G1 binds to actin monomers in a Ca^{2+}- independent manner, and the complex is capable of capping actin fragments. G2 contains a Ca^{2+}-independent actin polymer binding site and is capable of binding to actin filaments (Kamada *et al.*, 1998). The N-terminal fragment with G1-3 carries F-actin-cutting activity, and the C-terminal fragment with G4-6 carries a Ca^{2+}-dependent actin monomer binding activity (Kamada *et al.*, 1998).

Studies have also suggested an important role of gelsolin in apoptosis signal transduction. Human gelsolin has been shown to inhibit apoptosis by preventing cytochrome *C* release from mitochondria resulting in the lack of activation of caspase-3, -8, and -9 (Ohtsu *et al.*, 1997). An important role of mitochondria in apoptotic signalling is the translocation of cytochrome *C* from the mitochondrial intermembrane compartment into the cytosol (Kusano *et al.*, 2000). Once released, cytochrome *C* binds to apoptotic protease activating factor 1 (APAF-1) in the presence of ATP or dATP and forms a complex that processes and activates pro-caspase-9, which in turn cleaves and activates the executioner caspases, such as caspase-3 and -7 (Green and Reed, 1998). But this was not the same for mouse gelsolin, which is suspected to be as a result of differences in sequence homology of the G5 domain of the C-terminal of the gelsolin protein. The manner in which gelsolin may inhibit apoptosis in mouse cells has yet to be elucidated. Nevertheless, elevation of gelsolin levels in *mdx* mouse cerebellum is suggestive of increased levels of apoptosis.

6.4.1.1 Changes in gelsolin expression in other neurological disorders

Overexpression of gelsolin has been detected in the brain of patients with Down Syndrome (DS). The authors theorised that gelsolin may have a number of roles: it binds to actin and regulates actin polymerisation, binds to beta-amyloid and regulates its clearance, and it responds to oxidative stress by increasing its expression (Ji *et al.*, 2009).

Taken together these findings suggest that gelsolin plays a critical role in the *mdx* cerebellum and that its overexpression may be as a consequence of increased cell death. However, it is not possible to derive conclusive evidence that gelsolin overexpression in the *mdx* cerebellum has a positive or negative impact and further studies are required to confirm this.

6.4.1 Changes in mitochondrial proteins in mdx cerebellum

Overexpression of mitochondrial proteins was detected following both global and membrane enriched protein extraction methods and was confirmed by western blot analysis. Interestingly we did not detect any ultrastructural malformations in the mitochondria from *mdx* mice cerebellum at either 6 or 12 months old, which was expected considering the majority of DMD patients only

exhibit mild cognitive impairment. Additionally, we did not detect elevated levels of Porin/VDAC (outer membrane channel) in either proteomic profiling or western blot analysis of the cerebellum, which confirms our electron microscopy findings and further suggests that mitochondrial numbers were comparable between control *C57BL/10* and *mdx* cerebellum. We also did not find any abnormalities in cristae packing density between control *C57BL/10* and *mdx* cerebellum which suggests that the size of the inner membrane was comparable between both genotypes and consequently an increase in inner membrane proteins was not likely to result from this. These findings suggest that the mitochondrial inner membrane proteins were overexpressed in a compensatory manner to account for increasing energy demands of the *mdx* cerebellum, possibly due to increased amounts of stress or increased apoptosis occurring in the *mdx* cerebellum.

The primary function of the mitochondrial electron transport chain (ETC) is to synthesize ATP. The ETC, present in the inner mitochondrial membrane, is comprised of multiple polypeptide components which are grouped into four enzyme complexes. The polypeptides that constitute complexes I (NADH ubiquinone reductase), III (ubiquinol cytochrome c reductase), and IV (cytochrome *C* oxidase) are coded for by both nuclear and mitochondrial DNA, whilst complex II (succinate ubiquinone reductase) is exclusively coded for by nuclear DNA (DiMauro, 1996). Briefly, transfer of reducing equivalents from NADH or $FADH_2$ to molecular oxygen is coupled to the pumping of protons across the inner mitochondrial membrane resulting in the formation of a proton gradient (Heales *et al.*, 1999). Dissipation of this proton gradient through the membrane sector of the mitochondrial ATP synthase (complex V) induces a conformational change in the active site of this enzyme, which favours ADP phosphorylation and hence ATP synthesis (Heales *et al.*, 1999).

The defects in energy production, as a consequence of mitochondrial dysfunction, have been documented in neurodegenerative diseases such as dementia, Alzheimer's disease (AD), and Parkinson's diseases, all of which ultimately result in some level of cognitive impairment (Johri and Beal, 2012). High energy demanding tissues, such as the brain, contain a large number of

mitochondria and therefore have increased susceptibility to the effects of changes in aerobic energy metabolism.

The bioenergetics abnormalities reported in the DMD brain have also been documented in the *mdx* mouse, with an increased inorganic phosphate-to-phosphocreatine ratio, increased intracellular brain pH, and alteration in metabolism of glucose (Tracey *et al.*, 1996; Rae *et al.*, 2002). We have demonstrated altered abundance of mitochondrial proteins in the *mdx* mouse cerebellum. In this regard, changes in mitochondrial enzymes may affect the production of ATP, causing changes in energy metabolism in the *mdx* cerebellum. A previous report identified changes in the mitochondrial enzymes in the *mdx* mouse brain by monitoring creatinine kinase (CK) levels and mitochondrial enzyme activity levels (Tuon *et al.*, 2010). The report highlighted an increase in CK activity and theorised that this could be causing a protective effect against cellular damage, since it functions as a buffering system for cellular ATP levels. Additionally, the report identified changes in mitochondrial enzymes in various brain structures: complex I activity was decreased in the hippocampus, prefrontal cortex, cortex, striatum and cerebellum (Tuon *et al.*, 2010). Complex II remained unchanged in all the aforementioned brain structures. Complex IV was only elevated in the striatum and prefrontal cortex (Tuon *et al.*, 2010). Although the finding regarding complex II and complex III activity differ to those found in this current study, this could be as a result of different experimental techniques used to determine mitochondrial complex activities. Moreover, different ages of mice were studied.

6.4.2 Changes in mitochondrial function in other neurological disorders

There is strong evidence emerging suggesting mitochondrial dysfunction in the pathogenesis of numerous neurodegenerative diseases. Alzheimer's disease (AD) has strong association with mitochondrial dysfunction, which may be as a consequence of β-amyloid peptide accumulation within the mitochondria themselves (Johri and Beal, 2012). Additionally, a decrease in complex IV activity has been reported in the cerebral cortex of individuals who died with AD, where this complex is particularly susceptible to oxidative damage (Johri and Beal, 2012). In Parkinson's disease, the second most common

neurodegenerative disorder, a decreased complex I activity has been reported in the substantia nigra of post mortem samples obtained from patients (Beal, 2007).

Our study is the pioneer study in showing altered abundance in mitochondrial proteins in the cerebellum of the *mdx* mouse, as a consequence of full length dystrophin loss. Further studies are needed to better elucidate the neurobiological alterations in the *mdx* mouse cerebellum, investigations into mitochondrial copy number (to detect DNA damage) or level of fission and fusion proteins (to detect mitochondrial development) could be studied to provide a better understanding of mitochondrial dysfunction in the *mdx* cerebellum.

6.4.3 Elevation of fibrinogen expression in the mdx cerebellum

Following both global and membrane enriched protein extraction methods, fibrinogen was found to be elevated in the *mdx* cerebellum, which we confirmed with both western blot analysis and immunofluorescent staining. We have established a progressive disruption of the BBB in *mdx* mice between 6 and 14 months old using EBD extravasation and T_1- mapping with contrast enhancement (Chapter 5). Elevated levels of fibrinogen have been documented in AD and recent studies demonstrated that as a consequence of BBB impairment the extravasation of the glycoprotein fibrinogen can be found in brain parenchyma. This effect is similar to that seen in the *mdx* cerebellum and this is the first time that this has been documented in dystrophin deficiency.

Infiltration of fibrinogen into parenchymal regions acts to amplify and sustain chronic inflammatory microenvironments, which are proposed as toxic to bystander neurons. Both thrombospondin-1 (TSP-1) and fibrinogen are released following tissue injury and exogenous TSP-1 enhances thrombin-stimulated aggregation.

Given the increased levels of TSP-1, indicating a potential increase in the inflammatory response in *mdx* mouse cerebellum, we can speculate that insoluble fibrin deposits, following extravasation of fibrinogen through a leaky

BBB, causes a toxic environment for neurons and thus impacts upon normal cognitive functioning.

To the best of our knowledge this is the first time that a substantial change in the cerebellar microenvironment of *mdx* mice had been reported. Investigations into the combined effect of enhanced fibrinogen and TSP-1 levels in the *mdx* cerebellum need to be performed, but recently there has been evidence that they have opposite effects at inhibitory synapses *in vitro* via the mediation and inhibition of neurite outgrowth, respectively (Charrier *et al.*, 2010).

6.4.4 Elevated levels of GABA Transporter 3 in the mdx cerebellum

GABA is a predominant neurotransmitter, mediating fast inhibitory synaptic transmission and regulating the excitatory activity of neurons (Macdonald and Olsen, 1994). GABAergic neurons control the onset of large-scale network oscillations at various frequency ranges during development and in the mature brain, and their dysfunction is implicated with the onset of disease states like epilepsy, schizophrenia, and autism (Le Magueresse and Monyer, 2013). In the cerebellar cortex, four of the five types of neurons, Purkinje, satellite, basket, and Golgi cells release GABA as a neurotransmitter (Takayama and Inoue, 2005). The stellate cell axons make many GABAergic synaptic contacts with the dendritic shafts of PCs in the molecular layer (ML). Whereas, the basket cell axons form GABAergic synapses with PC bodies and the initial segment of the PC axons in the PCL (Takayama and Inoue, 2005). Additionally, Golgi cell axons form inhibitory synapses with granule cell dendrites at the peripheral part of the synaptic glomeruli in the granular layer (GL). GABAergic inputs regulate the neuronal activity of Purkinje and granule cells, which organise the major stream of neural circuitry in the cerebellar cortex.

Physiological and biochemical studies have demonstrated that the non-vesicular form of GABA is released via the plasma membrane by the reverse transporter action of plasma membrane GABA transporters (GATs) (Varju *et al.*, 2001). GATs mediate the GABA-uptake from the synaptic cleft by exchanging Na^+ and Cl^- ions in the mature brain (Gadea and Lopez-Colome, 2001). GAT-1 and GAT-3 have been found to be widely localised in neural and glial cells in the rodent cerebellum (Itouji *et al.*, 1996; Rosina *et al.*, 1999). Recent studies

have found that GABA might be extra synaptically released only by exocytosis from GABAergic axons in the developing mouse cerebellar cortex (Takayama and Inoue, 2005). During formation of GABAergic synapses, GABA could be re-uptaken, firstly into the presynaptic terminals via GAT-1, and subsequently into both presynaptic terminals via GAT-1 and astrocyte processes via GAT-3 (Takayama and Inoue, 2005).

The overexpression of GAT-3 detected in the *mdx* cerebellum indicates abnormalities in the GABAergic system. It is hypothesised that altered spatial localization of $GABA_A$ receptors due to Dp427 loss is a pathological mechanism associated with brain dysfunction in DMD, and researchers suggest that targeting extra synaptic $GABA_A$ receptors could provide useful therapeutic targets (Vaillend and Chaussenot, 2017). In this study we found no difference in the expression levels of $GABA_A$ α_2 receptor in the *mdx* cerebellum but we did not look at the spatial distribution of this receptor. It is necessary to perfectly time GABA release from pre-synaptic terminals with GABA receptors activation in pre- and post-synaptic membranes, and GABA clearance from the extracellular space, in order to coordinate normal neuronal functioning. Overexpressing GABA transporter (GAT) alters the rate of uptake of GABA from the extracellular space and has direct impact upon excitatory and inhibitory events in the cerebellum. It remains unclear whether GABA transporters can shape the GABA concentration profile inside the synaptic cleft, given what is currently known about their expression, binding kinetics, and transport efficiency (Le Magueresse and Monyer, 2013).

Interestingly depolarizing events that induce activation of voltage-gated Ca^{2+} channels increase the recycling rate of GABA transporters (Deken *et al.*, 2003); proteins of the SNARE complex that mediate neurotransmitter vesicle release, like syntaxin-1A, interact with GABA transporters and increase their surface expression (Deken *et al.*, 2000). We also identified elevated levels of syntaxin-1A in the *mdx* cerebellum (Table 6.3), although we did not confirm this finding, and future studies should focus on how, if at all, syntaxin-1A and GAT3 overexpression affects neuronal excitability in the *mdx* cerebellum. There is little information regarding the functioning of Dp40, the shortest dystrophin brain isoform, which contains only the β-dystrogylcan binding portion of the protein

and is produced via alternative splicing of the Dp71 transcript (the most abundant dystrophin isoform in the brain). Recently Dp40 has been identified to interact with syntaxin-1A and synaptosomal-associated protein 25 (SNAP25) (Tozawa *et al.*, 2012), which is theorised to form a novel protein complex and play a crucial role in presynaptic function. Future experiments could investigate GABA expression in the cerebellum other *mdx* mouse models (e.g. *mdx4cv*) to elucidate which dystrophin isoforms are involved in GABA dysfunction other than Dp427.

Overall, our findings demonstrate numerous and complex biochemical changes occurring in the CNS due to the loss of Dp427. We speculate that some of the changes in the mdx cerebellar proteome, in comparison to control mice, serve as compensatory mechanisms whilst others may contribute directly to cognitive dysfunction in DMD. Additionally, candidate proteins identified could be evaluated for their suitability as proteomic biomarkers for monitoring treatment of cognitive dysfunction in DMD

Chapter 7. General discussion and future direction

7.1 Discussion

The overall aim of this thesis was to use non-invasive methods to develop outcome measures to monitor CNS pathology longitudinally in DMD mice. The *mdx* mouse is used for preclinical drug development studies and there is urgent need to develop reliable, reproducible, and robust outcome measures, as there is an increasing focus upon understanding and treating cognitive dysfunction in DMD patients. Additionally, we sought to determine if the *Cmah-/-mdx* mouse model was a more superior mouse model to that of the *mdx* for studying CNS pathology associated with dystrophin deficiency.

The majority of studies have examined intellectual function in young DMD boys (Anderson *et al.*, 1988; Hinton *et al.*, 2007; Doorenweerd *et al.*, 2014) and cognitive symptoms in DMD adults have received less attention (Ueda *et al.*, 2017). As treatment options, life expectancy, and the prognosis of DMD patients has dramatically improved (Passamano *et al.*, 2012) over the past few decades, more attention needs to be paid to the natural history of cognitive deficits in DMD to improve overall quality of life. Historically, the majority of research regarding the pathophysiology of DMD was focused upon the study of muscular impairment. To date, the understanding of the psychocognitive manifestations in DMD and its aetiopathogenic basis is yet to be defined.

There is no concrete genotype-phenotype relationship between the position of a mutation in the *DMD* gene and the subsequent risk of cognitive impairment. It has been postulated that differences in the neuropsychological profiles observed in DMD patients are related to the number and isoforms of CNS–expressed dystrophin (Taylor *et al.*, 2010). It is hypothesised that mutations in the distal portion of the *DMD* gene are more commonly associated with an increased risk of mental retardation in comparison to more proximal gene mutations (Muntoni *et al.*, 2003). However, there is reported evidence of various patients whose mutation does not correlate with this hypothesis (Erturk *et al.*, 2010). Additionally, many structures in the brain express full-length dystrophin (cerebellum, hippocampus, amygdala, prefrontal cortex) and understanding the

implications of the loss of full-length dystrophin in the CNS is vital to better understand how cognition is affected in DMD.

A recent study examining the cognitive profiles and characteristics of adults with DMD (n=15 and an average age of 30.4 years) found a significant deficit in scores for picture completion, arithmetic, matrix reasoning, symbol search, letter-number sequencing, and digit span of the Wechsler Adult Intelligence Scale III (WAIS-III) (Ueda *et al.*, 2017). Logical memory and delayed logical memory, measured using Clinical Assessment for Attention (CAT), were also impaired in DMD adult patients (Ueda *et al.*, 2017). However, the study found that cognitive ability that does not require sequential processing was not impaired in DMD adults. These findings were consistent with previous studies (Cotton *et al.*, 2005), indicating that VIQ improved with age. Moreover, a recent study investigating cognitive dysfunction in 14 DMD patients (age range 18-37 years) identified $GABA_A$-R clustering to be functionally abnormal, utilising 123 I-MZ Single-photon emission computed tomography (SPECT) imaging, and demonstrated that there was progressive $GABA_A$-R functional abnormality in the prefrontal cortex of DMD patients (Suzuki *et al.*, 2017). Remarkably, the progressive reduction of $GABA_A$-R correlated with worsening neuropsychological performance with increasing age. These studies highlight the importance of studying cognitive abilities with increasing age in DMD patients and support to the premise that intellectual functioning in the DMD patients changes with age (Suzuki *et al.*, 2017; Ueda *et al.*, 2017).

To the best of our knowledge this is the first study to investigate if cognitive dysfunction is progressive in *mdx* mice. Additionally, this is the first study to characterise the *Cmah-/-mdx* mouse brain phenotype. The work presented in this thesis established a progressive decline in cognitive ability in the *mdx* mouse, due to the loss of full length dystrophin only, with increasing age. Additionally, we report numerous changes in the brains of DMD mouse models, which are exacerbated with age, including: an increased total brain volume, increased lateral ventricular volume, changes in brain fluid handling, reduced AQP4 expression, and reduced integrity of the BBB. We further identified potential molecular pathways in the *mdx* cerebellum which are altered in response to Dp427 deficiency. We speculated that some of the changes in comparison to control mice serve as compensatory mechanisms, such as

mitochondrial changes, whilst others may contribute directly to the cognitive dysfunction observed in DMD.

7.1.1 Identification of progressive cognitive dysfunction in mdx mice

The *mdx* mouse was studied between 4 and 12 months old with the Barnes maze test and the NOR task and we identified an effect of ageing on the behavioural responses of these mice. At 4 months old the *mdx* mice had a comparable performance to that of control *C57BL/10* mice during the Barnes maze test, and only showed a slight increase in their acquisition times to learn where the target hole was located (primary latency). However, by 12 months old we identified profound memory impairments in the *mdx* mice, particularly with respect to long-term memory ability, and *mdx* mice primary latencies differed considerably to that of the control *C57BL/10* mice. This study reinforced the importance of measuring cognitive abilities longitudinally in *mdx* mice in order to assess how the loss of full-length dystrophin affects learning abilities with age. Mice are not men and although we have identified a progressive cognitive dysfunction in the *mdx* mouse model of DMD, the literature highlights a particular deficit in VIQ in DMD patients, a cognitive aspect not measurable in mice. However, there are now an increasing number of studies focusing upon understanding the molecular and biological aetiology of this cognitive dysfunction and it is envisaged that future studies will have an increasing emphasis upon monitoring cognitive impairment progressively in both DMD patients and *mdx* mice, which will be vital for therapy development.

7.1.2 The study of the effect of Neu5Gc expression in the brain

Although mice are widely used in research, questions remain about their reliability as a model for human diseases. Indeed, 99% of mouse genes have an equivalent in humans, making mice a valuable model for studying the function of human genes both in healthy and disease states (Vandamme, 2014). The *CMAH* gene is one of the genes that differ between mice and men (Okerblom and Varki, 2017).

The evolution of modern humans from the great apes coincided with a series of genetic changes that caused alterations in the composition of sialic acids on the surface of human cells, in addition to changes in the properties of sialic acid-

binding proteins. In mouse brain, Neu5Gc is most highly expressed in endothelial cells, although not all blood vessels have strong expression and some microglia/macrophages show no expression (Naito-Matsui *et al.*, 2017). Moreover, no species (rat, chimpanzees, rabbits, xenopus and whitefish) demonstrate clear staining of Neu5Gc in neural cells or neutrophils. There are theorised advantages to this change in sialyation capacity, for example diminishing infections by lethal pathogens such as malaria (Okerblom and Varki, 2017). However, we have demonstrated an increasing similarity in brain aging between *Cmah-/-* mice and humans (brain atrophy with age) which may or may not be considered advantageous.

This current study has established that the loss of the *Cmah* gene has a profound impact on the CNS of mice. We have demonstrated enlarged TBV in *Cmah-/-mdx* between 4 and 18 months old, abnormal ventricular structures, and changes in cognitive abilities between 4 and 12 months old. Conversely we found a reduced TBV in *Cmah-/-* mice between 4 and 18 months old, significant reduction in lateral ventricular volume, and focal brain atrophy at 18 months old. This is the first time that MR brain imaging has been applied to mice lacking the *Cmah* gene, allowing us to study the same cohort of mice longitudinally. Given the results presented in this thesis it is likely that this gene has an essential function in the brain and suggests a direct role of sialic acids (Neu5Ac and Neu5Gc) for modifications in brain development, although their exact role is yet to be fully elucidated.

Interestingly, the initial paper detailing the muscle pathology of the *Cmah-/-mdx* mice (Chandrasekharan *et al.*, 2010) indicated that these mice better mimic the dystrophic characteristics observed in DMD patients. *Cmah-/-mdx* mice had accelerated onset of loss of ambulation, cardiac and respiratory muscle weakness, and a reduction in lifespan, compared to the *mdx* mice, which are all major phenotypes contributing to DMD morbidity and mortality (Chandrasekharan *et al.*, 2010). Surprisingly, in our study we did not detect any shortening of lifespan in the *Cmah-/-mdx* mice. In fact, we had a higher frequency of mortality in the *mdx* mouse colony due to the development of an increased frequency of rhabdomyosarcoma in this genotype (Chamberlain *et al.*, 2007). Cardiac studies in our lab suggested that the cardiac function of *Cmah-/-mdx* mice is not significantly different from *mdx* mice at baseline,

although *Cmah-/-mdx* mice performed worse under dobutamine stress conditions (Blain *et al.* 2017, under review). However, further characterisation of this mouse model, in terms of the cumulative loss of both dystrophin and Neu5Gc expression in muscle and in brain is necessary to determine if this mouse model is a relevant model to study either the cognitive dysfunction or the muscle pathophysiological aspects of DMD.

The *mdx* mouse remains the gold standard and best characterised mouse model for DMD (Bulfield *et al.*, 1984). Although the *mdx* mouse model has a relatively mild muscle phenotype compared to that of DMD patients and the lifespan is not significantly reduced, these differences in the severity of phenotype between humans and mice are usually anticipated by the investigator, and subsequently overcome by critical evaluation of the experimental design (TREAT-NMD protocols (Willmann *et al.*, 2012)). For example using older *mdx* mice where the muscle pathology is more severe and exacerbating the phenotype by exercise. Difficulties arise in trying to establish a mouse model that might better mimic the human disease phenotype given that advancements may have already been made in pre-existing models. Indeed, the *Cmah-/-mdx* is a better phenocopy of DMD than the *mdx* mouse and some suggest that *Cmah*-deficient *mdx* mice represent a new small animal model for DMD that better approximates the human glycome and its contributions to muscular dystrophy (Chandrasekharan *et al.*, 2010). However, limited studies utilising this model make it difficult to translate and interpret findings and given the abnormalities we have detected in the *Cmah-/-* mouse we believe that the *mdx* mouse still remains the best model for studying the cognitive dysfunction in DMD.

7.1.3 Phenotypes observed in wild type mice

Selection of an appropriate animal model is a crucial first step in many research investigations. Throughout this study we used control *C57BL/10* mice which are a popular inbred strain used as ‘wild type’ and all mice in this study were bred onto a *C57BL/10* background. In this model hydrocephalus is known to occur spontaneously in approximately 3% of pups. Throughout this present study we identified changes in this mouse model, which are important when considering the changes observed in our mutant mice. We observed an increased TBV with

increasing age, increased impairment of the BBB with increasing age, and reduced spatial learning and memory with increasing age. As well as revealing some interesting observations with regards to the effect of ageing on the normal mouse brain, this current study highlights the importance of breeding mice onto the same genetic background in order to deduce which characteristics are simply inherent and which are pathogenic in mutant mice. The *C57BL/10* strain has previously demonstrated behavioural characteristics which are not present in the *C57BL/6* strain, despite the high genetic similarity between these two mouse strains. In cognitive tests, female *C57BL/10* mice showed marked deficits in spatial working memory, but not in reference memory, whether spatial or non-spatial and impaired coordination and balance, compared to *C57BL/10* mice (Deacon *et al.*, 2007). Nonetheless, this is an important consideration when comparing cognitive behaviour in *mdx* mice, given that differences exist in innate behavioural characteristics between background mouse strains, and it is therefore not advisable to utilise these strains interchangeably.

7.1.4 Complex changes identified in the mdx mouse cerebellar proteome

We analysed the cerebellar proteome from control *C57BL/10* mice and *mdx* mice at 6 months old using an LC-MS approach, and identified major differences in the expression levels of numerous proteins between the two genotypes. The study was the first investigation for evaluating the proteomic profile of the cerebellum due to the loss of full-length dystrophin and we identified numerous elevated proteins which we hypothesise occur in a compensatory manner. Increased mitochondrial proteins in the *mdx* cerebellum may be expressed to cope with elevated demands for ATP suggesting the *mdx* cerebellum requires a higher output to function normally due to full-length dystrophin loss.

GAT3 was also elevated in the *mdx* cerebellum and it has long been hypothesised that dystrophin loss affects the brain GABAergic system (Anderson *et al.*, 2002; Sekiguchi *et al.*, 2009; Suzuki *et al.*, 2017). The GABAergic system is one of the key modulators of neuronal plasticity, and plays an important role in the control of “critical periods” during brain development (Varju *et al.*, 2001). This study indicates that in the absence of dystrophin, there is an abnormality of the molecular machinery which underlies

the precise GABAergic synaptic transmission in the cerebellum due to overexpression of GABA transporters (GAT3). Further studies are necessary to determine the mechanisms behind GAT3 overexpression in the *mdx* cerebellum and how this impacts on both motor and cognitive function.

The identification of elevated levels of fibrinogen in the *mdx* cerebellum at 6 months old reinforced our findings of BBB defects as elevated fibrinogen deposits are suggestive of weakened BBB. Interestingly, in AD it has been reported that vascular perturbations manifest in a leaky BBB and extravasation of fibrinogen (Ryu and McLarnon, 2009). Taken together, elevated fibrinogen deposits with elevated TSP-1 levels suggest an increased inflammatory environment for neurons within the *mdx* cerebellum, which could be detrimental to their survival.

7.1.5 Difference in brain morphology and function between the mdx and Cmah-/-mdx mouse models of DMD

The behavioural testing performed in this study has demonstrated that the *mdx* and *Cmah-/-mdx* mice behave differently in terms of spatial learning and memory and object recognition memory. The *Cmah-/-mdx* mice out performed even the control *C57BL/10* and *Cmah-/-* mice on the Barnes maze test between 6 and 12 months old, whereas the *mdx* mice performed worse with increasing age. Additionally during the NOR task the *Cmah-/-mdx* mice had a preference for the novel object rather than the familiar object compared to *mdx* mice, who showed a significant preference for the familiar object. The *Cmah-/-mdx* mice displayed little anxiety related behaviour (repetitive jumping, freezing, etc.). The *Cmah-/-mdx* also had a larger total brain volume (at all time points), increased T_2 relaxation times at 18 months old (in all ROIs compared between the two genotypes), additional brain ventricle abnormalities (CSP), and reduced BBB impairment in the cortex, cerebellum, and caudate putamen at 6 months old (identified via Gd uptake).

The *Cmah-/-mdx* mice did however display numerous comparable brain characteristics to that of the *mdx* mice including: reduced AQP4 expression with increasing age, similar levels of EBD extravasation between 6 and 18 months old in the cerebrum, enlarged lateral ventricle volume (enlargement increasing with increasing age), reduced long-term spatial learning and memory at 12

months old on the Barnes maze test and similar skeletal abnormalities (skull widening, kyphosis and scoliosis).

It is therefore possible that the loss of the *Cmah* gene in conjunction with the loss of full length dystrophin confers some resistance to the loss of full length dystrophin alone. It is difficult to come to a precise conclusion given that the loss of the *Cmah* gene on brain function and structure, in both humans and mice, is yet to be elucidated and this is the first study to investigate the brain in *Cmah-/-mdx* mice. Our studies have found that the *Cmah-/-* mouse differs considerable to the control *C57BL/10* mice with regards to brain structure and function, therefore our finding in the *Cmah-/-mdx* mice are confounded by the fact that the *Cmah-/-* mice have a brain phenotype. We have identified numerous quantifiable changes in the CNS pathology of *mdx* mice, therefore this model is relevant for studying full-length dystrophin loss on brain function longitudinally.

7.1.6 Dystrophin loss in other neurological disorders

Dystrophin has a function in many other neurological diseases, often as a secondary effect. It has been shown that AQP4 deficiency increases the propensity for seizures (Badaut *et al.*, 2014) and in human mesial temporal lobe epilepsy (TLE), associated with hippocampal degeneration and sclerosis, there is a loss of the DGC and AQP4 expression. In patients with TLE the loss of Kir4.1 expression was associated with loss of dystrophin and α-syntrophin, but not with loss of β-dystroglycan, suggesting partial disruption of the DGC which likely interferes with K^+ homeostasis and may contribute to the epileptogenicity of the sclerotic hippocampus (Heuser *et al.*, 2012). Conversely, other studies have found that hippocampal full-length dystrophin (Dp427b) levels are upregulated in human TLE (Hendriksen *et al.*, 2016b). Taken together these findings suggest that changes in hippocampal dystrophin expression may contribute to the underlying pathology of TLE. Furthermore, DMD patients have an increased susceptibility to seizures (Pane *et al.*, 2013).

Moreover, dystrophin deficiency is associated with neurodegenerative disorders. We only identified an obvious cognitive decline in old *mdx* mice (~6 months) and *mdx* mice have a normal lifespan. Therefore, if the life expectancy of DMD

patients increases further, due to better treatment options, a decline in cognitive function could be detrimental to overall quality of life. For example, in Alzheimer's disease (AD), a reduction and even loss of Dp71 and AQP4 have been reported where a reduction of these proteins was associated with increased vascular amyloid deposits (cerebral amyloid angiopathy) similar effects have been demonstrated in AD mice and autopsied AD patient brains (Wilcock *et al.*, 2009).

Recent reports propose that altered AQP4 and Dp71 complex contribute to the sub-ischemia prevalent in the brain tissue of idiopathic pressure hydrocephalus (iNPH). iNPH is associated with clinical triad gait disturbance, cognitive impairment (dementia), and enlarged cerebral ventricles, affecting patients >65 years old (Eide and Hansson, 2017). It has been shown that iNPH patients have prominent astrogliosis and reduced expression of AQP4 and Dp71 immunoreactivities in the astrocytic perivascular endfeet, where higher levels of astrogliosis correlated with a lower levels of AQP4 and Dp71 at astrocytic endfeet (Eide and Hansson, 2017).

Dystrophin is involved in the pathology of various neurological disorders, this reinforces the importance of rare disease research, where advances in the understanding of the physiology and pathophysiology related to cognitive dysfunction in DMD can have a positive impact on much wider fields of study. Therefore, fully elucidating the function of neuronal dystrophin may also help to ameliorate symptoms in other neurological disorders.

7.1.7 Study limitations

The number of mice used in this study was limited to only 8 mice per genotype for each time point. Although this study demonstrated numerous significant findings across all genotypes, increasing the number of mice studied will ultimately provide further reinforcement of the findings already established. Increasing the number of mice will help reduce the variability and allow for the identification of a more robust phenotype.

Another limitation of this study, which may have an impact on the *Cmah* null mouse phenotype, is the diet the mice are fed. Normal mouse chow contains

exogenous Neu5Gc. It is theorised that exogenous dietary sources of Neu5Gc (red meats, milk, cheese etc.) can enter human cells via micropinocytosis to reach the endosomal/lysosomal system (Bardor *et al.*, 2005). There it can be transported into the cytosolic compartment and get activated to Neu5Gc, which would eventually enter the Golgi apparatus, where sialyltransferases can catalyse transfer of Neu5Gc to newly synthesised glycoconjugates. It has also been shown that humans absorb a portion of ingested Neu5Gc, excrete it into the urine, and incorporate a small amount into newly synthesised glycoconjugates (Tangvoranuntakul *et al.*, 2003). Providing the mice with a diet containing Neu5Gc should therefore not be a fundamental issue impacting upon the brain changes observed during this study. Additionally, all mice, regardless of genotype, had free access to the same diet. However, absorption of Neu5Gc from the gut into the blood-stream could be considerably different between species and was not studied here. Nevertheless, it is an interesting question to address in future studies.

We identified that hippocampal spatial learning and memory declines in *mdx* mice with age utilising the Barnes maze test. Additionally, we identified a reduced recognition memory in *mdx* mice and behavioural changes characterised by elevated levels of anxiety related behaviour at 12 months old, evident using the NOR task. However, unfortunately the Barnes maze test and NOR tasks detailed in this project are not standardised procedures and many modifications to already established protocols can be made easily i.e. changing the number of habituation days, the length of time the mouse had to search, the number of days between short and long-term memory tasks etc. Additionally, many factors can influence a behavioural test in rodents including: test environment (noise, light etc.), previous exposure to testing equipment, laboratory housing conditions, the investigator/s, and complexity of tasks. It is important to acknowledge that there is a large amount of inherent variation with behavioural assays in rodents and the findings in this study pertain to the outlined procedures for the Barnes maze test and NOR task detailed in the material and methods (chapter 2).

7.1.8 Outcome measures to monitor cognitive dysfunction in DMD mouse models

As therapy development for DMD is rapidly increasing and the life expectancy

of DMD patients is likely to increase further, there is urgent need for reliable biomarkers in the brain to monitor both disease progression but also provide potential therapeutic targets. It is evident from both this study and the current literature that the loss of full-length dystrophin from the *mdx* brain has numerous and complex implications in a variety of brain regions. The multifunctional actions that dystrophin appears to play within in the brain could provide a possible explanation for the heterogeneous cognitive phenotype observed in DMD patients. We have demonstrated that the average primary latency of *mdx* mice to find the target hole during Barnes maze testing increased with increasing age (spatial memory is progressively worse with age in *mdx* mice). Additionally, we have found that the extravasation of contrast agents into the *mdx* mouse brain parenchyma increased significantly with increasing age (similar effect seen for both EBD and Gd). Targeting the integrity of the BBB, by restoring dystrophin expression, could help improve the cognitive dysfunction observed in DMD. Additionally, the increase in average latency to locate the target hole observed in *mdx* mice during the Barnes maze test could be a useful outcome measure for monitoring treatment efficacy.

Ultimately, the long-term goal is the discovery of therapeutic strategies for the treatment of both the muscle and brain involvement in DMD and it is hoped that the identification of possible roles for brain dystrophin and potential outcome measures to monitor cognitive function presented in this thesis will help to drive future research.

7.2 Future direction

7.2.1 Further validation of proteomic studies and elucidation of protein function

The characterisation of the pathways involved in the CNS pathology due to dystrophin loss will be instrumental for the identification of novel therapeutic targets, which may be useful in the treatment of cognitive dysfunction associated with DMD. It is therefore important to perform studies to determine the functional significance of regulated proteins that we identified using proteomic profiling studies in the cerebellum. Other interesting proteins identified with increased abundance following proteomic profiling in the *mdx* cerebellum, which were not verified in this study, but are interesting candidates with function roles in the CNS, include:

- Aspartoacylase: catalyses the deacetylation of N-acetylaspartic acid (NAA) to produce acetate and L-aspartate. NAA occurs in high concentration in brain and its hydrolysis NAA plays a significant part in the maintenance of intact white matter (Pundir *et al.*, 2017). Changes in NAA concentration have been reported in the brains of both *mdx* mice (Tracey *et al.*, 1996) and DMD patients (Rae *et al.*, 1998).
- Syntaxin-1A: plays a role in hormone and neurotransmitter exocytosis. It is potentially involved in the docking of synaptic vesicles at presynaptic active zones (Pundir *et al.*, 2017). Furthermore, syntaxin-1A has been reported to interact with the shortest dystrophin isoform-Dp40 (Tozawa *et al.*, 2012) in the brain.
- Purkinje cell protein 4-like protein 1: expressed at early stages of development in metencephalic and mesencephalic roof plates (Pundir *et al.*, 2017). At later stages of development, it is expressed in structures corresponding to circumventricular organs which in adults control the production of the CSF (Bulfone *et al.*, 2004). Purkinje cell protein 4-like protein 1 has been demonstrated to positively regulate nitrite outgrowth and neurotransmitter release (Harashima *et al.*, 2011). We identified increased lateral ventricles in the *mdx* mouse brain with age. Given that Purkinje cell protein 4-like protein 1 has a functional role in controlling CSF production it would be interesting to determine if this protein is responsible for the ventricular abnormalities we observe, potentially due

to increasing the CSF circulating in the brain ventricles.

-

Additionally performing proteomic profiling on other brain regions known to be dystrophin-rich, such as the hippocampus where Dp427b is expressed abundantly in pyramidal neurons, could provide additional insights into how specific brain structures are affected at the protein level due to full-length dystrophin loss.

7.2.2 Imaging techniques to further monitor dystrophin deficiency on mouse brain structure and function with age

Magnetic resonance spectroscopy (MRS) is a non-invasive method that could be used to measure the concentration of brain metabolites including NAA, Creatine, Choline, Myo-inositol, Total Glutamate + Glutamine (as standards), within a predefined voxel in ROIs of the brain. This could be used to additionally confirm aspartoacylase overexpression in the *mdx* mouse cerebellum (by confirming increased NAA concentrations) and provide further information regarding the functional integrity of specific brain regions paramount to a normal cognitive functioning. Furthermore, this technique would provide evidence of specific neurometabolites that indicate biochemical changes in the brain that are thought to underpin abnormalities in cognitive performance. There have been previous reports of decreased NAA to Cho ratio in the *mdx* mouse cerebral cortex (Tracey *et al.*, 1996). Interestingly, there are conflicting reports regarding changes in the metabolic composition in the cerebellum, frontal and temporo-parietal cortex in DMD patients. A reduction in glutamate, an elevation and reduction in choline containing compounds, and an increase in NAA have been identified via MRS (Rae *et al.*, 1998; Kreis *et al.*, 2011). However, most recently an MRS study in DMD patients indicated preservation in cerebral biochemical composition (Doorenweerd *et al.*, 2017b). Discrepancies regarding the cerebral biochemical composition in DMD patients could be attributed to differences in field strength, smaller cohorts, and differences in statistical analyses. Nevertheless, this is an interesting parameter to focus on in future investigations both in animal and human studies.

Diffusion tensor imaging (DTI) has been reported in one study in the *mdx* mouse brain. DTI is predominantly used to measure brain white matter structural integrity by taking advantage of the natural phenomenon of diffusion:

the random movement of molecules. Without restriction this movement is isotropic (equal in all direction). However, in the brain, due to differing cell shapes and size, movement is restricted (i.e. molecules cannot cross membranes), making the diffusion anisotropic. Fractional Anisotropy (FA) is given a value between 0 and 1, where 0 is isotropic and 1 is very anisotropic. In *mdx* mice there is evidence of elevations in diffusion diffusivities in the prefrontal cortex and a reduction of fractional anisotropy in the hippocampus. There was no change reported in the DTI measurements from either the grey or white matter of the *mdx* cerebellum (Xu *et al.*, 2015). This paper did not show the cerebellar results making it hard to deduce if the finding signified very little change between control and *mdx* mice or a larger change which just precluded significance. Moreover, this study (Xu *et al.*, 2015) used a relatively small sample size (7-8 male mice) and only investigated one time point (9 months old), so it would therefore be interesting to employ DTI to a larger sample size at different ages to determine if DTI was a valuable in *vivo* tool for monitoring changes in the *mdx* brain (including the cerebellum) over time.

7.2.3 Further confirmation of a progressive cognitive dysfunction in mdx mice

Prospective studies could also include further behavioural analysis of both *mdx* and *Cmah-/-mdx* mice. Preforming additional cognitive tests which measure different aspects of learning and memory from that of the Barnes maze test and NOR task may help to understand if the cognitive impairment observed currently in the *mdx* mice is globally progressive or is restricted to certain aspects of cognition. For example, the Y maze spontaneous alteration test assesses the rodents' willingness to explore new environments, and relies heavily of proper functioning of the hippocampus, septum, basal forebrain, and prefrontal cortex (Sarnyai *et al.*, 2000; Wolf *et al.*, 2016). It would also be interesting to perform the reversal Barnes memory approach as (Remmelink *et al.*, 2016) previously demonstrated where *mdx* mice showed inflexibility to learn the reversal task, given that cognitive inflexibility remains a paradoxical question in autistic patients (Geurts *et al.*, 2009), and further distinguish if this element of learning worsens with increasing age.

There is increasing evidence in the literature that the majority of patients with mutations affecting Dp71 are intellectually disabled (Daoud *et al.*, 2009).

Additionally, studies in DMD patients have identified that mild mental retardation is significantly more frequent with mutations affecting Dp140 (Doorenweerd *et al.*, 2014). Therefore, it would be interesting to perform a longitudinal MR imaging and behavioural analysis, similar to this study, in the *mdx*^{4cv} mouse model of DMD, where a nonsense point mutation in exon 53 leads to premature translation termination (Im *et al.*, 1996), and consequently does not express the brain Dp427, Dp140, and Dp71 dystrophin isoforms. This model has already been studied briefly, utilising a comparative proteomic whole brain analysis identifying protein changes which differ to those observed in the *mdx* mouse (Murphy *et al.*, 2015), but no longitudinal characterisation of cognitive dysfunction has been performed.

7.2.4 Histological investigations

Additional histological investigations are vital to provide an insight into how dystrophin deficiency affects brain structure at a cellular level. Basic staining could provide information on how the brain ventricle system is changed due to loss of full length dystrophin, for example if damage or rearrangement of the ependymal cell layer could impact CSF production and cause alterations in the brain ventricular volumes. Staining for dystrophin in various brain regions is also essential to provide further information regarding isoform specific expression within defined brain regions. This study identified for the first time that dystrophin could be expressed in the *mdx* mouse caudate putamen, given that this is the brain region which demonstrated increased T_2 relaxation rate and enhanced Gd extravasation, therefore it would be interesting to stain for dystrophin in this brain region.

Appendix

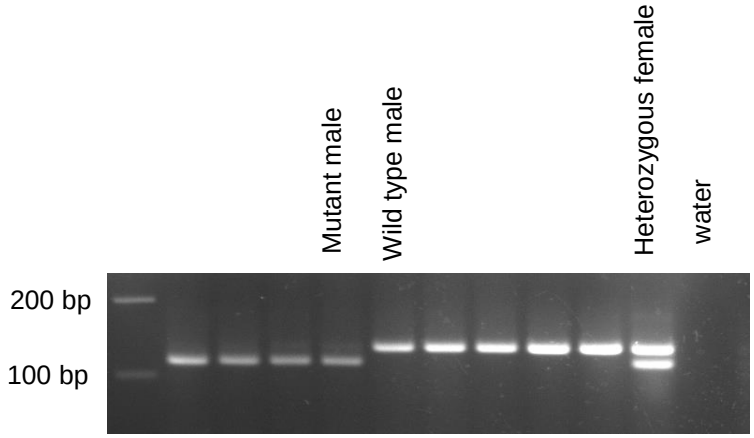

Genotyping *mdx* mice
Representative PCR on genomic DNA extracted from ear clips showing amplified fragments of ~134 bp for wild type allele and 117 bp for mutant allele. All bands are measured against a 100 bp DNA ladder. Water lane is a negative control without any DNA sample.

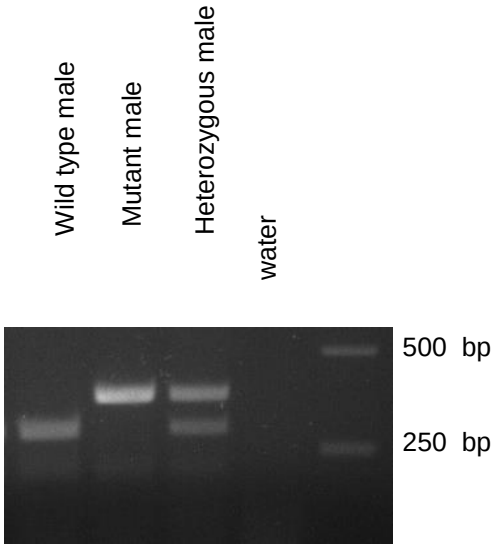

Genotyping *Cmah-/-mdx* mice
Representative PCR on genomic DNA extracted from ear clips showing amplified fragments of ~297 bp for wild type allele and 400 bp for mutant allele. All bands are measured against a 1 kb DNA ladder. Water lane is a negative control without any DNA sample.

References

Aartsma-Rus, A., Van Deutekom, J.C., Fokkema, I.F., Van Ommen, G.J. and Den Dunnen, J.T. (2006) 'Entries in the Leiden Duchenne muscular dystrophy mutation database: an overview of mutation types and paradoxical cases that confirm the reading-frame rule', *Muscle Nerve*, 34(2), pp. 135-44.

Abbott, N.J. and Friedman, A. (2012) 'Overview and introduction: the blood-brain barrier in health and disease', *Epilepsia*, 53 Suppl 6, pp. 1-6.

Abbott, N.J., Patabendige, A.A., Dolman, D.E., Yusof, S.R. and Begley, D.J. (2010) 'Structure and function of the blood-brain barrier', *Neurobiol Dis*, 37(1), pp. 13-25.

Abeysinghe, H.C.S., Phillips, E.L., Chin-Cheng, H., Beart, P.M. and Roulston, C.L. (2016) 'Modulating Astrocyte Transition after Stroke to Promote Brain Rescue and Functional Recovery: Emerging Targets Include Rho Kinase', *International Journal of Molecular Sciences*, 17(3), p. 288-290.

Adams, M.E., Mueller, H.A. and Froehner, S.C. (2001) 'In vivo requirement of the α-syntrophin PDZ domain for the sarcolemmal localization of nNOS and aquaporin-4', *The Journal of Cell Biology*, 155(1), pp. 113-122.

Ahn, A.H. and Kunkel, L.M. (1993) 'The structural and functional diversity of dystrophin', *Nat Genet*, 3(4), pp. 283-91.

Akshoomoff, N.A. and Courchesne, E. (1992) 'A new role for the cerebellum in cognitive operations', *Behav Neurosci*, 106(5), pp. 731-8.

Alessi, A., Bragg, A.D., Percival, J.M., Yoo, J., Albrecht, D.E., Froehner, S.C. and Adams, M.E. (2006) 'gamma-Syntrophin scaffolding is spatially and functionally distinct from that of the alpha/beta syntrophins', *Exp Cell Res*, 312(16), pp. 3084-95.

Allen, D.G., Gervasio, O.L., Yeung, E.W. and Whitehead, N.P. (2010) 'Calcium and the damage pathways in muscular dystrophy', *Can J Physiol Pharmacol*, 88(2), pp. 83-91.

Allikian, M.J. and McNally, E.M. (2007) 'Processing and assembly of the dystrophin glycoprotein complex', *Traffic*, 8(3), pp. 177-83.

Amann, K.J., Renley, B.A. and Ervasti, J.M. (1998) 'A cluster of basic repeats in the dystrophin rod domain binds F-actin through an electrostatic interaction', *J Biol Chem*, 273(43), pp. 28419-23.

Amiry-Moghaddam, M., Otsuka, T., Hurn, P.D., Traystman, R.J., Haug, F.M., Froehner, S.C., Adams, M.E., Neely, J.D., Agre, P., Ottersen, O.P. and Bhardwaj, A. (2003) 'An alpha-syntrophin-dependent pool of AQP4 in astroglial end-feet confers bidirectional water flow between blood and brain', *Proc Natl Acad Sci U S A*, 100(4), pp. 2106-11.

Andersen, B.B., Korbo, L. and Pakkenberg, B. (1992) 'A quantitative study of the human cerebellum with unbiased stereological techniques', *J Comp Neurol*, 326(4), pp. 549-60.

Anderson, J.L., Head, S.I., Rae, C. and Morley, J.W. (2002) 'Brain function in Duchenne muscular dystrophy', *Brain*, 125(Pt 1), pp. 4-13.

Anderson, S.W., Routh, D.K. and Ionasescu, V.V. (1988) 'Serial position memory of boys with Duchenne muscular dystrophy', *Dev Med Child Neurol*, 30(3), pp. 328-33.

Antequera, D., Vargas, T., Ugalde, C., Spuch, C., Molina, J.A., Ferrer, I., Bermejo-Pareja, F. and Carro, E. (2009) 'Cytoplasmic gelsolin increases mitochondrial activity and reduces Abeta burden in a mouse model of Alzheimer's disease', *Neurobiol Dis*, 36(1), pp. 42-50.

Antunes, M. and Biala, G. (2012) 'The novel object recognition memory: neurobiology, test procedure, and its modifications', *Cognitive Processing*, 13(2), pp. 93-110.

Aragon, J., Gonzalez-Reyes, M., Romo-Yanez, J., Vacca, O., Aguilar-Gonzalez, G., Rendon, A., Vaillend, C. and Montanez, C. (2017) 'Dystrophin Dp71 Isoforms Are Differentially Expressed in the Mouse Brain and Retina: Report of New Alternative Splicing and a Novel Nomenclature for Dp71 Isoforms', *Mol Neurobiol*.pp1-11

Austin, R.C., Morris, G.E., Howard, P.L., Klamut, H.J. and Ray, P.N. (2000) 'Expression and synthesis of alternatively spliced variants of Dp71 in adult human brain', *Neuromuscul Disord*, 10(3), pp. 187-93.

Badaut, J., Fukuda, A.M., Jullienne, A. and Petry, K.G. (2014) 'Aquaporin and brain diseases(,)', *Biochimica et biophysica acta*, 1840(5), pp. 1554-1565.

Bakshi, R., Benedict, R.H., Bermel, R.A., Caruthers, S.D., Puli, S.R., Tjoa, C.W., Fabiano, A.J. and Jacobs, L. (2002) 'T2 hypointensity in the deep gray matter of patients with multiple sclerosis: a quantitative magnetic resonance imaging study', *Arch Neurol*, 59(1), pp. 62-8.

Bardor, M., Nguyen, D.H., Diaz, S. and Varki, A. (2005) 'Mechanism of uptake and incorporation of the non-human sialic acid N-glycolylneuraminic acid into human cells', *J Biol Chem*, 280(6), pp. 4228-37.

Bartzokis, G., Beckson, M., Lu, P.H., Nuechterlein, K.H., Edwards, N. and Mintz, J. (2001) 'Age-related changes in frontal and temporal lobe volumes in men: a magnetic resonance imaging study', *Arch Gen Psychiatry*, 58(5), pp. 461-5.

Basu, D., Le, J., Zakharova, T., Mallery, E.L. and Szymanski, D.B. (2008) 'A SPIKE1 signaling complex controls actin-dependent cell morphogenesis through the heteromeric WAVE and ARP2/3 complexes', *Proceedings of the National Academy of Sciences of the United States of America*, 105(10), pp. 4044-4049.

Beal, M.F. (2007) 'Mitochondria and neurodegeneration', *Novartis Found Symp*, 287, pp. 183-92; discussion 192-6.

Becker, S. (2005) 'A computational principle for hippocampal learning and neurogenesis', *Hippocampus*, 15(6), pp. 722-38.

Benson, M.A., Newey, S.E., Martin-Rendon, E., Hawkes, R. and Blake, D.J. (2001) 'Dysbindin, a novel coiled-coil-containing protein that interacts with the dystrobrevins in muscle and brain', *J Biol Chem*, 276(26), pp. 24232-41.

Bergfeld, A. and Varki, A. (2014) 'Cytidine Monophospho-N-Acetylneuraminic Acid Hydroxylase (CMAH)', in Taniguchi, N., Honke, K., Fukuda, M., Narimatsu, H., Yamaguchi, Y. and Angata, T. (eds.) *Handbook of Glycosyltransferases and Related Genes*. Springer Japan, pp. 1559-1580.

Berta, S., Gert, L., Harald, H. and Sudarshan, P. (2007) 'Barnes maze, a useful task to assess spatial reference memory in the mice'.Nature protocols.

Bertram, J., Koschutzke, L., Pfannmoller, J.P., Esche, J., van Diepen, L., Kuss, A.W., Hartmann, B., Bartsch, D., Lotze, M. and von Bohlen Und Halbach, O. (2016) 'Morphological and behavioral characterization of adult mice deficient for SrGAP3', *Cell Tissue Res*, 366(1), pp. 1-11.

Billard, C., Gillet, P., Signoret, J.L., Uicaut, E., Bertrand, P., Fardeau, M., Barthez-Carpentier, M.A. and Santini, J.J. (1992) 'Cognitive functions in Duchenne muscular dystrophy: a reappraisal and comparison with spinal muscular atrophy', *Neuromuscul Disord*, 2(5-6), pp. 371-8.

Binder, D.K., Yao, X., Verkman, A.S. and Manley, G.T. (2006) 'Increased seizure duration in mice lacking aquaporin-4 water channels', *Acta Neurochir Suppl*, 96, pp. 389-92.

Black, F.W. (1973) 'Intellectual ability as related to age and stage of disease in muscular dystrophy: a brief note', *J Psychol*, 84(2d Half), pp. 333-4.

Bladen, C.L., Salgado, D., Monges, S., Foncuberta, M.E., Kekou, K., Kosma, K., Dawkins, H., Lamont, L., Roy, A.J., Chamova, T., Guergueltcheva, V., Chan, S., Korngut, L., Campbell, C., Dai, Y., Wang, J., Barisic, N., Brabec, P., Lahdetie, J., Walter, M.C., Schreiber-Katz, O., Karcagi, V., Garami, M., Viswanathan, V., Bayat, F., Buccella, F., Kimura, E., Koeks, Z., van den Bergen, J.C., Rodrigues, M., Roxburgh, R., Lusakowska, A., Kostera-Pruszczyk, A., Zimowski, J., Santos, R., Neagu, E., Artemieva, S., Rasic, V.M., Vojinovic, D., Posada, M., Bloetzer, C., Jeannet, P.Y., Joncourt, F., Diaz-Manera, J., Gallardo, E., Karaduman, A.A., Topaloglu, H., El Sherif, R., Stringer, A., Shatillo, A.V., Martin, A.S., Peay, H.L., Bellgard, M.I., Kirschner, J., Flanigan, K.M., Straub, V., Bushby, K., Verschuuren, J., Aartsma-Rus, A., Beroud, C. and Lochmuller, H. (2015) 'The TREAT-NMD DMD Global Database: analysis of more than 7,000 Duchenne muscular dystrophy mutations', *Hum Mutat*, 36(4), pp. 395-402.

Blake, D.J., Hawkes, R., Benson, M.A. and Beesley, P.W. (1999) 'Different dystrophin-like complexes are expressed in neurons and glia', *J Cell Biol*, 147(3), pp. 645-58.

Blake, D.J. and Kroger, S. (2000) 'The neurobiology of duchenne muscular dystrophy: learning lessons from muscle?', *Trends Neurosci*, 23(3), pp. 92-9.

Blake, D.J., Nawrotzki, R., Loh, N.Y., Górecki, D.C. and Davies, K.E. (1998) 'β-dystrobrevin, a member of the dystrophin-related protein family', *Proceedings of the National Academy of Sciences of the United States of America*, 95(1), pp. 241-246.

Blake, D.J., Schofield, J.N., Zuellig, R.A., Górecki, D.C., Phelps, S.R., Barnard, E.A., Edwards, Y.H. and Davies, K.E. (1995) 'G-utrophin, the autosomal homologue of dystrophin Dp116, is expressed in sensory ganglia and brain', *Proceedings of the National Academy of Sciences of the United States of America*, 92(9), pp. 3697-3701.

Blake, D.J., Weir, A., Newey, S.E. and Davies, K.E. (2002) 'Function and genetics of dystrophin and dystrophin-related proteins in muscle', *Physiol Rev*, 82(2), pp. 291-329.

Borden, L.A. (1996) 'GABA transporter heterogeneity: pharmacology and cellular localization', *Neurochem Int*, 29(4), pp. 335-56.

Brandao, M.L., Anseloni, V.Z., Pandossio, J.E., De Araujo, J.E. and Castilho, V.M. (1999) 'Neurochemical mechanisms of the defensive behavior in the dorsal midbrain', *Neurosci Biobehav Rev*, 23(6), pp. 863-75.

Bresolin, N., Castelli, E., Comi, G.P., Felisari, G., Bardoni, A., Perani, D., Grassi, F., Turconi, A., Mazzucchelli, F., Gallotti, D., Moggio, M., Prelle, A., Ausenda, C., Fazio, G. and Scarlato, G. (1994) 'COGNITIVE IMPAIRMENT IN DUCHENNE MUSCULAR-DYSTROPHY', *Neuromuscular Disorders*, 4(4), pp. 359-369.

Brovelli, A., Nazarian, B., Meunier, M. and Boussaoud, D. (2011) 'Differential roles of caudate nucleus and putamen during instrumental learning', *Neuroimage*, 57(4), pp. 1580-90.

Brown, E.S. and Chandler, P.A. (2001) 'Mood and Cognitive Changes During Systemic Corticosteroid Therapy', *Primary Care Companion to The Journal of Clinical Psychiatry*, 3(1), pp. 17-21.

Brown, E.S., Woolston, D.J. and Frol, A.B. (2008) 'Amygdala Volume in Patients Receiving Chronic Corticosteroid Therapy', *Biological Psychiatry*, 63(7), pp. 705-709.

Brown, R.H., Jr. (1997) 'Dystrophin-associated proteins and the muscular dystrophies', *Annu Rev Med*, 48, pp. 457-66.

Brunig, I., Suter, A., Knuesel, I., Luscher, B. and Fritschy, J.M. (2002) 'GABAergic terminals are required for postsynaptic clustering of dystrophin but not of GABA(A) receptors and gephyrin', *J Neurosci*, 22(12), pp. 4805-13.

Buckmaster, C.A., Eichenbaum, H., Amaral, D.G., Suzuki, W.A. and Rapp, P.R. (2004) 'Entorhinal cortex lesions disrupt the relational organization of memory in monkeys', *J Neurosci*, 24(44), pp. 9811-25.

Bulfield, G., Siller, W.G., Wight, P.A. and Moore, K.J. (1984) 'X chromosome-linked muscular dystrophy (mdx) in the mouse', *Proceedings of the National Academy of Sciences of the United States of America*, 81(4), pp. 1189-1192.

Bulfone, A., Caccioppoli, C., Pardini, C., Faedo, A., Martinez, S. and Banfi, S. (2004) 'Pcp4l1, a novel gene encoding a Pcp4-like polypeptide, is expressed in specific domains of the developing brain', *Gene Expr Patterns*, 4(3), pp. 297-301.

Bushby, K., Finkel, R., Birnkrant, D.J., Case, L.E., Clemens, P.R., Cripe, L., Kaul, A., Kinnett, K., McDonald, C., Pandya, S., Poysky, J., Shapiro, F., Tomezsko, J. and Constantin, C. (2010) 'Diagnosis and management of Duchenne muscular dystrophy, part 2: implementation of multidisciplinary care', *Lancet Neurol*, 9(2), pp. 177-89.

Bushby, K.M. (1992) 'Genetic and clinical correlations of Xp21 muscular dystrophy', *J Inherit Metab Dis*, 15(4), pp. 551-64.

Bushby, K.M., Appleton, R., Anderson, L.V., Welch, J.L., Kelly, P. and Gardner-Medwin, D. (1995) 'Deletion status and intellectual impairment in Duchenne muscular dystrophy', *Dev Med Child Neurol*, 37(3), pp. 260-9.

Bushby, K.M., Hill, A. and Steele, J.G. (1999) 'Failure of early diagnosis in symptomatic Duchenne muscular dystrophy', *Lancet*, 353(9152), pp. 557-8.

Bushby, K.M., Thambyayah, M. and Gardner-Medwin, D. (1991) 'Prevalence and incidence of Becker muscular dystrophy', *Lancet*, 337(8748), pp. 1022-4.

Byers, T.J., Lidov, H.G. and Kunkel, L.M. (1993) 'An alternative dystrophin transcript specific to peripheral nerve', *Nat Genet*, 4(1), pp. 77-81.

Campbell, K.P. and Kahl, S.D. (1989) 'Association of dystrophin and an integral membrane glycoprotein', *Nature*, 338(6212), pp. 259-62.

Chamberlain, J.S. (2010) 'Duchenne muscular dystrophy models show their age', *Cell*, 143(7), pp. 1040-2.

Chamberlain, J.S., Metzger, J., Reyes, M., Townsend, D. and Faulkner, J.A. (2007) 'Dystrophin-deficient mdx mice display a reduced life span and are susceptible to spontaneous rhabdomyosarcoma', *Faseb j*, 21(9), pp. 2195-204.

Chamova, T., Guergueltcheva, V., Raycheva, M., Todorov, T., Genova, J., Bichev, S., Bojinova, V., Mitev, V., Tournev, I. and Todorova, A. (2013) 'Association between loss of dp140 and cognitive impairment in duchenne and becker dystrophies', *Balkan J Med Genet*, 16(1), pp. 21-30.

Chan, P., Gonzalez-Maeso, J., Ruf, F., Bishop, D.F., Hof, P.R. and Sealfon, S.C. (2005) 'Epsilon-sarcoglycan immunoreactivity and mRNA expression in mouse brain', *J Comp Neurol*, 482(1), pp. 50-73.

Chandrasekharan, K., Yoon, J.H., Xu, Y., deVries, S., Camboni, M., Janssen, P.M., Varki, A. and Martin, P.T. (2010) 'A human-specific deletion in mouse Cmah increases disease severity in the mdx model of Duchenne muscular dystrophy', *Sci Transl Med*, 2(42), p. 42ra54.

Charrier, C., Machado, P., Tweedie-Cullen, R.Y., Rutishauser, D., Mansuy, I.M. and Triller, A. (2010) 'A crosstalk between [beta]1 and [beta]3 integrins controls glycine receptor and gephyrin trafficking at synapses', *Nat Neurosci*, 13(11), pp. 1388-1395.

Chaussenot, R., Edeline, J.M., Le Bec, B., El Massioui, N., Laroche, S. and Vaillend, C. (2015) 'Cognitive dysfunction in the dystrophin-deficient mouse model of Duchenne muscular dystrophy: A reappraisal from sensory to executive processes', *Neurobiol Learn Mem*, 124, pp. 111-22.

Chen, J.K., Zhan, Y.J., Yang, C.S. and Tzeng, S.F. (2011) 'Oxidative stress-induced attenuation of thrombospondin-1 expression in primary rat astrocytes', *J Cell Biochem*, 112(1), pp. 59-70.

Cheng, A., Wang, S., Cai, J., Rao, M.S. and Mattson, M.P. (2003) 'Nitric oxide acts in a positive feedback loop with BDNF to regulate neural progenitor cell proliferation and differentiation in the mammalian brain', *Dev Biol*, 258(2), pp. 319-33.

Chou, H.H., Hayakawa, T., Diaz, S., Krings, M., Indriati, E., Leakey, M., Paabo, S., Satta, Y., Takahata, N. and Varki, A. (2002) 'Inactivation of CMP-N-acetylneuraminic acid hydroxylase occurred prior to brain expansion during human evolution', *Proc Natl Acad Sci U S A*, 99(18), pp. 11736-41.

Christopherson, K.S., Ullian, E.M., Stokes, C.C., Mullowney, C.E., Hell, J.W., Agah, A., Lawler, J., Mosher, D.F., Bornstein, P. and Barres, B.A. (2005) 'Thrombospondins are astrocyte-secreted proteins that promote CNS synaptogenesis', *Cell*, 120(3), pp. 421-33.

Cohen, H.J., Molnar, G.E. and Taft, L.T. (1968) 'The genetic relationship of progressive muscular dystrophy (Duchenne type) and mental retardation', *Dev Med Child Neurol*, 10(6), pp. 754-65.

Cohn, R.D., van Erp, C., Habashi, J.P., Soleimani, A.A., Klein, E.C., Lisi, M.T., Gamradt, M., ap Rhys, C.M., Holm, T.M., Loeys, B.L., Ramirez, F., Judge, D.P., Ward, C.W. and Dietz, H.C. (2007) 'Angiotensin II type 1 receptor blockade attenuates TGF-beta-induced failure of muscle regeneration in multiple myopathic states', *Nat Med*, 13(2), pp. 204-10.

Connolly, A.M., Keeling, R.M., Mehta, S., Pestronk, A. and Sanes, J.R. (2001) 'Three mouse models of muscular dystrophy: the natural history of strength and fatigue in dystrophin-, dystrophin/utrophin-, and laminin alpha2-deficient mice', *Neuromuscul Disord*, 11(8), pp. 703-12.

Cotton, S., Voudouris, N.J. and Greenwood, K.M. (2001) 'Intelligence and Duchenne muscular dystrophy: full-scale, verbal, and performance intelligence quotients', *Dev Med Child Neurol*, 43(7), pp. 497-501.

Cotton, S.M., Voudouris, N.J. and Greenwood, K.M. (2005) 'Association between intellectual functioning and age in children and young adults with Duchenne muscular dystrophy: further results from a meta-analysis', *Dev Med Child Neurol*, 47(4), pp. 257-65.

Courchesne, E., Carper, R. and Akshoomoff, N. (2003) 'Evidence of brain overgrowth in the first year of life in autism', *Jama*, 290(3), pp. 337-44.

Courchesne, E., Chisum, H.J., Townsend, J., Cowles, A., Covington, J., Egaas, B., Harwood, M., Hinds, S. and Press, G.A. (2000) 'Normal brain development and aging: quantitative analysis at in vivo MR imaging in healthy volunteers', *Radiology*, 216(3), pp. 672-82.

Craig, A.M. and Kang, Y. (2007) 'Neurexin–neuroligin signaling in synapse development', *Current opinion in neurobiology*, 17(1), p. 43-48.

Crosbie, R.H., Dovico, S.A., Flanagan, J.D., Chamberlain, J.S., Ownby, C.L. and Campbell, K.P. (2002) 'Characterization of aquaporin-4 in muscle and muscular dystrophy', *Faseb j*, 16(9), pp. 943-9.

Cyrulnik, S.E. and Hinton, V.J. (2008) 'Duchenne muscular dystrophy: a cerebellar disorder?', *Neurosci Biobehav Rev*, 32(3), pp. 486-96.

D'Souza, V.N., Nguyen, T.M., Morris, G.E., Karges, W., Pillers, D.A. and Ray, P.N. (1995) 'A novel dystrophin isoform is required for normal retinal electrophysiology', *Hum Mol Genet*, 4(5), pp. 837-42.

Daoud, F., Angeard, N., Demerre, B., Martie, I., Benyaou, R., Leturcq, F., Cossee, M., Deburgrave, N., Saillour, Y., Tuffery, S., Urtizberea, A., Toutain, A., Echenne, B., Frischman, M., Mayer, M., Desguerre, I., Estournet, B., Reveillere, C., Penisson, B., Cuisset, J.M., Kaplan, J.C., Heron, D., Rivier, F. and Chelly, J. (2009) 'Analysis of Dp71 contribution in the severity of mental retardation through comparison of Duchenne and Becker patients differing by mutation consequences on Dp71 expression', *Hum Mol Genet*, 18(20), pp. 3779-94.

Davies, K.E., Smith, T.J., Bundey, S., Read, A.P., Flint, T., Bell, M. and Speer, A. (1988) 'Mild and severe muscular dystrophy associated with deletions in Xp21 of the human X chromosome', *J Med Genet*, 25(1), pp. 9-13.

Deacon, R.M., Thomas, C.L., Rawlins, J.N. and Morley, B.J. (2007) 'A comparison of the behavior of C57BL/6 and C57BL/10 mice', *Behav Brain Res*, 179(2), pp. 239-47.

Deconinck, N., Tinsley, J., De Backer, F., Fisher, R., Kahn, D., Phelps, S., Davies, K. and Gillis, J.M. (1997) 'Expression of truncated utrophin leads to major functional improvements in dystrophin-deficient muscles of mice', *Nat Med*, 3(11), pp. 1216-21.

Deichmann, R., Hahn, D. and Haase, A. (1999) 'Fast T1 mapping on a whole-body scanner', *Magn Reson Med*, 42(1), pp. 206-9.

Deken, S.L., Beckman, M.L., Boos, L. and Quick, M.W. (2000) 'Transport rates of GABA transporters: regulation by the N-terminal domain and syntaxin 1A', *Nat Neurosci*, 3(10), pp. 998-1003.

Deken, S.L., Wang, D. and Quick, M.W. (2003) 'Plasma Membrane GABA Transporters Reside on Distinct Vesicles and Undergo Rapid Regulated Recycling', *The Journal of Neuroscience*, 23(5), pp. 1563-1568.

Deng, B., Glanzman, D. and Tidball, J.G. (2009) 'Nitric oxide generated by muscle corrects defects in hippocampal neurogenesis and neural differentiation caused by muscular dystrophy', *The Journal of Physiology*, 587(Pt 8), pp. 1769-1778.

Diaz, S.L., Padler-Karavani, V., Ghaderi, D., Hurtado-Ziola, N., Yu, H., Chen, X., Brinkman-Van der Linden, E.C., Varki, A. and Varki, N.M. (2009) 'Sensitive and specific detection of the non-human sialic Acid N-glycolylneuraminic acid in human tissues and biotherapeutic products', *PLoS One*, 4(1), p. e4241.

DiFrancesco, M.W., Rasmussen, J.M., Yuan, W., Pratt, R., Dunn, S., Dardzinski, B.J. and Holland, S.K. (2008) 'Comparison of SNR and CNR for in vivo mouse brain imaging at 3 and 7 T using well matched scanner configurations', *Med Phys*, 35(9), pp. 3972-8.

DiMauro, S. (1996) 'Mitochondrial encephalomyopathies: what next?', *J Inherit Metab Dis*, 19(4), pp. 489-503.

Doorenweerd, N., Dumas, E.M., Ghariq, E., Schmid, S., Straathof, C.S., Roest, A.A., Wokke, B.H., van Zwet, E.W., Webb, A.G., Hendriksen, J.G., van Buchem, M.A., Verschuuren, J.J., Asllani, I., Niks, E.H., van Osch, M.J. and Kan, H.E. (2017a) 'Decreased cerebral perfusion in Duchenne muscular dystrophy patients', *Neuromuscul Disord*, 27(1), pp. 29-37.

Doorenweerd, N., Hooijmans, M., Schubert, S.A., Webb, A.G., Straathof, C.S., van Zwet, E.W., van Buchem, M.A., Verschuuren, J.J., Hendriksen, J.G., Niks, E.H. and Kan, H.E. (2017b) 'Proton Magnetic Resonance Spectroscopy Indicates Preserved Cerebral Biochemical Composition in Duchenne Muscular Dystrophy Patients', *J Neuromuscul Dis*, 4(1), pp. 53-58.

Doorenweerd, N., Straathof, C.S., Dumas, E.M., Spitali, P., Ginjaar, I.B., Wokke, B.H., Schrans, D.G., van den Bergen, J.C., van Zwet, E.W., Webb, A., van Buchem, M.A., Verschuuren, J.J., Hendriksen, J.G., Niks, E.H. and Kan, H.E. (2014) 'Reduced cerebral gray matter and altered white matter in boys with Duchenne muscular dystrophy', *Ann Neurol*, 76(3), pp. 403-11.

Dorman, C., Hurley, A.D. and D'Avignon, J. (1988) 'Language and learning disorders of older boys with Duchenne muscular dystrophy', *Dev Med Child Neurol*, 30(3), pp. 316-27.

Dow, R.S. (1961) 'Some aspects of cerebellar physiology', *J Neurosurg*, 18, pp. 512-30.

Dubois, L.G., Campanati, L., Righy, C., D'Andrea-Meira, I., Spohr, T.C.L.d.S.e., Porto-Carreiro, I., Pereira, C.M., Balça-Silva, J., Kahn, S.A., DosSantos, M.F., Oliveira, M.d.A.R., Ximenes-da-Silva, A., Lopes, M.C., Faveret, E., Gasparetto, E.L. and Moura-Neto, V. (2014) 'Gliomas and the vascular fragility of the blood brain barrier', *Frontiers in Cellular Neuroscience*, 8, pp. 418-423.

Dubowitz, V. and Crome, L. (1969a) 'The central nervous system in Duchenne muscular dystrophy', *Brain*, 92(4), pp. 805-8.

Dubowitz, V. and Crome, L. (1969b) *THE CENTRAL NERVOUS SYSTEM IN DUCHENNE MUSCULAR DYSTROPHY,*pp.805-808

Duchenne (1868) 'Recherches sur le paralysie musculaire pseudohypertrophique ou paralysie myo-sclérosique.', *Arch Gen Med* 11, pp. 178, 305, 421, 552.

Dunn, J.F. and Zaim-Wadghiri, Y. (1999) 'Quantitative magnetic resonance imaging of the mdx mouse model of Duchenne muscular dystrophy', *Muscle Nerve*, 22(10), pp. 1367-71.

Eagle, M., Baudouin, S.V., Chandler, C., Giddings, D.R., Bullock, R. and Bushby, K. (2002) 'Survival in Duchenne muscular dystrophy: improvements in life expectancy since 1967 and the impact of home nocturnal ventilation', *Neuromuscul Disord*, 12(10), pp. 926-9.

Eagle, M., Bourke, J., Bullock, R., Gibson, M., Mehta, J., Giddings, D., Straub, V. and Bushby, K. (2007) 'Managing Duchenne muscular dystrophy--the additive effect of spinal surgery and home nocturnal ventilation in improving survival', *Neuromuscul Disord*, 17(6), pp. 470-5.

Egli, F., Botteron, S., Morel, C. and Kiliaridis, S. (2017) 'Growing patients with Duchenne muscular dystrophy: longitudinal changes in their dentofacial morphology and orofacial functional capacities', *Eur J Orthod*. [Epub ahead of print].

Eide, P.K. and Hansson, H.A. (2017) 'Astrogliosis and impaired aquaporin-4 and dystrophin systems in idiopathic normal pressure hydrocephalus', *Neuropathol Appl Neurobiol*.pp, 124-120.

Elizabeth, O.H. and Molliver, M.E. (2001) 'Organizational principles and microcircuitry of the cerebellum', *International Review of Psychiatry*, 13(4), pp. 232-246.

Ellegood, J., Anagnostou, E., Babineau, B.A., Crawley, J.N., Lin, L., Genestine, M., DiCicco-Bloom, E., Lai, J.K.Y., Foster, J.A., Peñagarikano, O., Geschwind, D.H., Pacey, L.K., Hampson, D.R., Laliberté, C.L., Mills, A.A., Tam, E., Osborne, L.R., Kouser, M., Espinosa-Becerra, F., Xuan, Z., Powell, C.M., Raznahan, A., Robins, D.M., Nakai, N., Nakatani, J., Takumi, T., van Eede, M.C., Kerr, T.M., Muller, C., Blakely, R.D., Veenstra-VanderWeele, J., Henkelman, R.M. and Lerch, J.P. (2015) 'Clustering autism - using neuroanatomical differences in 26 mouse models to gain insight into the heterogeneity', *Molecular psychiatry*, 20(1), pp. 118-125.

Emery, A.E. (1991) 'Population frequencies of inherited neuromuscular diseases--a world survey', *Neuromuscul Disord*, 1(1), pp. 19-29.

Ennaceur, A. and Delacour, J. (1987) 'Effect of combined or separate administration of piracetam and choline on learning and memory in the rat', *Psychopharmacology*, 92(1), pp. 58-67.

Ennaceur, A. and Delacour, J. (1988) 'A new one-trial test for neurobiological studies of memory in rats. 1: Behavioral data', *Behav Brain Res*, 31(1), pp. 47-59.

Ennaceur, A., Michalikova, S., Bradford, A. and Ahmed, S. (2005) 'Detailed analysis of the behavior of Lister and Wistar rats in anxiety, object recognition and object location tasks', *Behav Brain Res*, 159(2), pp. 247-66.

Erturk, O., Bilguvar, K., Korkmaz, B., Bayri, Y., Bayrakli, F., Arlier, Z., Ozturk, A.K., Yalcinkaya, C., Tuysuz, B., State, M.W. and Gunel, M. (2010) 'A patient with Duchenne muscular dystrophy and autism demonstrates a hemizygous deletion affecting Dystrophin', *Am J Med Genet A*, 152a(4), pp. 1039-42.

Ervasti, J.M. and Campbell, K.P. (1991) 'Membrane organization of the dystrophin-glycoprotein complex', *Cell*, 66.

Ervasti, J.M. and Campbell, K.P. (1993) 'A role for the dystrophin-glycoprotein complex as a transmembrane linker between laminin and actin', *J Cell Biol*, 122(4), pp. 809-23.

Ervasti, J.M., Ohlendieck, K., Kahl, S.D., Gaver, M.G. and Campbell, K.P. (1990) 'Deficiency of a glycoprotein component of the dystrophin complex in dystrophic muscle', *Nature*, 345(6273), pp. 315-319.

Evans, A.E., Kelly, C.M., Precious, S.V. and Rosser, A.E. (2012) 'Molecular Regulation of Striatal Development: A Review', *Anatomy Research International*, 2012, pp. 106-9.

Fayssoil, A., Nardi, O., Orlikowski, D. and Annane, D. (2010) 'Cardiomyopathy in Duchenne muscular dystrophy: pathogenesis and therapeutics', *Heart Fail Rev*, 15(1), pp. 103-7.

Felisari, G., Martinelli Boneschi, F., Bardoni, A., Sironi, M., Comi, G.P., Robotti, M., Turconi, A.C., Lai, M., Corrao, G. and Bresolin, N. (2000) 'Loss of Dp140 dystrophin isoform and intellectual impairment in Duchenne dystrophy', *Neurology*, 55(4), pp. 559-64.

Filippidis, A.S., Carozza, R.B. and Rekate, H.L. (2017) 'Aquaporins in Brain Edema and Neuropathological Conditions', *International Journal of Molecular Sciences*, 18(1), pp. 55-9.

Finsterer, J. and Stollberger, C. (2003) 'The heart in human dystrophinopathies', *Cardiology*, 99(1), pp. 1-19.

Fitzpatrick, C., Barry, C. and Garvey, C. (1986) 'Psychiatric disorder among boys with Duchenne muscular dystrophy', *Dev Med Child Neurol*, 28(5), pp. 589-95.

Fredriksson, L., Nilsson, I., Su, E.J., Andrae, J., Ding, H., Betsholtz, C., Eriksson, U. and Lawrence, D.A. (2012) 'Platelet-Derived Growth Factor C Deficiency in C57BL/6 Mice Leads to Abnormal Cerebral Vascularization, Loss of Neuroependymal Integrity, and Ventricular Abnormalities', *The American Journal of Pathology*, 180(3), pp. 1136-1144.

Frigeri, A., Nicchia, G.P., Balena, R., Nico, B. and Svelto, M. (2004) 'Aquaporins in skeletal muscle: reassessment of the functional role of aquaporin-4', *Faseb j*, 18(7), pp. 905-7.

Frigeri, A., Nicchia, G.P., Nico, B., Quondamatteo, F., Herken, R., Roncali, L. and Svelto, M. (2001) 'Aquaporin-4 deficiency in skeletal muscle and brain of dystrophic mdx mice', *Faseb j*, 15(1), pp. 90-98.

Gadea, A. and Lopez-Colome, A.M. (2001) 'Glial transporters for glutamate, glycine, and GABA: II. GABA transporters', *J Neurosci Res*, 63(6), pp. 461-8.

Garton, H.J. and Piatt, J.H., Jr. (2004) 'Hydrocephalus', *Pediatr Clin North Am*, 51(2), pp. 305-25.

Gee, S.H., Madhavan, R., Levinson, S.R., Caldwell, J.H., Sealock, R. and Froehner, S.C. (1998) 'Interaction of muscle and brain sodium channels with multiple members of the syntrophin family of dystrophin-associated proteins', *J Neurosci*, 18(1), pp. 128-37.

Genovese, C.R., Lazar, N.A. and Nichols, T. (2002) 'Thresholding of statistical maps in functional neuroimaging using the false discovery rate', *Neuroimage*, 15(4), pp. 870-8.

Geurts, H.M., Corbett, B. and Solomon, M. (2009) 'The paradox of cognitive flexibility in autism', *Trends Cogn Sci*, 13(2), pp. 74-82.

Giedd, J.N., Blumenthal, J., Jeffries, N.O., Castellanos, F.X., Liu, H., Zijdenbos, A., Paus, T., Evans, A.C. and Rapoport, J.L. (1999) 'Brain development during childhood and adolescence: a longitudinal MRI study', *Nat Neurosci*, 2(10), pp. 861-3.

Glickstein, M. and Doron, K. (2008) 'Cerebellum: connections and functions', *Cerebellum*, 7(4), pp. 589-94.

Goodnough, C.L., Gao, Y., Li, X., Qutaish, M.Q., Goodnough, L.H., Molter, J., Wilson, D., Flask, C.A. and Yu, X. (2014) 'Lack of dystrophin results in abnormal cerebral diffusion and perfusion in vivo', *Neuroimage*, 102 Pt 2, pp. 809-16.

Goodwin, F.C. and Muntoni, F. (2005) 'Cardiac involvement in muscular dystrophies: molecular mechanisms', *Muscle Nerve*, 32(5), pp. 577-88.

Gorecki, D.C., Abdulrazzak, H., Lukasiuk, K. and Barnard, E.A. (1997) 'Differential expression of syntrophins and analysis of alternatively spliced dystrophin transcripts in the mouse brain', *Eur J Neurosci*, 9(5), pp. 965-76.

Gould, E. and Gross, C.G. (2002) 'Neurogenesis in adult mammals: some progress and problems', *J Neurosci*, 22(3), pp. 619-23.

Gowers, W.R. (1879) 'A Study of the so-called Tendon-Reflex Phemomena', *Med Chir Trans*, 62, pp. 269-305.

Grady, R.M., Wozniak, D.F., Ohlemiller, K.K. and Sanes, J.R. (2006) 'Cerebellar synaptic defects and abnormal motor behavior in mice lacking alpha- and beta-dystrobrevin', *J Neurosci*, 26(11), pp. 2841-51.

Grahn, J.A., Parkinson, J.A. and Owen, A.M. (2008) 'The cognitive functions of the caudate nucleus', *Progress in Neurobiology*, 86(3), pp. 141-155.

Greaves, M.W. (1976) 'Anti-inflammatory action of corticosteroids', *Postgraduate Medical Journal*, 52(612), pp. 631-633.

Green, D.R. and Reed, J.C. (1998) 'Mitochondria and Apoptosis', *Science*, 281(5381), pp. 1309-1312.

Griggs, R.C., Moxley, R.T., 3rd, Mendell, J.R., Fenichel, G.M., Brooke, M.H., Pestronk, A. and Miller, J.P. (1991) 'Prednisone in Duchenne dystrophy. A randomized, controlled trial defining the time course and dose response. Clinical Investigation of Duchenne Dystrophy Group', *Arch Neurol*, 48(4), pp. 383-8.

Grounds, M.D., Radley, H.G., Lynch, G.S., Nagaraju, K. and De Luca, A. (2008) 'Towards developing standard operating procedures for pre-clinical testing in the mdx mouse model of Duchenne muscular dystrophy', *Neurobiology of disease*, 31(1), pp. 1-19.

Gruhn, N., Larsen, F.S., Boesgaard, S., Knudsen, G.M., Mortensen, S.A., Thomsen, G. and Aldershvile, J. (2001) 'Cerebral blood flow in patients with chronic heart failure before and after heart transplantation', *Stroke*, 32(11), pp. 2530-3.

Guglieri, M. and Bushby, K. (2010) 'Molecular treatments in Duchenne muscular dystrophy', *Curr Opin Pharmacol*, 10(3), pp. 331-7.

Gumerson, J.D. and Michele, D.E. (2011) 'The dystrophin-glycoprotein complex in the prevention of muscle damage', *J Biomed Biotechnol*, 2011, pp.210-15

Haenggi, T., Soontornmalai, A., Schaub, M.C. and Fritschy, J.M. (2004) 'The role of utrophin and Dp71 for assembly of different dystrophin-associated protein complexes (DPCs) in the choroid plexus and microvasculature of the brain', *Neuroscience*, 129(2), pp. 403-13.

Haines, D.E. and Dietrichs, E. (2012) 'Chapter 1 - The cerebellum – structure and connections', in Sankara, H.S. and Alexandra, D. (eds.) *Handbook of Clinical Neurology*. Elsevier, pp. 3-36.

Hall, C.N., Reynell, C., Gesslein, B., Hamilton, N.B., Mishra, A., Sutherland, B.A., O'Farrell, F.M., Buchan, A.M., Lauritzen, M. and Attwell, D. (2014) 'Capillary pericytes regulate cerebral blood flow in health and disease', *Nature*, 508(7494), pp. 55-60.

Hammond, R.S., Tull, L.E. and Stackman, R.W. (2004) 'On the delay-dependent involvement of the hippocampus in object recognition memory', *Neurobiol Learn Mem*, 82(1), pp. 26-34.

Harashima, S., Wang, Y., Horiuchi, T., Seino, Y. and Inagaki, N. (2011) 'Purkinje cell protein 4 positively regulates neurite outgrowth and neurotransmitter release', *J Neurosci Res*, 89(10), pp. 1519-30.

Hashimoto, T., Nguyen, Q.L., Rotaru, D., Keenan, T., Arion, D., Beneyto, M., Gonzalez-Burgos, G. and Lewis, D.A. (2009) 'Protracted developmental trajectories of GABAA receptor alpha1 and alpha2 subunit expression in primate prefrontal cortex', *Biol Psychiatry*, 65(12), pp. 1015-23.

Hawkins, B.T. and Egleton, R.D. (2006) 'Fluorescence imaging of blood-brain barrier disruption', *J Neurosci Methods*, 151(2), pp. 262-7.

Heales, S.J.R., Bolaños, J.P., Stewart, V.C., Brookes, P.S., Land, J.M. and Clark, J.B. (1999) 'Nitric oxide, mitochondria and neurological disease', *Biochimica et Biophysica Acta (BBA) - Bioenergetics*, 1410(2), pp. 215-228.

Hedlund, M., Tangvoranuntakul, P., Takematsu, H., Long, J.M., Housley, G.D., Kozutsumi, Y., Suzuki, A., Wynshaw-Boris, A., Ryan, A.F., Gallo, R.L., Varki, N. and Varki, A. (2007) 'N-glycolylneuraminic acid deficiency in mice: implications for human biology and evolution', *Mol Cell Biol*, 27(12), pp. 4340-6.

Hendriksen, J.G., Klinkenberg, S., Collin, P., Wong, B., Niks, E.H. and Vles, J.S. (2016a) 'Diagnosis and treatment of obsessive compulsive behavior in a boy with Duchenne muscular dystrophy and autism spectrum disorder: A case report', *Neuromuscul Disord*, 26(10), pp. 659-661.

Hendriksen, J.G. and Vles, J.S. (2006) 'Are males with Duchenne muscular dystrophy at risk for reading disabilities?', *Pediatr Neurol*, 34(4), pp. 296-300.

Hendriksen, R.G., Hoogland, G., Schipper, S., Hendriksen, J.G., Vles, J.S. and Aalbers, M.W. (2015a) 'A possible role of dystrophin in neuronal excitability: a review of the current literature', *Neurosci Biobehav Rev*, 51, pp. 255-62.

Hendriksen, R.G.F., Hoogland, G., Schipper, S., Hendriksen, J.G.M., Vles, J.S.H. and Aalbers, M.W. (2015b) 'A possible role of dystrophin in neuronal excitability: A review of the current literature', *Neuroscience & Biobehavioral Reviews*, 51(0), pp. 255-262.

Hendriksen, R.G.F., Schipper, S., Hoogland, G., Schijns, O.E.M.G., Dings, J.T.A., Aalbers, M.W. and Vles, J.S.H. (2016b) 'Dystrophin Distribution and Expression in Human and Experimental Temporal Lobe Epilepsy', *Frontiers in Cellular Neuroscience*, 10, p. 174.

Heuser, K., Eid, T., Lauritzen, F., Thoren, A.E., Vindedal, G.F., Taubøll, E., Gjerstad, L., Spencer, D.D., Ottersen, O.P., Nagelhus, E.A. and de Lanerolle, N.C. (2012) 'Loss of Perivascular Kir4.1 Potassium Channels in the Sclerotic Hippocampus of Patients With Mesial Temporal Lobe Epilepsy', *Journal of neuropathology and experimental neurology*, 71(9), pp. 814-825.

Heye, A.K., Culling, R.D., Valdes Hernandez Mdel, C., Thrippleton, M.J. and Wardlaw, J.M. (2014) 'Assessment of blood-brain barrier disruption using dynamic contrast-enhanced MRI. A systematic review', *Neuroimage Clin*, 6, pp. 262-74.

Hinton, V.J., Cyrulnik, S.E., Fee, R.J., Batchelder, A., Kiefel, J.M., Goldstein, E.M., Kaufmann, P. and De Vivo, D.C. (2009) 'Association of autistic spectrum disorders with dystrophinopathies', *Pediatr Neurol*, 41(5), pp. 339-46.

Hinton, V.J., Fee, R.J., De Vivo, D.C. and Goldstein, E. (2007) 'Poor Facial Affect Recognition Among Boys with Duchenne Muscular Dystrophy', *Journal of autism and developmental disorders*, 37(10), pp. 1925-1933.

Hoddevik, E.H., Khan, F.H., Rahmani, S., Ottersen, O.P., Boldt, H.B. and Amiry-Moghaddam, M. (2017) 'Factors determining the density of AQP4 water channel molecules at the brain-blood interface', *Brain Struct Funct*, 222(4), pp. 1753-1766.

Hoffman, E.P., Brown, R.H. and Kunkel, L.M. (1992) 'Dystrophin: the protein product of the Duchene muscular dystrophy locus. 1987', *Biotechnology*, 24, pp. 457-66.

Hoffman, E.P., Brown, R.H.J. and Kunkel, L.M. (1987a) 'Dystrophin: the protein product of the Duchenne muscular dystrophy locus', *Cell*, 51.

Hoffman, E.P., Knudson, C.M., Campbell, K.P. and Kunkel, L.M. (1987b) 'Subcellular fractionation of dystrophin to the triads of skeletal muscle', *Nature*, 330(6150), pp. 754-8.

Holder, E., Maeda, M. and Bies, R.D. (1996) 'Expression and regulation of the dystrophin Purkinje promoter in human skeletal muscle, heart, and brain', *Hum Genet*, 97(2), pp. 232-9.

Holland, A., Carberry, S. and Ohlendieck, K. (2013) 'Proteomics of the dystrophin-glycoprotein complex and dystrophinopathy', *Curr Protein Pept Sci*, 14(8), pp. 680-97.

Huard, J. and Tremblay, J.P. (1992) 'Localization of dystrophin in the Purkinje cells of normal mice', *Neurosci Lett*, 137(1), pp. 105-8.

Iacovetta, C., Rudloff, E. and Kirby, R. (2012) 'The role of aquaporin 4 in the brain', *Vet Clin Pathol*, 41(1), pp. 32-44.

Ilay, A., Pelin, D., Gizem, G. and Michelle, M.A. (2013) 'Novel object recognition is not affected by age despite age-related brain changes', *World Journal of Neuroscience*, Vol.03No.04, p. 6.

Im, W.B., Phelps, S.F., Copen, E.H., Adams, E.G., Slightom, J.L. and Chamberlain, J.S. (1996) 'Differential expression of dystrophin isoforms in strains of mdx mice with different mutations', *Hum Mol Genet*, 5(8), pp. 1149-53.

Inoue, M., Wakayama, Y., Liu, J.W., Murahashi, M., Shibuya, S. and Oniki, H. (2002) 'Ultrastructural localization of aquaporin 4 and alpha1-syntrophin in the vascular feet of brain astrocytes', *Tohoku J Exp Med*, 197(2), pp. 87-93.

Ishihara, K., Amano, K., Takaki, E., Shimohata, A., Sago, H., J. Epstein, C. and Yamakawa, K. (2010) 'Enlarged Brain Ventricles and Impaired Neurogenesis in the Ts1Cje and Ts2Cje Mouse Models of Down Syndrome', *Cerebral Cortex*, 20(5), pp. 1131-1143.

Ito, M. (2006) 'Cerebellar circuitry as a neuronal machine', *Prog Neurobiol*, 78(3-5), pp. 272-303.

Itoh, K., Jinnai, K., Tada, K., Hara, K., Itoh, H. and Takahashi, K. (1999) 'Multifocal glial nodules in a case of Duchenne muscular dystrophy with severe mental retardation', *Neuropathology*, 19(3), pp. 322-327.

Itouji, A., Sakai, N., Tanaka, C. and Saito, N. (1996) 'Neuronal and glial localization of two GABA transporters (GAT1 and GAT3) in the rat cerebellum', *Brain Res Mol Brain Res*, 37(1-2), pp. 309-16.

Itti, E., Gaw Gonzalo, I.T., Pawlikowska-Haddal, A., Boone, K.B., Mlikotic, A., Itti, L., Mishkin, F.S. and Swerdloff, R.S. (2006) 'The structural brain correlates of cognitive deficits in adults with Klinefelter's syndrome', *J Clin Endocrinol Metab*, 91(4), pp. 1423-7.

Jagadha, V. and Becker, L.E. (1988) 'Brain morphology in Duchenne muscular dystrophy: a Golgi study', *Pediatr Neurol*, 4(2), pp. 87-92.

Ji, L., Chauhan, A., Muthaiyah, B., Wegiel, J. and Chauhan, V. (2009) 'Gelsolin Levels are increased in the brain as a Function of Age During Normal Development in Children That are further increased in Down Syndrome', *Alzheimer disease and associated disorders*, 23(4), pp. 319-322.

Jiménez, A.J., Domínguez-Pinos, M.-D., Guerra, M.M., Fernández-Llebrez, P. and Pérez-Fígares, J.-M. (2014) 'Structure and function of the ependymal barrier and diseases associated with ependyma disruption', *Tissue Barriers*, 2, p. e28426.

Jin, X.-T., Paré, J.-F. and Smith, Y. (2012) 'The GABA Transporters GAT-1 and GAT-3 modulate glutamatergic transmission via activation of presynaptic GABA(B) receptors in the rat globus pallidus', *The European journal of neuroscience*, 36(4), pp. 2482-2492.

Johanson, C.E., Stopa, E.G. and McMillan, P.N. (2011) 'The blood-cerebrospinal fluid barrier: structure and functional significance', *Methods Mol Biol*, 686, pp. 101-31.

Johri, A. and Beal, M.F. (2012) 'Mitochondrial Dysfunction in Neurodegenerative Diseases', *The Journal of Pharmacology and Experimental Therapeutics*, 342(3), pp. 619-630.

Joyal, C.C., Meyer, C., Jacquart, G., Mahler, P., Caston, J. and Lalonde, R. (1996) 'Effects of midline and lateral cerebellar lesions on motor coordination and spatial orientation', *Brain Res*, 739(1-2), pp. 1-11.

Judge, D.P., Kass, D.A., Thompson, W.R. and Wagner, K.R. (2011) 'Pathophysiology and therapy of cardiac dysfunction in Duchenne muscular dystrophy', *Am J Cardiovasc Drugs*, 11(5), pp. 287-94.

Kamada, S., Kusano, H., Fujita, H., Ohtsu, M., Koya, R.C., Kuzumaki, N. and Tsujimoto, Y. (1998) 'A cloning method for caspase substrates that uses the yeast two-hybrid system: cloning of the antiapoptotic gene gelsolin', *Proc Natl Acad Sci U S A*, 95(15), pp. 8532-7.

Kameya, S., Miyagoe, Y., Nonaka, I., Ikemoto, T., Endo, M., Hanaoka, K., Nabeshima, Y. and Takeda, S. (1999) 'alpha1-syntrophin gene disruption results in the absence of neuronal-type nitric-oxide synthase at the sarcolemma but does not induce muscle degeneration', *J Biol Chem*, 274(4), pp. 2193-200.

Kamogawa, Y., Biro, S., Maeda, M., Setoguchi, M., Hirakawa, T., Yoshida, H. and Tei, C. (2001) 'Dystrophin-deficient myocardium is vulnerable to pressure overload in vivo', *Cardiovasc Res*, 50(3), pp. 509-15.

Kanai, A.J., Pearce, L.L., Clemens, P.R., Birder, L.A., VanBibber, M.M., Choi, S.Y., de Groat, W.C. and Peterson, J. (2001) 'Identification of a neuronal nitric oxide synthase in isolated cardiac mitochondria using electrochemical detection', *Proc Natl Acad Sci U S A*, 98(24), pp. 14126-31.

Kavaler, S., Morinaga, H., Jih, A., Fan, W., Hedlund, M., Varki, A. and Kim, J.J. (2011) 'Pancreatic beta-cell failure in obese mice with human-like CMP-Neu5Ac hydroxylase deficiency', *Faseb j*, 25(6), pp. 1887-93.

Khanra, S., Srivastava, N.K., Chail, V. and Khess, C.R. (2016) 'Prevalence and Characteristics of Cavum Septum Pellucidum in Schizophrenia: A 16 Slice Computed Tomography Study', *Indian J Psychol Med*, 38(5), pp. 455-459.

Khurana, T.S. and Davies, K.E. (2003) 'Pharmacological strategies for muscular dystrophy', *Nat Rev Drug Discov*, 2(5), pp. 379-390.

Kilborn, S.H., Trudel, G. and Uhthoff, H. (2002) 'Review of growth plate closure compared with age at sexual maturity and lifespan in laboratory animals', *Contemp Top Lab Anim Sci*, 41(5), pp. 21-6.

Kim, J., Choi, I.-Y., Michaelis, M.L. and Lee, P. (2011) 'Quantitative in vivo measurement of early axonal transport deficits in a triple transgenic mouse model of Alzheimer's disease using manganese-enhanced MRI', *NeuroImage*, 56(3), pp. 1286-1292.

Kinali, M., Main, M., Eliahoo, J., Messina, S., Knight, R.K., Lehovsky, J., Edge, G., Mercuri, E., Manzur, A.Y. and Muntoni, F. (2007) 'Predictive factors for the development of scoliosis in Duchenne muscular dystrophy', *Eur J Paediatr Neurol*, 11(3), pp. 160-6.

Knuesel, I., Mastrocola, M., Zuellig, R.A., Bornhauser, B., Schaub, M.C. and Fritschy, J.M. (1999) 'Short communication: altered synaptic clustering of GABAA receptors in mice lacking dystrophin (mdx mice)', *Eur J Neurosci*, 11(12), pp. 4457-62.

Koenig, M., Beggs, A.H., Moyer, M., Scherpf, S., Heindrich, K., Bettecken, T., Meng, G., Muller, C.R., Lindlof, M., Kaariainen, H., de la Chapellet, A., Kiuru, A., Savontaus, M.L., Gilgenkrantz, H., Recan, D., Chelly, J., Kaplan, J.C., Covone, A.E., Archidiacono, N., Romeo, G., Liechti-Gailati, S., Schneider, V., Braga, S., Moser, H., Darras, B.T., Murphy, P., Francke, U., Chen, J.D., Morgan, G., Denton, M., Greenberg, C.R., Wrogemann, K., Blonden, L.A., van Paassen, M.B., van Ommen, G.J. and Kunkel, L.M. (1989) 'The molecular basis for Duchenne versus Becker muscular dystrophy: correlation of severity with type of deletion', *Am J Hum Genet*, 45(4), pp. 498-506.

Koenig, M., Monaco, A.P. and Kunkel, L.M. (1988) 'The complete sequence of dystrophin predicts a rod-shaped cytoskeletal protein', *Cell*, 53(2), pp. 219-28.

Komoto, J., Usui, S., Otsuki, S. and Terao, A. (1984) 'Infantile autism and Duchenne muscular dystrophy', *J Autism Dev Disord*, 14(2), pp. 191-5.

Kreis, R., Wingeier, K., Vermathen, P., Giger, E., Joncourt, F., Zwygart, K., Kaufmann, F., Boesch, C. and Steinlin, M. (2011) 'Brain metabolite composition in relation to cognitive function and dystrophin mutations in boys with Duchenne muscular dystrophy', *NMR Biomed*, 24(3), pp. 253-62.

Kreutzberg, G.W. (1996) 'Microglia: a sensor for pathological events in the CNS', *Trends Neurosci*, 19(8), pp. 312-8.

Kristjansdottir, R., Uvebrant, P. and Rosengren, L. (2001) 'Glial fibrillary acidic protein and neurofilament in children with cerebral white matter abnormalities', *Neuropediatrics*, 32(6), pp. 307-12.

Kueh, S.L., Dempster, J., Head, S.I. and Morley, J.W. (2011) 'Reduced postsynaptic GABAA receptor number and enhanced gaboxadol induced change in holding currents in Purkinje cells of the dystrophin-deficient mdx mouse', *Neurobiol Dis*, 43(3), pp. 558-64.

Kusano, H., Shimizu, S., Koya, R.C., Fujita, H., Kamada, S., Kuzumaki, N. and Tsujimoto, Y. (2000) 'Human gelsolin prevents apoptosis by inhibiting apoptotic mitochondrial changes via closing VDAC', *Oncogene*, 19(42), pp. 4807-14.

Kwiatkowski, D.J., Mehl, R. and Yin, H.L. (1988) 'Genomic organization and biosynthesis of secreted and cytoplasmic forms of gelsolin', *J Cell Biol*, 106(2), pp. 375-84.

Kwon, D.N., Park, W.J., Choi, Y.J., Gurunathan, S. and Kim, J.H. (2015) 'Oxidative stress and ROS metabolism via down-regulation of sirtuin 3 expression in Cmah-null mice affect hearing loss', *Aging (Albany NY)*, 7(8), pp. 579-94.

Labisch, T., Buchkremer, S., Phan, V., Kollipara, L., Gatz, C., Lentz, C., Nolte, K., Vervoorts, J., Coraspe, J.A., Sickmann, A., Carr, S., Zahedi, R.P., Weis, J. and Roos, A. (2017) 'Tracking Effects of SIL1 Increase: Taking a Closer Look Beyond the Consequences of Elevated Expression Level', *Mol Neurobiol*.[Epub ahead of print].

Lai, E.C. (2010) 'CHAPTER 10 - Cerebellar Disease A2 - Rolak, Loren A', in *Neurology Secrets (Fifth Edition)*. Philadelphia: Mosby, pp. 157-167.

Lalonde, R. and Strazielle, C. (2003) 'The effects of cerebellar damage on maze learning in animals', *Cerebellum*, 2(4), pp. 300-9.

Lapidos, K.A., Kakkar, R. and McNally, E.M. (2004) 'The dystrophin glycoprotein complex: signaling strength and integrity for the sarcolemma', *Circ Res*, 94(8), pp. 1023-31.

Laws, N. and Hoey, A. (2004) 'Progression of kyphosis in mdx mice', *J Appl Physiol (1985)*, 97(5), pp. 1970-7.

Le Magueresse, C. and Monyer, H. (2013) 'GABAergic Interneurons Shape the Functional Maturation of the Cortex', *Neuron*, 77(3), pp. 388-405.

Lee, J.S., Pfund, Z., Juhasz, C., Behen, M.E., Muzik, O., Chugani, D.C., Nigro, M.A. and Chugani, H.T. (2002) 'Altered regional brain glucose metabolism in Duchenne muscular dystrophy: a pet study', *Muscle Nerve*, 26(4), pp. 506-12.

Lenk, U., Hanke, R., Thiele, H. and Speer, A. (1993) 'Point mutations at the carboxy terminus of the human dystrophin gene: implications for an association with mental retardation in DMD patients', *Hum Mol Genet*, 2(11), pp. 1877-81.

Leonoudakis, D., Conti, L.R., Anderson, S., Radeke, C.M., McGuire, L.M., Adams, M.E., Froehner, S.C., Yates, J.R., 3rd and Vandenberg, C.A. (2004) 'Protein trafficking and anchoring complexes revealed by proteomic analysis of inward rectifier potassium channel (Kir2.x)-associated proteins', *J Biol Chem*, 279(21), pp. 22331-46.

Leppert, I.R., Almli, C.R., McKinstry, R.C., Mulkern, R.V., Pierpaoli, C., Rivkin, M.J. and Pike, G.B. (2009) 'T(2) relaxometry of normal pediatric brain development', *J Magn Reson Imaging*, 29(2), pp. 258-67.

Levi, S., Grady, R.M., Henry, M.D., Campbell, K.P., Sanes, J.R. and Craig, A.M. (2002) 'Dystroglycan is selectively associated with inhibitory GABAergic synapses but is dispensable for their differentiation', *J Neurosci*, 22(11), pp. 4274-85.

Liddelow, S.A. (2015) 'Development of the choroid plexus and blood-CSF barrier', *Frontiers in Neuroscience*, 9, p. 32.

Lidov, H.G. (1996) 'Dystrophin in the nervous system', *Brain Pathol*, 6(1), pp. 63-77.

Lidov, H.G., Byers, T.J. and Kunkel, L.M. (1993) 'The distribution of dystrophin in the murine central nervous system: an immunocytochemical study', *Neuroscience*, 54(1), pp. 167-87.

Lidov, H.G., Byers, T.J., Watkins, S.C. and Kunkel, L.M. (1990) 'Localization of dystrophin to postsynaptic regions of central nervous system cortical neurons', *Nature*, 348(6303), pp. 725-8.

Lidov, H.G., Selig, S. and Kunkel, L.M. (1995) 'Dp140: a novel 140 kDa CNS transcript from the dystrophin locus', *Hum Mol Genet*, 4(3), pp. 329-35.

Lo Mauro, A., D'Angelo, M.G., Romei, M., Motta, F., Colombo, D., Comi, G.P., Pedotti, A., Marchi, E., Turconi, A.C., Bresolin, N. and Aliverti, A. (2010) 'Abdominal volume contribution to tidal volume as an early indicator of respiratory impairment in Duchenne muscular dystrophy', *Eur Respir J*, 35(5), pp. 1118-25.

Lobe, S.L., Bernstein, M.C. and German, R.Z. (2006) 'Life-long protein malnutrition in the rat (Rattus norvegicus) results in altered patterns of craniofacial growth and smaller individuals', *J Anat*, 208(6), pp. 795-812.

Love, D.R., Morris, G.E., Ellis, J.M., Fairbrother, U., Marsden, R.F., Bloomfield, J.F., Edwards, Y.H., Slater, C.P., Parry, D.J. and Davies, K.E. (1991) 'Tissue distribution of the dystrophin-related gene product and expression in the mdx

and dy mouse', *Proceedings of the National Academy of Sciences of the United States of America*, 88(8), pp. 3243-3247.

Lowery, L.A. and Sive, H. (2009) 'Totally Tubular: The Mystery behind Function and Origin of the Brain Ventricular System', *BioEssays : news and reviews in molecular, cellular and developmental biology*, 31(4), pp. 446-458.

Lv, S.Y., Zou, Q.H., Cui, J.L., Zhao, N., Hu, J., Long, X.Y., Sun, Y.C., He, J., Zhu, C.Z., He, Y. and Zang, Y.F. (2011) 'Decreased gray matter concentration and local synchronization of spontaneous activity in the motor cortex in Duchenne muscular dystrophy', *AJNR Am J Neuroradiol*, 32(11), pp. 2196-200.

Macdonald, R.L. and Olsen, R.W. (1994) 'GABAA receptor channels', *Annu Rev Neurosci*, 17, pp. 569-602.

Mah, J.K. (2016) 'Current and emerging treatment strategies for Duchenne muscular dystrophy', *Neuropsychiatr Dis Treat*, 12, pp. 1795-807.

Mah, J.K., Korngut, L., Dykeman, J., Day, L., Pringsheim, T. and Jette, N. (2014) 'A systematic review and meta-analysis on the epidemiology of Duchenne and Becker muscular dystrophy', *Neuromuscul Disord*, 24(6), pp. 482-91.

Malykh, Y.N., Schauer, R. and Shaw, L. (2001) 'N-Glycolylneuraminic acid in human tumours', *Biochimie*, 83(7), pp. 623-34.

Maren, S. and Fanselow, M.S. (1995) 'Synaptic plasticity in the basolateral amygdala induced by hippocampal formation stimulation in vivo', *J Neurosci*, 15(11), pp. 7548-64.

Mark F. Bear, B.W.C., Michael A. Paradiso (2007) *Neuroscience: Exploring the brain*. Third edn. Philadelphia: Lippincott Williams & Wilkins.

Markham, L.W., Kinnett, K., Wong, B.L., Woodrow Benson, D. and Cripe, L.H. (2008) 'Corticosteroid treatment retards development of ventricular dysfunction in Duchenne muscular dystrophy', *Neuromuscul Disord*, 18(5), pp. 365-70.

Martigne, L., Salleron, J., Mayer, M., Cuisset, J.M., Carpentier, A., Neve, V., Tiffreau, V., Guimber, D. and Gottrand, F. (2011) 'Natural evolution of weight status in Duchenne muscular dystrophy: a retrospective audit', *Br J Nutr*, 105(10), pp. 1486-91.

Martinez-Cue, C., Rueda, N., Garcia, E. and Florez, J. (2006) 'Anxiety and panic responses to a predator in male and female Ts65Dn mice, a model for Down syndrome', *Genes Brain Behav*, 5(5), pp. 413-22.

Masser, D.R., Bixler, G.V., Brucklacher, R.M., Yan, H., Giles, C.B., Wren, J.D., Sonntag, W.E. and Freeman, W.M. (2014) 'Hippocampal Subregions Exhibit Both Distinct and Shared Transcriptomic Responses to Aging and Nonneurodegenerative Cognitive Decline', *J Gerontol A Biol Sci Med Sci*.

McEwen, B.S. (1997) 'Possible mechanisms for atrophy of the human hippocampus', *Mol Psychiatry*, 2(3), pp. 255-62.

McLaughlin, K.J., Baran, S.E. and Conrad, C.D. (2009) 'Chronic stress- and sex-specific neuromorphological and functional changes in limbic structures', *Mol Neurobiol*, 40(2), pp. 166-82.

Mehler, M.F. (2000) 'Brain dystrophin, neurogenetics and mental retardation', *Brain Res Brain Res Rev*, 32(1), pp. 277-307.

Mehler, M.F., Haas, K.Z., Kessler, J.A. and Stanton, P.K. (1992) 'Enhanced sensitivity of hippocampal pyramidal neurons from mdx mice to hypoxia-induced loss of synaptic transmission', *Proc Natl Acad Sci U S A*, 89(6), pp. 2461-5.

Mendell, J.R., Moxley, R.T., Griggs, R.C., Brooke, M.H., Fenichel, G.M., Miller, J.P., King, W., Signore, L., Pandya, S., Florence, J. and et al. (1989) 'Randomized, double-blind six-month trial of prednisone in Duchenne's muscular dystrophy', *N Engl J Med*, 320(24), pp. 1592-7.

Mendell, J.R., Rodino-Klapac, L.R., Sahenk, Z., Roush, K., Bird, L., Lowes, L.P., Alfano, L., Gomez, A.M., Lewis, S., Kota, J., Malik, V., Shontz, K., Walker, C.M., Flanigan, K.M., Corridore, M., Kean, J.R., Allen, H.D., Shilling, C., Melia, K.R., Sazani, P., Saoud, J.B. and Kaye, E.M. (2013) 'Eteplirsen for the treatment of Duchenne muscular dystrophy', *Ann Neurol*, 74(5), pp. 637-47.

Mensen, V.T., Wierenga, L.M., van Dijk, S., Rijks, Y., Oranje, B., Mandl, R.C. and Durston, S. (2017) 'Development of cortical thickness and surface area in autism spectrum disorder', *Neuroimage Clin*, 13, pp. 215-222.

Meryon, E. (1852) 'On Granular and Fatty Degeneration of the Voluntary Muscles', *Med Chir Trans*, 35, pp. 73-84.1.

Michinaga, S. and Koyama, Y. (2017) 'Protection of the Blood-Brain Barrier as a Therapeutic Strategy for Brain Damage', *Biol Pharm Bull*, 40(5), pp. 569-575.

Miller, G., Tunnecliffe, M. and Douglas, P.S. (1985) 'IQ, prognosis and Duchenne muscular dystrophy', *Brain Dev*, 7(1), pp. 7-9.

Miranda, R., Laroche, S. and Vaillend, C. (2016) 'Reduced neuronal density in the CA1 anterodorsal hippocampus of the mdx mouse', *Neuromuscul Disord*, 26(11), pp. 775-781.

Miranda, R., Nagapin, F., Bozon, B., Laroche, S., Aubin, T. and Vaillend, C. (2015) 'Altered social behavior and ultrasonic communication in the dystrophin-deficient mdx mouse model of Duchenne muscular dystrophy', *Mol Autism*, 6, pp 60.

Moizard, M.P., Billard, C., Toutain, A., Berret, F., Marmin, N. and Moraine, C. (1998) 'Are Dp71 and Dp140 brain dystrophin isoforms related to cognitive impairment in Duchenne muscular dystrophy?', *Am J Med Genet*, 80(1), pp. 32-41.

Monaco, A.P., Bertelson, C.J., Liechti-Gallati, S., Moser, H. and Kunkel, L.M. (1988) 'An explanation for the phenotypic differences between patients bearing partial deletions of the DMD locus', *Genomics*, 2(1), pp. 90-5.

Monaco, A.P., Neve, R.L., Colletti-Feener, C., Bertelson, C.J., Kurnit, D.M. and Kunkel, L.M. (1986) 'Isolation of candidate cDNAs for portions of the Duchenne muscular dystrophy gene', *Nature*, 323(6089), pp. 646-50.

Morrow, R.S. and Cohen, J. (1954) 'The psychosocial factors in muscular dystrophy', *J Child Psychiatry*, 3(1), pp. 70-80.

Moxley, R.T., 3rd, Ashwal, S., Pandya, S., Connolly, A., Florence, J., Mathews, K., Baumbach, L., McDonald, C., Sussman, M. and Wade, C. (2005) 'Practice parameter: corticosteroid treatment of Duchenne dystrophy: report of the Quality Standards Subcommittee of the American Academy of Neurology and the Practice Committee of the Child Neurology Society', *Neurology*, 64(1), pp. 13-20.

Muntoni, F., Mateddu, A. and Serra, G. (1991) 'Passive avoidance behaviour deficit in the mdx mouse', *Neuromuscul Disord*, 1(2), pp. 121-3.

Muntoni, F., Torelli, S. and Ferlini, A. (2003) 'Dystrophin and mutations: one gene, several proteins, multiple phenotypes', *The Lancet Neurology*, 2(12), pp. 731-740.

Murphy, S., Dowling, P., Zweyer, M., Henry, M., Meleady, P., Mundegar, R.R., Swandulla, D. and Ohlendieck, K. (2017) 'Proteomic profiling of mdx-4cv serum reveals highly elevated levels of the inflammation-induced plasma marker haptoglobin in muscular dystrophy', *Int J Mol Med*, 39(6), pp. 1357-1370.

Murphy, S., Zweyer, M., Henry, M., Meleady, P., Mundegar, R.R., Swandulla, D. and Ohlendieck, K. (2015) 'Label-free mass spectrometric analysis reveals complex changes in the brain proteome from the mdx-4cv mouse model of Duchenne muscular dystrophy', *Clin Proteomics*, 12, pp. 27.

Naito-Matsui, Y., Davies, L.R., Takematsu, H., Chou, H.H., Tangvoranuntakul, P., Carlin, A.F., Verhagen, A., Heyser, C.J., Yoo, S.W., Choudhury, B., Paton, J.C., Paton, A.W., Varki, N.M., Schnaar, R.L. and Varki, A. (2017) 'Physiological Exploration of the Long Term Evolutionary Selection against Expression of N-Glycolylneuraminic Acid in the Brain', *J Biol Chem*, 292(7), pp. 2557-2570.

Nakao, K., Matsuyama, K., Matsuki, N. and Ikegaya, Y. (2004) 'Amygdala stimulation modulates hippocampal synaptic plasticity', *Proc Natl Acad Sci U S A*, 101(39), pp. 14270-5.

Neves, G., Cooke, S.F. and Bliss, T.V.P. (2008) 'Synaptic plasticity, memory and the hippocampus: a neural network approach to causality', *Nat Rev Neurosci*, 9(1), pp. 65-75.

Nguyen, D.H., Tangvoranuntakul, P. and Varki, A. (2005) 'Effects of natural human antibodies against a nonhuman sialic acid that metabolically incorporates into activated and malignant immune cells', *J Immunol*, 175(1), pp. 228-36.

Nicchia, G.P., Nico, B., Camassa, L.M., Mola, M.G., Loh, N., Dermietzel, R., Spray, D.C., Svelto, M. and Frigeri, A. (2004a) 'The role of aquaporin-4 in the blood-brain barrier development and integrity: studies in animal and cell culture models', *Neuroscience*, 129(4), pp. 935-45.

Nicchia, G.P., Nico, B., Camassa, L.M.A., Mola, M.G., Loh, N., Dermietzel, R., Spray, D.C., Svelto, M. and Frigeri, A. (2004b) 'The role of aquaporin-4 in the blood–brain barrier development and integrity: Studies in animal and cell culture models', *Neuroscience*, 129(4), pp. 935-944.

Nichols, B., Takeda, S., ichi and Yokota, T. (2015) 'Nonmechanical Roles of Dystrophin and Associated Proteins in Exercise, Neuromuscular Junctions, and Brains', *Brain Sciences*, 5(3), p. 275.

Nico, B., Frigeri, A., Nicchia, G.P., Quondamatteo, F., Herken, R., Errede, M., Ribatti, D., Svelto, M. and Roncali, L. (2001) 'Role of aquaporin-4 water channel in the development and integrity of the blood-brain barrier', *J Cell Sci*, 114(Pt 7), pp. 1297-307.

Nico, B., Paola Nicchia, G., Frigeri, A., Corsi, P., Mangieri, D., Ribatti, D., Svelto, M. and Roncali, L. (2004) 'Altered blood-brain barrier development in dystrophic MDX mice', *Neuroscience*, 125(4), pp. 921-35.

Nico, B., Roncali, L., Mangieri, D. and Ribatti, D. (2005) 'Blood-brain barrier alterations in MDX mouse, an animal model of the Duchenne muscular dystrophy', *Curr Neurovasc Res*, 2(1), pp. 47-54.

Nico, B., Tamma, R., Annese, T., Mangieri, D., De Luca, A., Corsi, P., Benagiano, V., Longo, V., Crivellato, E., Salmaggi, A. and Ribatti, D. (2010) 'Glial dystrophin-associated proteins, laminin and agrin, are downregulated in the brain of mdx mouse', *Lab Invest*, 90(11), pp. 1645-60.

Obermeier, B., Daneman, R. and Ransohoff, R.M. (2013) 'Development, maintenance and disruption of the blood-brain barrier', *Nat Med*, 19(12), pp. 1584-96.

Ohtsu, M., Sakai, N., Fujita, H., Kashiwagi, M., Gasa, S., Shimizu, S., Eguchi, Y., Tsujimoto, Y., Sakiyama, Y., Kobayashi, K. and Kuzumaki, N. (1997) 'Inhibition of apoptosis by the actin-regulatory protein gelsolin', *Embo j*, 16(15), pp. 4650-6.

Okerblom, J. and Varki, A. (2017) 'Biochemical, Cellular, Physiological and Pathological Consequences of Human loss of N-glycolylneuraminic Acid', *Chembiochem*.pp 124.

Owler, B.K., Pitham, T. and Wang, D. (2010) 'Aquaporins: relevance to cerebrospinal fluid physiology and therapeutic potential in hydrocephalus', *Cerebrospinal Fluid Res*, 7, pp. 15-9.

Pagnamenta, A.T., Holt, R., Yusuf, M., Pinto, D., Wing, K., Betancur, C., Scherer, S.W., Volpi, E.V. and Monaco, A.P. (2011) 'A family with autism and rare copy number variants disrupting the Duchenne/Becker muscular dystrophy gene DMD and TRPM3', *J Neurodev Disord*, 3(2), pp. 124-31.

Palta, S., Saroa, R. and Palta, A. (2014) 'Overview of the coagulation system', *Indian Journal of Anaesthesia*, 58(5), pp. 515-523.

Pane, M., Messina, S., Bruno, C., D'Amico, A., Villanova, M., Brancalion, B., Sivo, S., Bianco, F., Striano, P., Battaglia, D., Lettori, D., Vita, G.L., Bertini, E.,

Gualandi, F., Ricotti, V., Ferlini, A. and Mercuri, E. (2013) 'Duchenne muscular dystrophy and epilepsy', *Neuromuscul Disord*, 23(4), pp. 313-5.

Papadopoulos, M.C., Manley, G.T., Krishna, S. and Verkman, A.S. (2004) 'Aquaporin-4 facilitates reabsorption of excess fluid in vasogenic brain edema', *Faseb j*, 18(11), pp. 1291-3.

Papadopoulos, M.C. and Verkman, A.S. (2007) 'Aquaporin-4 and brain edema', *Pediatr Nephrol*, 22(6), pp. 778-84.

Passamano, L., Taglia, A., Palladino, A., Viggiano, E., D'Ambrosio, P., Scutifero, M., Rosaria Cecio, M., Torre, V., De Luca, F., Picillo, E., Paciello, O., Piluso, G., Nigro, G. and Politano, L. (2012) 'Improvement of survival in Duchenne Muscular Dystrophy: retrospective analysis of 835 patients', *Acta Myologica*, 31(2), pp. 121-125.

Paul, J., Strickland, S. and Melchor, J.P. (2007) 'Fibrin deposition accelerates neurovascular damage and neuroinflammation in mouse models of Alzheimer's disease', *The Journal of Experimental Medicine*, 204(8), pp. 1999-2008.

Paxinos, K.B.J.G. (2008) *The mouse brain in stereotaxic coordinates* Compact Third Edition edn. Elsevier

Percival, J.M., Siegel, M.P., Knowels, G. and Marcinek, D.J. (2013) 'Defects in mitochondrial localization and ATP synthesis in the mdx mouse model of Duchenne muscular dystrophy are not alleviated by PDE5 inhibition', *Hum Mol Genet*, 22(1), pp. 153-67.

Piluso, G., Mirabella, M., Ricci, E., Belsito, A., Abbondanza, C., Servidei, S., Puca, A.A., Tonali, P., Puca, G.A. and Nigro, V. (2000) 'Gamma1- and gamma2-syntrophins, two novel dystrophin-binding proteins localized in neuronal cells', *J Biol Chem*, 275(21), pp. 15851-60.

Prosser, E.J., Murphy, E.G. and Thompson, M.W. (1969) 'Intelligence and the gene for Duchenne muscular dystrophy', *Arch Dis Child*, 44(234), pp. 221-30.

Pundir, S., Martin, M.J. and O'Donovan, C. (2017) 'UniProt Protein Knowledgebase', *Methods Mol Biol*, 1558, pp. 41-55.

Purves D, A.G., Fitzpatrick D, (2001) 'Neuroscience ', in Sinauer Associates.

Qiu, G.P., Xu, J., Zhuo, F., Sun, S.Q., Liu, H., Yang, M., Huang, J., Lu, W.T. and Huang, S.Q. (2015) 'Loss of AQP4 polarized localization with loss of beta-dystroglycan immunoreactivity may induce brain edema following intracerebral hemorrhage', *Neurosci Lett*, 588, pp. 42-8.

Rae, C., Griffin, J.L., Blair, D.H., Bothwell, J.H., Bubb, W.A., Maitland, A. and Head, S. (2002) 'Abnormalities in brain biochemistry associated with lack of dystrophin: studies of the mdx mouse', *Neuromuscul Disord*, 12(2), pp. 121-9.

Rae, C., Scott, R.B., Thompson, C.H., Dixon, R.M., Dumughn, I., Kemp, G.J., Male, A., Pike, M., Styles, P. and Radda, G.K. (1998) 'Brain biochemistry in Duchenne muscular dystrophy: a 1H magnetic resonance and neuropsychological study', *J Neurol Sci*, 160(2), pp. 148-57.

Rapaport, D., Passos-Bueno, M.R., Brandao, L., Love, D., Vainzof, M. and Zatz, M. (1991) 'Apparent association of mental retardation and specific patterns of deletions screened with probes cf56a and cf23a in Duchenne muscular dystrophy', *Am J Med Genet*, 39(4), pp. 437-41.

Reiss, A.L., Abrams, M.T., Greenlaw, R., Freund, L. and Denckla, M.B. (1995) 'Neurodevelopmental effects of the FMR-1 full mutation in humans', *Nat Med*, 1(2), pp. 159-67.

Reiss, A.L., Abrams, M.T., Singer, H.S., Ross, J.L. and Denckla, M.B. (1996) 'Brain development, gender and IQ in childrenA volumetric imaging study', *Brain*, 119(5), pp. 1763-1774.

Remmelink, E., Aartsma-Rus, A., Smit, A.B., Verhage, M. and Loos, M. (2016) 'Cognitive flexibility deficits in a mouse model for the absence of full-length dystrophin', 15(6), pp. 558-67.

Ricotti, V., Mandy, W.P., Scoto, M., Pane, M., Deconinck, N., Messina, S., Mercuri, E., Skuse, D.H. and Muntoni, F. (2016) 'Neurodevelopmental, emotional, and behavioural problems in Duchenne muscular dystrophy in relation to underlying dystrophin gene mutations', *Dev Med Child Neurol*, 58(1), pp. 77-84.

Risher, W.C. and Eroglu, C. (2012) 'Thrombospondins as key regulators of synaptogenesis in the central nervous system', *Matrix biology : journal of the International Society for Matrix Biology*, 31(3), pp. 170-177.

Roberts, R.G., Coffey, A.J., Bobrow, M. and Bentley, D.R. (1993) 'Exon structure of the human dystrophin gene', *Genomics*, 16(2), pp. 536-8.

Robinson-Hamm, J.N. and Gersbach, C.A. (2016) 'Gene therapies that restore dystrophin expression for the treatment of Duchenne muscular dystrophy', *Hum Genet*, 135(9), pp. 1029-40.

Roos, A., Kollipara, L., Buchkremer, S., Labisch, T., Brauers, E., Gatz, C., Lentz, C., Gerardo-Nava, J., Weis, J. and Zahedi, R.P. (2016) 'Cellular Signature of SIL1 Depletion: Disease Pathogenesis due to Alterations in Protein Composition Beyond the ER Machinery', *Mol Neurobiol*, 53(8), pp. 5527-41.

Rosina, A., Morara, S. and Provini, L. (1999) 'GAT-1 developmental expression in the rat cerebellar cortex: basket and pinceau formation', *Neuroreport*, 10(7), pp. 1613-8.

Rosman, N.P. (1970) 'The cerebral defect and myopathy in Duchenne muscular dystrophy. A comparative clinicopathological study', *Neurology*, 20(4), pp. 329-35.

Rosman, N.P. and Kakulas, B.A. (1966) 'Mental deficiency associated with muscular dystrophy. A neuropathological study', *Brain*, 89(4), pp. 769-88.

Rudolph, U. and Mohler, H. (2014) 'GABAA receptor subtypes: Therapeutic potential in Down syndrome, affective disorders, schizophrenia, and autism', *Annu Rev Pharmacol Toxicol*, 54, pp. 483-507.

Ryding, E., Decety, J., Sjoholm, H., Stenberg, G. and Ingvar, D.H. (1993) 'Motor imagery activates the cerebellum regionally. A SPECT rCBF study with 99mTc-HMPAO', *Brain Res Cogn Brain Res*, 1(2), pp. 94-9.

Ryu, J.K. and McLarnon, J.G. (2009) 'A leaky blood–brain barrier, fibrinogen infiltration and microglial reactivity in inflamed Alzheimer's disease brain', *Journal of Cellular and Molecular Medicine*, 13(9a), pp. 2911-2925.

Ryu, J.K., Petersen, M.A., Murray, S.G., Baeten, K.M., Meyer-Franke, A., Chan, J.P., Vagena, E., Bedard, C., Machado, M.R., Coronado, P.E.R., Prod'homme, T., Charo, I.F., Lassmann, H., Degen, J.L., Zamvil, S.S. and Akassoglou, K. (2015) 'Blood coagulation protein fibrinogen promotes autoimmunity and demyelination via chemokine release and antigen presentation', *Nature Communications*, 6, p. 8164.

Sah, P., Faber, E.S., Lopez De Armentia, M. and Power, J. (2003) 'The amygdaloid complex: anatomy and physiology', *Physiol Rev*, 83(3), pp. 803-34.

Sarig, R., Mezger-Lallemand, V., Gitelman, I., Davis, C., Fuchs, O., Yaffe, D. and Nudel, U. (1999) 'Targeted inactivation of Dp71, the major non-muscle product of the DMD gene: differential activity of the Dp71 promoter during development', *Hum Mol Genet*, 8(1), pp. 1-10.

Sarnyai, Z., Sibille, E.L., Pavlides, C., Fenster, R.J., McEwen, B.S. and Tóth, M. (2000) 'Impaired hippocampal-dependent learning and functional abnormalities in the hippocampus in mice lacking serotonin1A receptors', *Proceedings of the National Academy of Sciences*, 97(26), pp. 14731-14736.

Sawiak, S.J., Wood, N.I., Williams, G.B., Morton, A.J. and Carpenter, T.A. (2009) 'Voxel-based morphometry in the R6/2 transgenic mouse reveals differences between genotypes not seen with manual 2D morphometry', *Neurobiology of Disease*, 33(1), pp. 20-27.

Sawiak, S.J., Wood, N.I., Williams, G.B., Morton, A.J. and Carpenter, T.A. (2013) 'Voxel-based morphometry with templates and validation in a mouse model of Huntington's disease()', *Magnetic Resonance Imaging*, 31(9), pp. 1522-1531.

Schmidt-Hieber, C., Jonas, P. and Bischofberger, J. (2004) 'Enhanced synaptic plasticity in newly generated granule cells of the adult hippocampus', *Nature*, 429(6988), pp. 184-7.

Schmidt-Kastner, R. (2015) 'Genomic approach to selective vulnerability of the hippocampus in brain ischemia-hypoxia', *Neuroscience*, 309, pp. 259-79.

Sebastiani, A., Hirnet, T., Jahn-Eimermacher, A. and Thal, S.C. (2017) 'Comparison of speed-vacuum method and heat-drying method to measure brain water content of small brain samples', *Journal of Neuroscience Methods*, 276, pp. 73-78.

Sekiguchi, M., Zushida, K., Yoshida, M., Maekawa, M., Kamichi, S., Yoshida, M., Sahara, Y., Yuasa, S., Takeda, S. and Wada, K. (2009) 'A deficit of brain dystrophin impairs specific amygdala GABAergic transmission and enhances defensive behaviour in mice', *Brain*, 132(Pt 1), pp. 124-35.

Senanayake, P.K., Rogers, N.J., Finney, K.N., Harvey, P., Funk, A.M., Wilson, J.I., O'Hogain, D., Maxwell, R., Parker, D. and Blamire, A.M. (2017) 'A new paramagnetically shifted imaging probe for MRI', *Magn Reson Med*, 77(3), pp. 1307-1317.

Shin, J.H., Hakim, C.H., Zhang, K. and Duan, D. (2011) 'Genotyping mdx, mdx3cv, and mdx4cv mice by primer competition polymerase chain reaction', *Muscle Nerve*, 43(2), pp. 283-6.

Shoji, H., Takao, K., Hattori, S. and Miyakawa, T. (2016) 'Age-related changes in behavior in C57BL/6J mice from young adulthood to middle age', *Mol Brain*, 9, p. 11.

Silverman, J.L., Yang, M., Lord, C. and Crawley, J.N. (2010) 'Behavioural phenotyping assays for mouse models of autism', *Nature reviews. Neuroscience*, 11(7), pp. 490-502.

Smalheiser, N.R. and Kim, E. (1995) 'Purification of cranin, a laminin binding membrane protein. Identity with dystroglycan and reassessment of its carbohydrate moieties', *J Biol Chem*, 270(25), pp. 15425-33.

Snow, W.M., Anderson, J.E. and Fry, M. (2014) 'Regional and genotypic differences in intrinsic electrophysiological properties of cerebellar Purkinje neurons from wild-type and dystrophin-deficient mdx mice', *Neurobiol Learn Mem*, 107, pp. 19-31.

Snow, W.M., Fry, M. and Anderson, J.E. (2013) 'Increased density of dystrophin protein in the lateral versus the vermal mouse cerebellum', *Cell Mol Neurobiol*, 33(4), pp. 513-20.

Sparks, B.F., Friedman, S.D., Shaw, D.W., Aylward, E.H., Echelard, D., Artru, A.A., Maravilla, K.R., Giedd, J.N., Munson, J., Dawson, G. and Dager, S.R. (2002) 'Brain structural abnormalities in young children with autism spectrum disorder', *Neurology*, 59(2), pp. 184-92.

Spijker, S. (2011) *Neuroproteomics*. Spinger Protocols

Spurney, C.F. (2011) 'Cardiomyopathy of Duchenne muscular dystrophy: current understanding and future directions', *Muscle Nerve*, 44(1), pp. 8-19.

Squire, S., Raymackers, J.M., Vandebrouck, C., Potter, A., Tinsley, J., Fisher, R., Gillis, J.M. and Davies, K.E. (2002) 'Prevention of pathology in mdx mice by expression of utrophin: analysis using an inducible transgenic expression system', *Hum Mol Genet*, 11(26), pp. 3333-44.

Stedman, H.H., Sweeney, H.L., Shrager, J.B., Maguire, H.C., Panettieri, R.A., Petrof, B., Narusawa, M., Leferovich, J.M., Sladky, J.T. and Kelly, A.M. (1991) 'The mdx mouse diaphragm reproduces the degenerative changes of Duchenne muscular dystrophy', *Nature*, 352(6335), pp. 536-9.

Straathof, C.S., Doorenweerd, N., Wokke, B.H., Dumas, E.M., van den Bergen, J.C., van Buchem, M.A., Hendriksen, J.G., Verschuuren, J.J. and Kan, H.E. (2014) 'Temporalis muscle hypertrophy and reduced skull eccentricity in Duchenne muscular dystrophy', *J Child Neurol*, 29(10), pp. 1344-8.

Straub, V., Rafael, J.A., Chamberlain, J.S. and Campbell, K.P. (1997) 'Animal models for muscular dystrophy show different patterns of sarcolemmal disruption', *J Cell Biol*, 139(2), pp. 375-85.

Südhof, T.C. (2008) 'Neuroligins and Neurexins Link Synaptic Function to Cognitive Disease', *Nature*, 455(7215), pp. 903-911.

Sunyer, B., Patil, S., Höger, H. and Lubec, G. (2007) 'Barnes maze, a useful task to assess spatial reference memory in the mice'.

Suzuki, Y., Higuchi, S., Aida, I., Nakajima, T. and Nakada, T. (2017) 'Abnormal distribution of GABAA receptors in brain of duchenne muscular dystrophy patients', *Muscle Nerve*, 55(4), pp. 591-595.

Szu, J.I. and Binder, D.K. (2016) 'The Role of Astrocytic Aquaporin-4 in Synaptic Plasticity and Learning and Memory', *Frontiers in Integrative Neuroscience*, 10, p. 8.

Takayama, C. and Inoue, Y. (2005) 'Developmental expression of GABA transporter-1 and 3 during formation of the GABAergic synapses in the mouse cerebellar cortex', *Developmental Brain Research*, 158(1–2), pp. 41-49.

Tamma, R., Annese, T., Capogrosso, R.F., Cozzoli, A., Benagiano, V., Sblendorio, V., Ruggieri, S., Crivellato, E., Specchia, G., Ribatti, D., De Luca, A. and Nico, B. (2013) 'Effects of prednisolone on the dystrophin-associated proteins in the blood-brain barrier and skeletal muscle of dystrophic mdx mice', *Lab Invest*, 93(5), pp. 592-610.

Tangvoranuntakul, P., Gagneux, P., Diaz, S., Bardor, M., Varki, N., Varki, A. and Muchmore, E. (2003) 'Human uptake and incorporation of an immunogenic nonhuman dietary sialic acid', *Proc Natl Acad Sci U S A*, 100(21), pp. 12045-50.

Taylor, P.J., Betts, G.A., Maroulis, S., Gilissen, C., Pedersen, R.L., Mowat, D.R., Johnston, H.M. and Buckley, M.F. (2010) 'Dystrophin Gene Mutation Location and the Risk of Cognitive Impairment in Duchenne Muscular Dystrophy', *PLoS ONE*, 5(1), p. e8803.

Tinsley, J.M., Blake, D.J., Roche, A., Fairbrother, U., Riss, J., Byth, B.C., Knight, A.E., Kendrick-Jones, J., Suthers, G.K., Love, D.R. and et al. (1992) 'Primary structure of dystrophin-related protein', *Nature*, 360(6404), pp. 591-3.

Tokarz, S.A., Duncan, N.M., Rash, S.M., Sadeghi, A., Dewan, A.K. and Pillers, D.A. (1998) 'Redefinition of dystrophin isoform distribution in mouse tissue by RT-PCR implies role in nonmuscle manifestations of duchenne muscular dystrophy', *Mol Genet Metab*, 65(4), pp. 272-81.

Tozawa, T., Itoh, K., Yaoi, T., Tando, S., Umekage, M., Dai, H., Hosoi, H. and Fushiki, S. (2012) 'The Shortest Isoform of Dystrophin (Dp40) Interacts with a Group of Presynaptic Proteins to Form a Presumptive Novel Complex in the Mouse Brain', *Molecular Neurobiology*, 45(2), pp. 287-297.

Tracey, I., Dunn, J.F. and Radda, G.K. (1996) 'Brain metabolism is abnormal in the mdx model of Duchenne muscular dystrophy', *Brain*, 119 (Pt 3), pp. 1039-44.

Tran, M.D. and Neary, J.T. (2006) 'Purinergic signaling induces thrombospondin-1 expression in astrocytes', *Proc Natl Acad Sci U S A*, 103(24), pp. 9321-6.

Tuon, L., Comim, C.M., Fraga, D.B., Scaini, G., Rezin, G.T., Baptista, B.R., Streck, E.L., Vainzof, M. and Quevedo, J. (2010) 'Mitochondrial respiratory chain and creatine kinase activities in mdx mouse brain', *Muscle Nerve*, 41(2), pp. 257-60.

Turk, R., Sterrenburg, E., de Meijer, E.J., van Ommen, G.J., den Dunnen, J.T. and t Hoen, P.A.C. (2005) 'Muscle regeneration in dystrophin-deficient mdx mice studied by gene expression profiling', *BMC Genomics*, 6(1), pp.98.

Uchino, M., Teramoto, H., Naoe, H., Yoshioka, K., Miike, T. and Ando, M. (1994) 'Localisation and characterisation of dystrophin in the central nervous system of controls and patients with Duchenne muscular dystrophy', *J Neurol Neurosurg Psychiatry*, 57(4), pp. 426-9.

Ueda, H., Baba, T., Terada, N., Kato, Y., Fujii, Y., Takayama, I., Mei, X. and Ohno, S. (2000) 'Immunolocalization of dystrobrevin in the astrocytic endfeet and endothelial cells in the rat cerebellum', *Neurosci Lett*, 283(2), pp. 121-4.

Ueda, Y., Suwazono, S., Maedo, S. and Higuchi, I. (2017) 'Profile of cognitive function in adults with duchenne muscular dystrophy', *Brain Dev*, 39(3), pp. 225-230.

Vago, D.R., Bevan, A. and Kesner, R.P. (2007) 'The role of the direct perforant path input to the CA1 subregion of the dorsal hippocampus in memory retention and retrieval', *Hippocampus*, 17(10), pp. 977-87.

Vaillend, C., Billard, J.M., Claudepierre, T., Rendon, A., Dutar, P. and Ungerer, A. (1998) 'Spatial discrimination learning and CA1 hippocampal synaptic plasticity in mdx and mdx3cv mice lacking dystrophin gene products', *Neuroscience*, 86(1), pp. 53-66.

Vaillend, C., Billard, J.M. and Laroche, S. (2004) 'Impaired long-term spatial and recognition memory and enhanced CA1 hippocampal LTP in the dystrophin-deficient Dmd(mdx) mouse', *Neurobiol Dis*, 17(1), pp. 10-20.

Vaillend, C. and Chaussenot, R. (2017) 'Relationships linking emotional, motor, cognitive and GABAergic dysfunctions in dystrophin-deficient mdx mice', *Hum Mol Genet*, 26(6), pp. 1041-1055.

Vaillend, C., Rampon, C., Davis, S. and Laroche, S. (2002) 'Gene control of synaptic plasticity and memory formation: implications for diseases and therapeutic strategies', *Curr Mol Med*, 2(7), pp. 613-28.

Vaillend, C., Rendon, A., Misslin, R. and Ungerer, A. (1995) 'Influence of dystrophin-gene mutation on mdx mouse behavior. I. Retention deficits at long delays in spontaneous alternation and bar-pressing tasks', *Behav Genet*, 25(6), pp. 569-79.

van Praag, H., Christie, B.R., Sejnowski, T.J. and Gage, F.H. (1999) 'Running enhances neurogenesis, learning, and long-term potentiation in mice', *Proc Natl Acad Sci U S A*, 96(23), pp. 13427-31.

van Putten, M., Hulsker, M., Nadarajah, V.D., van Heiningen, S.H., van Huizen, E., van Iterson, M., Admiraal, P., Messemaker, T., den Dunnen, J.T., t Hoen, P.A. and Aartsma-Rus, A. (2012) 'The effects of low levels of dystrophin on mouse muscle function and pathology', *PLoS One*, 7(2), p. e31937.

Vandamme, T.F. (2014) 'Use of rodents as models of human diseases', *Journal of Pharmacy & Bioallied Sciences*, 6(1), pp. 2-9.

Varga, O.E., Hansen, A.K., Sandoe, P. and Olsson, I.A. (2010) 'Validating animal models for preclinical research: a scientific and ethical discussion', *Altern Lab Anim*, 38(3), pp. 245-8.

Varju, P., Katarova, Z., Madarasz, E. and Szabo, G. (2001) 'GABA signalling during development: new data and old questions', *Cell Tissue Res*, 305(2), pp. 239-46.

Verkman, A.S. (2005) 'More than just water channels: unexpected cellular roles of aquaporins', *J Cell Sci*, 118(Pt 15), pp. 3225-32.

Vilmann, H. (1969) 'The growth of the cranial base in the albino rat revealed by roentgenocephalometry*', *Journal of Zoology*, 159(3), pp. 283-291.

Waite, A., Brown, S.C. and Blake, D.J. (2012) 'The dystrophin–glycoprotein complex in brain development and disease', *Trends in Neurosciences*, 35(8), pp. 487-496.

Wallace, G.Q. and McNally, E.M. (2009) 'Mechanisms of muscle degeneration, regeneration, and repair in the muscular dystrophies', *Annu Rev Physiol*, 71, pp. 37-57.

Wallis, T., Bubb, W.A., McQuillan, J.A., Balcar, V.J. and Rae, C. (2004) 'For want of a nail. ramifications of a single gene deletion, dystrophin, in the brain of the mouse', *Front Biosci*, 9, pp. 74-84.

Wang, S., Scott, B.W. and Wojtowicz, J.M. (2000) 'Heterogenous properties of dentate granule neurons in the adult rat', *J Neurobiol*, 42(2), pp. 248-57.

Wilcock, D.M., Vitek, M.P. and Colton, C.A. (2009) 'Vascular amyloid alters astrocytic water and potassium channels in mouse models and humans with Alzheimer's disease', *Neuroscience*, 159(3), pp. 1055-69.

Willmann, R., De Luca, A., Benatar, M., Grounds, M., Dubach, J., Raymackers, J.-M. and Nagaraju, K. (2012) 'Enhancing translation: guidelines for standard pre-clinical experiments in mdx mice', *Neuromuscular Disorders*, 22(1), pp. 43-49.

Willmann, R., Possekel, S., Dubach-Powell, J., Meier, T. and Ruegg, M.A. (2009) 'Mammalian animal models for Duchenne muscular dystrophy', *Neuromuscul Disord*, 19(4), pp. 241-9.

Wiskott, L., Rasch, M.J. and Kempermann, G. (2006) 'A functional hypothesis for adult hippocampal neurogenesis: avoidance of catastrophic interference in the dentate gyrus', *Hippocampus*, 16(3), pp. 329-43.

Wolf, A., Bauer, B., Abner, E.L., Ashkenazy-Frolinger, T. and Hartz, A.M.S. (2016) 'A Comprehensive Behavioral Test Battery to Assess Learning and Memory in 129S6/Tg2576 Mice', *PLoS ONE*, 11(1), p. e0147733.

Wong, B.L., Rybalsky, I., Shellenbarger, K.C., Tian, C., McMahon, M.A., Rutter, M.M., Sawnani, H. and Jefferies, J.L. (2017) 'Long-Term Outcome of Interdisciplinary Management of Patients with Duchenne Muscular Dystrophy Receiving Daily Glucocorticoid Treatment', *J Pediatr*, 182, pp. 296-303.e1.

Wu, J.Y., Kuban, K.C., Allred, E., Shapiro, F. and Darras, B.T. (2005) 'Association of Duchenne muscular dystrophy with autism spectrum disorder', *J Child Neurol*, 20(10), pp. 790-5.

Xu, S., Shi, D., Pratt, S.J., Zhu, W., Marshall, A. and Lovering, R.M. (2015) 'Abnormalities in brain structure and biochemistry associated with mdx mice measured by in vivo MRI and high resolution localized (1)H MRS', *Neuromuscul Disord*, 25(10), pp. 764-72.

Yamamoto, K., Yamada, D., Kabuta, T., Takahashi, A., Wada, K. and Sekiguchi, M. (2010) 'Reduction of abnormal behavioral response to brief restraint by information from other mice in dystrophin-deficient mdx mice', *Neuromuscul Disord*, 20(8), pp. 505-11.

Yamashita, T., Kanaya, K., Kawaguchi, S., Murakami, T. and Yokogushi, K. (2001) 'Prediction of progression of spinal deformity in Duchenne muscular dystrophy: a preliminary report', *Spine (Phila Pa 1976)*, 26(11), pp. E223-6.

Yang, R.J., Mozhui, K., Karlsson, R.M., Cameron, H.A., Williams, R.W. and Holmes, A. (2008) 'Variation in mouse basolateral amygdala volume is associated with differences in stress reactivity and fear learning', *Neuropsychopharmacology*, 33(11), pp. 2595-604.

Yoshida, M., Suzuki, A., Yamamoto, H., Noguchi, S., Mizuno, Y. and Ozawa, E. (1994) 'Dissociation of the complex of dystrophin and its associated proteins into several unique groups by n-octyl beta-D-glucoside', *Eur J Biochem*, 222(3), pp. 1055-61.

Yoshihara, Y., Onodera, H., Iinuma, K. and itoyama, Y. (2003) 'Abnormal kainic acid receptor density and reduced seizure susceptibility in dystrophin-deficient mdx mice', *Neuroscience*, 117(2), pp. 391-5.

Yoshioka, M., Okuno, T., Honda, Y. and Nakano, Y. (1980) 'Central nervous system involvement in progressive muscular dystrophy', *Archives of Disease in Childhood*, 55(8), pp. 589-594.

Zaccaria, M.L., Di Tommaso, F., Brancaccio, A., Paggi, P. and Petrucci, T.C. (2001) 'Dystroglycan distribution in adult mouse brain: a light and electron microscopy study', *Neuroscience*, 104(2), pp. 311-24.

Zamani, G., Heidari, M., Azizi Malamiri, R., Ashrafi, M.R., Mohammadi, M., Shervin Badv, R., Hosseini, S.A., Salehi, S., Shahrokhi, A., Qorbani, M. and Fathi, M.R. (2016) 'The quality of life in boys with Duchenne muscular dystrophy', *Neuromuscul Disord*, 26(7), pp. 423-7.

Zikopoulos, B. and Barbas, H. (2013) 'Altered neural connectivity in excitatory and inhibitory cortical circuits in autism', *Frontiers in Human Neuroscience*, 7, p. 609.

Zwaigenbaum, L. and Tarnopolsky, M. (2003) 'Two children with muscular dystrophies ascertained due to referral for diagnosis of autism', *J Autism Dev Disord*, 33(2), pp. 193-9.